

ECIO 2017

European Conference on Integrated Optics

Eindhoven University of Technology, Netherlands

Collected Manuscripts

(c) Copyright 2017 The ECIO Board. All rights reserved.

Contents

ID	Author	Title
S1.1	Ang Li, Yufei Xing, Wim Bogaerts	An integrated tunable reflector
S1.2	Jorge PARRA, Pablo SANCHIS	Particle Swarm Optimization for PolarizationIndependent and Low Loss Grating Couplers
S2.1	Fumi NAKAMURA, Keijiro SUZUKI, K	1 × 2 Wavefront Control Type Wavelength-Selective Switch by Silicon Waveguides
S2.2	Mu-Chieh Lo, Robinson Guzmán, Ca	Frequency Tuning of Symmetric Colliding Pulse ModeLocked Laser through Asymmetric Biasing IntraCavity Phase Modulators
S2.3	Niklas HOPPE, Philipp DIERSING,	Integrated Dual-Mode Interferometer with Differential Single-Mode Outputs
S2.4	Luis A. BRU, Gloria MICÓ, Daniel	Full field Group Velocity Dispersion characterization of 300nm film height Silicon Nitride waveguides
S2.5	Alison H. PERROTT, Ludovic CARO,	Mutual Injection Locking of Lasers in a Photonic Integrated Circuit
S2.6	Caterina TABALLIONE, Temitope AG	Temperature-immune readout of an integrated optical wavelength meter based on microring resonators
S2.7	Matthieu ROUSSEY, Ségolène PELIS	Strip-loaded horizontal slot waveguide: confinement with negligible losses
S2.8	Andrea ZANZI, Pablo SANCHIS, Jav	Design and Optimization of a High Speed Slow-Light Silicon Modulator in the O-Band
S2.9	Michiel DE GOEDE, Meindert DIJKS	High-Q Al2O3 Microring Resonator for Sensing Applications
S2.10	Stanisław STOPIŃSKI, Luc AUGUSTI	A single-frequency integrated ring laser for gyro applications
S2.11	Abi WAQAS, Daniele MELATI and An	Analysis of the sensitivity of Mach-Zehnder interferometer filter to fabrication tolerances through elementary effect test
S2.12	Tianran LIU, Francesco PAGLIANO,	Low-voltage Optical Switching by a Four-waveguide Directional Coupler
S2.13	Pascual MUÑOZ, Gloria MICÓ, Luis	Linear and non-linear propagation properties of state of the art Silicon Nitride waveguides
S2.14	Michiel DE GOEDE, Meindert DIJKS	Double Al2O3 Microring Resonator for Self-Referenced Sensing Applications
S2.15	Daniel GRAJALES, Jose Ramón SEND	Simulation and Experimental Evaluation of Optical Chirp Modulation for Bimodal Waveguide Interferometer Biosensors
S2.16	Alice BERNARD, Marco RAVARO, Jea	Widely tunable mid-IR monolithic coherent source
S2.17	Stanisław STOPIŃSKI, Krzysztof S	A multi-channel photonic integrated transmitter driven by an application specific integrated circuit
S2.18	Hiroki KISHIKAWA, Kensuke INOSHI	Noise Tolerance in Integrated-Optic Recognition Circuit for Optical 16QAM Codes
S2.19	B. Imran Akca	Design of a Multiple-reference Time-domain Optical Coherence Tomography System
S2.20	João M. MAIA, Vítor A. AMORIM, D	Fabrication of Monolithic Optofluidic Evanescent Probing Device for Sensing Applications
S2.21	Daniel Benedikovic, Carlos Alons	Dispersion controlling in strained silicon waveguides using sub-wavelength grating metamaterials
S2.22	Benjamin WOHLFEIL, Danish RAFIQU	Photonic Integrated Circuits for Data Center Interconnects
S3.1	Mitsuru TAKENAKA, Shinichi TAKAG	Photonic Integrated Circuit Platform using III-V on SiC Wafer
S3.2	Stéphane CALVEZ, Alexandre ARNOU	Buried Waveguides using a Quasi-Planar Process
S3.3	Marco A. G. PORCEL, Jörn P. EPPI	Inducing second-order susceptibility in amorphous silicon nitride waveguides

S3.4	Nikolay NIKONOROV, Sergey IVANOV	Photo-Thermo-Refractive Glass Doped with Rare Earth Ions as a Substrate for Monolithic Integration of Optical Elements
S3.5	Leili Abdollahi Shiramin, Dries	Design of Hybrid Integrated Graphene Optical Switch with an III-V-on-Si laser
S3.6	Joan Manel RAMIREZ, Vladyslav VA	Ge-rich graded-index SiGe waveguides as enabling building blocks for broadband mid Infrared integrated photonics
S3.7	Gerrit W. STEEN, Adam D. WEXLER,	Fabrication considerations for differential absorption based optofluidic sensors to measure ionic content in water
S3.8	Natalia MORAIS, Fares CHOUCHANE,	AlGaAs nanowires for phase-matched SHG in the telecom range
S3.9	A. MICHARD, N. MICHIT, JB. QUELE	Influence of Thermo-mechanical Effects induced by 3D Assembly on Silicon Microring Resonator
S3.10	Valerio Flavio GILI, Lavinia GHI	Polarization properties of second harmonic signal from monolithic AlGaAs nanoantennas
S3.11	Jonathan LEMAITRE, Aldo GUTIERRE	Chalcogenides photonic integrated circuits for near- and mid-infrared applications
S3.12	Shane P. DUGGAN, Niall P. KELLY,	Development of Inverted p-Substrate InP/AlGaInAs Lasers for Vertical Integration with Multiple Passive or Active Intrinsic Regions
S3.13	J. Martínez de Mendívil, G. Lifa	Ridge waveguide lasers based on fs-laser writing on rare-earth doped crystals
S3.14	Anna Lena GIESECKE, Jens BOLTEN,	PIC Fabrication Platforms for SOI and Si3N4 in a Flexible Photonic Foundry Concept
S3.15	S. Hosseini, M. Cătuneanu, R. He	Energy consumption study of reverse-biased modulators in monolithic electronic-photonic technology
S3.16	Tommaso LUNGHI, Florent DOUTRE,	Soft-proton exchange on Lithium Niobate substrates doped with Magnesium-oxide: route toward efficient and powerresistant nonlinear converters.
S3.17	Aldo GUTIERREZ-ARROYO, Loïc BOD	Mid-Infrared chemical sensing using a chalcogenide integrated transducer
S3.18	Jorn P. VAN ENGELEN, Longfei SHE	Improving thermal performance of a UTC photodetector in the IMOS platform
S3.19	Getachew T. AYENEW, Pascal BALDI	Proton Exchanged Waveguides on Congruent Lithium Tantalate and MgO-doped Lithium Tantalate
S4.1	Frank Koppens	Graphene opto-electronics for data communication, image sensing and plasmonics
S4.2	Roman Koerner, Daniel Schwarz, C	The Germanium Zener-Emitter for Silicon Photonics
S4.3	Elena DURAN-VALDEIGLESIAS1, Weih	Hybrid integration of carbon nanotubes in silicon photonic resonators
S4.4	Giovanni MAGNO, Vy YAM, Béatrice	Integrated magneto-plasmonics for non-reciprocal optical devices
S5.1	Song TANG, Lianping HOU, Iain ED	Novel Sampled Grating Design for High Precision, Multiple Wavelength DFB Laser Arrays
S5.2	Mohamad Dernaika, Ludovic Caro,	Tunable Deeply Etched V-notch Reflectors
S5.3	Karen SOLIS-TRAPALA, Boudewijn D	Latest Developments in Low-Cost Integrated WDM Transceivers for Telecom Applications
S5.4	Dan Zhao, Dzmitry Pustakhod, Luc	Optical Frequency Domain Reflectometry for Characterization of Distributed Bragg Reflectors
S5.5	Luis A. BRU, Gloria MICÓ, Daniel	Fully Integrated Optical Frequency Domain Reflectometry
S6.1	Anatoly V Zayats	Active Plasmonics
S6.2	Alejandro ORTEGA-MOÑUX, Robert H	Subwavelength waveguide devices for Near and MidInfrared applications
S6.3	Robert HALIR, Pavel CHEBEN, Jose	Ultra-broadband Silicon Photonic Multimode Interference Coupler
S6.4	Wen Zhou, Zhenzhou Cheng, Yun Ga	Fully suspended slot waveguide racetrack resonators

S7.1	Hercules AVRAMOPOULOS1	The effect of photonic integration on the evolution of communication systems
S7.2	Sören DHOORE, Gunther ROELKENS,	Heterogeneously Integrated III-V/SOI DBR Laser with Over 7 nm Continuous Wavelength Tuning Range
S7.3	Maryam SHAYESTEH, Kevin SHORTISS	Se-multiplexing coherent optical combs within Photonic Integrated Circuits
S7.4	Jian-Jun He, Sen Zhang, Jianjun	Monolithic tunable lasers for low cost DWDM networks
S8.1	Xingyuan Xu, Jiayang Wu, Mehrdad	Microwave and RF Photonic Applications of Micro-Combs
S8.2	Maksym GROMOVYI, Fabrice SEMO	Efficient nonlinear interactions in GaN waveguides
S8.3	Panagiotis VERGYRIS, Thomas MEAN	Hybrid Integrated Photonics for On-Chip Heralded Photon-Number States
S8.4	Pierce MUNNELLY, Tobias HEINDEL,	Integrated Quantum Optics with Electrically Driven Quantum Dot – Micropillars
S8.5	Diego PEREZ-GALACHO, Carlos ALON	Sub-Wavelength engineered waveguide Bragg filter for optical pump-rejection
S9.1	Jing ZHANG, Amin ABASSI, Andreas	Silicon Photonic Transceiver Array based on the Transfer Printing of III-V O-band Photodetectors
S9.2	Tobias BECKERWERTH, Gan ZHOU, S	Balanced Waveguide Avalanche Photodetector Chip
S9.3	Douglas O. M. de AGUIAR, Andrea	Noise Insensitive Transparent Light Monitoring on a Silicon Photonics Chip
S9.4	Jose D. SARMIENTO-MERENGUEL, Jos	Demonstration of Silicon-On-Insulator Coherent receiver for Radio-Over-Fiber applications
S9.5	Andreas UMBACH	Photonic ICs for Ultrahigh Speed and Coherent Systems
S10.1	Di LIANG, Geza KURCZVEIL, Xue HU	Robust and energy efficient heterogeneous light sources in silicon
S10.2	Jason S. ORCUTT	Integrated photonic systems on silicon
S10.3	Rob GRIFFIN	InP PICs for Coherent Optical Transmission
S11.1	Sören DHOORE, Gunther ROELKENS,	Heterogeneously Integrated III-V/SOI DBR Laser with Over 7 nm Continuous Wavelength Tuning Range
S11.2	Julien Favreau, Jean-Michel Hart	Development of a SiGe Arrayed Waveguide Grating in the 2185-2285 cm-1 range
S11.3	Gloria MICÓ, Luis BRU, Daniel PA	C-band linear propagation characteristics for a 300 nm film height Silicon Nitride photonics platform
S11.4	Sanja Radosavljevic, Bart Kuyken	A Fiber-to-Chip Grating Coupler for the Ge-on-Si Platform at 5μm wavelength
S11.5	Goran Z. MASHANOVICH, Wei CAO, Z	Mid-infrared integrated photonics in silicon and germanium
S12.1	Daniel PEREZ, Ivana GASULLA, Jos	Integrated Microwave Photonics: The evolution from ASICs to Universal Processors
S12.2	Cyril C. Renaud, Katarzyna Balak	Recent development in integrated photonic solutions for THz systems
S12.3	Robinson GUZMÁN, Guillermo CARPI	Monolithically Integrated 1GHz Extended Cavity Linear Mode-Locked Laser
S12.4	Kasper VAN GASSE, Joris VAN KERR	26 GHz Carrier Frequency 10 Gbit/s Radio-over-Fiber Link based on a Directly Modulated III-V/Si DFB Laser
S13.1	Richard PITWON	Photonic Integration in Converged Data Centre Systems
S13.2	Jeremy WITZENS, Alvaro MOSCOSO-M	Silicon Photonics based WDM Systems: Chip and Module Level Integration
S13.3	M. Ding, A. Wonfor, Q. Cheng, R.	Dilated 4×4 Hybrid MZI-SOA Switch with Relaxed Active Bias Control
S13.4	Fengyuan SHI, Nikos BAMIEDAKIS,	Flexible Multimode Polymer Waveguides for High-Speed Optical Interconnects
S14.1	Yean-Sheng YONG, Sergio A. VÁZQU	High-gain waveguide amplifiers based on potassium rare-earth double tungstates
S14.2	Youwen FAN, Jörn P. EPPING, Ruud	Optically integrated InP-Si3N4 hybrid laser
S14.3	Artur HERMANS, Michiel VAN DAELE	Electro-Optic Modulation in Silicon Nitride Photonic Integrated Circuits by means of ALD ZnO Overlays
S14.4	Anne Talneau, I. Sagnes and G. P	High Optical Quality, Electrically-driven-compatible InP-on-Si Hybrid Interface

		elaborated at 300°C
S14.5	Amin ABBASI, Hongtao CHEN, Joche	Chirp Managed Optical Link based on a Directly Modulated InP/Si DFB Laser
S14.6	Vítor A. AMORIM, João M. MAIA, D	Fabrication of Add-Drop Multiplexers in Fused Silica by Femtosecond Laser Direct Writing
S15.1	Luc AUGUSTIN	InP based generic platform: the complete and versatile solution for photonic integrated circuits
S15.2	A.J. MILLAN-MEJIA, J.J.G.M. VAN	1×2 Multimode interference coupler with ultra-low reflections in membrane photonic integrated circuits
S15.3	Moritz Baier, Francisco M. Soare	Fully Integrated Serial Dual-Polarization Electroabsorption Modulator PIC in InP
S15.4	Marija TRAJKOVIC, Florian LEMAIT	First comparison of InGaAsP and InGaAlAs electroabsorption modulator in COBRA generic platform
S15.5	Mathias BERCIANO, Pedro DAMAS, X	Pockels Effect in Strained Silicon Waveguides
S16.1	Victor TSVIRKUN, Alessandro SURR	Integrated III-V Photonic Crystal – Si waveguide platform with tailored Optomechanical coupling
S16.2	Geert A.J. BESSELINK, Denys MARC	Evanescent Field based Optofluidic Platform in TriPleX for Sensitive Absorbance Detection of Chromophores
S16.3	Roel Baets	Silicon Photonics and its Applications in Life Science
S16.4	Ali Raza, Pieter Wuytens, Freder	On-chip Enhanced Raman spectroscopy using metal slot waveguide
S16.5	Loïc BODIOU, Jonathan LEMAITRE,	Rare-earth doped selenides active waveguides for integrated mid-infrared sensing applications
S17.1	Laura M. LECHUGA	Photonic lab-on-a-chip nanobiosensors for early diagnostics at the point-of-care
S17.2	James A. GUPTA, Andrew BEZINGER,	GaSb-based single-mode distributed feedback lasers for sensing
S17.3	Daniel J. Blumenthal	Ultra-Low Loss Si3N4 Waveguide Passive and Active Next Generation Photonic Integration for Optical Gyroscopes and Communications Applications
S18.1	Andrea FIORE, Maurangelo PETRUZZ	Integrated Quantum Photonics on a IIIV platform
S18.2	Avishek CHOWDHURY, Sylvain BARB	Stochastic Resonance with an Integrated NanoElectro-Mechanical Photonic Crystal Membrane
S18.3	X.J.M. Leijtens, R. Santos, M. T	MEMS-assisted fiber-chip coupling
S18.4	Kristinn B. GYLFASON, Carlos ERR	Photonic Biosensors Enabled by MEMS and Microfluidics Integration
S19.1	Piero ORLANDI, Marco PIAZZA, Luc	Silicon photonics: from present status to future developments
S19.2	Kengo NOZAKI, Shinji MATSUO, Tak	Ultralow-capacitance opto-electronic devices for femtojoule/bit photonics
S19.3	Yasuhiko ISHIKAWA, Kazuki ITO, M	Germanium-on-Silicon Photonic Devices

An integrated tunable reflector

Ang Li[1,2,*], Yufei Xing[1,2], Wim Bogaerts[1,2]
[1]Photonics Research Group, Ghent University-IMEC, 9052 Ghent, Belgium
[2]Center for Nano and Biophotonics, Ghent University, 9052 Ghent, Belgium
[*] ang.li@ugent.be

With past decade's development, silicon photonics grows to be one of the most promising platforms for integrated optics. Despite its rich component library that includes grating couplers, multi-mode interferometers (MMI), Mach-Zender-Interferometers (MZI), ring resonators, modulators, germanium photodetectors and doped heaters etc., some key basic building blocks are still missing or not very well developed and standardized. An integrated tunable reflector is one of them. Suggested by its name, such a device should provide a widely tunable reflectivity controlled by common tuning mechanism, like thermo-optic and free carrier plasma effects. Besides, it should fully fit into existing silicon photonics platforms, meaning no CMOS incompatible materials involved. In terms of its reflection spectrum, preferably it can switch between flat and wavelength dependent spectrum depending on the specific application.

Popular approaches for such devices are either Bragg grating based or ring resonator based [1,2]. The former one has poor tunability while ring resonator based devices are usually narrow band in its spectrum. Here, we propose a loop-ended MZI based reflector, as in Fig. 1(a). This structure can easily be incorporated in circuits shown in Fig. 1(b-c).

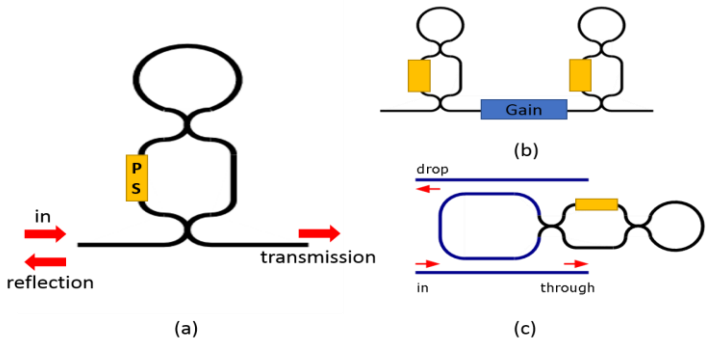


Fig. 1 (a) gives the schematic of our reflector with a phase shifter. (b) and (c) present two potential applications of such reflectors.

We use the optical circuit simulator *Caphe* by Luceda Photonics to perform rich simulations for such a device. The main design freedoms include the two arm lengths of the MZI and the coupling coefficients of the two directional couplers (DCs). A balanced MZI ($\Delta L = 0$) will generate a flat reflection spectrum as shown in Fig. 2(a), while a length difference $\Delta L \neq 0$ will result in a periodic wavelength dependence as in Fig. 2(b). For the latter case, a special spectrum where only one wavelength has zero reflection (shown in Fig. 2(c)) can be obtained if $m\lambda = 2\Delta L n_{eff}$, where m is the interference order, similar to that of a MZI. λ is the wavelength that has zero reflection, and n_{eff} is the effective index. This special reflection spectrum can have valuable applications in optical sensors and novel filters [3]. The simulated tunability is shown in Fig. 2(d). The blue and red curves in Fig. 2 (a,b,d) correspond to a circuit with ideal (DCs) and with dispersive (DCs), respectively.

Besides the length difference of the MZI, the performance of the reflector depends strongly on the coupling coefficients of its two directional couplers as evident in Fig. 3.

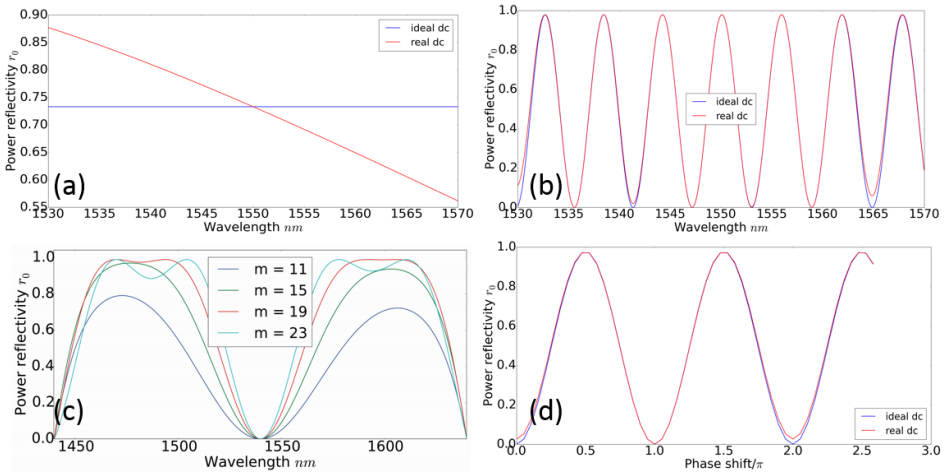


Fig. 2 (a) presents a flat reflection spectrum. (b) shows a wavelength dependent spectrum. (c) is a special case where only one point in a wide wavelength range suffers 0 reflection. (d) gives the simulated tunability.

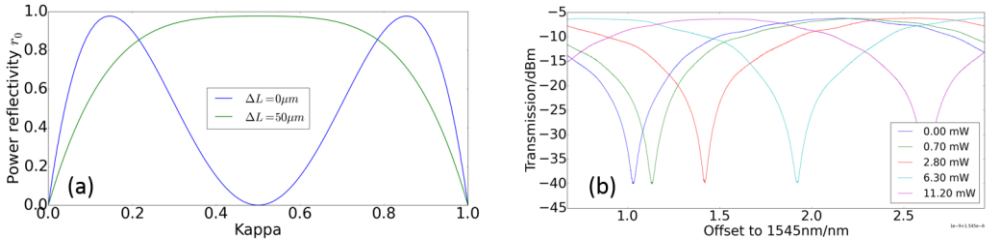


Fig. 3 (a) shows the influence of coupling coefficients on the reflectivity at 1550nm, (b) presents our active measurement. Less than 6.3mW can generate a 35dB change in transmission/reflection

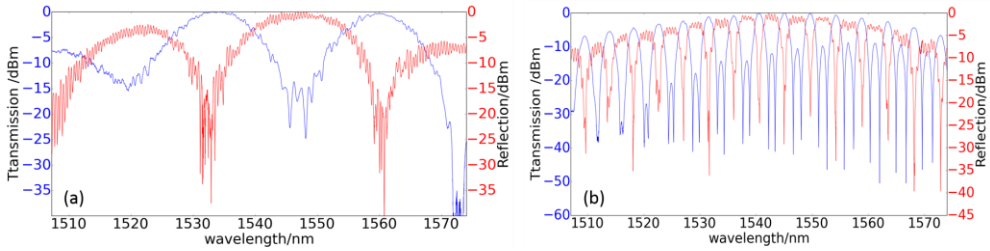


Fig. 4 (a) is a measured flat reflection spectrum. (b) is wavelength dependent.

In Fig. 4 we present our measurement results. Fig. 4(a) demonstrates a relatively flat reflection spectrum while (b) gives a strongly wavelength dependent spectrum. The index matching fluid with an index equals 1.54 was used in order to minimize the reflection at the fiber/air interface. The dynamic tuning by thermo-optic heater is given in Fig. 3(b). Less than 6mW can generate a 35 dB change in transmission/reflection.

References

[1] I. Giuntoni et al., *Tunable Bragg reflectors on silicon-on-insulator rib waveguides*, Optics Express, vol. 17, no. 21, pp. 18518-18524, 2009

[2] X. Li et al., *A tunable silicon ring reflector*, Journal of optics, vol. 44, no. 1, pp. 26-29, 2015

[3] A. Li et al., *Design of a single all-silicon ring resonator with a 150 nm free spectral range and a 100 nm tuning range around 1550 nm,* Photonics Research, vol. 4, no. 2, pp. 84-92, 2016



Particle Swarm Optimization for Polarization-Independent and Low Loss Grating Couplers

Jorge PARRA[1*], Pablo SANCHIS[1+]
[1]Universitat Politècnica de València, Nanophotonics Technology Center
Camino de Vera s/n, Valencia, 46022, Spain
[*]jorpargo@ntc.upv.es, [+]pabsanki@ntc.upv.es

Silicon-on-insulator waveguide grating couplers suffers from some key problems like high polarization dependency due to its high index contrast. In order to overcome this problem refractive index engineering has been demonstrated as a suitable solution [1, 2]. However, the design complexity is highly increased interfering with the search of the optimal design. This work presents a particle swarm optimization (PSO) strategy applied to a polarization-independent grating coupler based on subwavelength structures for the near-infrared band. Furthermore, the achieved design is suitable to be fabricated with a single-fully-etch step and was constrained to have a minimum feature size ≥ 100 nm.

The first step is to define the silicon layer thickness. Although, experimental sub-decibel efficiencies with standard 220nm-thick-Si has been demonstrated [3], this layer thickness cannot fully exploit the basis of metamaterial polarization-independent grating couplers due to the small difference between the effective indices of TE and TM modes within the artificial material. We choose 320nm as the Si-thickness since it provides single-mode condition in a square Si/SiO_2 strip waveguide for polarization-independent performance in silicon photonic circuits (see Fig. 1b insets). Then, the non-optimized grating parameters are selected and fixed. In our case we fixed a total number of 20 grating periods, the depth of the buried-oxide-layer (2 μm) and top-oxide-layer (750 nm), fibre angle θ (10°), fibre-to-first-period grating (3.85 μm) and the pitch of the subwavelength structure (400 nm).

Due to time computational simulation constraints, it was necessary to make a trade-off between population size and the total optimized variable. We found that a good strategy was to treat each grating period separately and only put in the swarm as independent variables the filling-factor of the subwavelength trenches and the operating wavelengths. Hence, the longitudinal filling-factor and pitch are calculated to satisfy the phase matching condition. By this manner, a small population of 20 particles can work out the problem. Additionally, position boundary limits were taken into account to fulfil the fabrication constraints.

Coupling efficiency was calculated with 2D-FDTD simulations and the effective refractive

index of the metamaterial trenches were obtained from a look-up table approximated by finite element method. To implement the algorithm, we developed an in-house script made in C along with RSoft software. Nonetheless, this algorithm can be implemented in any photonic software that supports scripting.

The algorithm took 150 iterations to converge towards the minimum fitness (see Fig. 1a). It has to be noted that there is a chance that the algorithm converged to a local minimum. However, the results show that coupling efficiency peak rises previous top-oxide-cladding PDL free gratings designs [1]. Fig. 1b shows the spectra coupling efficiency obtained by 2D-FDTD with the reported algorithm design. The peak coupling efficiency rises -3.5 dB for both polarizations and a PDL bandwidth of ~80 nm below 0.5 dB is also achieved. 3D-FDTD simulations were carried out for a waveguide width of 12 μm. It is interesting to notice that the 3D spectra are shifted with respect to the 2D results. Furthermore, the wavelength shift is larger for TE polarization. Similar differences for the 3D-FDTD simulated TE and TM spectra have also been shown in previous works [2].

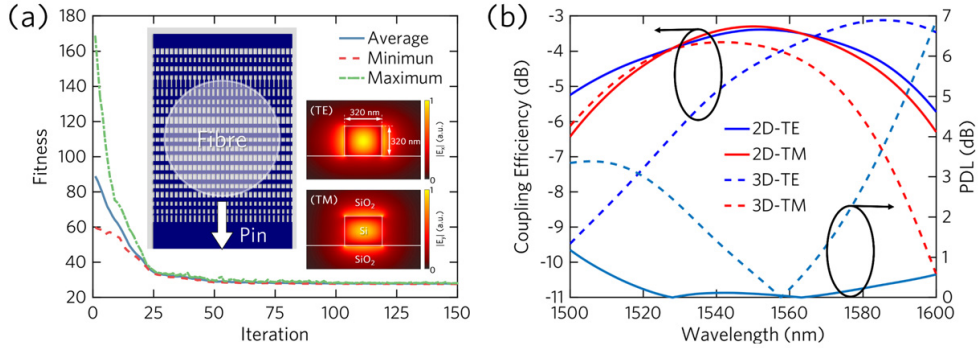


Fig. 1. (a) Fitness as function of iterations (insets show optimal grating top view and strip waveguide cross section). (b) Coupling efficiency calculated with 2D and 3D-FDTD.

In conclusion, particle swarm optimization has been used to obtain low loss grating couplers for enabling a polarization-independent performance in silicon photonics. Discrepancies between 2D and 3D-FDTD results have been obtained and are currently under investigation.

Acknowledgment. Funding from grants TEC2016-76849-C2-2-R (MINECO/FEDER, UE) and NANOMET PLUS- Conselleria d'Educació, Cultura i Esport -PROMETEOII/2014/034.

References

[1] X. Chen, H. K. Tsang, *Polarization-independent grating coupler for silicon-on-insulator nanophotonic waveguides*, Optics Letters, vol. 36, no. 6, pp. 796-798, 2011

[2] Z. Cheng, H. K. Tsang, *Experimental demonstration of polarization-insensitive air-cladding grating couplers for silicon-on-insulator waveguides*, Optics Letters, vol. 39, no. 7, pp. 2206-2209, 2014

[3] D. Benedikovic, P. Cheben, J. Schmid, D. Xu, B. Lamontagne, S. Wang, J. Lapointe, R. Halir, A. Ortega-Moñux, S. Janz, and M. Dado, *Subwavelength index engineered surface grating coupler with sub-decibel efficiency for 220-nm silicon-on-insulator waveguides*, Optics Express, vol. 23, no. 17, pp. 22628-22635, 2015

1 × 2 Wavefront Control Type Wavelength-Selective Switch by Silicon Waveguides

Fumi NAKAMURA[1*], Keijiro SUZUKI[2], Ken TANIZAWA[2], Minoru OHTSUKA[2], Nobuyuki YOKOYAMA[2], Kazuyuki MATSUMARO[2], Miyoshi SEKI[2], Keiji KOSHINO[2], Kazuhiro IKEDA[2], Shu NAMIKI[2], Hitoshi KAWASHIMA[2], Hiroyuki TSUDA[1]

[1]Faculty of Science and Technology, Keio University, 3-14-1, Hiyoshi, Kohoku-ku, Yokohama, Kanagawa, 223-0061, Japan

[2]National Institute of Advanced Industrial Science and Technology (AIST), 16-1 Onogawa, Tsukuba, Ibaraki, 305-8569, Japan

[*] f_nakamura@tsud.elec.keio.ac.jp

1. Introduction

A wavelength-selective switch (WSS) can route each of the input wavelength division multiplexed (WDM) signal to any one of the output ports. A WSS is the key device of an optical node in the optical network system. We previously proposed a 1 × 2 wavefront control type WSS [1], [2]. This WSS has no waveguide crossing; therefore the crosstalk between channels and the variation in loss among channels can be reduced. In this paper, we demonstrate successful switching operations with this WSS.

2. Design of the 1 × 2 wavefront control type WSS

The configuration of the 1 × 2 wavefront control type WSS is shown in Fig.1. The WSS consists of one arrayed waveguide grating (AWG) for the input, two AWGs for the output, one shared slab waveguide, and wavefront control waveguides. The incident WDM signal is demultiplexed by the input AWG. Each separated signal is expanded by propagation in the large slab waveguide and couple to eight wavefront control waveguides, each of which has a phase shifter with heater and a distributed Bragg reflector (DBR). The eight wavefront control waveguides of each channel are the same length. When the heaters on the wavefront control waveguides are OFF, the signal light is reflected by the DBRs and propagated in the slab waveguide toward output AWG #1, which is located symmetrically about the optical axis. On the other hand, when they are ON, the optical path length is changed due to the thermo-optical effect. The wavefront of the signal light is tilted and routed to output AWG #2.

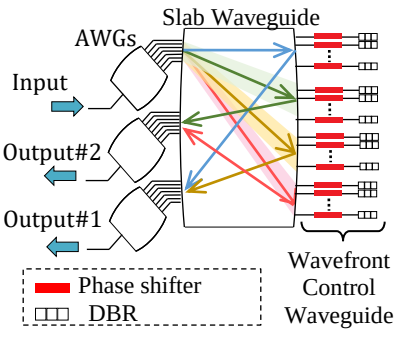


Fig. 1. Configuration of 1 × 2 wavefront control type WSS

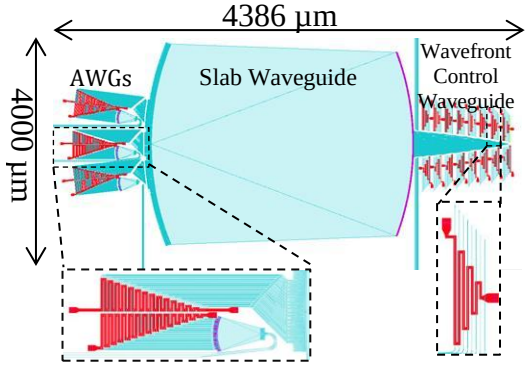


Fig. 2. Layout of 1 × 2 wavefront control type WSS

The layout of the 1 × 2 WSS is shown in Fig. 2. It has 16 channels and the channel spacing is 200 GHz. Each channel has eight wavefront control waveguides of the same

length. As shown in the inset in Fig. 2, the heaters on the eight wavefront control waveguides are connected. A rib structure was adopted at the boundary part between the slab waveguide and array waveguides, in order to reduce the coupling loss. The designs of the input AWG and the output AWGs are the same. The WSS chip was fabricated on a 12" SOI wafer by using a CMOS pilot line at AIST.

3. Switching Characteristics

Fig. 3 shows a photograph of the 1 × 2 wavefront control type WSS chip. The each wavelength signal is switched by controlling the injection current to the heaters. The switching current required was about 6-11 mA. The switching characteristics are shown in Figs 4, 5, and 6. Figures 4 and 5 show transmittance to Output #1 and Output #2 respectively, when the heaters on wavefront control waveguides for all 16 channels were ON. Fig. 6 shows the transmittance to Output #2 when the heaters on the even channels were ON. The 9th channel could not be switched due to the bonding wire having broken. The transmittances shown in the figures do not include the coupling loss to optical fibers. The average insertion loss to Output #1 and Output #2 were 20.1 dB and 19.5 dB, respectively.

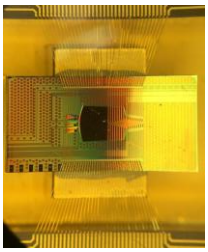


Fig. 3 Photo of the chip wire-bonded.

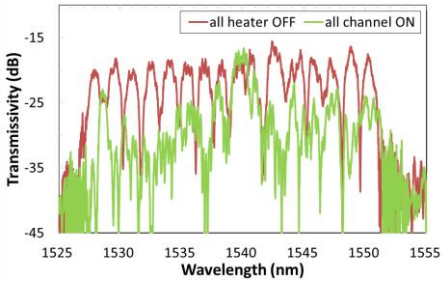


Fig. 4 Transmittance to Output #1.

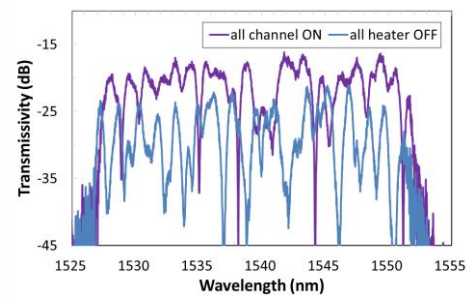


Fig. 5. Transmittance to Output #2.

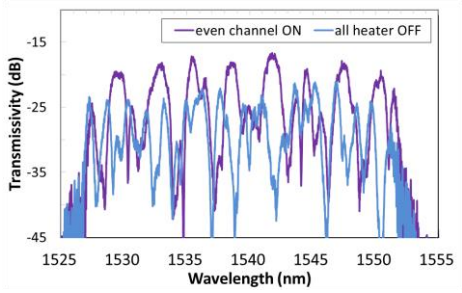


Fig. 6. Transmittance to Output #2 when even channel switched to Output #2.

4. Conclusion

We fabricated a 16-channel, 1 × 2 wavefront control type WSS using silicon waveguides and performed switching experiments. The switching current for each channel was about 6-11 mA. The variation in loss among the channels was reduced since this wavefront control type WSS has no waveguide crossing.

References

[1] Kyosuke Muramatsu et al., Photonics in Switching 2015, WeI2-4, Sep. 22-25, Florence, Italy. (2015).

[2] Fumi Nakamura, et al., Frontiers in Optics 2016, JW4A.144, Rochester, U.S.A. (2016).

Frequency Tuning of Symmetric Colliding Pulse Mode-Locked Laser through Asymmetric Biasing Intra-Cavity Phase Modulators

Mu-Chieh Lo*, Robinson Guzmán, Carlos Gordón, Muhsin Ali, Guillermo Carpintero

Departamento de Tecnología Electrónica, Universidad Carlos III de Madrid, Leganés, Madrid, 28911, Spain

*mlo@ing.uc3m.es

In this paper we report a multimode interference reflector (MIR)-based linear cavity mode-locked laser (MLL) operating in the telecom C-band with a repetition rate of 30 GHz as shown in Fig. 1. A pair of intra-cavity electro-optic phase modulators (EOPM) enables spectral tuning of the optical and the photo-detected RF spectrum. As an asymmetric bias voltage increases up to 6 V, the RF frequency shift reaches 3 MHz. This photonic integrated circuit (PIC) was rapidly prototyped using generic photonic integration technology platform via industrial Multi-Project Wafer (MPW) run [1].

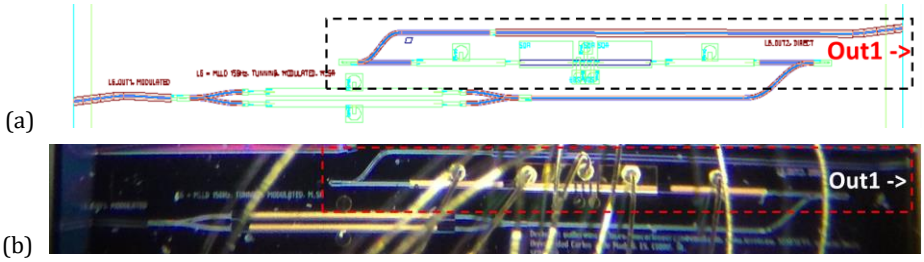


Fig. 1. (a) Layout (b) Microscope view of the proposed PIC

MLLs generating short optical pulse and wide coherent optical frequency comb have attracted interest in areas such as telecommunications, sensing systems and microwave photonics. The feasibility to on-chip integrate semiconductor optical amplifiers (SOA), saturable absorbers (SA), EOPM and passive waveguide devices such as MMI couplers and MIR allows for advanced controllable manipulation [2,3].

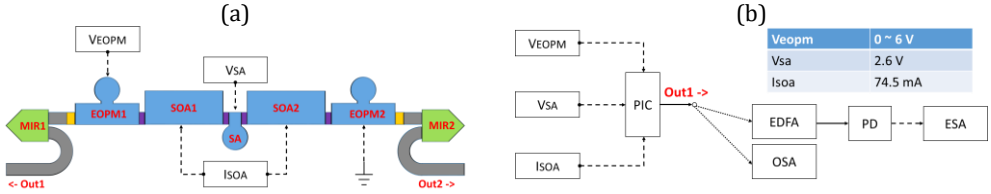


Fig. 2. (a) Schematic of PIC (b) Block diagram of experimental setup

In Fig. 2(a) the core MLL is depicted schematically, corresponding to the area bounded by the dashed line in Fig. 1. It is of the symmetric colliding pulse mode-locking configuration [4] surrounded by a pair of identical EOPMs. The left EOPM was biased (V_{EOPM}) from 0 to 6 V while the right EOPM was always grounded. Two SOAs shared one current source (I_{SOA}) of 74.5 mA and the middle SA was fed with a reverse bias voltage (V_{SA}) of 2.6 V. As presented in Fig. 2(b), the emitted optical signal was measured with a lensed fiber to couple light from the angled waveguide output Out1. By using either an optical or an electrical spectrum analyser (OSA, ESA) the spectra were monitored and collected. An EDFA was deployed, followed by a photodiode (PD) and the ESA.

At V_{EOPM} = 0 and 6 V the optical spectrum was recorded as presented in Fig. 3(a) and (b), respectively. In Fig. 3(a) the comb has a signal-to-noise ratio (SNR) of 30 dB and side-mode-suppression ratio (SMSR) of 15 dB. The mode spacing is 0.24 nm equal to 30 GHz. Similarly, in Fig. 3(b) the SNR is still around 30 dB but the SMSR degrades to less than 10 dB. The shape of comb becomes a sharp triangle, not as same as the flatter plateau in Fig. 3(a). In Fig. 3(c) a series of beat tones produced by the PD are exhibited where the influence of V_{EOPM} is visualized. As V_{EOPM} increases, the peak moves to the left and the shift is gradually weaker. The blue (6V) peak is at 29.5198 GHz and the red (0V) is at 29.5224 GHz, separated by 3 MHz.

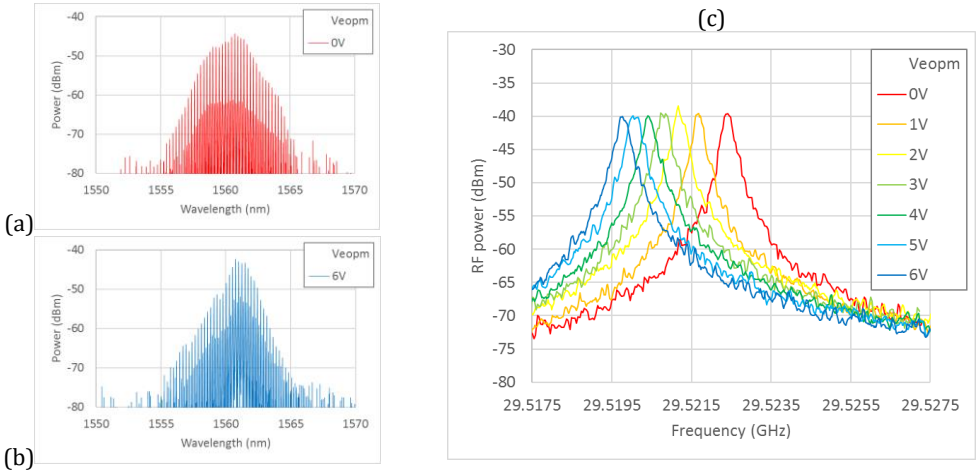


Fig. 3. (a) Optical spectrum when V_{EOPM} = 0 V (b) Optical spectrum when V_{EOPM} = 6 V (c) Electrical spectrum of beat tones when V_{EOPM} = 0 - 6 V

The spectral tuning has been experimentally demonstrated with an asymmetrically biased pair of EOPM. Since the symmetric colliding pulse mode-locking is inherently in conflict with the asymmetric biasing condition [5], further theoretical investigation on the tuning mechanism as well as the limited tuning range should be performed.

References

[1] K. A. Williams, E. A. J. M. Bente, D. Heiss, Y. Jiao, K. Ławniczuk, X. J. M. Leijtens, J. J. G. M. van der Tol, and M. K. Smit, *InP photonic circuits using generic integration*, Photonics Research, vol. 3, issue 5, pp. B60-B68, 2015

[2] S. Latkowski, V. Moskalenko, S. Tahvili, L. Augustin, M. Smit, K. Williams, and E. Bente, *Monolithically integrated 2.5 GHz extended cavity mode-locked ring laser with intracavity phase modulators*, Optics Letters, vol. 40, issue 1, pp. 77-80, 2015

[3] M.-C. Lo, R. Guzmán, C. Gordón, and G. Carpintero, *Tunable Mode-Locked Laser Photonic Integrated Circuit Using Intracavity Phase Modulators*, in Optical Fiber Communications Conference and Exhibition (OFC), pp. W2A.1, 2017

[4] C. Gordón, R. Guzmán, V. Corral, M.-C. Lo, and G. Carpintero, *On-Chip Multiple Colliding Pulse Mode-Locked Semiconductor Laser*, Journal of Lightwave Technology, vol. 34, issue 20, pp. 4722-4728, 2016

[5] M.-C. Lo, R. Guzmán, C. Gordón and G. Carpintero, *Photonic integrated circuit comprising mode-locked laser and pulse interleaver for wavelength tunable THz signal generation*, in IEEE International Topical Meeting on Microwave Photonics (MWP), pp. 340-343, 2016

Integrated Dual-Mode Interferometer with Differential Single-Mode Outputs

Niklas HOPPE[1*], Philipp DIERSING[1], Thomas FÖHN[1], Mathias KASCHEL[2], Thomas POLDER[1], Wolfgang VOGEL[1], Lotte RATHGEBER[1], Maria FELIX ROSA[1], Manfred BERROTH[1]

[1]Institute of Electrical and Optical Communications, University of Stuttgart, 70569, Stuttgart, Germany

[2]Institut für Mikroelektronik Stuttgart (IMS CHIPS), 70569, Stuttgart, Germany

[*] niklas.hoppe@int.uni-stuttgart.de

Abstract: We present for the first time the realization of an integrated dual-mode interferometer containing two differential single-mode outputs. The structure realized in a 250 nm silicon-on-insulator platform enables the monitoring of total optical output power. Hence, the estimation of phase relation becomes tolerant to input power fluctuations and can be realized by a single-wavelength operation even when the optical input power is unknown.

Introduction: For lab-on-a-chip approaches a massive on-chip-parallelization of interferometric structures is a huge benefit. Besides the established Mach-Zehnder interferometer (MZI), the dual-mode or bimodal interferometer (DMI) is utilized in modern biosensors [1]. In general, the detection of a substance concentration with a DMI is based on the estimation of a phase difference at the sensing region end, which is related to the DMI transmission as e.g. explained in [2]. Due to the use of only one waveguide arm, a higher robustness to on-chip-fluctuations of temperature compared to MZIs is achievable in a DMI. Enabling high sensitivities comparable to state-of-the-art devices [3], the development of parallelizable integrated DMIs with a small footprint [4] and low excess loss [2] is an important step to establish DMIs in lab-on-a-chip applications. The measured output power of a DMI with a single-mode output depends on the optical input power and the varying losses in the sensing region. Therefore, the estimation of the phase relation with a single-wavelength laser source is susceptible to damping fluctuations and requires precise knowledge of the input power. These issues can be circumvented by implementing a second differential output as depicted in Fig. 1. Harnessing the total output power with the help of a second single-mode output allows for a stable estimation of phase relations as basis for robust biosensor applications.

Design and Fabrication: DMIs with two single-mode output ports are fabricated at IMS CHIPS Stuttgart on a 250 nm silicon-on-insulator Soitec wafer. Following the design given in Fig. 1, the device contains a mode converter with two curved outputs and tapers to single-mode waveguides. Access waveguides are connected to single-mode fibers via grating couplers. A microscopic image of a fabricated DMI can be seen in Fig. 1 (right), which is structured utilizing electron beam processing. A 1 µm thick SiO_2 cladding is added to protect the device. The dual-mode waveguide of the DMI has the width W and the length L.

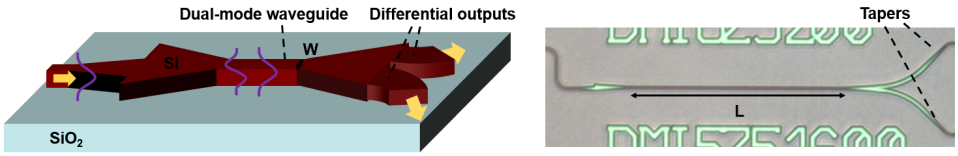


Fig. 1. Schematic view (left) and microscopic image (right) of an integrated DMI with two single-mode outputs. The shown footprint is around 100 µm x 400 µm.

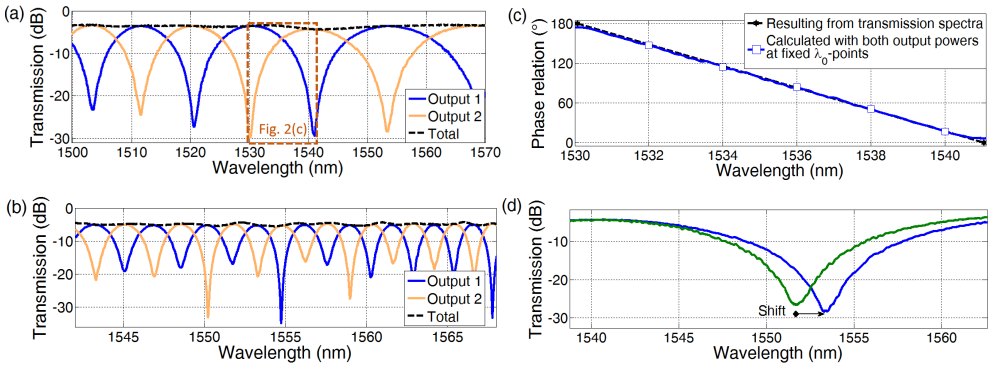


Fig. 2. (a) Transmission spectra of the two differential DMI outputs and corresponding sum with L = 200 µm and W ≈ 625 nm, (b) L = 1700 µm and W ≈ 575 nm. (c) Calculated phase relation for the DMI in (a) by utilizing transmission spectra or both output powers. (d) Shift of the resonance wavelength caused by a top cladding change for the DMI in (a).

Measurements: Evaluating the measured output power spectra of two fabricated DMIs (see Fig. 2(a) and 2(b)), the differential behaviour of the two outputs can be verified. The sum of the two output transmissions is almost constant in the depicted wavelength range. Further, the phase relation in a range of π can be calculated at a single wavelength utilizing both output powers and the phase relation dependent transmission formula. The result is shown in Fig. 2(c) for different wavelengths λ_0 and is in good accordance to the phase relation estimated by evaluating the transmission spectra. Adding an index matching oil on top of the passivated DMI results in a phase shift, thus demonstrating the application of the DMI as sensor (Fig. 2(d)).

Conclusion and acknowledgement: We demonstrate the tracking of total optical output power with parallelizable dual-mode interferometers by implementing two differential single-mode outputs. The fabricated samples provide a robust detection of the phase relation with a single-wavelength source for lab-on-a-chip applications, even with unknown or varying optical input power and waveguide losses. Measured transmission spectra of both interferometer outputs are in good agreement with theory.

We would like to thank the IMS CHIPS Stuttgart for fabricating the devices and Dr.-Ing. W. Sfar Zaoui for providing the design of the implemented grating couplers.

References

[1] K. E. Zinoviev, A. B. Gonzalez-Guerrero, C. Dominguez, and L. M. Lechuga, "Integrated bimodal waveguide interferometric biosensor for label-free analysis," J. Lightw. Technol., vol. 29, no. 13, pp. 1926–1930, Jul. 2011.

[2] N. Hoppe, T. Föhn, P. Diersing, P. Scheck, W. Vogel, M. Felix Rosa, M. Kaschel, M. Bach, and M. Berroth, "Design of an Integrated Dual-Mode Interferometer on 250 nm Silicon-on-Insulator," IEEE J. Sel. Topics Quantum Electron., vol. 23, no. 2, pp. 1-8, March-April 2017.

[3] E. Makarona, P. Petroub, S. Kakabakos, K. Misiakos, and I. Raptis, "Point-of-Need bioanalytics based on planar optical interferometry," Biotechnol. Adv., vol. 34, no. 3, pp. 209–233, May/Jun. 2016.

[4] Q. Liu, K. W. Kim, Z. Gu, J. S. Kee, and M. K. Park, "Single-channel Mach-Zehnder interferometric biochemical sensor based on two-lateral-mode spiral waveguide," Opt. Express, vol. 22, no. 23, pp. 27910–27920, Nov. 2014.

Full field Group Velocity Dispersion characterization of 300nm film height Silicon Nitride waveguides

Luis A. BRU[1], Gloria MICÓ[1], Daniel PASTOR[1*], David DOMENECH[2], Ana M. SÁNCHEZ[3], Josep M. CIRERA[3], Javier SANCHEZ[3], Carlos DOMÍNGUEZ[3] and Pascual MUÑOZ[1,2]

[1]Photonic-IC group @ Photonic Research Labs, Universitat Politècnica de Valencia, Spain
[2]VLC Photonics S.L., Ed9B-UPV, c/ Camino de Vera s/n, Valencia, Spain
[3]IMB-CNM-CSIC, Campus Belaterra UAB, Barcelona, Spain
[*]dpastor@dcom.upv.es

Optical Frequency Domain Reflectometry (OFDR) [1-5] allows retrieving amplitude and phase features from optical devices in the time and frequency domains. Characterization of the propagation features in new photonics platforms and waveguide designs is essential in different applications where dispersion tailoring and birefringence need to be controlled over a wide wavelength range. In this paper we present the full-field Group Velocity Dispersion (GVD) assessment of Si_3N_4 waveguides employing the time resolved features of OFDR techniques. The devices were fabricated on a 100mm Si wafer, composed of a SiO_2 buffer (2.5µm thick, n=1.464) grown by thermal, following a LPCVD Si_3N_4 layer with thickness 300nm (n= 2.01) and a 2.0µm thick SiO_2 (n=1.45) deposited by PECVD. A set of test of ring resonators (RRs), Fig. 1(a), was deployed for strip waveguides of width 1.0µm. The bend radius was set to 150µm for which no significant additional loss was expected.

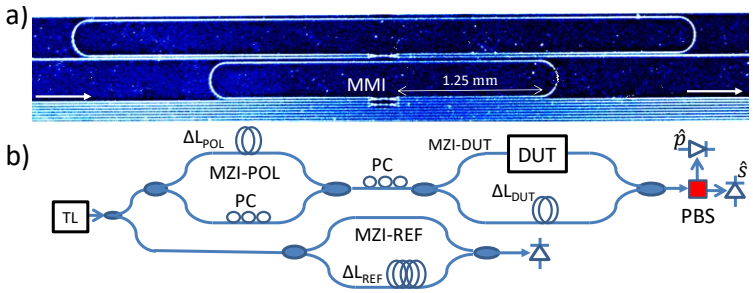


Fig. 1. a) DUT: RRs designed for GVD measurement, b) OFDR set up

The OFDR set up was composed of set of imbalanced fiber based Mach-Zehnder interferometers (MZI) , fed by a scanning Tunable Laser (TL), Fig. 1(b). The first upper MZI is used for polarization conditioning for the full-field and polarization assessment as described in [5]. The second upper MZI includes the device under test (DUT), in our case the Silicon Nitride chip in/out coupled by lensed fibers. Two interferograms are recorded after a Polarization Beam Splitter (PBS). Moreover, the lower MZI provides the reference (or triggering signal) for the phase error due to imperfect TL tuning. As described in [5], the time responses of the DUT can be isolated after a Fast Fourier Transform (FFT) of the interferograms, providing the complete Jones Matrix description of the DUT on the PBS bases $\hat{s}$ and $\hat{p}$. The polarization diversity set up avoids the environmental and manipulation polarization changes on fiber pigtails and lensed fibers on the DUT branch. The TL scanning speed was 40nm/s with a 100nm span (1555nm center). After the FFT, the power time response was calculated $|h|^2=|h_s|^2+|h_p|^2$, Fig. 2(a). Multiple time recirculating contributions from the RR can be easily identified, but also the TE and TM splitting in time is observed revealing strong differences in propagation losses and group delay between polarizations. Taking the RR dimensions $L_{sw} = 11mm$ (straight waveguide facet to facet) and $L_{loop} = 6.63mm$, the group indexes are n_g^{TE} =1.892 and n_g^{TM} =1.717.

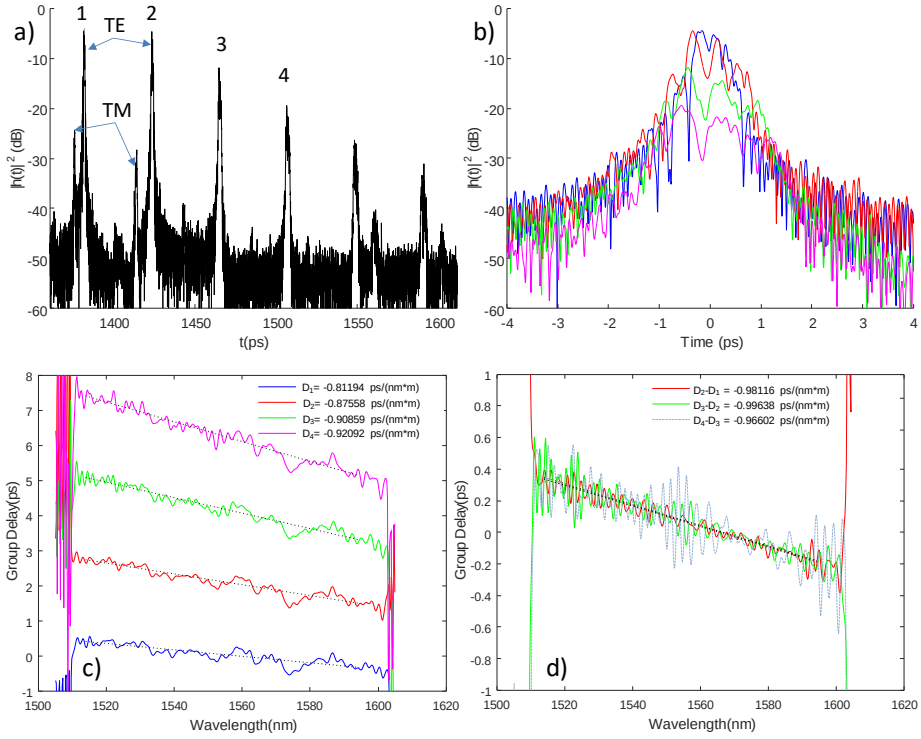


Fig. 2. a) RR time response, b) Dispersion broadening of recirculations ,c) GVD measured over for each temporal recirculation 1 to 4, d) GVD difference inter pulses.

Moreover $|h(t)|^2$ shows also clearly a broadening effect due to GVD and this information can be extracted from the retrieved signals. So we proceed selecting the desired pulse (recirculation) slicing the TE time responses $(h_s(t), h_p(t))$ around $\pm 4ps$ from its center. Hence, Fig. 2(b) shows the progressive broadening. Then, each truncated response is transformed into frequency domain to calculate the group delay $\tau_g(\omega)$[4-5] and linearly fitted between 1514nm and 1594nm to obtain the dispersion parameters D[ps/(nm*m)], Fig. 2(c). Absolute delay difference between traces was reduced for better representation. For D calculations, we employed the physical design lengths $L_{sw} + L_{loop} * [0, 1, 2, 3]$. Notice that D values were not constant as expected, that suggests a positive value of dispersion is added to that coming from the chip, originated by the measurement set up. Fortunately, RRs multiple samples can be related between them to isolate a *single round trip pass* along the Ring. In this way Fig. 2(d) shows the group delay difference between adjacent time samples $(D_i(\lambda) - D_j(\lambda))$, their linear fitting and the estimated Dispersion calculated over L_{loop}, leading to an average dispersion D=-0.981 ps/(nm*mm) with $\pm 1.5\%$ relative error. From this values it is straightforward to obtain the dispersion offset from the set-up as $(DL)_{setup} = 0.00178\ ps/nm$.

References

[1] U. Glombitza and E. Brinkmeyer, J. Lightwave Technol. 11 1377–1384 (1993)
[2] K. Takada and T. Hirose, Optics Letters 34, 24, 3914-3916 (2009)
[3] L. A. Bru, B. Gargallo, e.a., in Proc. ECIO, paper ecio-o–08, 2016.
[4] B. J. Soller, D. K. Gifford, e. a., Optics Express 13, 2, 666-674 (2005)
[5] D. K. Gifford, B. J. Soller, e. a., Applied Optics 44, 34, 7282-7286 (2005)

Mutual Injection Locking of Lasers in a Photonic Integrated Circuit

Alison H. PERROTT[1,2*], Ludovic CARO[1,2], Mohamad DERNAIKA[1,3], Niall P. KELLY[1,2], Padraic E. MORRISSEY[2], Frank H. PETERS[1,2]

[1]Physics Department, University College Cork, College Road, Cork, Ireland, T12 YN60
[2]Tyndall National Institute, Lee Maltings, Dyke Parade, Cork, Ireland, T12 R5CP
[3]Engineering Department, University College Cork, College Road, Cork, Ireland, T12 YN60

[*]alison.perrott@tyndall.ie

Photonic integrated circuits (PICs) offer many advantages in the area of photonics. In particular, complex optical systems which were once restricted to large table top setups are now finding their way onto integrated devices. Not only does this vastly decrease the size of these systems, it allows for lower power consumption and reduced cost [1].

We are interested in examining the stable regime of mutually injection locked lasers, which will be applied to the creation of optical superchannels for high bandwidth communications. The monolithic integration of multiple Slotted Fabry-Pérot (SFP) lasers [2] onto a single PIC has been investigated [3]. Injection locking of such a system is highly complex, due to mutual feedback between the lasers. Yet, stable optical-phase locking between two SFP lasers on-chip has been demonstrated for the case where one laser, the master, is much higher powered than the other laser, the slave [3]. In this paper, we investigate the mutual injection locking of two integrated, identical, equally powered SFP lasers while varying the coupling ratio between them.

The PIC consisted of two identical single facet slotted Fabry-Pérot (SF-SFP) lasers coupled together through a 1 mm waveguide interconnect, referred to as the "Variable Optical Attenuator" section (VOA). A schematic of the full device, with each variable parameter labelled, is shown in Figure 1. The single facet lasers consisted of a 650 μm long gain section and a 760 μm long mirror section, comprised of seven etched slots, each with a gap of 0.88 μm and 108 μm separation between the slots. The SFPs were controlled by independently biasing their respective mirror, I_{Mirror}, and gain, I_{Gain}, sections. Forward or reverse biasing the VOA section controlled the amplification or attenuation of the optical signal and hence varied the power coupled between the lasers.

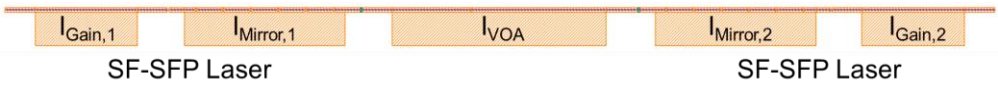


Fig. 1. Schematic of the PIC, with each variable parameter labelled.

Both lasers were biased at a mirror and gain section bias of 40 mA and 65 mA, respectively. At these biases both lasers had very similar spectra, see Figure 2, and output powers. The bias of the VOA section was varied between -1 V and +1V and the behaviour of both lasers was observed on an Optical Spectrum Analyser (OSA), an Electrical Spectrum Analyser (ESA) and a High Speed Oscilloscope (HSO). At a VOA section bias below -1 V, the waveguide interconnect between the lasers was absorbing, therefore the lasers were isolated from each other and behaved as independent lasers. At approximately -0.5 V the VOA section began to become transparent and light could pass between the lasers. The VOA section was fully transparent at a bias of approximately 0.7 V. Above this bias the device behaved as coupled cavity laser from facet to facet. The coupling between the lasers was controlled by sweeping the VOA

section bias between -0.5 V and 0.7 V. Various stable locking regions were obtained. Regions of multimode behaviour were also observed. An OSA trace was recorded at each VOA bias. The resulting traces were concatenated and a two dimensional colour intensity plot was generated as a graphical representation of the evolution of the output of the lasers during the VOA bias sweep. The colour intensity plot of the OSA traces from one of the lasers is shown in Figure 2, where the various behavioural regimes can clearly be observed.

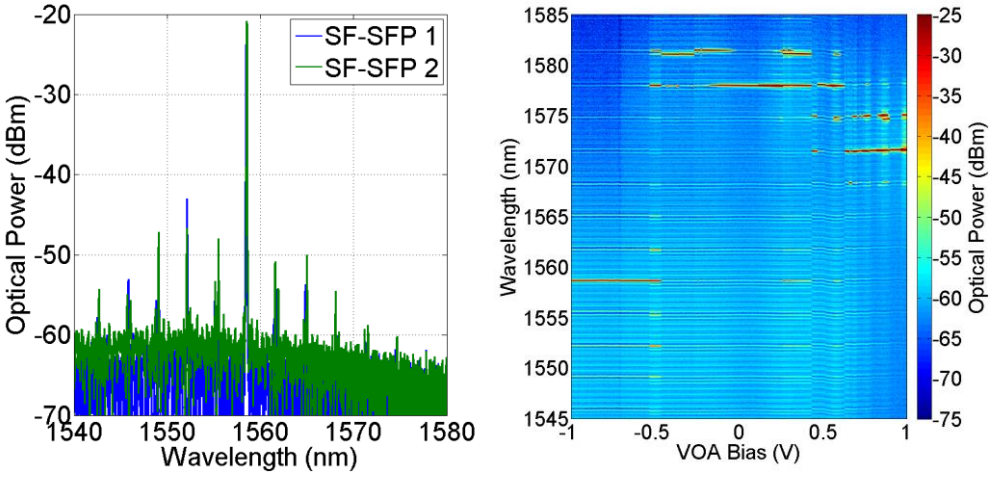


Fig. 2. Left: Free-running spectra of both lasers for mirror and gain section biases of 40 mA and 65 mA, respectively. Both lasers have very similar spectra at these biases. Right: Colour intensity plot of the OSA traces from one of the lasers, recorded while sweeping the bias of the VOA section.

We have successfully demonstrated stable locking between two equally powered SFP lasers on an integrated device. Further work will examine the dependence of the locking behaviour on the length of the delay between the lasers. It is hoped that this work will lead to a better understanding of the injection locking behaviour of lasers in next generation PICs.

References

[1] R. Nagarajan, M. Kato, J. Pleumeekers, P, Evans, S. Corzine, S. Hurtt, A. Dentai, S. Murthy, M. Missey, R. Muthuah, R.A. Salvatore, C. Joyner, R. Schneider, Jr., M. Ziari, F. Kish and D. Welch, *InP integrated photonic circuits*, IEEE Journal of Selected Topics in Quantum Electronics, Vol. 16, No. 5, pp. 1113-1125, 2010

[2] D. Byrne, Q. Lu, W.H. Guo, J.F. Donegan, B. Corbett, B. Roycroft, P. Lambkin, J-P Engelstaedter and F. Peters, *A facetless laser suitable for monolithic integration*, in Proceedings of the Conference on Lasers and Electro-Optics/Quantum Electronics and Laser Science Conference and Photonic Applications Systems Technologies, pp 1-2, 2008

[3] P.E. Morrissey, W. Cotter, D. Goulding, B. Kelleher, S. Osborne, H. Yang, J. O'Callaghan, B. Roycroft, B. Corbett and F. H. Peters, On-chip optical phase locking of single growth monolithically integrated slotted fabry pérot lasers, Optics Express, Vol. 21, No. 14, pp. 17315-17323, 2013

Temperature-immune readout of an integrated optical wavelength meter based on microring resonators

Caterina TABALLIONE[1], Temitope AGBANA[2], Gleb VDOVINE[2], Marcel HOEKMAN[3], Lennart WEVERS[3], Jeroen KALKMAN[2], Michel VERHAEGEN[2], Peter J.M. VAN DER SLOT[1] and Klaus-Jochen BOLLER[1]

[1] University of Twente, P.O. Box 217, 7500 AE Enschede,

[2] University of Delft, P.O. Box 5, 2600 AA Delft,

[3] LioniX International BV, P.O. Box 456, 7500 AL Enschede

E-mail: c.taballione@utwente.nl

Wavelength meters are central for many applications such as in telecommunication systems [1] or laser monitoring [2]. The primary function of a wavelength meter is to provide an output signal that changes sensitively with the wavelength of the input light. Of central importance is the reproducibility of the output signal even in the presence of external perturbations, e.g., temperature changes causing thermal drift. Various different methods are usually applied to improve reproducibility, e.g., thermal stabilization or repeated calibration with an additional reference light source of well-known and stable wavelength.

We present an integrated optical wavelength meter that is immune to thermal drift, requiring no thermal stabilization or repeated calibration with additional light sources. Our experimental approach is depicted in Fig.1. The first central component is an optically integrated Si_3N_4 waveguide micro ring resonator (MRR) whose optical transmission spectrum can be changed via applying a heating voltage, V, as a control parameter. The second essential component is a neural network-based readout algorithm that is able to detect temperature changes and reduce their effect on the displayed output wavelength. The wavelength meter is calibrated and characterized with input from a tunable laser and a detector that measures the transmitted power. For the initial calibration the laser is tuned to a large number (e.g. 1000) of different but known wavelengths, for each wavelength a set of different values for the control parameter (e.g. 20 voltages) is sequentially applied, and for each wavelength-control parameter combination the output power signal is recorded.

Thereafter, for measuring a single unknown input wavelength, the transmitted power is measured for the same set of control parameters values. This provides a set of output powers per unknown wavelength. Minimizing the mean-square deviation as compared to the calibration[3] yields the measured (displayed) value for the unknown wavelength.

Three main results can be reported so far: first, when increasing the number of known input wavelengths and heating voltages in the initial calibration the measured wavelengths become increasingly more precise; second, we demonstrate for the first time the long-term reproducibility of such a wavelength meter (here up to one week); third, we observe that the displayed output wavelength does not change when deliberately changing the ambient temperature up to several degrees. The latter result shows that the readout provides temperature-immune operation of the wavelength meter, which makes a precise temperature stabilization or re-calibration after temperature change obsolete.

The current wavelength range of operation spans one free spectral range (FSR) of the MRR of 4 nm with a high spectral resolution of ~75 pm. An extension of the FSR is possible via exploiting waveguide birefringence of the MRR or using sequential resonators, e.g., in a Vernier fashion.

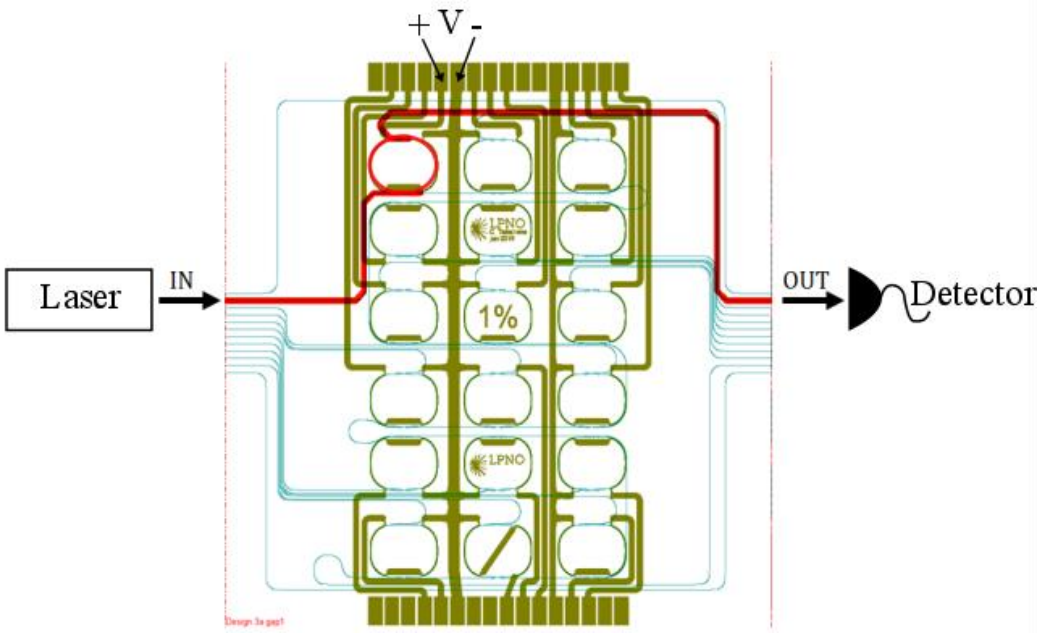


Fig. 1 Schematic setup for calibrating and characterizing the wavelength meter. Current measurements are carried out with resonators having moderate quality factors (Q~1000). The shown resonator circuit has been fabricated for higher Q-values (~ 1 million). The light path through on the resonators is shown in red (other waveguides shown in blue). Electric microwires (green) are used for resistive heating via a voltage, V, as control parameter.

References

[1] Y. Zhang, et al., *Towards adaptively tuned silicon microring resonators for optical networks-on-chip applications,* IEEE JSTQE, vol. 20, no. 4, 2014

[2] S. A. Saakyan et al., *Frequency control of tunable lasers using a frequency-calibrated lambda-meter in an experiment on preparation of Rydberg atoms in a magneto-optical trap*, Quantum Electronics, vol. 45, no. 9, pp. 828-832, 2015

[3] R. M. Oldenbeuving et al., *High precision wavelength estimation method for integrated optics,* Optics Express, vol. 21, no. 14, pp. 17042-17052, 2013

EUROPEAN CONFERENCE ON INTEGRATED OPTICS

Strip-loaded horizontal slot waveguide: confinement with negligible losses

Matthieu ROUSSEY[1*], Ségolène PELISSET[1], Leila Ahmadi[1], Markku KUITTINEN[1], and Seppo HONKANEN[1]

[1]Institute of Photonics, University of Eastern Finland, P.O. BOX 111, 80101 Joensuu, Finland

[*] matthieu.roussey@uef.fi

From optical computing to data storage, from bio-sensing to quantum applications, integrated photonic nano-structures in waveguides are widely used. However, an ideal platform is still to be found to provide, at the same time, an easy fabrication, a low power consumption, low losses, and wavelength scalable devices. A promising solution is presented here.

More than forty years ago the concept of strip-loaded waveguides was proposed by Furuta *et al.* [1]. It consists of a slab waveguide and a lower refractive index material deposited on top of it. The top layer is patterned in order to create an effective index increase providing lateral confinement for the guided light. Such a channel waveguide enables low-loss waveguiding with many materials. In 2004, Almeida *et al.* impacted integrated optics by proposing the idea of a waveguide where light is mostly confined in a low index sub-wavelength gap: the slot waveguide [2]. Since then, tremendous efforts have been put on research in this field to push integration to its limit.

Both of the above mentioned waveguides have unique properties that researcher are seeking in integrated optics: the quasi-independence of the substrate and the low propagation losses of the strip-loaded waveguide, and the huge light confinement of the slot waveguide. Unfortunately, both have drawbacks that restrain their applications. A strip-loaded waveguide has a low refractive index contrast, and the slot waveguide is usually highly lossy.

We present here a novel waveguide type combining the advantages of the two structures, while minimizing their negative aspects: the strip-loaded horizontal slot waveguide [3]. Two rails of a high refractive index are separated by a few tens of nanometers thin layer of a low refractive index medium. This slab structure provides vertical confinement of light. All the materials are atomic layer deposited ensuring minimal roughness at the media interfaces. On top of the multilayer a strip is created using a polymer electron beam resist to provide a lateral confinement. A schematic of the structure is presented in Fig. 1a).

Such a channel waveguide enables localization of the quasi-TM fundamental mode, see Fig. 1b), far enough under the surface to yield a negligible effect of the surface roughness. This results in very low scattering losses. The loading strip can be pattern with any geometry leading to a possibility for a variety of functions, e.g., filters and cavities.

A first experimental demonstration has been done in order to show the response of the device at $\lambda = 1550$ nm. The high index material is titanium dioxide ($n_{TiO2} = 2.23$), the low index material is silicon dioxide ($n_{SiO2}=1.444$), and the strip is made of a homemade polymer of refractive index (1.547). The rail width is 215 nm, the slot width is 80 nm, and the strip has a thickness of 500 nm and a width of 2 µm.

An SEM picture of the fabricated structure is shown in Fig. 1c). Figure 1d) is a picture of the output optical mode observed with a x40 microscope objective.

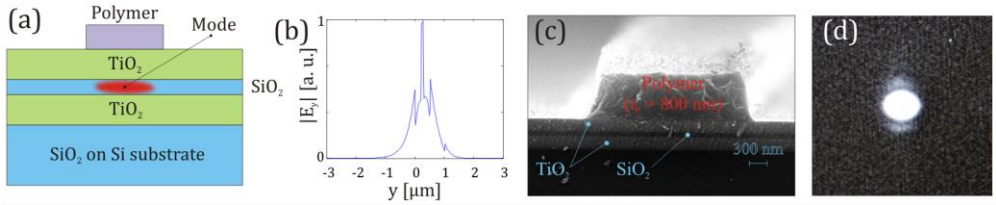


Fig. 1. a) sketch of a strip-loaded slot waveguide; b) profile along the vertical direction of the fundamental quasi-TM mode; c) SEM picture of the fabricated sample; d) picture of the output mode.

In addition to the demonstration of the existence of the waveguide mode by using several experimental techniques, we are also showing the response of a multimode interferometer, a ring resonator, and a Y-junction fabricated on this platform. The preliminary propagation loss measurements revealed losses as low as 2 ± 2 dB/cm, which is rather low compared to other slot waveguide-based structures reported in literature.

References

[1] H. Furuta, H. Noda, and A. Ihaya, *Novel Optical Waveguide for Integrated Optics,* Appl. Opt. 13, pp. 322–326, 1974.

[2] V. R. Almeida, Q. Xu, C. A. Barrios, and M. Lipson, "*Guiding and confining light in void nanostructure,* Opt. Lett. 29, pp. 1209–1211, 2004.

[3] M. Roussey, L. Ahmadi, S. Pélisset, M. Häyrinen, V. Kontturi, J. Laukkanen, A. Bera, S. Honkanen, and M. Kuittinen, *Strip-loaded horizontal slot waveguide,* Opt. Lett. 42, pp. 211-214, 2017.

EUROPEAN CONFERENCE ON INTEGRATED OPTICS

Design and Optimization of a High Speed Slow-Light Silicon Modulator in the O-Band

Andrea ZANZI[1*], Pablo SANCHIS[1], Javier MARTI[1], Antoine BRIMONT[1]
[1]Valencia Nanophotonics Technology Center, Universitat Politècnica de València
Building 8F | 1st Floor, Camino de Vera, s/n, 46022 Valencia, Spain
[*] anzan@ntc.upv.es

The ever-growing increase in global internet traffic imposes significant challenges in data centre (DC) operators equipment manufacturers. These modern DCs utilized hundreds of thousands of servers in several hierarchy layers, which require an efficient interconnection network that have to be both low-cost and energy-efficient. This is precisely where silicon photonics can play a key role. Indeed, Silicon-on insulator (SOI) technologies is currently considered as one of the most promising platforms to achieve high density levels of integration of photonic devices at low cost, owing to its high-index contrast and compatibility with mature complementary metal-oxide semi-conductor (CMOS) fabrication process.

In this paper, we present the design of a compact slow-light modulator in a Mach-Zehnder configuration. The proposed slow light modulator device exploits the silicon free-carriers plasma dispersion effects produced by a reverse-biased vertical PN junction in a shallow etched configuration (Fig. 1(a)) [1]. In this configuration, the optical mode overlaps the carrier depletion region in an optimized fashion (Fig 1(b)). Additionally, the vertical pn junction is defined by the implantation energy with one single lithography step rather than using two masks that must be accurately positioned in the middle of the waveguide [2] as in laterally/horizontally formed pn junction. This makes our optical device cost-effective and more tolerant to potential fabrication variations, with a better yield across the processed wafer. The combination a highly efficient pn with the use of properly apodized slow-light waveguides will dramatically improve the performance of the modulator in terms of footprint and power consumption, making it compatible with advanced low power CMOS electronics

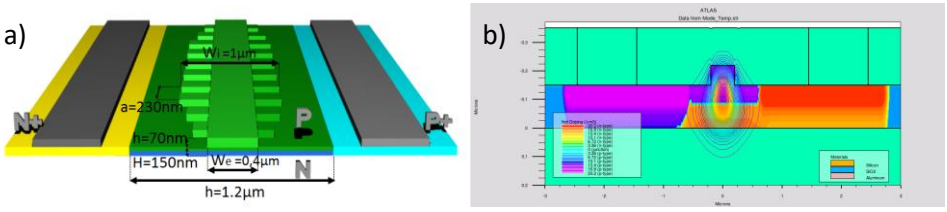


Fig. 1 – Fundamental schematics of the slow-light modulator and 2D-cut of the PN junction

The design of the proposed device consists of several steps. First, we model the phase shifter, using ATHENA and ATLAS, respectively process and device simulators by

SILVACO. For a complete design and analysis of the structures, finely meshed 3D FDTD and plane wave expansion (PWE) simulations have been performed. The PWE simulations allow studying the dispersion relation of the periodic structure followed by 3D FDTD in order to obtain the transmission spectra. The studied structure feature the following parameters: period (a=230 nm), w_e=400nm, w_i=1000nm, h=70nm and H=150nm (Fig.1(a)). The use of slow light will increase the efficiency [5] proportionally to the slow down factor which is given by the ratio between the group index of the optical mode in the normal "fast-light" regime (n_g ~3.64) and the slow-light "Bloch-mode" propagating with a moderately high group index (n_g~10-20). As a result, we obtain an enhancement factor ranging from 2.75 to 5.5. When translated in terms of efficiency, the figure of merit drops by the same factor, reaching record values below 0.1V*cm.

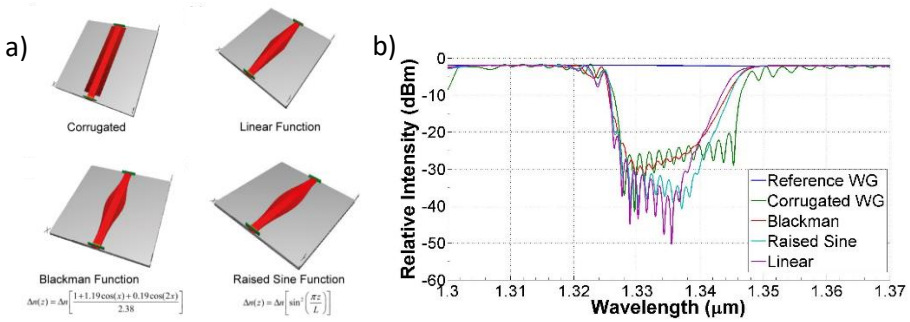


Fig. 2 – (a) Pictures of the tapered fast-to-slow-light transitions. (b) Spectral outputs of the three different tapers with apodization functions and corrugated waveguide (as reference).

The main issue linked with slow-light propagation is the coupling between light travelling in a standard single mode silicon waveguide and the periodic one. A major issue when dealing with slow light propagation is finding a way to achieve a gradual transition from the fundamental waveguide mode to the slow light mode of the periodic waveguide. To overcome this issue, the use of tapers and/or apodization technique is mandatory. Here, we designed and simulated three preliminary different apodization schemes to ensure smooth fast-to-slow light transitions (Fig. 2(a)). The resulting spectra are shown in Fig. 2(b). We can observe a clear improvement can be seen on the fast-to-slow transitions for the three apodization schemes when compared with the untapered corrugated waveguide. Further designs are under development implementing algorithms such as "Particle Swarm Optimization" and "Convex Optimization".

In conclusion, we have shown the promising use of slow light a means to enhance dramatically the efficiency of carrier depletion modulator with optimized apodization schemes to minimize the loss penalty produced by the fast-to-slow light transitions making slow light modulators readily compatible with advanced low power CMOS electronics.

Funding: H2020-ICT-2015, n° 688544, "L3MATRIX". Spanish Funding from "Comunitat Valenciana" under Grisolia Program.

References

[1] A. Brimont, et al, "High speed silicon electro-optical modulators enhanced via slow light propagation," *Opt. Express* 19, 20876-20885 (2011).

[2] Brimont, A., et al. "Compact and efficient silicon 2×2 switches based on a reverse biased vertical pn junction." *Group IV Photonics (GFP), 2014 IEEE*, vol., no., pp.159-160, 27-29 Aug.

EUROPEAN CONFERENCE ON INTEGRATED OPTICS

High-Q Al_2O_3 Microring Resonator for Sensing Applications

Michiel DE GOEDE[1*], Meindert DIJKSTRA, Sonia GARCÍA BLANCO
[1] Optical Sciences Group, MESA+ Institute for Nanotechnology, University of Twente,
P.O. Box 217, 7500 AE Enschede, The Netherlands
[*] m.degoede@utwente.nl

Waveguide based microring resonators (MRRs) are particularly suitable for on-chip integrated optical sensors. Their spectra contain resonance notches that shift due to the probing of the evanescent modal field of local dielectric variations. Sensors based on this shift have already been reported in the Si, Si_3N_4 and SiON technologies [1—3]. The Al_2O_3 technology has the prospect of very high quality (Q) factors due to its low propagation loss [4]. Furthermore, doping it with rare-earth ions enables the realization of on-chip laser based sensors for ease of detection [4]. Here, a high Q Al_2O_3 waveguide MRR sensor is presented as alternative to the traditional MRR technologies with the prospect of developing lasing-based Al_2O_3 MRR sensors.

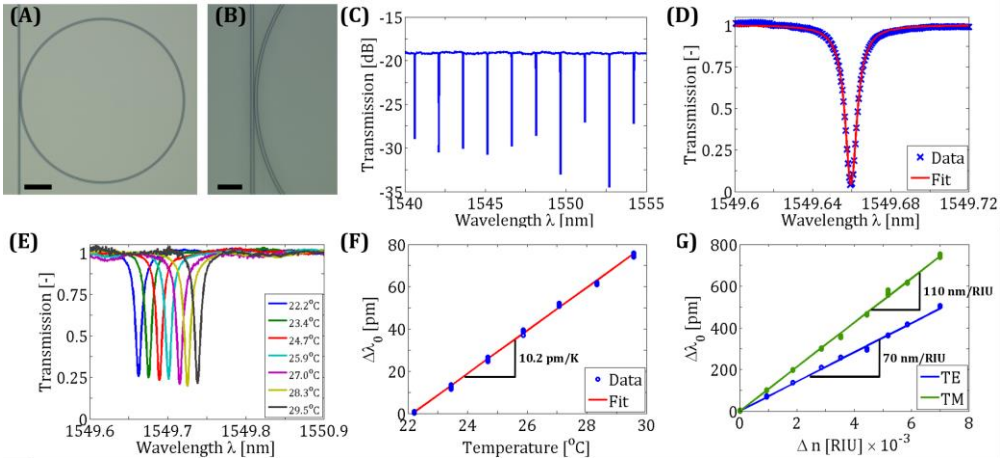


Fig. 1. (A), Optical microscope image of the MRR. Scale bar is 50 µm. (B), Close up of the MRR. Scale bar is 20 µm. (C), Transmission spectrum of the MRR. (D), Resonance with fit. (E), Spectral shift of resonance notch due to stage temperature. (F), Slope sensitivity of temperature sensing. (G), Slope sensitivity of refractive index sensing.

Geometrical parameters of the Al_2O_3 MRR were designed and then transferred to fabricated devices. The design was based on finite difference calculations of the modal

field profiles of the bus and ring waveguides. For operation at 1550 nm optimized geometrical parameters are a radius of 150 µm, a coupling gap of 0.8 µm and a waveguide width and height of 2.4 µm and 0.7 µm respectively. The fabrication starts with the sputter deposition of Al_2O_3 onto a thermally oxidized (8 µm) silicon wafer. The waveguides are then defined by UV-lithography and reactive ion etching. A shadow mask is then used to locally deposit a PECVD-SiO_2 everywhere apart from the MRRs, leaving them exposed to the environment. The MRR is shown in Figures 1 A and B.

The MRR sensor was characterized by transmission measurements with a tunable laser in the C-band. Figure 1 C shows a typical spectrum containing the resonance notches. By fitting these resonances with a Lorentzian function their resonance wavelength λ_0 and Q factor can be determined. In the case of TE-polarized light a Q of 2.1e5 is obtained in the C-band. This corresponds with a finesse F=204 and a propagation loss α=0.9 dB/cm. By varying the temperature of the stage, a shift of the resonance wavelength is induced, as shown in Figure 1 E. For the case of variations in the stage temperature, T, a slope sensitivity of S_T=10.2 pm/K was achieved for TE-polarized light, as shown in Figure 1 F. With a standard deviation in the determination of λ_0 of 0.5 pm this corresponds to a limit of detection LOD= 0.15 K.

The transmission experiment was repeated by immersing the MRR in a water droplet. Higher propagation losses are now obtained due to the combined effect of absorption of light by the H_2O cladding together with a higher coupling loss due to the reduced refractive index contrast of the MRR and the cladding, both resulting in a reduced Q. For TE-polarized light the Q drops down to 51e3, corresponding with a F=50 and α=4.5 dB/cm. For TM-polarized the effect is even more dramatic due to the mode being less confined in the waveguide and results in a Q=33e3, F=32 and α=7.7 dB/cm. By dissolving NaCl in water the refractive index of the solution changes by 0.0018 RIU/%wt of NaCl, resulting in a resonance wavelength shift. Solutions were prepared with NaCl weight variations up to 4%, corresponding with a water refractive index variation of 0.007 RIU. The solutions were then placed on top of the MRR while monitoring λ_0 for both TE- and TM-polarization. Figure 1 G shows the slope sensitivity S_n for a variation of bulk cladding refractive index n. For TE-polarized light S_n=70 nm/RIU and for TM-polarized light S_n=110 nm/RIU. With a standard deviation in the determination of λ_0 of 0.5 pm this corresponds to a LOD of 2.2e-5 RIU and 1.4e-5 for TE and TM-polarized light respectively.

In conclusion, a high Q Al_2O_3 MRR bulk refractive index and temperature sensor was presented with S_n=110 nm/RIU together with a LOD=1.4e-5 for TM-polarized light.

References

[1] M. Iqbal et al, *Label-free biosensor arrays based on silicon ring resonators and high-speed optical scanning instrumentation,* IEEE Journal of Selected Topics Quantum Electronics, vol. 16, no. 3, pp. 654-661, 2010

[2] R. Heideman et al, *Triplex-based integrated optical ring resonators for lab-on-a-chip and environmental detection,* IEEE Journal of Selected Topics in Quantum Electronics, vol. 18, no. 5 pp. 1583-1596, 2012

[3] A. Samusenko et al, *A SiON Microring resonator-based platform for biosensing at 850 nm,* Journal of Lightwave Technology, vol. 34, no. 3, pp. 969-977, 2016

[4] E. H. Bernhardi et al., *Intra-laser-cavity microparticle sensing with a dual-wavelength distributed-feedback laser,* Laser & Photonics Reviews, vol. 7, no. 4, pp. 589-598, 201

EUROPEAN CONFERENCE ON INTEGRATED OPTICS

A single-frequency integrated ring laser for gyro applications

Stanisław STOPIŃSKI[1*], Luc AUGUSTIN[2] and Ryszard PIRAMIDOWICZ[1]
[1]Institute of Microelectronics and Optoelectronics, Warsaw University of Technology, Koszykowa 75, 00-662 Warsaw, Poland
[2]SMART Photonics B.V., Horsten 1, 5612 AX Eindhoven, the Netherlands
*S.Stopinski@imio.pw.edu.pl

Inertial measurement unit (IMU) is an essential part of modern aircrafts, drones spacecrafts, ships, missiles and others. A typical IMU comprises a set of accelerometers and gyroscopes providing signals which enable accurate and reliable navigation. The application determines detailed requirements, however in any case high speed and accuracy, compact and robust design combined with low power consumption are strongly demanded. Optical gyroscopes, either interferometric or ring laser based devices, seem to be the most suitable for these applications. However, so far an integrated optical gyroscope has not been implemented on the market [1]. In our previous paper [2] we demonstrated the initial results of our research on multi-mode integrated ring lasers for gyro application, while in this work we present a system, based on a single-frequency integrated ring laser, which could be used as an optical gyro sensor.

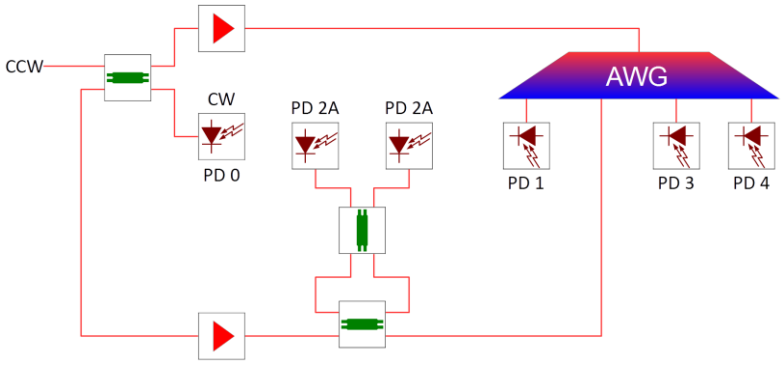


Fig. 1. Schematic diagram of the single-frequency integrated ring laser.

The scheme of the integrated ring laser is shown in Fig. 1. It comprises two semiconductor optical amplifiers (SOA, l = 750 μm) connected with each other by deeply etched waveguides forming a ring. A 1×4 arrayed waveguide grating (AWG, λ_c = 1550 nm, $\Delta\lambda$ = 1.6 nm, FSR = 12.8 nm) is used as an intra-cavity wavelength filter in order to force

the laser to operate on a single frequency. The top-left coupler (an 85:15 MMI) is used to tap the signal out of the laser cavity for characterization purposes. The two lower MMI couplers and two photodiodes (PD 2A and 2B) are used for detection of the wavelength split under rotation of the sensor. Fig. 2. presents the mask layout of the designed photonic circuit. The chip was fabricated in the generic process of SMART Photonics [3].

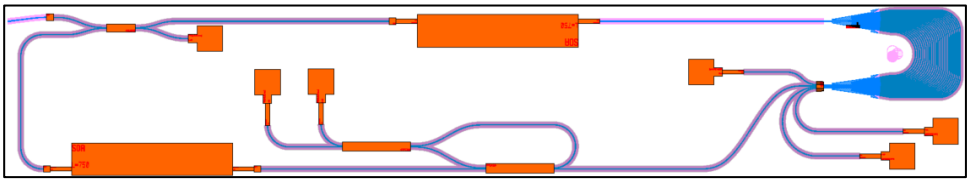


Fig. 2. The mask layout of the photonic chip (dimensions 4.6 × 0.8 mm).

The fabricated chip was initially characterized. Fig. 3. presents LI characteristics of the ring laser measured with a power meter at the chip output (counter-clockwise, CCW) and on-chip by reading the photocurrent on PD 0 (clockwise, CW). The threshold current is around 24 mA. The power of the CW and CCW modes is similar up to around 30 mA. For higher currents the CCW mode dominates. This phenomenon is similar to the results obtained in [4] for an AlGaAs ring laser, where also domination of one mode for higher supply currents was reported.

Fig. 3. presents also the output spectrum of the laser, measured while powering the SOAs with 70 mA, with a clearly visible singly frequency. The side mode corresponds to an adjacent AWG free spectral range, the side mode suppression ratio is as good as 52 dB.

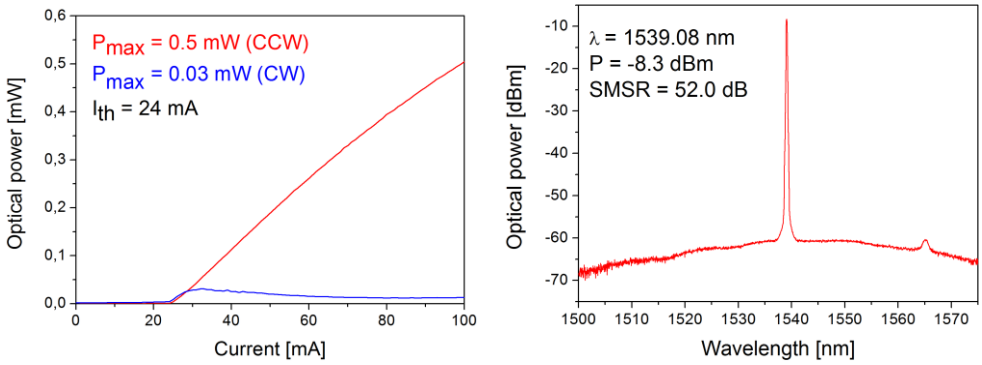


Fig. 3. Measured LI characteristics of CW and CCW signals and recorded output spectrum of the CCW signal.

Acknowledgement: The research leading to these results has received funding from the National Science Centre (decision DEC-2013/09/N/ST7/04430) and from the EU Horizon 2020 research and innovation programme under grant agreement No. 687777 (PICs4All).

References

[1] M.N. Armenise et al., Advances in Gyroscope Technologies, Springer-Verlag, Berlin 2010

[2] S. Stopinski et al., Integrated optical gyroscope, Proceedings of the 20th Annual Symposium of the IEEE Photonics Benelux Chapter, pp. xx-xx, Brussels, Belgium, 8-9.02.2016

[3] M.K. Smit et al., Semicond. Sci. Technol. 29, 8, (2014)

[4] M. Sorel et al., IEEE J. Sel. Topics Quantum Electron. 39, 10 (2003).

Analysis of the sensitivity of Mach-Zehnder interferometer filter to fabrication tolerances through elementary effect test

Abi WAQAS[1,2*], Daniele MELATI[1] and Andrea MELLONI[1]

[1]Dipartimento di Elettronica, Informazione e Bioingegneria, Politecnico di Milano, 20133, Italy

[2]Department of Telecommunication, Mehran University of Engineering and Technology, Pakistan

[*]abi.waqas@polimi.it

Abstract: Sensitivity analysis method is applied to the Mach-Zehnder interferometer filter to assess how the fabrication processes variations of some geometrical parameters can influence the performance of the photonics devices.

1. Introduction: Manufacturing variations are becoming an unavoidable issue in modern fabrication processes, because can have a strong effect on the functionality of the fabricated circuits, limiting the sustainable complexity and hampering the possibility to achieve high yield of the fabrication processes. Therefore, it is crucial to be able to include stochastic uncertainties in the design phase [1]. Sensitivity analysis techniques [2] are hence of fundamental importance for the identification of the uncertain parameters (e.g. waveguide width, doping level, height of the layers) that have the greatest influence on the overall circuit performance. Typically, these techniques are adopted to screen the whole range of uncertain parameters, with the aim to isolate the subset which has the strongest effect on the outputs, thus reducing the number of parameters that should be more carefully investigated to maximize the number of fabricated devices fulfilling design specifications [3]. The most common sensitivity techniques proposed in literature include the elementary effect test (Morris method) and variance based sensitivity analysis (Sobol). In this paper we focus on Morris method to analyse the behaviour of complex photonic circuits subject to fabrication uncertainties. In particular, we exploit the method of Morris to evaluate the variability of the 3-dB bandwidth of a seventh order Mach-Zehnder interferometer filter exposed to random fluctuations of the waveguide width and the gap of coupling regions.

2. Theoretical background: Morris method [4], is based on the computation of differential metrics, called elementary effects, evaluated on a statistical basis on the whole space of variation of the input parameters of an assigned model. Being f(x) the model whose sensitivity needs to be assessed, for a given vector of uncertain parameters x belonging to sample space Ω, the elementary effect EE_i of the input factor x_i on f is defined as the incremental ratio:

$$EE_i(x) = \frac{f(x_1, x_2, \dots, x_i + \Delta x_i, \dots, x_k) - f(x_1, x_2, \dots, x_i, \dots, x_k)}{\Delta x_i}. \quad (1)$$

The statistical parameters (mean and variance) of elementary effects EE_i provides a direct measure of the influence of the factor $x_i$on the output function f. In particular, a high value for the mean indicates that the considered parameter has an important overall influence on the output function f.

3. Sensitivity analysis of a seventh-order Mach-Zehnder interferometer filter: The goal is to measure the impact of the random variation of the waveguide width and gap of coupling regions on the 3- dB bandwidth of a seventh-order MZI filter. The designed MZI filter has 3-dB bandwidth of $BW_0 = 27.5GHz$ and the corresponding coupling coefficients for the eight directional couplers are $K_1 = K_8 = 0.9914$, $K_2 = K_7 = 0.0004$, $K_3 = K_6 = 0.0690$ and $K_4 = K_5 = 0.3489$. This value provided an in-band isolation of 20 dB. All the seven stages have the

same imbalance length of $134.3\mu m$ and the same effective index $n_{eff} = 2.23$ (SOI technology) with nominal waveguide width of $W_i = 407.7nm$. The nominal gap in eight coupling regions of coupler is $g_i = 0.3\mu m$. The free spectral range of the design is $100GHz$. Fig. 1a shows the transfer function of the filter based on Mach-Zehnder interferometer at bar and cross ports. In the described test case, random process variations are represented by noise applied to the relevant parameters of the filter, that is to the waveguides width and gap of the coupling regions of MZI filter. The vector $[\tilde{W}_1\ \tilde{W}_2\ \tilde{W}_3\ \tilde{W}_4\ \tilde{W}_5\ \tilde{W}_6\ \tilde{W}_7\ \tilde{g}_1\ \tilde{g}_2\ \tilde{g}_3\ \tilde{g}_4\ \tilde{g}_5\ \tilde{g}_6\ \tilde{g}_7\ \tilde{g}_8]$ of the random parameters represents the process variation variables that are assumed to be Gaussian distributed with $\mu_{width} = 407.7nm$, $\mu_g = 0.3\mu m$, $\sigma_W = 30pm$ and $\sigma_g = 1nm$. The considered fabrication process variation can heavily affect the performance of the circuit, as shown in Fig 1a with thin grey lines. The 3-dB passband have large fluctuation (see Fig. 1b) even under relatively small process variations. Hence, our goal is to assess the dependence of 3–dB filter bandwidth on waveguides width and gap of coupling regions of coupler and to find the most influential random input parameter which is contributing to the output variability. The obtained results for Morris sensitivity analysis with $r \times (M + 1)$ (where r is number of finite differences and M is number uncertain input parameters) model evaluations (where $r = 1000$ and $M = 15$) are presented in Fig. 1c, which shows the mean μ^* versus the standard deviation of the elementary effects for 3-dB bandwidth of filter as a function of the random waveguides width and gap of coupling regions. Result obtained for analysis took around 4-5 minutes (16000 samples) with computational speed of core i7 (2.4 GHz) with 16 GB ram. The circles in the Fig. 1c shows the impact of each waveguide width and the gaps of coupling region in defining bandwidth of filter while squares are the 95% confidence bounds of the corresponding circles. The more a point is placed on the right of the horizontal axis, the more influential is the factor. The higher up a point is along the vertical axis, the larger is its degree of interactions with other factors. By observing Fig. 1(c), it is possible to conclude that for defining the bandwidth of filter, the waveguide width is more important than the gap of coupling region for a given variations of 1 nm for the gaps and 30 pm for waveguide width.

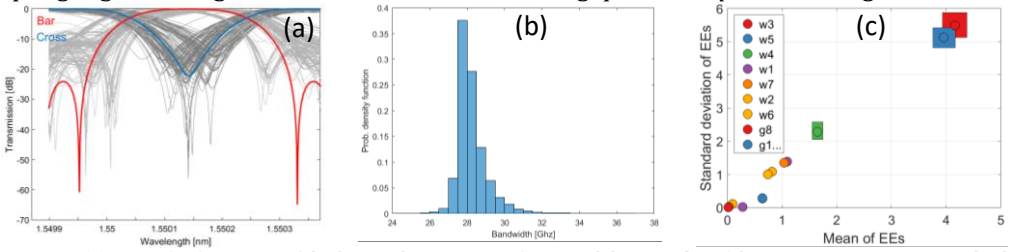


Figure 1:(a) Transfer functions of the bar and cross port of nominal design when fabrication variations is applied on the waveguide width and gap of coupling regions (grey thin lines). (b) Probability density function of the 3-dB bandwidth of the filter. Nominal bandwidth is 27.5 GHz. (c) Result of the Morris sensitivity analysis performed on the 3-dB bandwidth of the filter. Horizontal axis shows absolute mean (μ^*) of elementary effects. Vertical axis shows the standard deviation of elementary effects.

4. Conclusion: Sensitivity of the filter bandwidth has been analysed and the most influential random input parameter (waveguide width) have been identified. The discussed techniques can be easily extended to take into account also the influence of other parameters on the different responses of the investigated devices.

5. References

[1] TW Weng., et al., "Stochastic Simulation and Robust Design Optimization of Integrated Photonic Filters", Nanophotonics (2016)

[2] Saltelli, A., et al., "Global Sensitivity Analysis", The Primer (Wiley, 2008).

[3] Saltelli, A., "Sensitivity analysis for chemical models". Chem. Rev. 105(7), 2811–2827 (2005).

[4] Morris, M.D., Factorial sampling plans for preliminary computational experiments, Technometrics (1991).

Low-voltage Optical Switching by a Four-waveguide Directional Coupler

Tianran LIU*, Francesco PAGLIANO, Andrea FIORE

Department of Applied Physics and Institute for Photonic Integration, Eindhoven University of Technology, P.O. Box 513, 5600MB Eindhoven, The Netherlands

** t.liu@tue.nl*

Optical switches base on electrostatic movable micro-mirrors have been developed since nineties of the last century for their low power consumption and high optical performance [1]. As nano-fabrication technology advances, it is recently possible to build optical switches with other optical devices on a single chip. To reach higher level of integration, moving waveguides rather than mirrors to steer light is a better option since it involves less free-space alignment. Several works have been done in this direction in the recent years [2-4]. However, most of these devices require a high actuation voltage from 14V to 50V and the switching frequency is below 1MHz, which limit their diversity in application.

We propose a nano-opto-electro-mechanical switch based on three-dimensional four-waveguide directional coupler. Compared to most mechanical actuating optical switches, the actuation voltage of this novel device is small (3V). Thanks to the compact footprint, the natural mechanical frequency is above 1MHz range, allowing a fast switching speed.

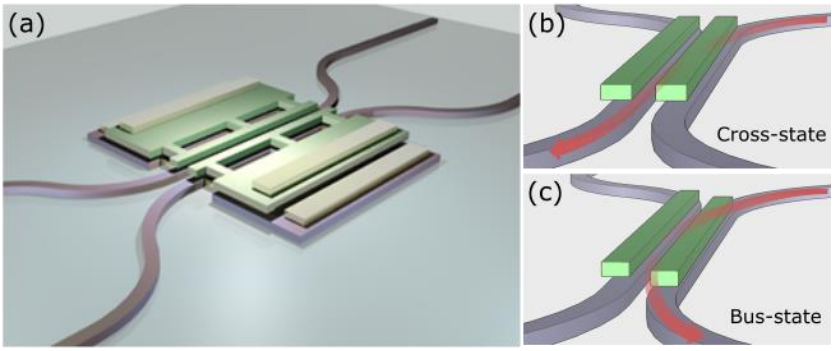


Fig. 1. (a) A simplified illustration of the switch. (b) Cross-state. (c) Bus-state.

The proposed switch is based on a directional coupler composed of four waveguides, with two of which are suspended. By inducing voltage bias, the two suspended waveguides can be actuated vertically, changing the state of switch between cross-state and bus-state, as showed in Fig.1(b) and (c).

The mechanism of our device can be depicted in the frame of coupled mode theory. Considering four identical waveguides arranged in the way described above, neglecting the diagonal coupling, the system can be depicted in Eq.1.

$$\frac{d}{dx}\begin{bmatrix} b_1(x) \\ b_2(x) \\ a_1(x) \\ a_2(x) \end{bmatrix} = -i\begin{bmatrix} \beta & \kappa_h & \kappa_{v1} & 0 \\ \kappa_h & \beta & 0 & \kappa_{v2} \\ \kappa_{v1} & 0 & \beta & \kappa_h \\ 0 & \kappa_{v2} & \kappa_h & \beta \end{bmatrix}\begin{bmatrix} b_1(x) \\ b_2(x) \\ a_1(x) \\ a_2(x) \end{bmatrix} \quad (1)$$

The solution of Eq.1 needs to satisfy $|b_2(L)|^2 = 1$ and $|a_1(L)|^2 = |a_2(L)|^2 = |b_1(L)|^2 = 0$ for the cross-state. By putting the solution into cross-state condition, we get Eq.2, which tells us the device length and coupling rates required by the state.

$$\begin{cases} \kappa_{v1} = \kappa_{v2} = 2l\kappa_h & l = 1,2,3 \dots \\ L = (2m+1)\frac{\pi}{2\kappa_h} & m = 0,1,2 \dots \end{cases} \quad (2)$$

The solution of Eq.1 needs to satisfy $|b_1(L)|^2 = 1$ and $|a_1(L)|^2 = |a_2(L)|^2 = |b_2(L)|^2 = 0$ for the bus-state. By putting the solution into this condition, we get Eq.3, which tells us the coupling rates required by the bus-state.

$$\begin{cases} \kappa_{v1} = \left(2p \pm \sqrt{4(2n-1)^2 - 1}\right)\kappa_h & p = 2,3,4 \dots;\ n = 1,2,3 \dots \\ \kappa_{v2} = \left(2p \mp \sqrt{4(2n-1)^2 - 1}\right)\kappa_h & p = 2,3,4 \dots;\ n = 1,2,3 \dots \end{cases} \quad (3)$$

The coupling rates can be related to vertical distances between waveguides after calibration. To demonstrate the concept, we build a FDTD model with following parameters. The length of the device is 25 μm. The width and thickness of the bottom waveguides are 370 nm and 220 nm. Initial vertical distance between waveguides is 220 nm. Suspended waveguides are 15 nm thicker to compensate the substrate effect. The material of waveguide is assumed to be silicon and the bottom waveguides sit on silica substrate.

Fig.2(a) shows the transmission evolution during actuating the device from cross-state to bus-state, given by FDTD simulations. The bandwidth of the switch is showed in Fig.2(b).

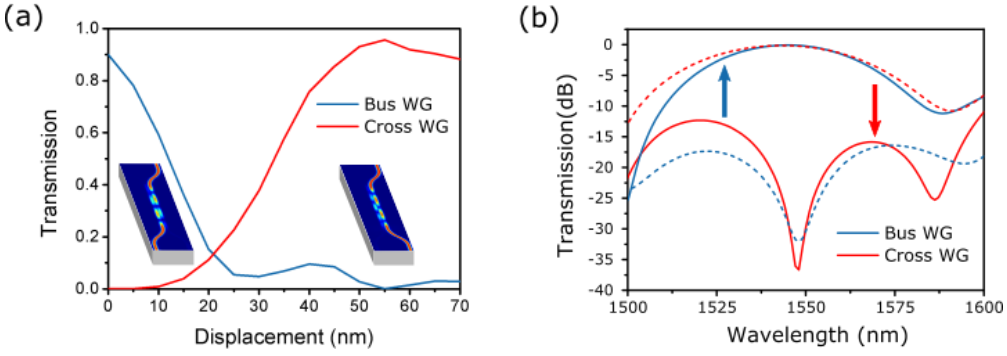


Fig. 2. (a) Simulated transmission characteristics as a function of the displacement of right suspended waveguide, with the displacement of left one fixed at 5 nm. (b) Simulated spectral response of Cross-state (solid line) and Bus-state (dashed line)

FEM simulations show that the actuation voltage of our design can be as low as 3.25V, thanks to the small displacement requirement compared to other designs [2-4]. The natural mechanical resonant frequency of the device is 1.29 MHz, which is also the highest among reported designs. The energy needed by each swithing operation is given by $E_s = \frac{\varepsilon_0 A V_s^2}{d-z}$, which is only 85 fJ here.

References

[1] Toshiyoshi, Hiroshi, and Hiroyuki Fujita. "Electrostatic micro torsion mirrors for an optical switch matrix." *Journal of Microelectromechanical Systems*, vol. 5, no. 4, pp. 231-237, 1996

[2] Seok, T.J., Quack, N., Han, S., Muller, R.S. and Wu, M.C., "Large-scale broadband digital silicon photonic switches with vertical adiabatic couplers." *Optica,* vol. 3, no. 1, pp. 64-70, 2016

[3] Han, S., Seok, T.J., Quack, N., Yoo, B.W. and Wu, M.C., "Large-scale silicon photonic switches with movable directional couplers." *Optica,* vol. 2, no. 4, pp. 370-375, 2015

[4] Abe, Syotaro, and Kazuhiro Hane. "Variable-gap silicon photonic waveguide coupler switch with a nanolatch mechanism." *IEEE Photonic Tech. L.* vol. 25, no. 7, pp. 675-677 , 2013

Linear and non-linear propagation properties of state of the art Silicon Nitride waveguides

Pascual MUÑOZ[1,2*], Gloria MICÓ[1], Luis BRU[1], Daniel PASTOR[1], David DOMENECH[2]
[1]Photonic-IC group @ Photonic Research Labs, Universitat Politècnica de Valencia, Spain
[2]VLC Photonics S.L., Ed9B-UPV, c/ Camino de Vera s/n, Valencia, Spain
[*]pascual@ieee.org

Among the materials for silicon based photonics, Silicon Nitride (Si_3N_4) has received considerable interest for non-linear photonics, due to its larger band gap with negligible two photon absorption [1]. Each of the non-linear applications requires a suitable dispersion [2,3]. Targeted at moderate or very low anomalous dispersion, high confinement strip waveguides have been reported by several groups [4-10] at NIR and above. Guiding nitride (in some Si rich) with heights 0.7-2.5μm, waveguide widths of 0.7-4.0μm and loss of 0.04-1.37 dB/cm at λ=1550nm (0.16-2.1dB/cm for λ in 2600-3700nm) have been reported. Strong anomalous dispersion can be well attained with smaller film height waveguides (h=200-400nm), with waveguide widths 0.8-1.0μm, and loss of 1.30-2.10 dB/cm at 1550 nm [11,12]. In the design workflow, time consuming simulations (preparation, computer time and results post-processing) of the waveguide fundamental properties, hamper the (comparatively) faster first steps of a design attempt. In this paper, we report on an interpolation strategy using Bernstein polynomials, and provide coefficients for the effective index and non-linear parameter for state of the art Si_3N_4 waveguides with film heights h=300nm [10] and h=800nm [2]. A strip waveguide structure was defined in a finite differences mode solver tool [13]. Despite each reported platform [4-12] employs different substrate and cladding SiO_2 heights, in the simulations a fixed height of 4.0μm was used for both, since the growth of different heights of SiO_2 is a matter of using the right fabrication recipe. The SiO_2 and (LPCVD) Si_3N_4 wavelength dependent refractive indices from [5,14] were used for the wavelength range of simulation (λ_0=0.47μm-λ_1=3.7μm). The waveguide width was swept from w_0=0.3μm to w_1=2.8μm. Bernstein polynomials [12], eqs. (1)(2), were employed to fit the results from the simulations, since they proved to be well suited to approximate versus width and wavelength, with a modest number of coefficients, Table 1, with normalized error average $<10^{-6}$ (with std of 10^{-4}). Furthermore, with a unique set of coefficients for the effective index, eqs. (3)(4), it is possible to describe the dispersion as well, eq. (5), through the polynomial derivatives [15]. The results for linear propagation match those of [3] with h=1200nm, and our own OFDR measurements for h=300nm (-0.8ps/km·m). The non-linear parameter was calculated from the field components as in [6], whose results were matched as well. In the interpolations, w and λ dimensions were normalized, $\Lambda=(\lambda-\lambda_0)/(\lambda_1-\lambda_0)$ and $W=(w-w_0)/(w_1-w_0)$ and $\Delta\lambda=\lambda_1-\lambda_0$. The results in Fig. 1 and Table 1 are for TE_0, despite these waveguides support TM_0 as well, cf. [15], having flat dispersion at different wavelengths, with different type (anomalous, normal), but from our simulations with comparatively larger nonlinear parameter for TM_0, albeit confinement (i.e. less loss due to sidewall roughness) is higher for TE_0. For the C-band and h=800nm, moderate anomalous D for comb generation is found for w=1.65μm, whereas low anomalous D for supercontinuum generation is met for w=2.0μm. For non-linear pulse compression with strong normal D, h=300nm and w=1.65μm for C-band or λ=2.0-2.4μm.

$$B(t)=\sum_{i=0}^{n} b_{i,n}(t)P_i \qquad (1) \qquad n_e(W,\Lambda)=\sum_{i=0}^{n} b_{i,n}(W)E_i(\Lambda) \qquad (3) \qquad D(W,\Lambda)=-\frac{\lambda}{c}\frac{1}{\Delta\lambda^2}\frac{\partial^2 n_e(W,\Lambda)}{\partial\Lambda^2} \qquad (5)$$

$$b_{i,n}(t) = \binom{n}{i} t^i (1-t)^{n-i} \quad (2) \qquad E_i(\Lambda) = \sum_{j=0}^{m} b_{j,m}(\Lambda) E_{i,j} \qquad (4) \qquad \frac{\gamma(W,\Lambda)}{n^2 n_2} = \sum_{i=0}^{n} b_{i,n}(W) \sum_{j=0}^{m} b_{j,m}(\Lambda) g_{i,j} \qquad (6)$$

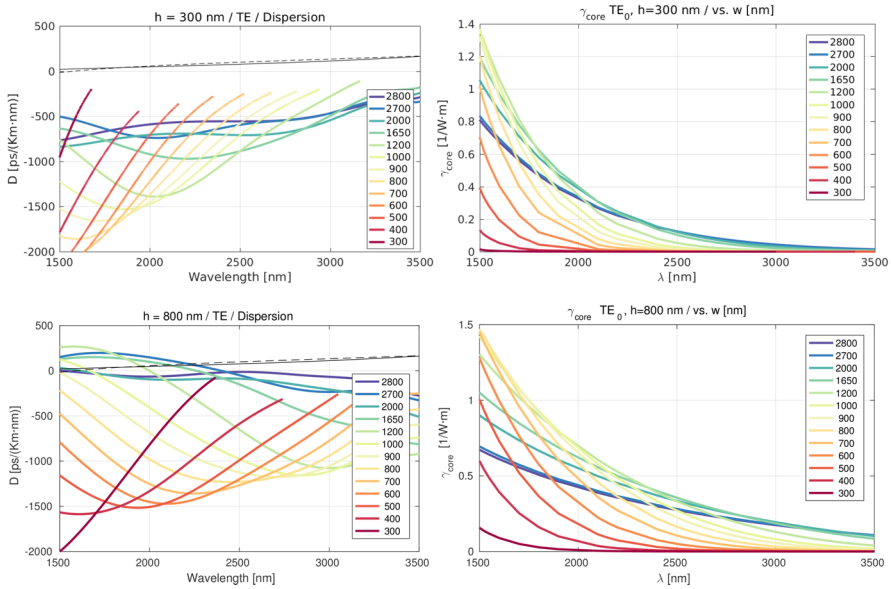


Fig. 1: Dispersion (Si_3N_4 –, SiO_2 --) and non-linear parameter (n_2=0.24 m²/W at 1.5µm for all wavelengths) vs. λ [nm] (λ>1500nm) for waveguide widths (color lines) [300,2800] nm

$E_{i,j}$	h = 300 nm, TE_0					
j↓ / i→	0	1	2	3	4	5
0	1.8776213	2.122918	1.8338975	2.1035948	1.9577628	1.9983654
1	1.5934236	2.0444746	1.5628135	1.9956184	1.7710133	1.8322354
2	1.4362759	2.1394231	1.3769242	2.1079449	1.7048331	1.8222323
3	1.1819761	1.6413274	1.7166467	1.404391	1.7171903	1.6057694
4	1.8481478	0.40673147	3.3983956	0.50210963	2.1211686	1.6983453
5	1.0641421	2.472913	-0.55656357	3.0907673	0.83795738	1.5242143
6	1.6845798	0.71592265	2.9017514	0.43428066	2.0751221	1.5781534
7	1.2956966	1.786315	0.68464599	2.0493862	1.1950669	1.4802472
8	1.4635626	1.2874377	1.7004149	1.2467895	1.5764815	1.4858896
9	1.3965793	1.4399491	1.3459126	1.4839961	1.4166315	1.4509043
10	1.3994648	1.3942841	1.4113342	1.4091712	1.4289707	1.4336455
11	1.3863866	1.3867627	1.3895039	1.3997934	1.4072365	1.4142388

$E_{i,j}$	h = 800 nm, TE_0					
j↓ / i→	0	1	2	3	4	5
0	1.9431049	2.1819427	1.9011389	2.1624505	2.0215404	2.0606737
1	1.7152609	2.1781848	1.6590277	2.1366677	1.8826102	1.9529519
2	1.6255761	2.2872693	1.6360497	2.2125712	1.9198212	1.9998641
3	1.3494673	2.0929693	1.4968905	2.0040504	1.7640568	1.8302874
4	1.5591429	1.665797	2.4213301	1.4949232	2.1294683	1.9411275
5	1.3026449	1.5242892	1.8250148	1.6108291	1.7285077	1.7197853
6	1.5460399	1.3276669	2.2218796	1.5220547	1.9157157	1.8320111
7	1.3651682	1.4516072	1.5863647	1.693414	1.642706	1.6839796
8	1.4486378	1.3644169	1.6577231	1.6545543	1.6607325	1.6928569
9	1.4032814	1.4150265	1.4930563	1.6113629	1.601017	1.6288002
10	1.4018272	1.3946444	1.4543351	1.5715799	1.5590783	1.5915393
11	1.388665	1.388823	1.4177338	1.5209248	1.5225521	1.5505139

$g_{i,j}$	h = 300 nm, TE_0					
j↓ / i→	0	1	2	3	4	5
0	3.8362107	2.2956705	-0.52159735	2.432606	0.13797359	0.68709093
1	-0.71449253	2.7699387	-2.6270367	2.2577456	-0.4980362	0.21254014
2	-1.1085944	5.5553406	-7.0130271	5.9631147	-1.8982644	0.34649937
3	1.4642427	-10.343148	18.209874	-15.298076	6.2120016	-0.40174322
4	-0.99087957	9.9119809	-18.880421	17.320314	-7.2764596	0.60477957
5	0.34561903	-6.9986065	14.116331	-13.41594	5.9589326	-0.4397413 2
6	0.06491204 1	3.7130759	-7.979316	7.990713	-3.6080734	0.30824375
7	-0.15910676	-1.4492067	3.351523	-3.5260698	1.6639435	-0.13072975
8	0.096807226	0.3972896	-1.0119507	1.1341267	-0.54227326	0.05266007
9	-0.031401585	-0.068990285	0.20015457	-0.23931782	0.12271787	-0.0081222481
10	0.0050752322	0.0060853095	-0.021668193	0.028655974	-0.013077666	0.0030896597
11	-0.00020783492	2.2365601e-06	0.0002953014	-0.00035186824	0.0012013796	0.0010157015

$g_{i,j}$	h = 800 nm, TE_0					
j↓ / i→	0	1	2	3	4	5
0	1.7031003	0.85570939	-0.047317729	0.91007486	0.10754949	0.29099344
1	-0.083329046	1.391734	-1.3389732	1.2539029	-0.27418309	0.12999258
2	0.1798207	1.0335475	-0.83285623	0.96864681	-0.16302979	0.13913136
3	-0.42401032	0.64319656	-0.11056688	-0.11210339	0.22204989	0.03001482
4	0.57064072	-1.1130712	1.7393345	-0.81913885	0.33496026	0.071001023
5	-0.6203145	1.4140379	-1.3818691	0.72585653	-0.11172567	0.024067798
6	0.49542487	-1.3018016	1.5525712	-0.66944185	0.19466881	0.045051879
7	-0.2829412	0.74661395	-0.76654336	0.42415594	-0.055587859	0.02134889
8	0.11549829	-0.32643877	0.3641926	-0.11817995	0.04651855	0.023965483
9	-0.029763945	0.08138206	-0.084726439	0.073636957	0.0049724388	0.016274544
10	0.0043839027	-0.012987769	0.012091056	0.016793747	0.011525181	0.013034842
11	-0.00011035055	0.00044499812	-0.0028199938	0.015079179	0.0083837375	0.0098542878

Table 1: Bernstein coefficients (for λ in 470-3700nm) for TE_0 effective index (left), eq. (3), and normalized non-linear parameter for the waveguide Si_3N_4 core (right), eq. (6

References

[1] K. Ikeda e.a., Optics Express, vol. 16, no. 17, pp. 12 987-12 994, Aug. 2008
[2] D. J. Moss e.a., Nature Photonics, vol. 7, no. 8, pp. 597-607, Jul. 2013.
[3] J.M. Chávez-Boggio e.a., J. OSA B, vol. 31, no. 11, pp. 2846-2857, 2014.
[4] T. J. Kippenberg e.a., Science, vol. 332, no. 6029, pp. 555–559, Apr. 2011.
[5] K. Luke e.a., Optics Letters, vol. 40, no. 21, pp. 4823-4826, 2015.
[6] C. J. Krückel e.a, Optics Express, vol. 23, no. 20, pp. 25827-25837, 2015.
[7] K. Luke e.a., Optics Express, vol. 21, no. 19, pp. 22829–22833, 2013.
[8] P. T. Lin e.a., Applied Physics Letters, vol. 102, no. 25, pp. 251121+, 2013
[9] J. P. Epping e.a., Optics Express, vol. 23, no. 2, pp. 642-648, 2015.
[10] M. H. P. Pfeiffer e.a., Optica, vol. 3, no. 1, pp. 20-25, 2016.
[11] D. Doménech e.a., in Proc. OPTOEL, PO-SII-27, 2015.
[12] K. Shang e.a., Optics Express, vol. 23, no. 16, pp. 21334-21342, 2015.
[13] T. Korthorst e.a., Advanced Optical Technologies, vol. 4, no. 2, pp. 147–155, 2015.
[14] C. Z. Tan and J. Arndt, J. Physics and Chemistry of Solids, vol. 61, no. 8, pp. 1315–1320, 2000.
[15] R. H. Bartels e.a, An Introduction to Splines for Use in Computer. Ed. M. Kaufmann, 1998.
[16] A. Kordts e.a., Optics Letters, vol. 41, no. 3, pp. 452-455, Jan. 2016

Double Al_2O_3 Microring Resonator for Self-Referenced Sensing Applications

Michiel DE GOEDE[1*], Meindert DIJKSTRA, Sonia GARCÍA BLANCO
[1] Optical Sciences Group, MESA+ Institute for Nanotechnology, University of Twente,
P.O. Box 217, 7500 AE Enschede, The Netherlands
[*] m.degoede@utwente.nl

Microring resonators (MRRs) find many applications for on-chip integrated optical sensors. Their operation is based on the spectral shift of resonance notches due to the probing of the evanescent modal field of local dielectric variations. MRR sensors are sensitive to any environmental perturbations, including temperature fluctuations and bulk refractive index variations, making it difficult to de-embed these from the actual analyte signal. By using a double MRR and by recording the differential spectral shift of the resonance notches of both a signal and a reference MRR the effect of the environment can be minimized [1]. Here, an Al_2O_3 double MRR with high quality factor Q=1.5e5 is demonstrated that is insensitive to both temperature and bulk refractive index changes. This system can be used for self-referenced and stable biosensing applications by functionalizing one of the two MRRs. Then, a change in differential resonance wavelength shift arises only due to the attachment of analytes to the sensing MRR surface, eliminating the environmental variations.

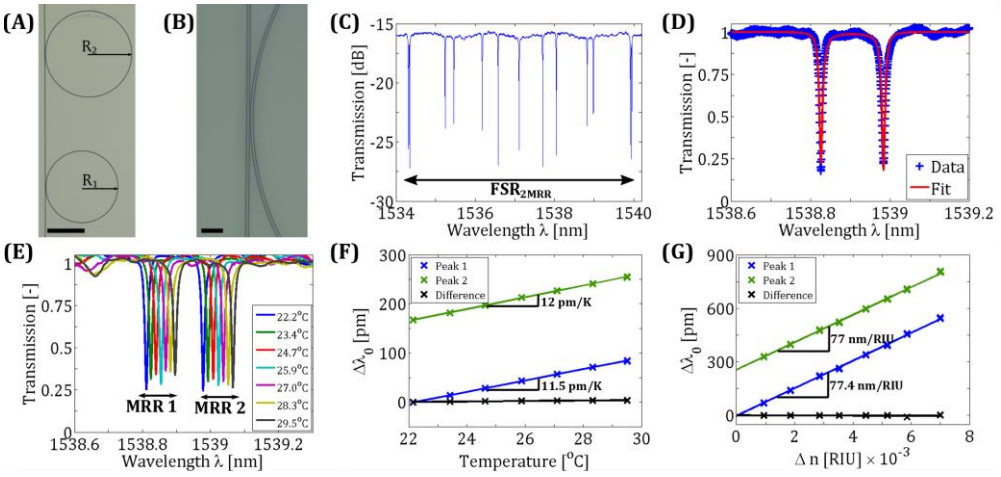


Fig. 1. (A), Optical microscope image of the double MRR indicating the MRR radii. Scale bar is 100 µm. (B), Close up of a MRR. Scale bar is 20 µm. (C), Transmission spectrum of the

double MRR. (D), Double resonance with fit. (E), Spectral shift of the double resonance due to stage temperature. (F), Slope sensitivity of double resonance for temperature variations. (G), Slope sensitivity of double resonance for refractive index sensing.

To measure the differential wavelength shift of the resonances of two MRRs in series two MRRs with radii of 200 µm and 240 µm were connected to the same bus waveguide. The ration between their radii was chosen to ensure that the free spectral range of the double MRR device (FSR_{2MRR}) is smaller than the spectral length of the C-band and that multiple closely spaced resonances will be present. Optimized geometrical parameters of the device are a waveguide width and height of 2.4 µm and 0.7 µm respectively, together with a coupling gap of 0.8 µm. Fabrication was done by the method described by [2] and the resulting device is shown in Figures 1 A and B.

The double MRR device was characterized by transmission measurements with a tunable laser for TE-polarized light in the C-band, as shown in Figure 1 C. By fitting a double resonance with a double Lorentzian function the location of the resonance wavelengths λ_0 and the corresponding Q factor can be determined, as shown in Figure 1 D. For an air cladding both the MRRs have a Q=1.5e5, corresponding with a finesse F=100 and propagation loss α=1.4 dB/cm. Using H_2O as cladding gives extra water absorption losses and results in Q=40e3, F=26 and α=6 dB/cm.

Self-referenced sensor operation is demonstrated by varying an external parameter while monitoring the difference of the λ_0's of two closely spaced resonances of the double MRR device. By varying the temperature of the stage the location of both resonances shifts, as shown in Figure 1 E. Figure 1 F shows the positions λ_0 of both MRRs together with their difference. It was found that the two MRRs have a slope sensitivity of 12 pm/K and 11.5 pm/K respectively, yielding in a slope of the differential spectral shift of 0.5 pm/K. A similar self-referenced experiment was repeated by keeping the temperature fixed with a precision of 0.05 K and by adding H_2O droplets of varying NaCl concentration, and thus bulk cladding refractive index, on top of the double MRR device. The shifts in λ_0 of both MRRs are shown in Figure 1 G. Slope sensitivities of respectively 77.4 nm/RIU and 77.0 nm/RIU were found for the two MRRs. Again, the small difference between these two slopes effectively cancels the response of the differential resonance wavelength of the double MRR device within 0.4 nm/RIU.

In conclusion, a double MRR was reported that operates self-referenced and stable under environmental perturbations, namely, temperature and bulk refractive index. Temperature and refractive index variations were effectively eliminated. Using this result, next steps involve the functionalization of one of the two MRRs such that analytes can only attach to a single MRR. Then, the self-referenced sensor operation can be used to demonstrate ultra-stable surface sensing for the detection of biomarkers.

References

[1] D. Xu et al, *Real-time cancellation of temperature induced resonance shifts in SOI wire waveguide ring resonator label-free biosensor arrays*, Optics Express, vol. 18, no. 22, pp. 15137-15148, 2010

[2] J. Bradley et al, *Fabrication of low-loss channel waveguides in Al2O3 and Y2O3 layers by inductively coupled plasma reactive ion etching*, Applied Physics B, vol. 89, no. 2, pp 311-318, 2007

Simulation and Experimental Evaluation of Optical Chirp Modulation for Bimodal Waveguide Interferometer Biosensors

Daniel GRAJALES[1], Jose Ramón SENDRA[2], Laura M. LECHUGA[1]*

[1]Catalan Institute of Nanoscience and Nanotechnology (ICN2), CSIC and the Barcelona Institute of Science and Technology, and CIBER-BBN. Campus UAB. Barcelona, Spain.

[2]IUMA, Institute for Applied Microelectronics, University of Las Palmas GC, Campus de Tafira, Las Palmas, Gran Canaria, Spain.

* Laura.Lechuga@icn2.cat

We report the simulation and implementation of an optical chirp modulation system for interferometric optical waveguides operating in the visible range to explore the sensor response to different wavelengths in order to ensure the maximum sensitivity.

Optical interferometers are powerful and sensitive tools for detecting small changes at nanometric scale. When working as biosensor devices they can provide the highest sensitivities for real-time and label-free biomolecular detection, without the need of additional amplification steps. Our group proposed a Bimodal Waveguide Interferometer (BiMW) as a high performance biosensor, which is an elegant, robust, simple yet powerful and sensitive device [1]–[3]. Nonetheless, due to the nature of the interferometric signals, sensitivity fades or signal ambiguities can be present. To overcome such difficulties we proposed an all-optical phase modulation [4]. However, this technique required the individual analysis of the visibility (signal amplitude) inherent to each BiMW sensor, previously to any experiment, in order to ensure that we can get the maximum sensitivity. As a replacement, we propose a chirp modulation as an exploratory mechanism previous to the detection.

Some Fabry-Perot laser diodes (LD) can exhibit the defect of wavelength excursions of a few nanometers as a function of the variation of the injected power current. Thus, while varying (modulating) the LD current we can obtain a wavelength and intensity sweep. Each wavelength will have a different propagation constant and effective index thus, some of them will be in the maximum sensitivity position. In the case of the bimodal interferometer, the interferometric signal is obtained from the variation of the phase difference of the two modes. Since the first order mode has a larger evanescent tail, it will be more affected by changes occurring in the sensing area. The changes of intensity distribution at the output can be related to the variations occurring in the sensing area. By placing a two quadrants photodiode, the output intensities can be used to recreate the interferometric signal:

$Sr = (I_{up} - I_{down})/(I_{up} + I_{down})$, where I_{up} and I_{down} are the light intensities in the upper and lower photodiode quadrant, respectively. For a constant wavelength, the interferometric signal is related to the phase change $\Delta\varphi(t)$ by $Sr \propto Vcos(\Delta\varphi(t))$, where V is the visibility factor or fringe amplitude. The interferometric phase change as a function of the optical wavelength λ is given by:

$$\Delta\varphi_s(\lambda) = \frac{2\pi L}{\lambda}[(N_S - N_R)] \quad (1)$$

where L is the length of the waveguide and N_S and N_R are the effective index of the fundamental and first order mode of the BiMW. We start simulating the intensity response to wavelengths variations of 1 nm in steps of 0.5 nm using numerical and scientific python libraries. Figure 1a shows the simulated intensity response of a BiMW device as a function of different laser wavelengths and optical path length.

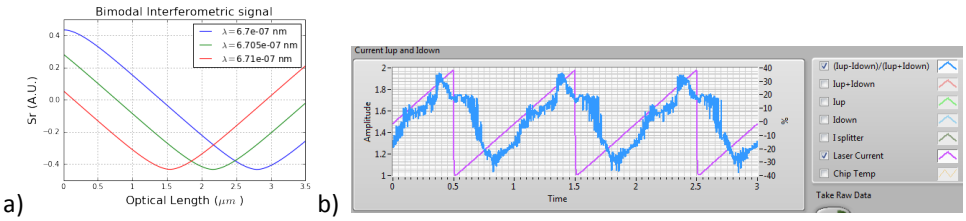


Fig. 1. Example of a simulated (a) and experimental (b) BiMW response for small wavelengths variations.

Using an experimental approach, different signal waveforms, amplitudes and offsets were evaluated modulating the LD current until finding the suitable ones for the BiMW devices. Because the biomolecular interactions taking place in the sensing area are slow (in the order of seconds), we can use slow modulation frequencies (1-100 Hz). The algorithm was implemented in LabView, modulating a Mitsubishi ML101J27 LD and using a Hamamatsu - S4349 Photodiode with micrometric positioning to obtain the signal. Figure 1b shows the response for a laser current sweep when having a constant refractive index in the sensing area. The micrometric positioning can help us to ensure a symmetric placement of the read-out photodiode thus obtaining an interferometric signal centred and ensuring the maximum sensitivity.

[1] K. E. Zinoviev, A. B. González-Guerrero, C. Domínguez, and L. M. Lechuga, "Integrated bimodal waveguide interferometric biosensor for label-free analysis," *J. Light. Technol.*, vol. 29, no. 13, pp. 1926–1930, 2011.

[2] J. Maldonado, A. B. González-Guerrero, C. Domínguez, and L. M. Lechuga, "Label-free bimodal waveguide immunosensor for rapid diagnosis of bacterial infections in cirrhotic patients," *Biosens. Bioelectron.*, vol. 85, pp. 310–316, 2016.

[3] D. Duval, A. B. González-Guerrero, S. Dante, C. Domínguez, and L. M. Lechuga, "Interferometric waveguide biosensors based on Si-technology for point-of-care diagnostic," 2012, vol. 8431, p. 84310P–84310P–11.

[4] S. Dante, D. Duval, B. Sepúlveda, A. B. González-Guerrero, J. R. Sendra, and L. M. Lechuga, "All-optical phase modulation for integrated interferometric biosensors," *Optics Express*, vol. 20, no. 7. p. 7195, 2012.

Widely tunable mid-IR monolithic coherent source

Alice BERNARD[1*], Marco RAVARO[1], Jean-Michel GERARD[2], Olivier PARILLAUD[3], Bruno GERARD[3], Ivan FAVERO[1], and Giuseppe LEO[1]

1 Laboratoire Matériaux et Phénomènes Quantiques, UMR 7162, Université Paris Diderot – CNRS, Paris, France

2 CEA-CNRS-UJF groupe Nanophysique et Semiconducteurs, CEA, INAC, SP2M, Grenoble, France

3 III-V Lab, Thales Research and Technology, Route départementale 128, 91767 Palaiseau, France

*giuseppe.leo@univ-paris-diderot.fr

InGaAsP lattice-matched to InP is widely used for optoelectronic components such as lasers, detectors and modulators. For the design of these devices, knowledge of refractive index is critical. While it has been well described up to 1.55 µm[1-4], only one publication offers its measurement at longer wavelengths[5], with limited precision. We have performed an accurate characterization of the refractive index up to 3.14 µm, lengthening the wavelength range and offering a significant increase in precision. This data is exploited to design a tunable source in the mid-IR range, through spontaneous downconversion (SPDC) of a laser beam at 1.55 µm.

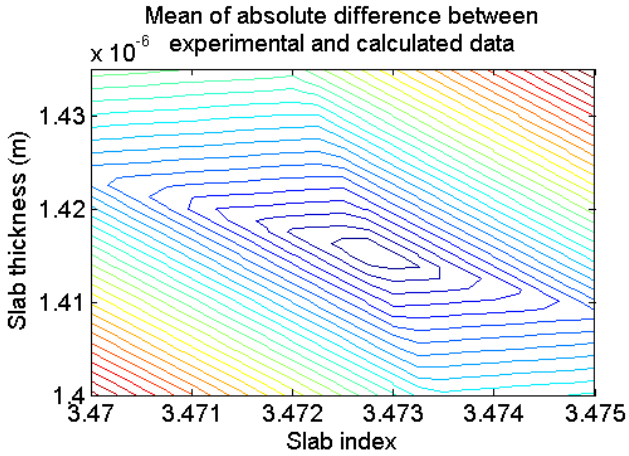


Figure 1. Determination of refractive index and thickness of an InGaAsP slab on InP at a wavelength of 1.55 µm. This figure shows the mean difference between calculated and measured effective indices. Area width gives an estimation of the error.

In the index measurement, we point a laser onto an InGaAsP slab waveguide covered by an integrated Bragg grating and mounted on a rotating stage. Light couples in at discrete values corresponding to the effective indices of guided modes. Since these effective indices are a function of both refractive index and thickness of the slab, it is necessary to measure more than one mode in order to lift the ambiguity. Fig. 1 shows the average difference between the measured and expected effective indices for a given slab thickness and index. Taking all uncertainties into account, we achieve a precision of 10^{-3} on the material index.

Index data is used to design a monolithic widely tunable source around 3 μm, by internal SPDC in a laser diode. The device consists of an InGaAsP/InP quantum-dash laser emitting at 1.55 μm, in which the laser field acts as a pump for intracavity SPDC towards a signal and idler around 3.11 μm. To compensate for the material dispersion, the index profile is tailored to ensure that the laser will emit on a higher-order mode of the waveguide. We show that the ridge width provides a useful parameter to reach phase matching despite the fabrication tolerances associated to epitaxy. The effective-index mismatch that must be set to 0 to achieve an efficient conversion is equal to

$$\Delta n = nTE_2(\lambda_{pump}) - [nTE_0(\lambda_{signal}) + nTM_0(\lambda_{idler})]/2 \quad (1)$$

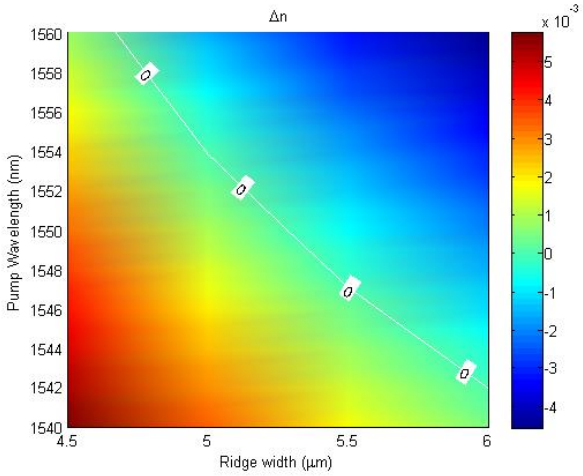


Figure 2. Effective-index mismatch as a function of ridge width and pump wavelength

As is apparent in Fig. 2, a shift of the wavelength satisfying phase matching at degeneracy can be readily compensated by a choice of a different ridge width, at the end of fabrication. Additionally, the signal and idler wavelengths can be widely modified outside of degeneracy by modifying the temperature during operation. The expected efficiency of this device is 240 % W^{-1} cm^{-2}.

References:

[1] B. Broberg, S. Lindgren, *Refractive index of $In_{1-x}Ga_xAs_yP_{1-y}$ layers and InP in the transparent wavelength region*, Journal of Applied Physics, vol. 55 no. 9, pp. 3376-3381, 1984

[2] M. Amiotti, G. Landgren, *Ellipsometric determination of thickness and refractive index at 1.3, 1.55, and 1.7 μm for $In_{(1-x)}Ga_xAs_yP_{(1-y)}$ films on InP*. Journal of Applied Physics, vol. 73, no. 6, pp. 965-2971, 1993

[3] C. Henry, L. Johnson, R. Logan, D. Clarke, *Determination of the Refractive Index of InGaAsP Epitaxial Layers by Mode Line Luminescence Spectroscopy*, J. Quantum Electron QE vol. 21 no. 12, pp. 1887–1892, 1985

[4] F. Fiedler, A. Schlachetzki, *Optical parameters of InP-based waveguides*, Solid-State Electronics, vol. 30, no. 1, pp. 73-83, 1987

[5] B. Chandra, L.A. Coldren, K.E. Strege, *Refractive index data from $Ga_xIn_{1-x}As_yP_{1-y}$ films*, IET, vol. 17, no. 1, pp. 6-7, 1981

EUROPEAN CONFERENCE ON INTEGRATED OPTICS

A multi-channel photonic integrated transmitter driven by an application specific integrated circuit

Stanisław STOPIŃSKI[1*], Krzysztof SIWIEC[1], Marcin MYŚLIWIEC[1], Ryszard KISIEL[1], Luc AUGUSTIN[2], Witold PLESKACZ[1] and Ryszard PIRAMIDOWICZ[1]

[1]Institute of Microelectronics and Optoelectronics, Warsaw University of Technology, Koszykowa 75, 00-662 Warsaw, Poland

[2]SMART Photonics B.V., Horsten 1, 5612 AX Eindhoven, the Netherlands

[*]S.Stopinski@imio.pw.edu.pl

The dynamically developing market of modern fiber-optic access networks calls for high-speed, multi-channel photonic transmitters and receivers, technologically suitable for volume production at low cost. Such devices can be potentially developed using cutting-edge photonic integration technologies. At present, one of the major obstacles for broad implementation of photonic integrated circuits on the market are packaging constraints, especially related to providing many electrical RF interfaces. In this work we demonstrate and discuss a concept of hybrid integration of a multi-channel photonic integrated transmitter driven by an electronic application specific integrated circuit (ASIC). The two circuits will be bonded using a standard flip-chip technology. Such a hybrid integration scheme can provide an efficient method of driving multi-channel photonic integrated devices at high speed. To the best knowledge of the authors, such a concept is presented for the first time.

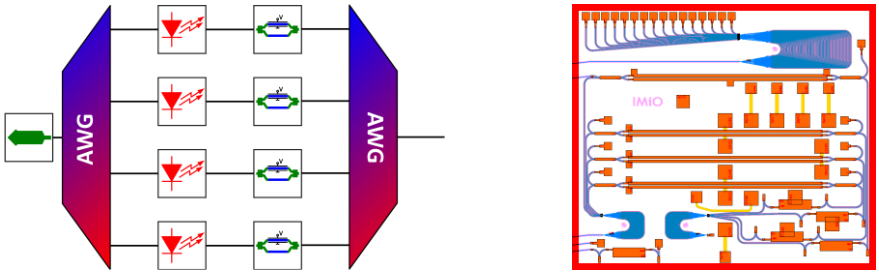


Fig. 1. The scheme of the four-channel photonic integrated transmitter and the mask layout of the photonic chip.

Fig. 1. presents the scheme of the realized photonic transmitter. It comprises four Fabry-Perot lasers constructed from a semiconductor optical amplifier and two-port multi-mode interference reflectors [1]. The lasers use filtered-feedback technique that enables single-frequency operation [2]. Filtering is provided by a 1×4 arrayed waveguide grating (λ_c = 1550 nm, $\Delta\lambda$ = 3.2 nm) and an MMI reflector. The lasers outputs are connected to

Mach-Zehnder modulators. The second AWG, with the same spectral properties as the filtering component, multiplexes four digital signals to a single chip output. The chip has been designed and fabricated in the generic process of SMART Photonics [3] – the mask layout (dimensions 4.6 mm × 4.0 mm) is presented in Fig. 1.

The application specific integrated circuit has been designed as an electronic driver of the photonic transmitter – DC supply for Fabry-Perot laser and digital signals for Mach-Zehnder modulators. The ASIC consists of three different wideband drivers and biasing circuits. It has been implemented and prototyped in the AMS 0.35 µm CMOS technology.

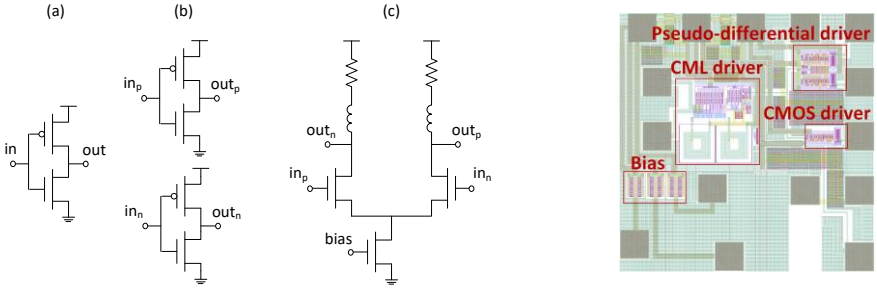


Fig. 2. Simplified schematics of: CMOS driver (a), pseudo-differential driver (b), current mode logic CML driver (c) and the ASIC chip layout.

The Mach-Zehnder modulators have two electric inputs, whose input impedance is capacitive. Measured capacitance of the modulators is around 4 pF. Fig. 2 shows simplified schematics of three different capacitance drivers that were implemented: a CMOS driver (a), a pseudo-differential driver (b), and a common mode logic CML [1] driver (c). The drivers (a) and (b) provide high output amplitude (rail to rail) and require small chip area. In the case of a simple CMOS buffer one of the modulator inputs is biased by a constant voltage. The driver (c) allows to achieve a higher bandwidth, but with a smaller output swing. To further increase the bandwidth of CML driver the inductive peaking technique [5] was used. Simulations show that the (a) and (b) drivers achieve 1.5 GHz bandwidth and CML drivers bandwidth is around 3 GHz, while driving 5 pF load.

The layout of the designed ASIC is presented in **Error! Reference source not found.**. The total chip dimensions are 2 mm × 2 mm. Big bonding pads (200 µm × 200 µm) visible on both the photonic and microelectronic chip will be used for flip-chip bonding of the two devices. Flip-chip technique will help to minimize the parasitic inductance and capacitance of the interconnection between ASIC and ASPIC.

Acknowledgement: This work was supported by the National Centre for Research and Development (project NIPPON, grant agreement PBS3/A3/21/2015). Stanisław Stopiński and Krzysztof Siwiec would like to thank for support granted by the dean of the Faculty of Electronics and Information Technology of Warsaw University of Technology.

References

[1] E. Kleijn et al. IEEE J. Ligthw. Technol 31, 3055–3063 (2013)

[2] B. Docter et al., IEEE J. Sel. Topics Quantum Electron. 16, 5 (2010).

[3] M.K. Smit et al., Semicond. Sci. Technol. 29, 8, (2014)

[4] P. Heydari, R. Mohavavelu, *Design of Ultra High-Speed CMOS CML Buffers and Latches,* in Proceedings of the 2003 International Symposium on Circuits and Systems, 2003.

[5] T. H. Lee, *The Design of CMOS Radio-Frequency Integrated Circuits*, Cambridge Univ. Press, 1998.

Noise Tolerance in Integrated-Optic Recognition Circuit for Optical 16QAM Codes

Hiroki KISHIKAWA*, Kensuke INOSHITA, Nobuo GOTO
Tokushima University, 2-1 Minamijosanjima-cho, Tokushima, 770-8506, Japan
* kishikawa.hiroki@tokushima-u.ac.jp

In photonic label routers, various optical signal processing functions are required, which include optical label extraction, recognition of the label, optical switching and buffering controlled by signals based on the label information and network routing tables, and label rewriting. Among these functions, we focus on photonic label recognition. We have proposed two kinds of optical waveguide circuits to recognize 16 quadrature amplitude modulation (QAM) codes.

We consider recognition of the 16QAM code by cascaded connection of two circuits for QPSK code recognition. Fig.1 shows a waveguide circuit for QPSK phase recognition circuit (QPRC) followed by phase adjustment waveguides [1]. The circuit consists of a 3-dB directional coupler, two Y-branches, and an asymmetric X-junction coupler. First, we consider a proposed circuit for recognition from the minimum-output port. Using two-stage connection of this QPRC, a proposed circuit for recognition of 16QAM codes from the minimum-output port is formed as shown in Fig.2 [2]. The 16QAM coded signal is incident in the upper port E_{in}, whereas a reference signal is incident in the lower port E_{ref}. The circuit consists of five QPRCs and an attenuator, a 1:2 divider, and a 1:4 divider. Only one output port corresponding to the incident QAM code has minimum output intensity. Thus, the incident code can be determined from the minimum-output port. To increase the contrast ratio at the ports, thresholders are required as post processing.

Next, we consider another circuit as shown in Fig.3(a) [3]. The incident 16QAM code is recognized from the maximum-output port. This circuit consists of an input signal part and a reference signal part. The input signal part consists of three Y-branches and an attenuator. The reference signal part consists of three Y-branches, attenuators, and a 3-dB directional coupler. By feeding the output fields to the four QPRCs, sixteen outputs are obtained. Three kinds of threshold devices are connected at the output ports of QPRCs 1 and 2, QPRC 3, and QPRC 4, respectively. After the thresholders, a logic circuit shown in (b) is required as post processing.

We consider a communication system in 16QAM format to evaluate noise tolerance of the proposed recognition circuits. To simulate the communication system, we employed a

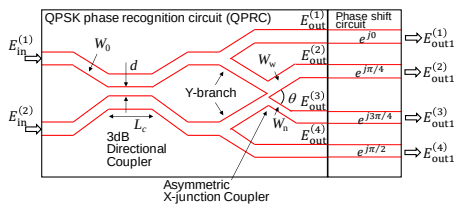


Fig.1 Optical waveguide circuit (QPRC) for recognition of a QPSK phase.

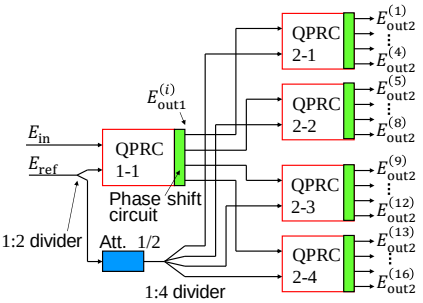
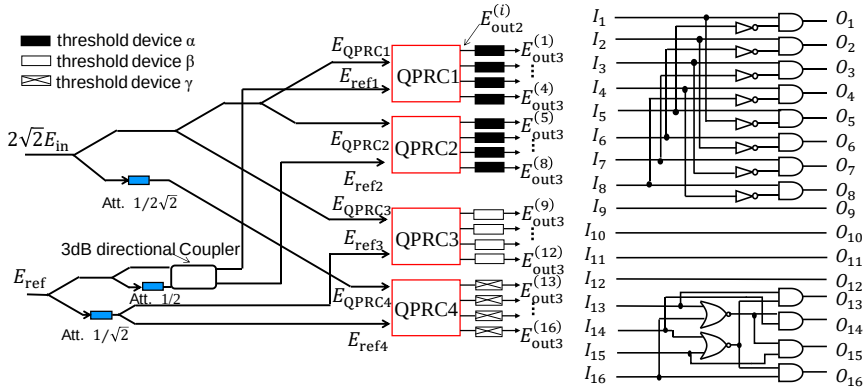


Fig.2 Recognition circuit for 16 QAM codes by detecting minimum output.



(a) (b)

Fig.3. Recognition circuit for 16QAM codes by detecting maximum output.

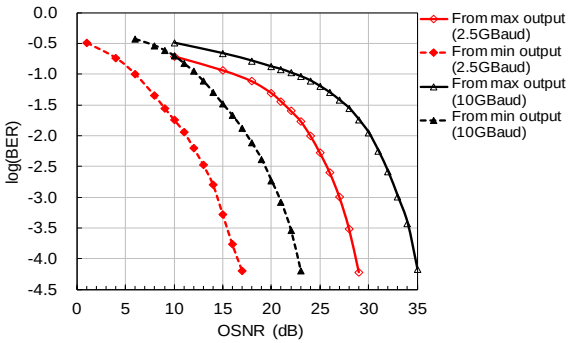


Fig.4. Simulated BER performance as a function of OSNR.

simulation software, OptiSystem (Optiwave Systems Inc.). An optical 16 QAM pulse sequence at bit rate of R_0 = 10 Gb/s and 40 Gb/s corresponding to symbol rate of $R_0/4$ = 2.5 GBaud and 10 GBaud is generated by pseudo-random bit sequence (PRBS) of 2^{15} -1.

Fig.4 shows the calculated bit error rate (BER) as a function of optical signal to noise ratio (OSNR) of the input 16QAM signal by the minimum-output and maximum-output configuration of the 16QAM recognition circuits. Resulted OSNRs for required BER at 1.0×10^{-3} are around 14.5 dB and 27.0 dB for the minimum-output and maximum-output configurations, respectively, at 2.5GBaud. The required OSNR for recognition by the maximum-output configuration is larger by 12.5 dB than that for recognition by the minimum-output configuration. Thus, it is concluded that the recognition from the minimum output port is much practical.

This work was supported in part by JSPS KAKENHI (15H06443).

References

[1] Y. Makimoto, H. Hiura, N. Goto, and S. Yanagiya, "Waveguide-type optical circuit for recognition of optical QPSK coded labels in photonic router," J. Lightwave Tech., vol.27, no.1, pp.60-67, 2009.

[2] K. Inoshita, H. Kishikawa, N. Goto and S. Yanagiya, "Proposal of optical waveguide circuits for recognition of optical QAM codes," J. Lightwave Tech., vol.31, no.13, pp.2271-2278, 2013.

[3] K. Inoshita, N. Goto, and S. Yanagiya, "Recognition of 16QAM codes by maximum output with optical waveguide circuits, thresholders, and post-processing logic circuit," IEICE Trans. Electron., vol. E97-C, no.5, pp.448-454, 2014.

Design of a Multiple-reference Time-domain Optical Coherence Tomography System

B. Imran Akca[1]

[1] Biomedical Engineering & Physics, Academic Medical Center, University of Amsterdam, 1100 DE Amsterdam, The Netherlands

* imran.akca@gmail.com

Optical coherence tomography (OCT) is a non-invasive, three-dimensional imaging technique that offers close-to-histology-level image quality [1]. In conventional time-domain (TD)-OCT systems depth scanning is achieved by modifying the relative optical path length difference of the reference and the sample arms in a sequential way using mechanical scanners. Due to the moving reference mirror TD-OCT systems require an inherently long acquisition time. To overcome this problem non-moving part solutions have been proposed such however, each solution has its own drawbacks [2-4].

Integrated optics offers unique solutions for OCT systems. Miniaturized OCT systems have recently garnered attention for their high potential in overcoming the size and cost issue of the bulky OCT systems. One major advantage of integrated optics is that the operation of the existing optical components can be reconfigured by controlling the material properties using temperature, voltage, or pressure. Despite this unique feature, OCT based on integrated optical components has as yet not utilized it properly.

In this work, by exploiting the unique features of integrated optics, the design of a novel high-speed TD-OCT system based on a non-moving scanning approach is presented. Figure 1 is the schematic of the integrated-optics-based multiple-reference TD-OCT system in which the micro-chip is outlined by the red dashed-rectangle. For ease of understanding the first two levels of the light tapping mechanism are demonstrated. Here, a central wavelength of 800 nm, an axial resolution of 20 μm, and a depth range of 1 mm are aimed at. Light coming from a broadband light source will be divided into two arms with a 3-dB coupler; half towards the sample, half towards the reference arm. There will be several electro-optically-controlled directional couplers placed on both sample and reference arms at certain distances. Imaging of different depths will be controlled by the additional length increment between consecutive reference beams (i.e. a in Fig. 1). According to the Nyquist sampling theorem the step size of the beam scanning should not be more than half of the axial resolution, i.e. 10 μm, which defines the length difference between consecutive reference points as a = 14 μm for this design.

The material system is 250 nm thick ion-sliced lithium niobate film on oxidized silicon wafer. The oxide thickness is 3 μm. The refractive index of the LN is 2.25 at 800 nm, and its electro-optic (EO) coefficient is (r_{33} ~ 30 pm/V) [5]. Single mode rib waveguides with 0.23 μm of slab height and 1 μm of waveguide width were designed. For defining the waveguides ion-implantation-assisted wet etching is a promising technique as it provides lower propagation losses compared to other methods.

Directional couplers used in this system were designed to act as voltage-controlled electro-optic switches with nanosecond switch time. A metallic electrode was placed on one of the straight waveguides of the coupler [Fig. 2(a)]. With applied voltage, the effective refractive index of the straight waveguide section is locally increased due to electro-optic effect which induces a phase difference between coupler arms. When there is no voltage on the electrodes, the lights on both arms will be in phase and the incoming light will be cross-coupled to the other coupler arm. The tapped lights from both sample and reference arms interfere at the beam combiner and directed to an on-chip photodetector. At a certain voltage value (i.e. V = 15 Volts for this design, Fig. 2 (b)), a π phase difference is generated between

coupler arms which avoids cross-coupling of the light and forwards it to the next stage where the next depth point will be imaged. This operation will be performed in a sequential order by switching the directional couplers on and off until all depth points are scanned (i.e. *N* in Fig. 1).

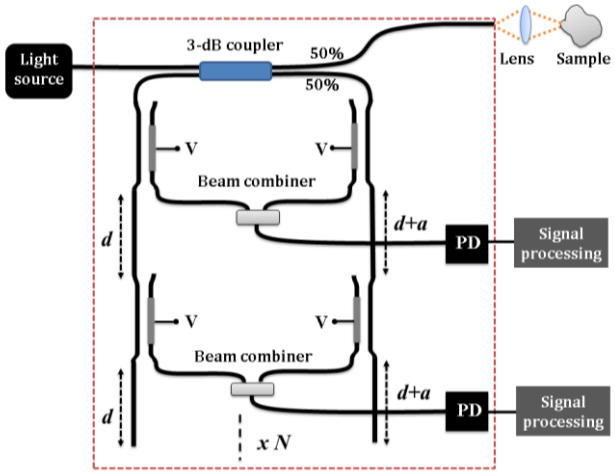


Fig. 1. Schematic of the proposed multiple-reference arm TD-OCT system based on integrated optics. The micro-chip is outlined by the red dashed-rectangle.

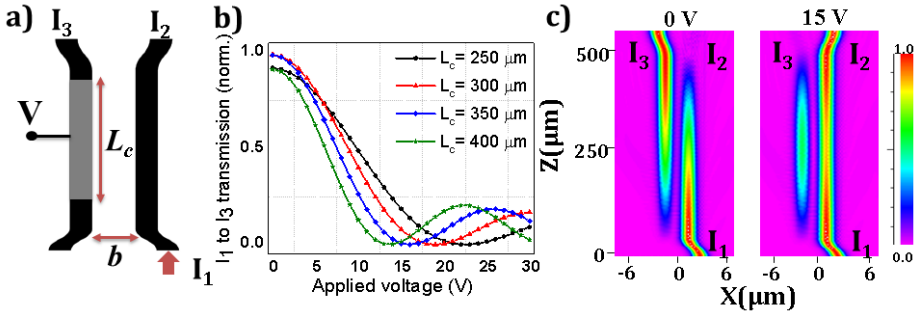


Fig. 2. (a) The schematic of the electro-optically-controlled directional coupler. (b) The amount of cross-coupling of input light at different voltage values for different electrode lengths. (c, right) Voltage is OFF, the light will be cross-coupled to the other channel, (c, left) For V = 15 Volts, the input light will stay in the same arm.

In summary, the concept and design of an integrated-optics-based multiple-reference TD-OCT system in LN-on-silicon platform were introduced. The proposed design will not only solve the speed limitation of the TD-OCT systems but also make it a widely accessible cheap and rugged point-of-care system.

References

[1] D. Huang, E. A. Swanson, C. P. Lin, J. S. Schuman, W. G. Stinson, W. Chang, M. R. Hee, T. Flotte, K. Gregory, C. A. Puliafito, and J. G. Fujimoto, *Optical coherence tomography*, Science vol.254, pp. 1178, 1991.

[2] Nabeel A. Riza, and Zahid Yaqoob *Submicrosecond speed optical coherence tomography system design and analysis using acousto-optics,* Proc. SPIE 4619, 26, 2002.

[3] G. J. Tearney, B. E. Bouma, S. A. Boppart, B. Golubovic, E. A. Swanson, J. G. Fujimoto, *Rapid acquisition of in vivo biological images by use of optical coherence tomography,* Opt. Lett. vol. 21, pp. 1408–1410, 1996.

[4] E. Margallo-Balbas, M. Gelion, G. Pandraud, and P. J. French, *Miniature 10 kHz thermo-optic delay line in silicon,* Opt. Lett. vol. 35(23), pp. 4027 – 4029 ,2010.

[5] E. L. Wooten, K. M. Kissa, A. Yi-Yan, E. J. Murphy, D. A. Lafaw, P. F. Hallemeier, D. Maack, D. V. Attanasio, D. J. Fritz, G. J. McBrien, and D. E. Bossi, *A review of lithium niobate modulators for fiber-optic communications systems,* IEEE J. Sel. Top. Quantum Electron. vol. 6, pp. 69–82, 2000.

Fabrication of Monolithic Optofluidic Evanescent Probing Device for Sensing Applications

João M. MAIA[1*], Vítor A. AMORIM[1], D. ALEXANDRE[1,2], P. V. S. MARQUES[1,3]
[1]CAP – Centre for Applied Photonics, INESC TEC, Rua Dr. Roberto Frias, Porto, 4200-465, Portugal
[2]Department of Physics, University of Trás-os-Montes e Alto Douro, Quinta de Prados, Vila Real, 5000-801, Portugal
[3]Department of Physics and Astronomy, Faculty of Sciences of University of Porto, Rua do Campo Alegre, Porto, 4169-007, Portugal
[*] joaomaia93@hotmail.com

Micromachining with femtosecond (fs) laser can be exploited to monolithically integrate optical components and microfluidic channels in pure fused silica substrates, due to internal modification of the glass properties that are induced by the laser beam. In this paper, the optimization of the fabrication of microfluidic channels, was conducted by examining etch rate and surface roughness as a function of the irradiation conditions, namely scanning speed, scanning depth, pulse energy, beam polarisation and scan lines separation. Moreover, careful positioning of an optical layer relative to the microchannel was performed by analysing in real-time the channel etching reaction. This latter feature enables precise control of the optical interaction between the two structures, which can be of use in optofluidic devices for sensing applications.

When a fs-laser beam is focused in fused silica, several changes can occur within the material, which include increase of the refractive index (RI) with high spatial resolution and generation of etching selectivity [1]. The former can be employed to form optical waveguides among other more complex devices such as first order Bragg gratings, while the latter is used to produce hollow structures after etching the sample in hydrofluoric acid (HF). This approach has the benefit of monolithic integration of optical and fluidic components and three-dimensional (3D) fabrication, which are of significant interest in the production of on-chip optofluidic devices [2].

To enable coupling with minimal optical losses, the channel must present smooth sidewalls, as depicted in Fig. 1a. Such characteristics were obtained by 3D stacking multiple laser passes with the following optimal exposure conditions: scanning speed of 500 μm/s, pulse energy between 60 nJ and 80 nJ, scanning depth between 50 μm and 150 μm, beam polarisation perpendicular to the scanning direction and scan separation along Y of 1 μm and along Z of 2 μm (according to the axial system of Fig. 1a). The fabrication of buried structures is possible, as shown in Fig. 1b, where the HF flows through laser written vertical holes that connect the buried channel to the silica surface.

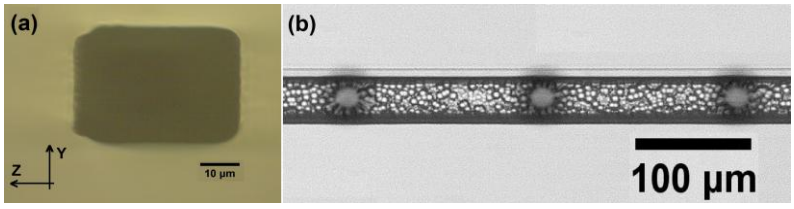


Figure 1: (a) optical microscopy image of the channel cross-section, (b) top view image of a microfluidic channel adjacent to a Bragg grating waveguide.

Optical sensing can be accomplished by writing a waveguide, containing a Bragg grating (BGW), adjacent to the channel. Efficient optical evanescent interaction with the fluids

requires a distance to the channel of less than a couple of microns, which is tough to accomplish as the etchant may diffuse into the channel, thereby damaging the device. Therefore, the etching reaction needs to be closely monitored in order to control the distance between both structures. Figure 2 shows the optical reflection spectra obtained during the etching reaction of a microfluidic channel placed parallel to a BGW, together with a reference grating placed in another region of the waveguide. Analysis of the obtained spectra yielded the following conclusions: (i) as the HF acid fills the channel and the gap channel-BGW decreases, the resonant wavelength increases, indicating a higher interaction; (ii) when the etchant starts carving into the BGW, the reflected peak strength decreases and the reaction has to be stopped. It should be noticed that the sensing Bragg grating has two functions: during fabrication it serves as an etching monitoring sensor and after as a coarse fluid refractometer (high resolution RI sensor can be accomplished if the set is fabricated in the arms of a Mach-Zehnder interferometer, for example).

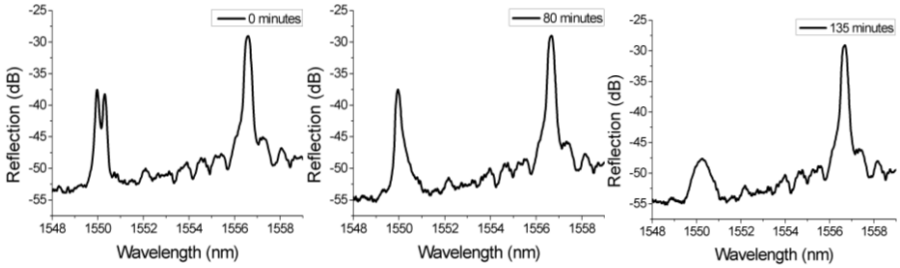


Figure 2: spectrum of the two BGWs (sensing at 1550nm and parallel to the channel, and reference grating at 1558nm) during etching at 0, 80 and 135 minutes. (left to right)

The resonant behaviour of the BGW depends on the fluid RI inserted on the channel, as demonstrated by the calibration results shown in Fig. 3, where a maximum sensitivity of 38 nm/RIU at 1.456 at 1550 nm was obtained for the device shown in Fig. 1b. Improvements on the device configuration can still be made, namely by fabricating multiple channels surrounding the BGW to further increase coupling between the evanescent field and the fluid. Nevertheless, the presented etching monitoring methodology reveals itself as a new opportunity for the precise fabrication of optofluidic devices.

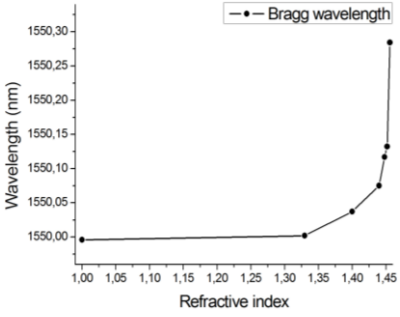


Figure 3: Bragg wavelength as a function of the fluid refractive index.

Acknowlegments

Project "NORTE-01-0145-FEDER-000036" is financed by the North Portugal Regional Operational Programme (NORTE 2020), under the PORTUGAL 2020 Partnership Agreement, and through the European Regional Development Fund (ERDF).

References

[1] R. Osellame, G. Cerullo, R. Ramponi, *Femtosecond Laser Micromachining*, Springer, 2012.

[2] N. Bellini, K. Vishnubhatla, F. Bragheri, L. Ferrara, P. Minzioni, R. Ramponi, I. Cristiani, R. Osellame, *Femtosecond laser fabricated monolithic chip for optical trapping and stretching of single cells*, Optics Express, vol. 18, no. 5, pp. 4679-4688, 2010.

EUROPEAN CONFERENCE ON INTEGRATED OPTICS

Dispersion controlling in strained silicon waveguides using sub-wavelength grating metamaterials

Daniel Benedikovic[1*], Carlos Alonso-Ramos[1], Mathias Berciano[1], Xavier Le Roux[1], Eric Cassan[1], Delphine Marris-Morini[1], and Laurent Vivien[1]

[1]Centre for Nanoscience and Nanotechnology, CNRS, Univ. Paris-Sud, Université Paris-Saclay, C2N – Orsay, 91405 Orsay Cedex, France

[*]daniel.benedikovic@u-psud.fr

We report on controlling of the group velocity dispersion in silicon (Si) strip waveguides, with refractive index engineered sub-wavelength grating (SWG) metamaterials, covered by silicon nitride (Si_3N_4) layer. This waveguide geometry is utilized for breaking the centrosymmetric nature of silicon and opening the route for second-order nonlinearities in the silicon-on-insulator technology. We show by calculations that attractive waveguide dispersion profiles over a broad spectral range can be flexibly tailored by proper control of transversal dimensions and appropriate refractive index engineering. Both normal and anomalous dispersion regimes can be obtained, being one important parameter for various nonlinear applications in photonics.

Waveguide dispersion is an essential characteristic of nanophotonic structures and careful control of this property is of critical importance, playing significant role in development of photonic components using nonlinear processes [1]. Substantial efforts have been put forward in the last years, elaborating various approaches to control the group velocity dispersion, both theoretically and experimentally [2-7]. This particularly includes changing the transversal dimensions [2], utilizing of slot-assisted geometries [3], using conformal dielectric overlayers [4], or adding thin material layers [5,6].

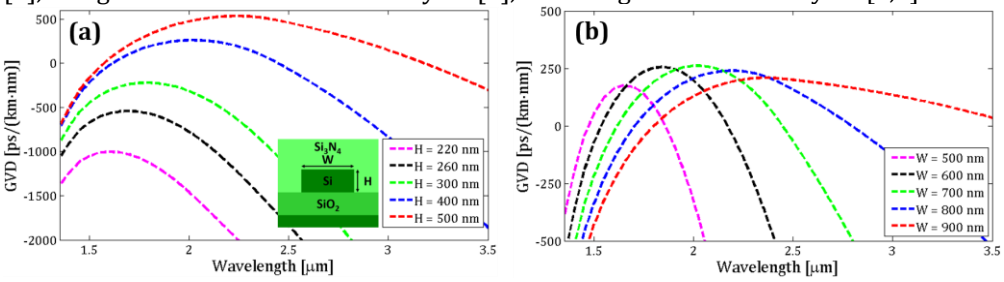


Fig. 1. GVD profiles of strained Si waveguides with different (a) height – H and width of 700 nm, (b) widths – W and height of 400 nm.

Figure 1 shows calculated profiles of the group velocity dispersion in conventional strip Si waveguides, covered by straining Si_3N_4 layer. By changing the cross-sectional dimensions (height x width), it becomes apparent that different dispersion profiles can

be obtained and thoroughly engineered. The key ingredient for this is the strong optical confinement, making the geometrical dispersion dominates against the intrinsic material dispersion. In Fig. 1(a) can be seen that the increase of the waveguide height produces a large vertical upshift of dispersion profiles, varying from the normal (~-1000 ps/(km·nm)) to the anomalous (~500 ps/(km·nm)) dispersion behaviors, while keeping the trends in the curve shape. On the other hand, by increasing the waveguide width, as shown in Fig. 1(b), the peak dispersion is shifted towards the longer wavelengths, and the dispersion profiles becomes flatter, i.e. yielding a broader spectral range. This is useful for nonlinear applications demanding phase-matching over a large bandwidths.

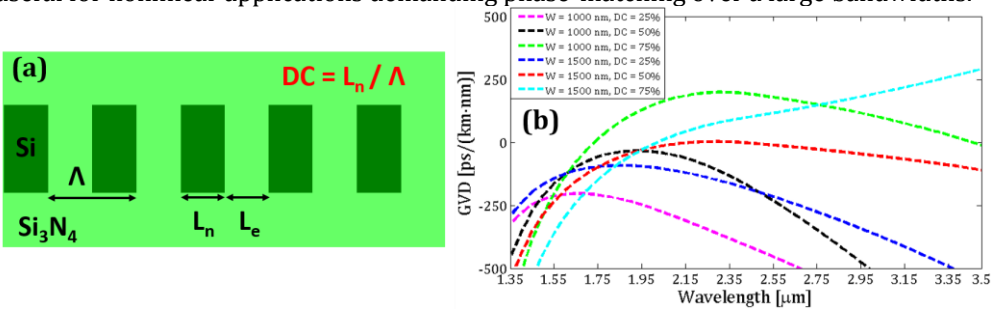


Fig. 2. (a) 2-D schematics of the SWG waveguide. (b) GVD profiles of the strained metamaterial waveguides for different waveguide widths and SWG geometries.

In general, the dispersion engineering in metamaterial waveguides presents a challenge because of the reduced index contrast between the composite waveguide core and the respective claddings, which, in turn, relaxes the mode confinement compared to conventional waveguide arrangements. Here, the local engineering of Si and Si_3N_4 materials, typically used in CMOS foundries, is advantageously exploited to synthesize wide range of optically equivalent metamaterials, with variable properties.

In Fig. 2(b) are shown calculated dispersion profiles as a function of wavelength, for waveguide cross-sections of 500 nm x 1000 nm and 500 nm x 1500 nm, and different longitudinal sub-wavelength grating geometries, i.e. different metamaterial refractive indexes. It becomes apparent that relatively low (up to 200 ps/(km·nm)) and broadband (up to ~1000 nm) dispersion profiles are possible to be tailored by using nano-structuration of Si and Si_3N_4 at sub-wavelength scale. For the same cross-sectional area of the waveguide, the dispersion profiles can be tuned, only by varying the longitudinal waveguide dimensions. This way, multitude of virtually identical waveguides, but with considerable different and variable optical properties (refractive index, mode profiles, and dispersion) can be implemented on the same material platform.

Acknowledgements: This work was supported by the European Research Council (ERC) under the European Union's Horizon 2020 research and innovation program (ERC POPSTAR - grant agreement N°647342).

References

[1] J. Leuthold, et al., Nat. Photonics 4, 535-544 (2010)
[2] A. C. Turner et al., Opt. Express 14(10), 4357-4362 (2006)
[3] M. Zhu et al., Opt. Express 20(14), 15899-15907 (2012)
[4] X. Liu et al., Opt. Letters 33(24), 2889-2891 (2008)
[5] H. Liang, et al., Opt. Express 24(26), 29444-29451 (2016)
[6] Y. Guo, et al., Opt. Letters 41(21), 4939-4942 (2016)

Photonic Integrated Circuits for Data Center Interconnects

Benjamin WOHLFEIL[1*], Danish RAFIQUE[1], Michael EISELT[1]
[1]ADVA Optical Networking SE, Märzenquelle 1-3, Meiningen, 98617, Germany
[*] bwohlfeil@advaoptical.com

Optical transceivers for data center interconnects (DCI) are projected to become a multi-billion dollar market by the end of this decade [1]. Due to the increasing demand for high data rates driven by cloud and mobile applications, next-generation DCIs will not only require higher capacity but also an improvement in bandwidth density, power efficiency and cost. Following the electronics industry's example, where a high level of integration has provided for these goals, the DCI market may also benefit from integration of optical functionality in so called photonic integrated circuits (PIC). In this paper we discuss PIC based solutions for DCIs and explore the challenges for deployment of PICs in DCIs.

DCIs can be categorized into two classes: Intra and inter data center interconnects (see figure 1 for a typical data center network architecture). Intra data center interconnects link individual switches within data centers with data rates up to 100 Gb/s to form a distributed fabric, whereas inter DCIs extend data center fabrics over multiple locations featuring amplified multi Tb/s dense wavelength-division multiplexing (DWDM) links over a single fiber pair.

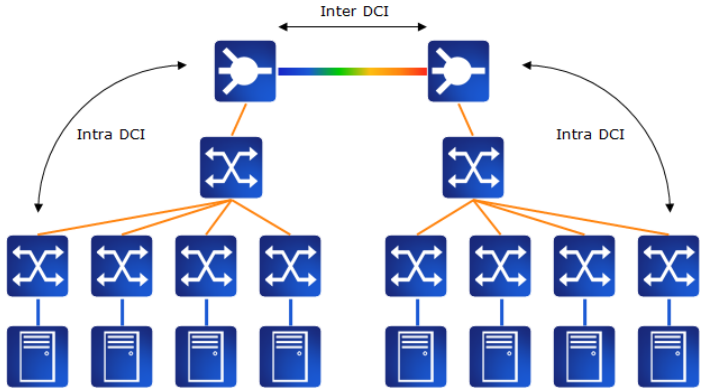


Figure 1: A typical data center network architecture.

Due to the large number of intra DCIs employed in each data center, a significant driver in the intra DCI market is cost – a combination, which highly favors integration. Traditionally, Indium Phosphide (InP) was the material of choice for PICs due to its ability to generate light - a property that is completely absent in silicon. However, silicon benefits from mature fabrication processes giving rise to larger scale integration and high yield. Nonetheless, both technologies suffer from high insertion loss, which is a critical parameter in unamplified intra DCI links, and also from higher power consumption compared to fiber coupled VCSELs, rendering PICs an inefficient solution at low bandwidths (< 10GHz). However, next-generation standards such as 400G Ethernet, which is expected to be ratified by the end of 2017 [2], will require higher line rates, potentially exceeding the bandwidth and signal integrity limits of VCSELs, and thus a need for PIC technology could be seen. Here, InP has the advantage of slightly lower

insertion loss compared to silicon since the laser is monolithically integrated on the PIC and does not need to be coupled externally. On the other hand, silicon photonics offers co-integration of electronic and photonic circuits, enabling higher density, better RF performance and lower cost than competing solutions. In addition, a high level of integration facilitates the move to smaller form factors allowing for higher face plate density, for instance compared to current QSFP28 devices.

Inter data center interconnects cover distances of up to several hundred kilometers and thus require amplification. Data rates are as high as 400 Gb/s per wavelength, employing modulation formats with high spectral efficiency such as 16-QAM. Several data signals are multiplexed on a dense wavelength grid with channel spacing down to 50 GHz. Due to the increased complexity on both transmitter and detector side required for coherent data transmission as compared to direct detection, costs are significantly higher for inter DCI transceivers. More sophisticated digital signal processing (DSP) coupled with larger footprint dual polarization coherent optics are the main contributors to high cost for this application. As a recent report shows, despite only a very low percentage of optical integrated components entering the communication market, the revenues generated by those components constitute approximately one third of the global market [3]. Contrary to the claim that PICs are suitable solutions for high quantity low cost applications, this indicates that as of today they are rather high-end products. Technical challenges facing PICs in the inter DCI environment are similar to those in the intra DCI space - with the exception of insertion loss, which plays a less significant role due to the availability of amplification on the transmission line. The increased complexity and tighter operation boundaries of coherent optics compared to direct detection requires a higher degree of control circuitry, e.g. for stabilization of laser emission wavelength or modulator bias points. Accommodating this additional functionality necessitates larger packages and therefore larger form factors such as CFP or CFP2. Recent standardization activities in OIF and the Consortium for On-Board Optics (COBO), however, reflected the industry's desire to move to smaller form factors, necessitating further miniaturization of optical components and therefore benefiting the share of PICs in the DCI market.

An additional challenge PICs are facing irrespective of application is packaging. As no standard solutions are available, as there are for electronic integrated circuits, packaging of PICs is very costly, contributing up to 80% of total device cost. A high degree of automation in assembly and passive alignment of photonic components is required to bring down costs significantly and thus facilitate a more rapid market uptake.

Nevertheless, despite all the challenges PICs are facing, we are seeing an increased employment of integrated optics in the DCI market. However, more effort is needed to further reduce cost, while at the same time scaling capacity, footprint and energy efficiency with market demand.

This work was partially funded by the EU and BMBF through research projects DIMENSION and SpeeD.

References

[1] http://news.ihsmarkit.com/press-release/technology/data-center-optics-market-40g-transceivers-ubiquitous-100g-accelerating
[2] http://www.ieee802.org/3/bs/timeline_3bs_0915.pdf
[3] http://www.lightcounting.com/

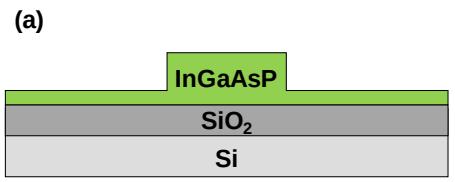
Photonic Integrated Circuit Platform using III-V on SiC Wafer

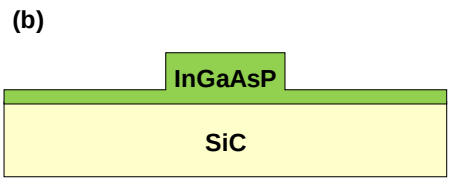
Mitsuru TAKENAKA*, Shinichi TAKAGI
Department of Electrical Engineering and Information Systems, The University of Tokyo, 7-3-1 Hongo, Bunkyo-ku, Tokyo, 113-8656, Japan
* takenaka@mosfet.t.u-tokyo.ac.jp

Photonic integrated circuits (PICs) based on a high-index-contrast waveguide have paved a pathway to large-scale integration for photonics in the past ten years. Similar to Si photonics, we have investigated III-V CMOS photonics platform based on III-V on insulator (III-V-OI) wafer as shown in Fig. 1(a) [1]. We are able to fabricate ultrasmall InP PICs owing to the high-index contrast between III-V layers and SiO_2 buried oxide (BOX). Like Si-on-insulator (SOI) wafers, III-V-OI wafers can be fabricated by using direct wafer bonding [2]. Thus, we have demonstrated various passive components based on InGaAsP strip/rib waveguides including micro bends [2], arrayed waveguide gratings [2], and grating couplers [3]. Active components including modulators/switches [4], laser didoes (LDs) [4, 5], photodetectors [6, 7], and variable optical attenuators [8] have also been reported so far.

While the III-V-OI structure provides significant impact on device miniaturization for InP photonics, its low thermal conductivity is one of the drawbacks particularly for LDs. When free carriers are injected into an InP-based waveguide on the III-V-OI wafer, heat generated by current injection hardly dissipates through the thick SiO_2 where the thermal conductivity is quite low. Thus, the maximum power emitted from a single LD is limited to a few mW when its cavity length is approximately 100 μm [4]. Moreover, the poor thermal dissipation restricts the density of active devices on a single chip.

In this paper, we propose to use a SiC BOX instead of SiO_2 as shown in Fig. 1(b). Since the thermal conductivity of SiC is more than 100 times greater than that of SiO_2, we expect that the heat dissipation can be improved drastically by introducing a III-V on SiC wafer. On the other hand, the medium refractive index contrast between III-Vs and SiC arises concern about device miniaturization. Here we numerically analyze an InGaAsP waveguide on SiC in terms of bend loss and heat dissipation for feasibility study.





III-V on SiO_2	III-V on SiC
Low thermal conductivity	High thermal conductivity
High index contrast	Medium index contrast

Fig. 1. Schematic of InGaAsP rib waveguide on (a) conventional III-V on insulator wafer and (b) III-V on SiC wafer proposed in this paper.

First, we evaluated the propagation loss of a 90° bend using 3D FD-TD simulation. Figure 2(a) is a comparison of bend loss of a Si strip waveguide on SiO_2 and InGaAsP strip waveguide on SiC as a function of the bend radius. While the medium index contrast of the InGaAsP on SiC waveguide resulted in the larger bend loss than that of the Si waveguide with the small bend radius, the difference in bend loss was negligible when the bend radius was greater than 7 μm, which is sufficient for large scale integration in most of PICs. Then, we analyzed the heat dissipation in the III-V on SiO_2/Si and III-V on SiC wafers as shown in Fig. 2(b). It was found that the increase in the device temperature of the III-V on SiC was 30 times smaller than that of the III-V on SiO_2/Si. Thus, the III-V on SiC platform enables large scale integration and high-power operation simultaneously.

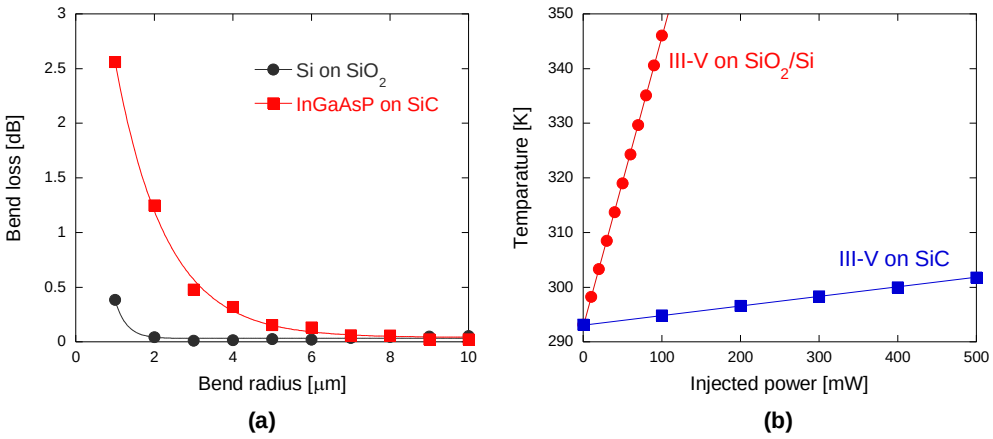


Fig. 2. (a) Bend loss of InGaAsP strip waveguide on SiC and Si strip waveguide on SiO_2 and (b) device temperature with injected power into III-V rib waveguide on SiO_2 and SiC.

Acknowledgement: This work was supported in part by a Grant-in-Aid for Young Scientists (A) from MEXT.

References

[1] M. Takenaka and Y. Nakano, "InP photonic wire waveguide using InAlAs oxide cladding layer.," *Opt. Express*, vol. 15, no. 13, pp. 8422–7, 2007.

[2] M. Takenaka, M. Yokoyama, M. Sugiyama, Y. Nakano, and S. Takagi, "InGaAsP Photonic Wire Based Ultrasmall Arrayed Waveguide Grating Multiplexer on Si Wafer," *Appl. Phys. Express*, vol. 2, no. 12, p. 122201, Nov. 2009.

[3] M. Takenaka, M. Yokoyama, M. Sugiyama, Y. Nakano, and S. Takagi, "InGaAsP Grating Couplers Fabricated Using Complementary-Metal–Oxide–Semiconductor-Compatible III–V-on-Insulator on Si," *Appl. Phys. Express*, vol. 6, no. 4, p. 42501, Apr. 2013.

[4] S. Matsuo, T. Fujii, K. Hasebe, K. Takeda, T. Sato, and T. Kakitsuka, "Directly modulated buried heterostructure DFB laser on SiO_2/Si substrate fabricated by regrowth of InP using bonded active layer," *Opt. Express*, vol. 22, no. 10, pp. 12139–12147, May 2014.

[5] D. Inoue, J. Lee, K. Doi, T. Hiratani, Y. Atsuji, T. Amemiya, N. Nishiyama, and S. Arai, *Appl. Phys. Express*, vol. 7, no. 7, p. 72701, Jul. 2014.

[6] Y. Cheng, Y. Ikku, M. Takenaka, and S. Takagi, *IEICE Electron. Express*, vol. 11, no. 16, pp. 20140609–20140609, 2014.

[7] L. Shen, Y. Jiao, W. Yao, Z. Cao, J. P. van Engelen, G. Roelkens, M. K. Smit, and J. J. G. M. van der Tol, "High-bandwidth uni-traveling carrier waveguide photodetector on an InP-membrane-on-silicon platform," *Opt. Express*, vol. 24, no. 8, p. 8290, 2016.

[8] J.-K. Park, J.-H. Han, M. Takenaka, and S. Takagi, MRS Adv., vol. 1, no. 48, pp. 3295–3300, May 2016.

Buried Waveguides using a Quasi-Planar Process

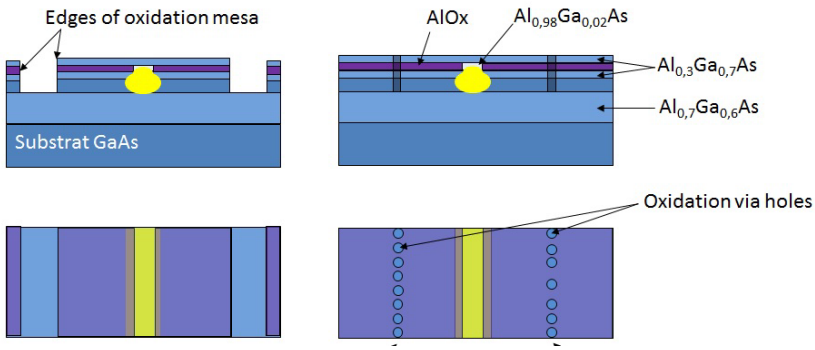
Stéphane CALVEZ[1], Alexandre ARNOULT[1], Pierre-François CALMON[1], Aurélie LECESTRE[1], Chantal FONTAINE[1], Antoine MONMAYRANT[1], Olivier GAUTHIER-LAFAYE[1], Guilhem ALMUNEAU[1]

[1] Laboratoire d'Analyse et d'Architecture des Systèmes, Université de Toulouse, CNRS, UPS, 7 avenue du colonel Roche, F-31400 Toulouse, France

* scalvez@laas.fr

The oxidation of Al-containing III-V semiconductors is an established technology to selectively transform a high-index (2.9) semiconductor layer into an insulating low-index (n~1.6) aluminium oxide (AlOx) and which, thereby, allows the fabrication of buried oxide apertures in either vertical-cavity surface-emitting lasers or waveguide-based devices [1-4]. Because of the chemical selectivity of the process, the oxidation is conventionally carried out as a lateral oxidation from the sides of etched mesas (see Fig. 1 left), resulting in a loss of wafer planarity which, in turns, renders the subsequent fabrication stages of waveguide devices more complex.

In this paper, we report the first demonstration of an alternative technique to make buried optical waveguides where the oxidation is carried out through via-holes (see Fig. 1 right) leading to a quasi-planar approach.



(a) Conventional approach **(b) Quasi-planar approach**

Fig. 1. The two approaches to make AlOx-based buried waveguide.

The oxide-confined waveguides consists of a 1.6µm-thick $Al_{0.7}Ga_{0.3}As$ bottom cladding layer, a 480-nm GaAs core, a 150-nm-thick $Al_{0.3}Ga_{0.7}As$ cladding, a 68 nm-thick $Al_{0.98}Ga_{0.02}As$ layer, a 330-nm-thick $Al_{0.3}Ga_{0.7}As$ layer, a second 68 nm-thick $Al_{0.98}Ga_{0.02}As$ layer and a final 50nm-thick $Al_{0.3}Ga_{0.7}As$ layer. Both $Al_{0.98}Ga_{0.02}As$ layers were oxidized simultaneously to form, under in-situ monitoring [5], ~4µm apertures 16µm away from the via-holes/mesa. The structure was post-processed in a single run to create oxide-confined waveguides using the conventional and the quasi-planar oxidation techniques. In the latter case the holes were 2µm in diameter and their separation was varied between 2.5 to 4.5 µm.

The transmission characteristics of ~2-mm-long cleaved-facet waveguides were measured using a tunable laser at wavelengths around 1.6 µm. Fig. 2 shows the recorded Fabry-Perot transmission curves for a set of hole-to-hole spacing. The waveguide losses were estimated to be ~1cm^{-1} and further shown to be independent of the hole-to-hole spacing and even of the fabrication method (conventional or quasi-planar).

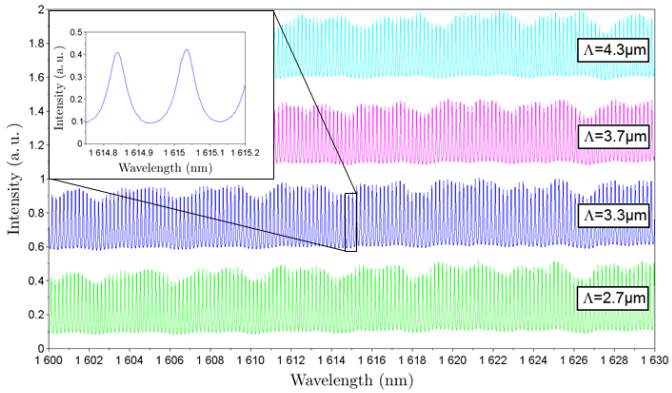


Fig. 2. Transmission characteristics of the waveguide made using the quasi planar process

In conclusion, we have introduced and demonstrated a quasi-planar approach to make buried AlOx/AlGaAs waveguides whose performance are equivalent to the one obtained using the conventional approach but which facilitates the further processing steps required in the fabrication of more complex photonic integrated circuits.

References

[1] J.M. Dallesasse and N. Holonyak Jr, *Oxidation of Al-bearing III-V materials: a review of key progress*, J. Appl. Phys. 113, 051101, 2013

[2] J. M. Dallesasse and D. G. Deppe, *III–V Oxidation: Discoveries and Applications in Vertical-Cavity Surface-Emitting Lasers*, in Proceedings of the IEEE, vol. 101, no. 10, pp. 2234-2242, 2013

[3] E. Peter, I. Sagnes, G. Guirleo, S. Varoutsis, J. Bloch, A. Lemaître and P. Senellart, *High-Q whispering-gallery modes in GaAs/AlOx microdisks*, Appl. Phys. Lett., vol. 86, no. 2, pp. 021103-1-021103-3, 2005

[4] S. Calvez, G. Lafleur, A. Larrue, P.-F. Calmon, A. Arnoult, G. Almuneau, and O. Gauthier-Lafaye, *Vertically Coupled Microdisk Resonators Using AlGaAs/AlOx Technology*, IEEE Photon. Technol. Lett., 27, 982-985, 2015

[5] G. Almuneau, R. Bossuyt, P. Collière, L. Bouscayrol, M. Condé, I. Suarez, V. Bardinal, and C. Fontaine, *Real-time in situ monitoring of wet thermal oxidation for precise confinement in VCSELs*, Semicond. Sci. Technol., 23, (10), pp. 105021, 2008

Inducing second-order susceptibility in amorphous silicon nitride waveguides

Marco A. G. PORCEL[1*], Jörn P. EPPING[2], Marcel HOEKMAN[2], Arne LEINSE[2], René G. HEIDEMAN[2], Peter J. M. VAN DER SLOT[1], Klaus-J. BOLLER[1]

[1]Laser Physics and Nonlinear Optics Group, MESA+ Institute for Nanotechnology, University of Twente, P.O. Box 217, Enschede 7500 AE, The Netherlands

[2]LioniX International B.V., PO Box 456, Enschede 7500 AL, The Netherlands

[*]m.a.garciaporcel@utwente.nl

Optical waveguides based on stoichiometric silicon nitride (Si_3N_4) grown via low-pressure chemical vapor deposition (LPCVD) provide a reliable photonics platform characterized by low loss and a spectrally broad transparency ranging from the visible to the mid-infrared. Engineering the waveguide dispersion is of special interest since it allows phase-matching of third-order nonlinear optical processes such as four-wave mixing, supercontinuum and frequency comb generation.

Second-order nonlinear processes such as second harmonic generation (SHG) have been observed already in other types of silicon nitride that cannot offer such low loss, such as grown via RF-sputtering. As in such amorphous materials there should be no bulk nonlinear second-order response, $\chi^{(2)}$, fabrication imperfections such as strained micro-crystalline silicon or at the free nitrogen dangling bonds were suggested as the origin [1]. Field enhancement in Si_3N_4 ring resonators and Bragg gratings have been used to increase the efficiency for SHG, with a maximum conversion efficiency of 0.14% [2].

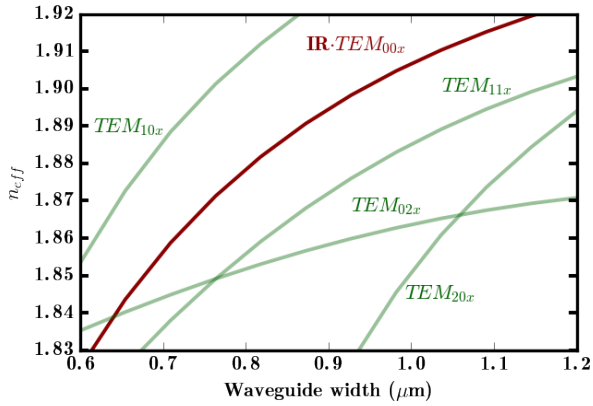


Fig.1. Effective refractive index of the different guided modes for IR and its SH in waveguides of 1 µm by width.

Here, we present for the time SHG in stoichiometric Si_3N_4 waveguides grown with LPCVD. Fig. 1 shows the modal dispersion vs. waveguide width which implies that phase-matching should only occur at a certain waveguide width. However, SHG was

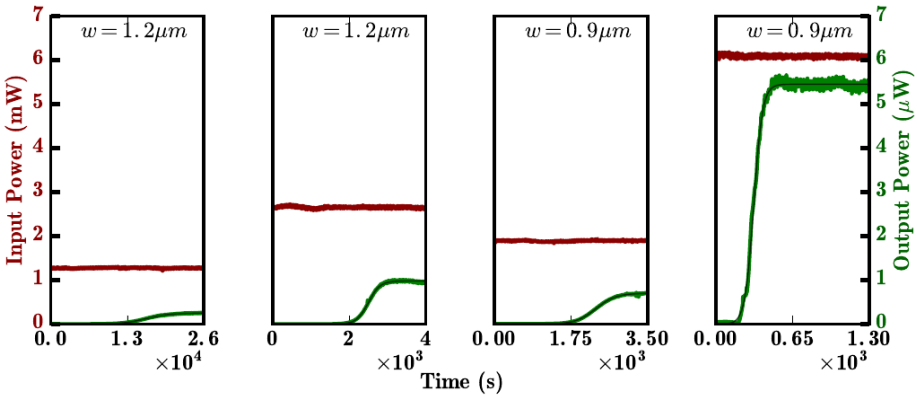


Fig. 2. Generation of photoinduced $\chi^{(2)}$ in four waveguide widths, w, and lengths 60, 74, 74, and 22 mm respectively.

observed with various different waveguide widths. Secondly, the output was seen to grow vs. time as shown in Fig. 2, when injecting the pump pulses from a mode-locked laser (6 ps pulses at 1064 nm with a 20 MHz repetition rate) with a constant average pump power.. These results show that the pump radiation induces a temporally growing nonlinear coefficient in the waveguides with a spatially periodic pattern that provides quasi-phase matching. The maximum conversion efficiency achieved so far is 0.5%, corresponding to 50 μW of 532 nm radiation with 10 mW of IR input radiation.

References

[1] Dianov, E.M., Starodubov, D.S., Quant.Electron. 22, 419-432, 1995

[2] Miller et al., Opt.Express **22**, 26517-26525, 2014

Photo-Thermo-Refractive Glass Doped with Rare Earth Ions as a Substrate for Monolithic Integration of Optical Elements

Nikolay NIKONOROV*, Sergey IVANOV, Yevgeniy SGIBNEV, Alexander IGNATIEV
ITMO University, Birzhevaya line 4, St. Petersburg, 199034, Russia
* nikonorov@oi.ifmo.ru

Today with progress of miniaturization, optical microsystems integrate a large number of functionalities in a small volume. There are two approaches for developing integrated optical devices: hybrid and monolithic integration. The latter one suggest performing all components of a device on one substrate. Materials for monolithic integration should allow emission, propagation, amplifying, multiplexing/demultiplexing, and detection of light. In this work, we present new material for monolithic integration that can be used in integrated optics.

The standard PTR glass is a photosensitive multi-component sodium–zinc–aluminosilicate one containing fluorine (6 mol.%), bromine (0.5 mol.%), and doped with small amounts of additives (cerium, antimony and silver) that are responsible for the photo-thermo-induced precipitation of silver nanoparticles and sodium fluoride nanocrystals [2]. Currently, Bragg gratings recorded in PTR glasses used as laser line narrowing and stabilizing filters, spectral and spatial filters, compressors for fs- and ps-lasers, spectral beam combiners, high power beam splitters, etc. [3]. For a long time PTR glass is considered only as a holographic material. However, application area of PTR glasses can be extended dramatically by developing polyfunctional PTR glass that combine properties of monofunctional materials.

For this purpose, Yb-Er co-doped PTR glass based on the Na_2O-ZnO-Al_2O_3-SiO_2-F system was synthesized. The glass synthesis was conducted in an electric furnace at T = 1500 °C in the air atmosphere using platinum crucibles; the melts being homogenized with the platinum stirrer.

Laser action on Yb-Er doped PTR glass is demonstrated for the first time. Dependence of output power on pumping is shown in Fig. 1a.The following parameters were obtained: laser wavelength 1575 nm, laser threshold ~ 3.3W, maximum output power 240mW, and slope efficiency 2.36%. It should be noted that doping PTR glass with rare earth ions had not effect on the recording Bragg gratings with high diffractive efficiency (more 95%). Thus, combination of laser and holographic properties of the PTR glasses can be used for developing solid state distributed feedback and distributed Bragg reflector lasers [4].

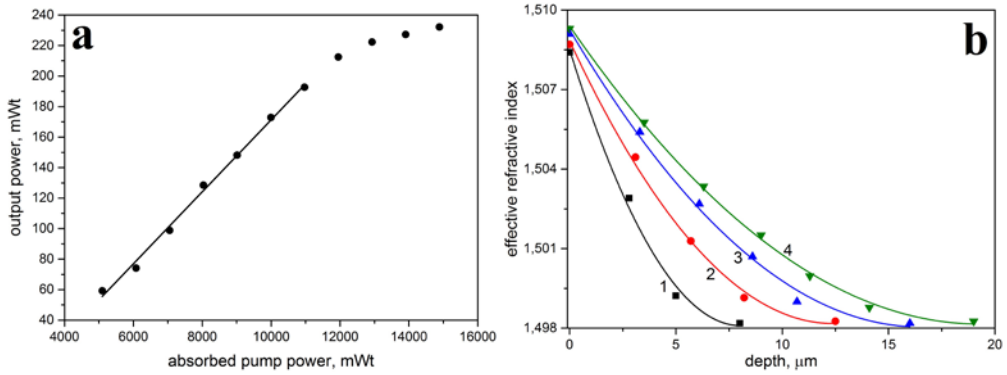


Fig.1. a - dependence of output power on pumping with output coupler 1%; b – refractive index profiles (λ=632.8 nm) of optical waveguides formed by $Na^+ \leftrightarrow K^+$ ion exchange for 1 h (1), 3h (2), 6h (3), and 9h (4).

The presence of sodium in the PTR glass composition allows one to focus on the ion exchange technology for fabricating the waveguide structures [5]. In order to investigate ion exchangeable properties, the PTR glass samples were immersed in a salt melt of KNO_3 at 350 °C for 1-9 hours. Multimode optical waveguides were formed in the PTR glass, refractive index profiles for TE polarization are presented in Fig. 1b. Increment of refractive index reaches 0.011 and waveguide depth varies from 8 to 18 microns with increasing duration of the ion exchange. Moreover, the waveguides reveal birefringence caused by stresses formed in ion exchange layer. Such stresses was shown to improve microhardness of PTR glasses [6].

In this work photo-refractive, laser, and ion exchangeable properties of the PTR glasses doped with Yb^{3+} and Er^{3+} ions were demonstrated for the first time. Thus, PTR glasses doped with rare earth ions allows to integrate waveguides, lasers and amplifiers, and Bragg gratings on one substrate with monolithic integration (Fig. 2). The developed PTR glass can be used for developing various devices of integrated optics and photonics.

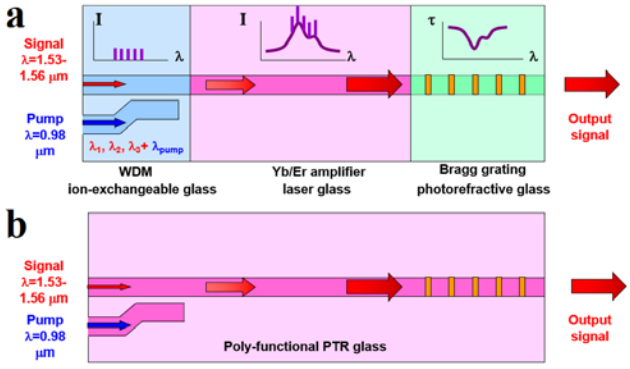


Fig. 2. Schematic image of a hybrid integration (a) of three elements: (i) WDM, (ii) amplifier channel and (iii) Bragg grating playing a role of spectral flattening filter that made with the use of three materials and monolithic integration (b) of these elements made with the use of polyfunctional PTR glass.

Research was funded by Russian Science Foundation (Agreement #14-23-00136).

References

[1] V.D. Dubrovin, A.I. Ignatiev, N.V. Nikonorov, *Chloride photo-thermo-refractive glasses*, Optical Materials Express, vol. 6, no. 5, pp. 1701-1713, 2016

[2] O. Andrusyak, V. Smirnov, G. Venus, V. Rotar, L. Glebov, *Spectral Combining and Coherent Coupling of Lasers by Volume Bragg Gratings*, IEEE Journal of selected topics in quantum electronics, vol. 15, no. 2, pp. 344-353, 2009

[3] H. Kogelnik, C. V. Shank, *Stimulated emission in a periodic structure*, Applied Physics Letters, vol. 18, no. 4, pp. 152–154, 1971

[4] A. Tervonen, B.R. West, S. Honkanen, *Ion-exchanged glass waveguide technology: a review*, Optical Engineering, vol. 50, no. 7, 71107, 2011.

[5] Y.M. Sgibnev, N.V. Nikonorov, V.N. Vasilev, A.I. Ignatiev, *Optical gradient waveguides in photo-thermo-refractive glass formed by ion exchange method*, Journal of Lightwave Technology, vol. 33, no. 17, pp. 3730-3735, 2015

Design of Hybrid Integrated Graphene Optical Switch with an III-V-on-Si laser

Leili Abdollahi Shiramin*, Dries Van Thourhout
Photonics Research Group, INTEC, Ghent University -IMEC, Ghent, 9052, Belgium
Center for Nano-and Biophotonics (NB-Photonics), Ghent University, Ghent B-9000, Belgium
*Leili.AbdollahiShiramin@ugent.be

Monolithic integration of photonic devices such as switches and modulators with lasers is a complex process. Often these devices require materials with different band-gaps, which makes their co-integration costly and complicated. As an alternative, materials exhibiting interesting optical and electronic functionality such as graphene and other 2D-materials can be hybridly combined with Si and III-V platforms, simplifying the fabrication process and providing complex integrated optical systems on a smaller footprint. A big advantage of graphene is its optically broadband operating window and the fact that its optoelectronic properties are tunable by electrical gating or chemical doping.

In this paper we propose a novel approach to integrate a graphene modulator or switch with a hybrid III-V on silicon laser device [3,5]. The most straightforward approach would be to integrate the graphene device next to but separate from the III-V amplifier, directly on the silicon waveguide. However, in most of the investigated graphene-on-Si waveguide based devices, the quasi-TM polarization is the dominant mode having the highest interaction with the graphene layer [1,2]. The quasi-TE mode, used in the III-V amplifiers has considerably less overlap with the graphene layer and results in very inefficient devices. This is certainly the case taking into account the 400nm thick silicon waveguides used in typical hybrid III-V on silicon lasers [5]. Therefore, a design resulting in enhanced interaction of the TE-like mode with the graphene optical device is needed. In addition our approach inherently provides the possibility to gate or modulate the Fermi-level in the graphene layer, without the need for any further processing steps thereby considerably simplifying the integration process.

Our approach is sketched in Figure 1. Most hybrid III-V on silicon lasers contain a taper section where the light is adiabatically coupled from the III-V gain section to the silicon waveguide (Figure 1, left [3]). We propose to integrate the graphene layer in this taper section. Figure 1, right shows the cross section of our structure. The InP epitaxial layers are chosen similar to that of a standard heterogeneously integrated laser design [5]. A single layer of graphene is included on the 400 nm Si rib waveguide. The InP mesa is placed above of graphene with an insulating layer of DVS-BCB in between. The latter has now two roles in this design. First, it serves as the adhesive bonding layer between the III-V and the Si chips. Second, it acts as a dielectric layer for the switch. Applying a voltage between the metal contact on the graphene and the doped bottom InP cladding layer of the laser allows controlling the chemical potential and hence the transparency of the graphene layer [1,2]. In Figure 2, the TE mode absorption is plotted as function of the InP mesa width and Si waveguide width as they vary along the taper. It shows that the absorption level changes drastically along the taper length and can be controlled by varying the respective waveguide widths. The graph also compares the absorption in the modulator with that of a layer of graphene directly deposited on the silicon waveguide. In the latter design, the Si waveguide has to be doped in order to apply a voltage over the graphene layer. This increases the complexity of the process and as the graph shows also has considerably lower performance. According to Figure 2, the TE mode absorption in the taper design is almost 4 times higher than for the standard device. The total absorption for a taper length of 150 μm is about 6dB in the Dirac point of graphene, sufficient for datacom applications. The figure also shows the effect of the

thickness of the bonding layer. A thicker BCB-layer, pushes the mode toward the Si waveguide and reduces its interaction with the graphene. Thinner bonding thickness not only increases the absorption (and hence the modulation efficiency, see [4] for details) but also is beneficial to boost the coupling from the III-V mesa to the Si waveguide and enhance the laser performance [5]. Figure 3 shows three cross sections along the taper length.

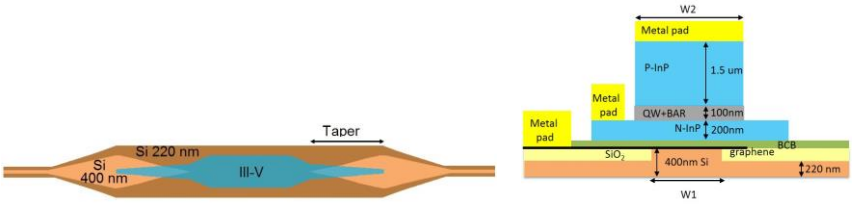


Fig. 1. Left: III-V on Si laser design, top view, Right: Schematic of the graphene device integrated with an InP/Si laser. The structure is on the taper section in the left image, therefore the width of Si waveguide and P-InP is varied.

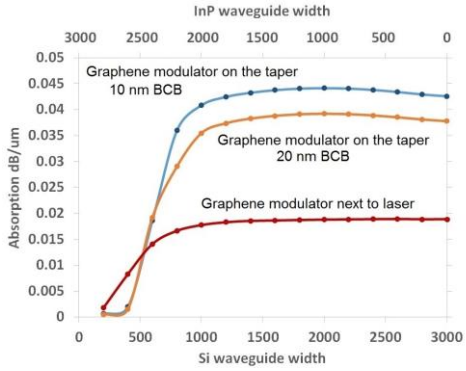


Fig. 2. The TE mode absorption as function of the InP taper width and Si waveguide width for two designs of graphene modulator next to laser and graphene modulator on the tapered Si integrated with laser.

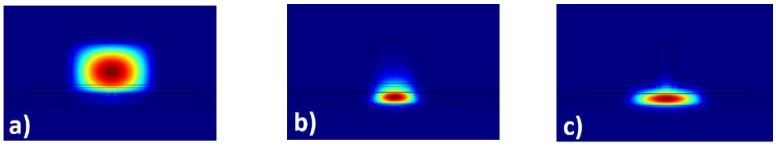


Fig. 3. Three cross section from the taper with a) P-InP width 3000nm, Si width 200 nm b) P-InP width 1600nm, Si width 1600 nm c) P-InP width 600nm, Si width 2.6 um.

References

[1] H. Dalir, et al, Athermal Broadband Graphene Optical Modulator with 35 GHz Speed, ACS Photonics, 2016.

[2] Y. Hu, et al, Broadband 10 Gb/s operation of graphene electro-absorption modulator on silicon, Laser Photonics Rev, pp. 1-10, 2016.

[3] S. Keyvaninia, et al, Heterogeneously integrated III-V/silicon distributed feedback lasers, Opt. Lett, 24, 5434–5437, 2013.

[4] L. Abdollahi Shiramin, D. Van Thourhout, Graphene Modulators and Switches Integrated on Silicon and Silicon Nitride Waveguide, JSTQE, 23, 2017.

[5] A. Abbasi, et al, Enhanced Modulation Bandwidth of Heterogeneously Integrated III-V-on-silicon DFB Laser for 40 Gb/s NRZ-OOK Direct Modulation, International Semiconductor Laser Conference (ISLC), Japan.

Ge-rich graded-index SiGe waveguides as enabling building blocks for broadband mid Infrared integrated photonics

Joan Manel RAMIREZ[1*], Vladyslav VAKARIN[1], Jacopo FRIGERIO[2], Qiankun LIU[1], Andrea BALLABIO[2], Papichaya CHAISAKUL[1], Xavier LE ROUX[1], Laurent VIVIEN[1], Giovanni ISELLA[2], Delphine MARRIS-MORINI[1]

[1]Centre de Nanosciences et de Nanotechnologies, Université Paris Sud, CNRS, Université Paris Saclay, 91405 Orsay, France

[2]L-NESS, Dipartimento di Fisica, Politecnico di Milano, Polo di Como, Via Anzani 42, 22100 Como, Italy

[*] joan-manel.ramirez@u-psud.fr

The mid-Infrared (mid-IR) photonic integrated platform is recently drawing attention due to its foreseen potential as alternative compact solution to several challenges and limitations taking place in current mainstream technologies [1]. Improved performance is expected in a wide palette of topics such as sensing, thermal imaging, nonlinear optical devices, astronomy or secure datacom, among others [2]. Up to date, different material platforms have been considered to develop mid-IR devices with functionalities beyond the state of the art. In that framework, Si and Ge have risen as promising alternative raw materials to develop mid-IR photonic devices leveraging from the higher refractive index of Ge over Si and their compatibility with the standardized CMOS platform. Also, Si and Ge possess a wavelength transparency window up to λ = 8 μm and 14 μm respectively, in concordance with the spectral range where several substances display their main spectral absorption peaks, hence opening the route towards highly-sensitive and selective label-free chemical sensors. Additionally, none of these materials experience significant nonlinear losses at those wavelengths, as Two-Photon Absorption (TPA) and other related second-order effects are strongly reduced in the mid-IR. This last point in particular, makes SiGe approaches an interesting choice to explore novel nonlinear optical devices operating in the mid-IR range, taking advantage from the commercially available high-power and largely tunable mid-IR quantum cascade lasers.

A large pool of devices using the Ge-on-Si platform have already been reported so far, including waveguides and interferometric devices [3], arrayed waveguide grating multiplexers [4], thermo-optic phase shifters [5] or supercontinuum light sources [6]. Similarly, SiGe alloys with promising nonlinear properties in the mid-IR have been reported [7], and other approaches using graded Ge concentration profiles have also been proposed to obtain low-defect SiGe layer stacks with variable vertical refractive index profiles [8, 9].

Recent advances in graded-index Ge-rich SiGe waveguides operating in the mid-IR will be presented in this work. Main experimental results from passive structures will be detailed first, obtained from an ad-hoc experimental setup that allows precise measurement of the guided mode size and its spectral evolution over a wide wavelength range, as depicted in figure 1. Then, a comprehensive study of the main design parameters that yields optimum nonlinear performance in a broadband mid-IR wavelength range (from 3 μm to 8 μm) will be reported and compared with other state of the art mid-IR integrated platforms, showing that the Ge-rich SiGe graded waveguides have a huge potential as an innovative and powerful platform for the mid IR.

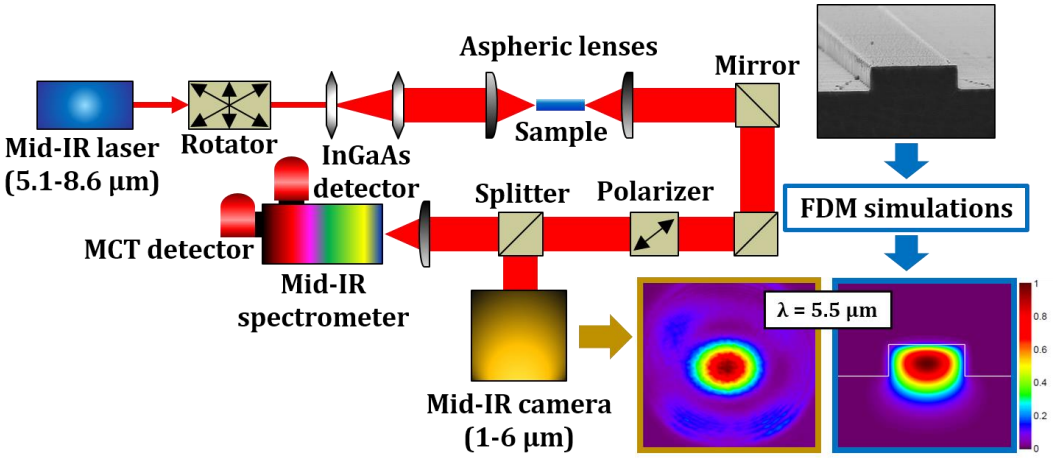


Fig. 1. Experimental setup used to characterize the broadband mid-IR Ge-rich SiGe waveguides. The SEM image located at the upper-right hand side shows a typical waveguide cross-section, with an etching depth of 1.5 µm and a waveguide width of 8 µm. Pictures at the bottom-right hand side compare the measured modal area (left image, boxed in orange) with the simulated one (right image, boxed in blue) using an FDM mode solver.

Acknowledgments

This project has received funding from the European Research Council (ERC) under the European Union's Horizon 2020 research and innovation programme (grant agreement N°639107-INsPIRE).

References

[1] R. Soref, "*Mid-infrared photonics in silicon and germanium,*" Nat. Photonics, 4(8), 495-497 (2010).
[2] Editorial "Extending opportunities," Nat. Photonics, 6(7) 407-407 (2012).
[3] A. Malik, M. Muneeb, Y. Shimura, … , & G. Roelkens, "*Germanium-on-silicon mid-infrared waveguides and Mach-Zehnder interferometers,*" In IEEE Photonics Conference 2013 (IPC-2013) (pp. 104-105). IEEE (2013).
[4] A. Malik, M. Muneeb, S. Pathak, … , & G. Roelkens, "*Germanium-on-silicon mid-infrared arrayed waveguide grating multiplexers,*" IEEE Photonics Technology Letters, 25(18), 1805-1808 (2013).
[5] A. Malik, S. Dwivedi, L. Van Landschoot, ... , & G. Roelkens, "*Ge-on-Si and Ge-on-SOI thermo-optic phase shifters for the mid-infrared,*" Optics express, 22(23), 28479-28488 (2014).
[6] M. Yang, Y. Guo, J. Wang, ... , & L. Zhang, "*Mid-infrared supercontinuum generation in a low-dispersion Ge-on-Si waveguide using sub-picosecond pulses,*" In Group IV Photonics (GFP), 2016 IEEE 13th International Conference on (pp. 36-37). IEEE (2016).
[7] L. Carletti, P. Ma, Y. Yu, ... , & S. Ortiz, "*Nonlinear optical response of low loss silicon germanium waveguides in the mid-infrared,*" Optics express, 23(7), 8261-8271 (2015).
[8] M. Brun, P. Labeye, G. Grand, … , & S. Nicoletti, "*Low loss SiGe graded index waveguides for mid-IR applications,* " Optics express, 22(1), 508-518 (2014).
[9] J. M. Ramirez, V. Vakarin, C. Gilles, … , & D. Marris-Morini, "*Low-loss Ge-rich Si0.2Ge0.8 waveguides for mid-infrared photonics,*" Accepted in Optics Letters.

Fabrication considerations for differential absorption based optofluidic sensors to measure ionic content in water

Gerrit W. STEEN[1*], Adam D. WEXLER[1], Elmar C. FUCHS[1], Herman L. OFFERHAUS[2]
[1]Wetsus, European Centre of Excellence for sustainable water technology, P.O. Box 1113, Leeuwarden, 8900 CC, The Netherlands
[2]University of Twente, P.O. Box 217, Enschede, 7500 AE, The Netherlands
[*]gerwin.steen@wetsus.nl

Introduction: The main conventional method to analyse ionic content in water is ion chromatography. Though this method works very well the time required for a sample to be collected and analysed is long (>1day). Also this method requires experts and an analytical lab. [1]

Optical techniques could be the solution to these problems: the integration of these techniques in optofluidic devices enables analysis on-site and on-line, furthermore, the use of these sensors enables remote signal data processing and localisation of a contamination. Ideally the implementation is label free and has a long life time. [2]

Not all optical methods are suitable for identification and quantification of ionic content. Fluorescence and chromatography methods require labels. Raman and IR absorption methods are hard to integrate and methods based on the real part of the refractive index give excellent detection limits, but fail to identify compounds without a filter (e.g. a membrane or coating).

An alternative optical method, yet to be utilized, is based on the difference in absorption of demineralized water and a saline solution. Ionic content in water can be identified and quantified using the spectral region of 940 – 1040 nm as shown in previous work [3]. That study was performed with a commercial photometer, but this optical technique could be integrated. [4] The spectral window allows for widely available cheap sources and detectors.

Design of device: The main drawback of the proposed method is the comparatively small differential absorption. For this reason we optimized the sensing length on a chip considering different on-chip losses and utilized interferometric measurement techniques. The expected normalized intensity of the signal for waveguide without losses can be calculated using the following equation, which follows from the Lambert-Beer law:

$$L_m = \frac{625}{C} log_{10}\left(\frac{C}{25} + 1\right) \quad (1)$$

This equation shows the normalized signal intensity to be hardly influence by the concentration. Therefore we show in Figure 1 the normalized signal intensity by the sensing length for different waveguide losses with a fixed (0.5 M) concentration of an electrolyte.

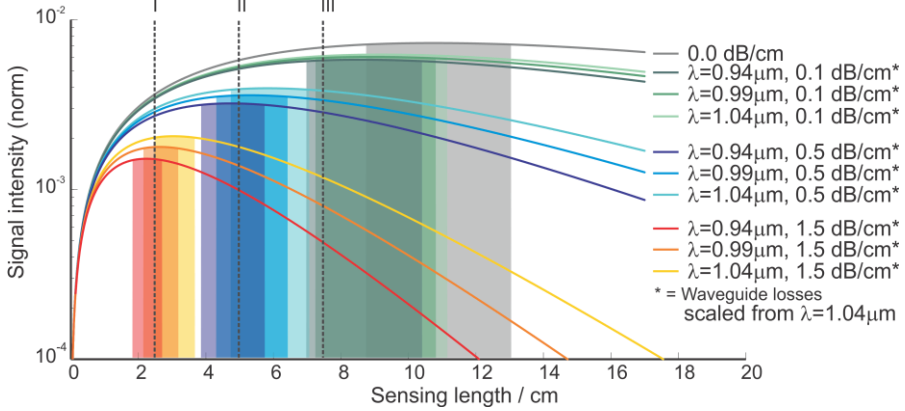


Fig. 1 The expected normalized intensity due to a 0.5 M concentration electrolyte is plotted against the sensing length. The grey line presents a waveguide without losses, while the green, blue and orange lines present waveguides with losses of 0.1, 0.5 and 1.5 dB/cm at λ=1 μm, respectively. The wavelength dependent losses are calculated with the scaling factor $(\lambda_0 / \lambda_1)^4$. Dotted lines I, II and III are plotted at 2.5 cm, 5.0 cm and 7.5 cm, respectively. The shaded areas represent 95% of the signal intensity for a given set of parameters.

We present optimal sensing lengths for differential absorption measurements on a chip. We also present calculations (using Phoenix simulation software) to determine the optimized cross section of the sensing and guiding waveguides, balancing single mode operation over 100 nm bandwidth, maximized sensitivity, minimized losses and maximized tolerances for fabrication. The designed optofluidic chips have been fabricated and the propagation through one of these devices is shown in figure 2.

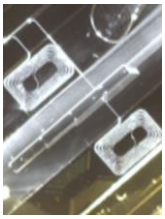


Fig. 2 Microscopic topview image of propagation through a fabricated optofluidic device.

References

[1] WHO Drinking Water Quality Committee, " Water Sampling and Analysis," in *Guidelines for drinking-water quality*, 4th ed. (World Health Organization, 2011), pp. 51-72

[2] J. Raich, Review of sensors to monitor water quality, European Commission Joint Research Centre, JRC85442, 2013

[3] G. W. Steen , E. C. Fuchs , A. D. Wexler , H. L. Offerhaus, *Title of book*, Applied Optics, vol. 54, no. 19, pp. 5937-5942, 2015

[4] G. Steen, A. D. Wexler, H. L. Offerhaus, *Optofluidic interferometry chip designs of differential NIR absorbance based sensors for identification and quantification of electrolytes,* in Proceedings of the Conference OSA Optical Sensors, pp. SeW3D.2, 2016

AlGaAs nanowires for phase-matched SHG in the telecom range

Natalia MORAIS[1*], Fares CHOUCHANE[1], Marco RAVARO[1], Maurizio DE ROSA[2], Iolanda RICCIARDI[2], Aristide LEMAITRE[3], Ivan FAVERO[1], and Giuseppe LEO[1]

[1] Laboratoire Matériaux et Phénomènes Quantiques, UMR 7162,
Université Paris Diderot – CNRS, Paris, France
[2] INO – CNR, Istituto Nazionale di Ottica, Via Campi Flegrei 34, I-80078 Pozzuoli (NA), Italy
[3] Alcatel-Thales III-V Lab, Palaiseau, France
*natalia.morais@univ-paris-diderot.fr

Phase-matched three-wave mixing is possible in optically isotropic zinc-blende materials, thanks to quasi-phase matching occurring when the interacting fields propagate along a curved path about a principal dielectric axis [1]. Following this scheme, efficient Second Harmonic Generation (SHG) was recently demonstrated in GaAs [2] and AlGaAs microdisks [3], and it was predicted in curved waveguides [4].

We designed and fabricated snake-shaped nanowires for SHG in the optical telecom range, both in fully suspended $Al_{0.19}Ga_{0.81}As$ waveguides and in $Al_{0.19}Ga_{0.81}As$ on aluminium oxide. These waveguides are composed by a series of quarters of a ring, as sketched in Fig. 1. The sign of $\chi^{(2)}$ is inverted every two adjacent 90° arcs. By doing so, it is possible to perform an "effective" quasi-phase matching, without any technological burden associated to $\chi^{(2)}$ domain inversion [1].

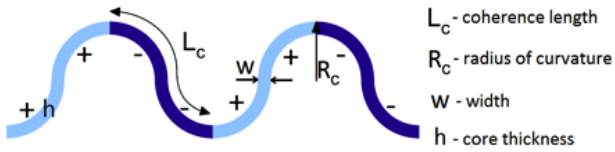


Fig. 1. Parameters for the design of snake-shaped waveguides

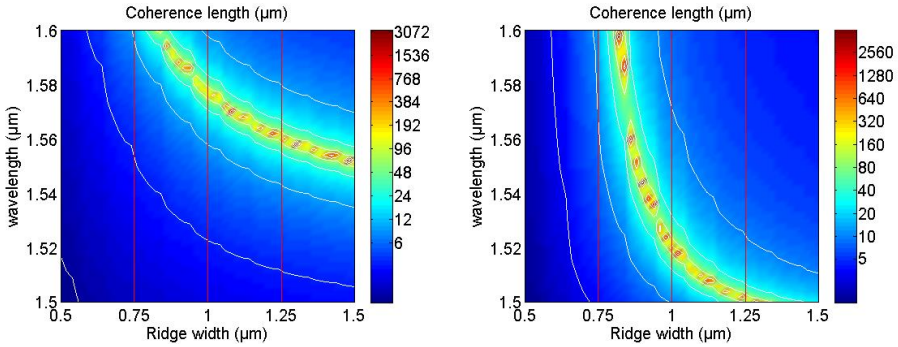
The coherence length, L_c, the maximum distance over which the nonlinear interaction is constructive, for SHG, depends on the difference between the effective indices at the second harmonic (SH) and the fundamental frequency (FF):

$$L_c = \frac{\lambda}{4} \frac{1}{n_{\mathrm{SH}}(\lambda_{\mathrm{SH}}, w, h) - n_{\mathrm{FF}}(\lambda_{\mathrm{FF}}, w, h)}, \qquad (1)$$

Since these effective indices depend on the geometry of the waveguide (w, h) and $R_c = L_c/\pi$, Eq. 1 relates all the parameters in the waveguide geometry. To minimize propagation losses, one needs $R_c \gg w$, and thus maximise L_c. The coherence length as a function of the wavelength and the width of the waveguide is shown in Fig. 2a for a suspended waveguide and in Fig. 2b for a waveguide on aluminium oxide.

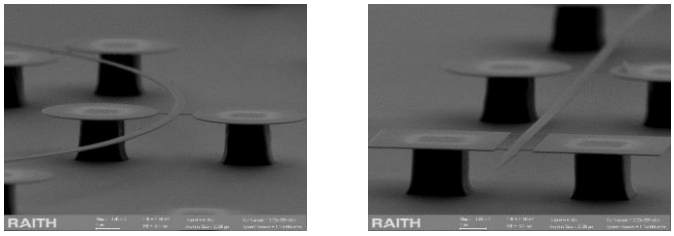
Both samples have been fabricated on a (100) GaAs wafer. For the first one, a 123nm $Al_{0.19}Ga_{0.81}As$ layer is grown over an $Al_{0.80}Ga_{0.20}As$ sacrificial layer, while for the second one, we grow a 100nm $Al_{0.19}Ga_{0.81}As$ layer on an $Al_{0.98}Ga_{0.02}As$ layer to be oxidised after lithography and etching. A few electron-microscope images are shown in Fig. 3.

Both waveguides are excited by a continuous-wave laser at a FF wavelength of 1.55µm, and we collect both FF throughput and SH output at 775nm with lock-in detection. End-fire input and output light coupling is performed via micro-lensed fibres and inverted tapers. The latter, of the type shown in Fig. 3b, are optimized for FF TE-polarized light at the input and SH TM-polarized light at the output.



(a) **(b)**

Fig. 2. Coherence length versus λ_{FF} and w, for the suspended waveguide (a) and for the waveguide on an aluminium-oxide substrate (b).



(a) **(b)**

Fig. 3. Scanning-electron-microscope pictures of a suspended waveguide: (a) bent geometry; (b) inverted taper for end-fire light coupling.

Ideal losses in snake waveguides are of two types: 1) radiation losses at the bent interface between the waveguide and the air; and 2) losses due to the non-ideal mode overlap at the waveguide sections where the sign of the snake curvature changes. Simulations performed with COMSOL on the suspended waveguides predict them to be smaller than 1dB/cm for w = 0.75 μm and R_c = 20 μm, as well as for w = 1 μm and R_c = 50 μm. In such waveguides, the calculated SHG conversion efficiencies are η_{SHG}= $7x10^3$ $W^{-1}cm^{-2}$ and η_{SHG}= $4.5x10^3$ $W^{-1}cm^{-2}$, respectively.

Although the overall losses also include scattering and residual absorption losses due to non-ideal fabrication and materials, their preliminary measurements show the good potential of high-index-contrast snake-shaped AlGaAs nanowires for three-wave mixing.

References:

[1] Y. Dumeige and P. Feron, "Whispering-gallery-mode analysis of phase-matched doubly resonant second-harmonic generation", Phys. Rev. A 74, 063804 (2006).

[2] P. S. Kuo, J. Bravo-Abad, and G. S. Solomon, "Second-harmonic generation using $\bar{4}$-quasi-phasematching in a GaAs whispering-gallery-mode microcavity", Nat. Commun. 5, 3109 (2014).

[3] S. Mariani, et al., "Second-harmonic generation in AlGaAs microdisks in the telecom range", Optics Letters 39, 3062 (2014).

[4] R. T. Horn, and G. Weihs, "Directional Quasi-Phase Matching in Curved Waveguides", arXiv: 1008.2190 (2010).

Influence of Thermo-mechanical Effects induced by 3D Assembly on Silicon Microring Resonator

A. MICHARD[1,2*], N. MICHIT[1], JB. QUELENE[1], JF. CARPENTIER[1], P. MARIS FERREIRA[2]
[1]STMicroelectronics, 850 rue Jean Monnet, Crolles, 38926, France
[2]GeePs, UMR CNRS 8507, CentraleSupélec, 3 rue Joliot Curie, Gif-sur-Yvette, 91192, France
*audrey.michard@st.com

Silicon photonics is considered as a prime technology for communication and high-speed computing applications. Ring resonator modulators are one of the key components, especially for next-generation high data-rate and high density interconnects. Indeed ring-based transceivers have been proposed to implement energy-efficient optical links in order to meet power and bandwidth datacoms standard [1]. The design of such a transceiver requires a careful integration between photonic and CMOS chips. The hybrid solution employed in [1] consists of a flip-chip integration and is often preferred thanks to separated design and process technology optimisation for the best performance of each circuit. However the introduction of micro copper-pillars to connect both chips can induce thermo-mechanical stresses on silicon waveguides. This issue is not without consequence for the optical properties which will be discussed in the following, after the quantification of 3D assembly-induced stress.

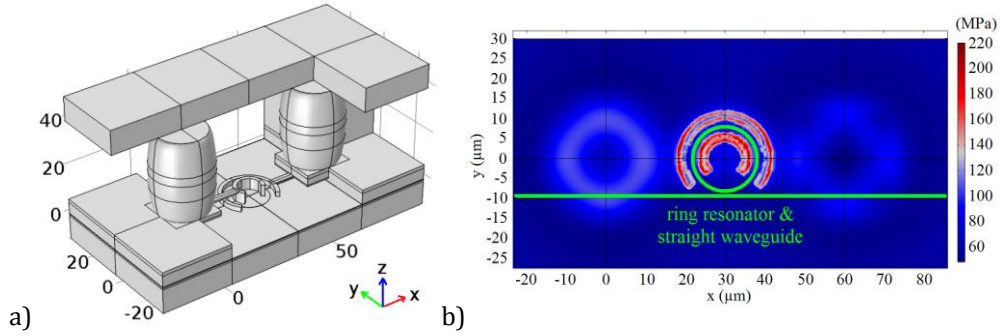


Fig. 1. a) 3D model of a photonic IC with a ring resonator connected to two Cu-pillars; b) Von Mises stress tensor map (MPa) on silicon plane.

During chips fabrication and micro-pillars contacting, high temperature processes are applied. The cooling leads to strained silicon waveguide since silicon and copper used for connections have distinct coefficients of thermal expansions. To evaluate the resulting stress, a finite element modelling was set similarly to the study performed in [2]. Figure 1.a) shows the geometries used to model the flip-chip assembly. The ring resonator has an 8-µm radius and is surrounded by two bumps spaced of 60 µm. The top, middle and bottom diameters of the Cu-pillars are respectively 25, 30, and 25 µm while their heights are 40 µm. The photonic die model includes also the aluminium pads and the ring copper contacts to simulate the BEoL stack. Flip-chip processes are simulated thanks to a uniform thermo-mechanical cooling with temperature differences of 220°C, 170°C, and 80°C for respectively the top die, the underfill material (a non-conductive paste was used), and the bottom die. Figure 1.b) represents the stress distribution in the silicon layer with ring and straight waveguides in green. More precisely, x, y, and z components of stress tensor (σ_x, σ_y, and σ_z) along the straight waveguide are reported on figure 2.a). It shows that the stress can reach the order of 60 MPa either in "tension" near the ring or in "compression" under the Cu-pillars. Waveguide optical properties are modified by

stress due to the photo-elastic effect. This effect was measured in a Si ring resonator in [3] and was demonstrated to be consistent with that of bulk Si. As a consequence, the change in refractive index tensor (Δn_x, Δn_y, and Δn_z) is modelled by the stress-optic constants of Si (C_1 and C_2) and is expressed as Eq. (1) [4]. The shear stresses are very small and, hence, their impact on refractive index is negligible in this paper. Wave propagation in photonic devices is dictated by the effective index. The stress-induced variations of effective index (Δn_{eff}) can be derived as Eq. (2), where coefficients a_1 and a_2 are given in [4] for a TE mode. For a TM mode, Eq. (2) is assumed to be also valid with $a_{1,TM} = a_{2,TE} = 0.219$ and $a_{2,TM} = a_{1,TE} = 0.844$. Figure 2.b) shows the estimated effective index profile along the straight waveguide for both TE and TM modes.

$$\begin{cases} \Delta n_x = -C_1\sigma_x - C_2(\sigma_y + \sigma_z) \\ \Delta n_y = -C_1\sigma_y - C_2(\sigma_x + \sigma_z) \\ \Delta n_z = -C_1\sigma_z - C_2(\sigma_x + \sigma_y) \end{cases} \quad (1)$$

$$\Delta n_{eff,TE/TM} = a_{1,TE/TM}\,\Delta n_y + a_{2,TE/TM}\,\Delta n_z \quad (2)$$

In the case of a ring, a change in effective index results in a resonance wavelength shift which can be critical especially for a WDM (wavelength division multiplexing) system. Indeed the previous study indicates a variation of $\Delta n_{eff,TE}$ between 0.0002 and 0.0008 in the ring waveguide, corresponding to a resonance shift of approximately 50 to 250 pm. By comparison, the channel spacing in a WDM transmission is typically 280 pm (50 GHz) or 560 pm (100 GHz) for a communication at 1.3 µm. Therefore the system performance can be greatly deviated from the designed devices. Moreover a cross-coupling between TE and TM modes can appear in the straight waveguide of a WDM system since the Cu-pillars introduce a periodic perturbation as shown in figure 2.b). Consequently a polarization conversion can be achieved resulting in a power loss in TE mode and a possible mode dispersion, degrading thus the global performance.

In conclusion, the impact of 3D assembly on a Si ring resonator has been theoretically investigated for the first time to the authors' knowledge. Next step would be to experimentally quantify the induced stress through the resonance wavelength shift.

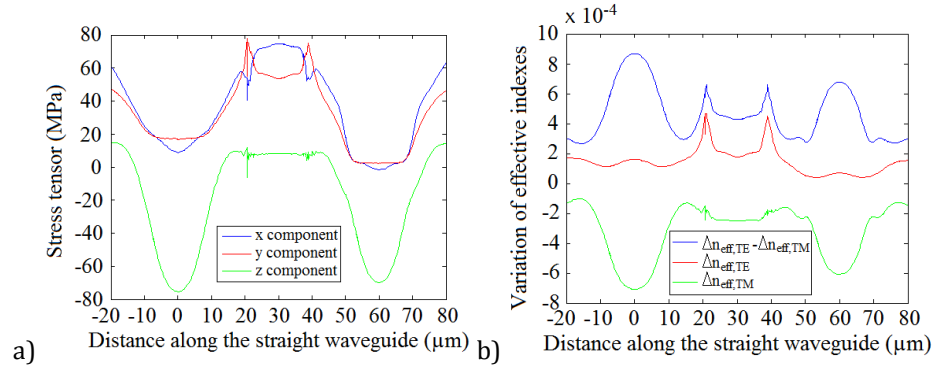


Fig. 2. a) Stress tensor profile and b) Variation of effective index along the straight waveguide.

References

[1] M. Rakowski et al., in IEEE International Solid-State Circuits Conference, pp. 408-410, 2015.
[2] V. Fiori et al., Microelectronics Reliability, vol. 54, no. 4, pp. 764-772, 2014.
[3] Y. Amemiya et al., Japanese Journal of Applied Physics, vol. 47, no. 4, pp. 2910-2914, 2008.
[4] Y. Yang et al., IEEE Photonics Journal, vol. 5, no. 6, 2013.

Polarization properties of second harmonic signal from monolithic AlGaAs nanoantennas

Valerio Flavio GILI,[1] Lavinia GHIRARDINI,[2] Luca CARLETTI,[3] Giovanni PELLEGRINI,[2] Lamberto DUO', [2] Marco FINAZZI,[2] Davide ROCCO,[3] Andrea LOCATELLI,[3] Ivan FAVERO,[1] Marco RAVARO,[1] Aristide LEMAITRE,[4] Michele CELEBRANO,[2] Costantino DE ANGELIS,[3] and Giuseppe LEO[1]

[1] Matériaux et Phénomènes Quantiques, Université Paris Diderot, 10 rue A. Domon et L. Duquet, 75013 Paris, France
[2] Department of Physics, Politecnico di Milano, Piazza Leonardo Da Vinci 32, 20133 Milano, Italy
[3] Department of Information Engineering, University of Brescia, Via Branze 38, 25123 Brescia, Italy
[4] Centre de Nanosciences et de Nanotechnologies, CNRS, Route de Nozay, 91460 Marcoussis, France
* corresponding author e-mail: giuseppe.leo@univ-paris-diderot.fr

Metal-less nanophotonics has recently raised an increasing interest because the optical response of high-permittivity dielectric nanoparticles exhibits negligible dissipative losses and strong magnetic multipole resonances [1–3] in the visible and near-IR. Here we propose all-dielectric $Al_{0.18}Ga_{0.82}As$-on-AlOx nanodiskrs, on which we measure second harmonic generation (SHG) with conversion efficiency up to 10^{-5} for a 1.6 GW/cm^2 pump in the optical telecom wavelength range [4]. Our samples were fabricated from a [100] non-intentionally doped GaAs wafer, with a 400nm layer of $Al_{0.18}Ga_{0.82}As$ on top of an aluminum-rich substrate. We first patterned circles with a scanning electron microscope (SEM) lithography system, followed by ICP-RIE dry etching. Finally the sample was selectively oxidized at 390°C for 30 min. The result is an array of nanoantennas on an aluminum-oxide (AlOx) substrate, as shown in Fig. 1(a).

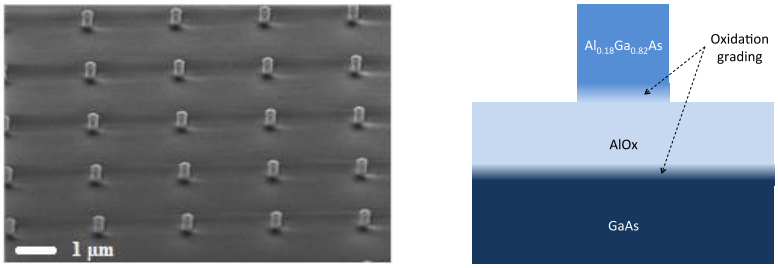


Fig. 1. Monolithic AlGaAs-on-AlOx nanoantennas: a) scanning-electron-microscope picture of a part of the array; b) schematics of a single nanoantenna.

The linear and nonlinear optical response of such nanoantennas are modeled by using frequency-domain finite element simulations in COMSOL [5]. We numerically predict a SH conversion efficiency higher than 10^{-5} for a pump wavelength between 1500 nm and 1700 nm.

To experimentally investigate the nonlinear properties of the fabricated nanopillars, we excited them with an ultrafast Erbium-doped fiber laser centered at 1554 nm (150 fs pulses, 80 MHz repetition rate). SHG signal was collected from an array of nanocylinders with radius varying from 175 to 225 nm, using single-photon avalanche photodiodes. The dependence of the detected SHG on the radius of the nanocylinders is in excellent agreement with the numerical simulations (see Fig. 2a). The polarization of the emitted SHG, reported in Fig. 2b as a function of the nanodisks radius, is also in very good agreement with numerical simulation (see Fig. 2c), demonstrating the strong dependence of the SHG polarization from the nanocavity modes involved for specific nanostructures dimensions [6].

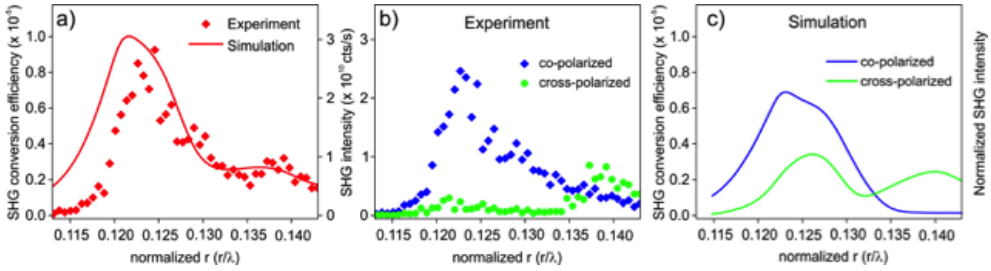


Fig. 2. a) Unpolarized second harmonic emission; b) Experimental polarized emission; c) Simulated polarized conversion efficiency.

Our results allow gaining further insight in the mechanisms underlying the polarized nonlinear emission in these systems, showing the potential of AlGaAs-on-insulator all-dielectric platforms in the nonlinear manipulation of light properties at the nanoscale.

References

[1] A. I. Kuznetsov, A. E. Miroshnichenko, Y. H. Fu, J. Zhang, and B. Luk'yanchuk, *Magnetic light*, Sci. Rep. 2, 1–6 (2012).

[2] A. B. Evlyukhin, S. M. Novikov, U. Zywietz, R. L. Eriksen, C. Reinhardt, S. I. Bozhevolnyi, and B. N. Chichkov, *Demonstration of magnetic dipole resonances of dielectric nanospheres in the visible region*, Nano Lett. 12, 3749–3755 (2012).

[3] S. Person, M. Jain, Z. Lapin, J. J. Sáenz, G. Wicks, and L. Novotny, *Demonstration of zero optical backscattering from single nanoparticles*, Nano Lett. 13, 1806–1809 (2013).

[4] V. F. Gili, L. Carletti, A. Locatelli, D. Rocco, M. Finazzi, L. Ghirardini, I. Favero, C. Gomez, A. Lemaître, M. Celebrano, C. De Angelis, and G. Leo, *Monolithic AlGaAs second-harmonic nanoantennas*, Opt. Express 24, 15965-15971 (2016).

[5] L. Carletti, A. Locatelli, O. Stepanenko, G. Leo, and C. De Angelis, *Enhanced second-harmonic generation from magnetic resonance in AlGaAs nanoantennas*, Opt. Express 23, 26544–26550 (2015).

[6] L. Ghirardini, L. Carletti, V. Gili, G. Pellegrini, L. Duò, M. Finazzi, D. Rocco, A. Locatelli, C. De Angelis, I. Favero, M. Ravaro, G. Leo, A. Lemaître, and M. Celebrano, *submitted*.

Chalcogenides photonic integrated circuits for near- and mid-infrared applications

Jonathan LEMAITRE[1], Aldo GUTIERREZ-ARROYO[1], Enguerran DELCOURT[1], Walid EL AYED[1], Parastesh PIRASTEH[1], Loïc BODIOU[1*], Yannick DUMEIGE[1], Isabelle HARDY[1], Joel CHARRIER[1*], Emeline BAUDET[2], Florent STARECKI[2], Radwan CHAHAL[2], Marion BAILLIEUL[2], Virginie NAZABAL[2],

[1]FOTON, UMR-CNRS 6082, ENSSAT BP80518, F-22305 Lannion Cedex, France
[2]ISCR, UMR-CNRS 6226, Glass and Ceramics Team, 35042 Rennes, France
* loic.bodiou@univ-rennes1.fr, joel.charrier@univ-rennes1.fr

Chalcogenide glasses are an important class of amorphous semiconductors that contain at least one of the chalcogen elements from group 6a of the periodic table (S, Se and Te but excluding oxygen) as major constituent [1]. These elements are covalently bonded to network formers such as As, Ge, Sb, Ga, Si or P. The unique optical properties of these glasses are motivating intense research towards the development of a wide range of photonic applications [2]. In particular, all-optical signal processing in near-infrared (IR) telecommunications window is taking advantage of their high optical nonlinearities [3]. These glasses also exhibit low maximum phonon energies (values range from 350-425 cm^{-1} for sulphide, 250-300 cm^{-1} for selenide and 150-200 cm^{-1} for telluride) which yields a broad transparency in the mid-IR, independently of the exact glass composition. Mid-IR trace molecules sensing platforms could therefore also benefit from the development of these materials. For both applications (telecommunication and sensing), the current trend is directed toward minimizing device footprints and cost by implementing integrated optical components.

In this paper, we will present the technological processing of photonic circuits based on selenides ridge waveguides for the implementation of integrated mid-IR sensing platform and ultrahigh-bandwidth signal processing. The selenides layers are deposited on a silicon substrate by RF magnetron sputtering. Different waveguiding structures such as straight ridge waveguides, micro-ring resonators or spiral waveguides are subsequently patterned using standard i-line photolithography and fluorine-based RIE/ICP dry etching techniques (Fig.1). Optical demonstration of integrated four-wave mixing and sensing are respectively presented in the near- and mid-IR.

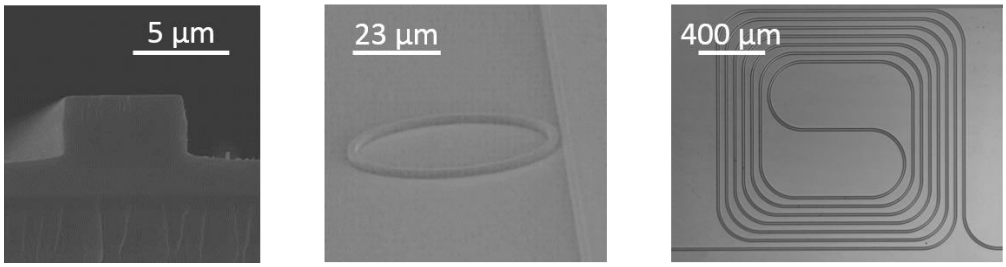


Fig. 1. Scanning electron microscope image of the processed waveguide after ICP-RIE a) ridge waveguide, b) micro-ring resonator and c) spiral waveguide.

Third order nonlinear effects such as four wave-mixing can be used for all-optical signal processing and frequency comb generation. The efficiency of such process depends on the waveguide nonlinear parameter $\gamma = \omega n_2/cA_{eff}$ where A_{eff} is the area of the propagating mode, c is the speed of light and ω is its frequency. In chalcogenides ridge waveguides,

this parameter can reach more than 100 $W^{-1}m^{-1}$ and enable the observation of four-wave mixing in cm-long waveguides (Fig2a). The use of chalcogenides-based high quality factor micro-ring resonators could further enhance the optical field in the cavity and therefore lead to an increase efficiency. The enhancement factor of the optical field using resonating structures will be presented in relation to the design of the micro-ring resonator (waveguide dimensions, coupling coefficient κ between bus waveguide and ring resonator, loss α per round trip).

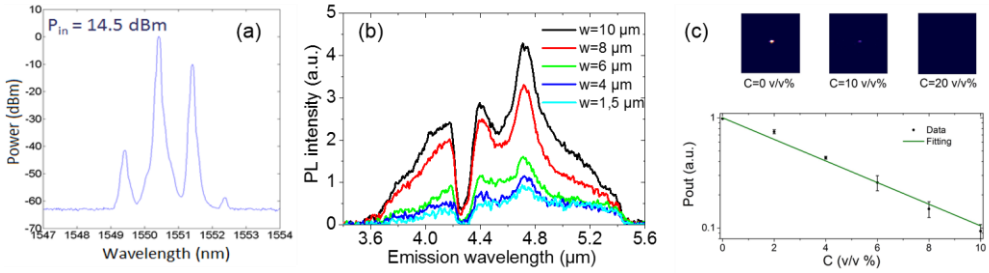


Fig. 2. a) Four-wave mixing spectrum obtained from 1-cm long selenides ridge waveguides, b) guided mid-IR photoluminescence spectrum from Pr^{3+}-doped selenides ridge waveguides c) Isopropanol detection @ 7.7µm using selenides waveguides.

The growing need for traces molecules detection is pushing towards the development of compact sensing platforms able to monolithically integrate a mid-IR light source, waveguides (also acting as transducers) and a detector [4]. Thanks to their broad mid-IR transparency, efficient waveguiding properties [5] and ability to be doped with rare earth (RE) ions, chalcogenides (ChGs) glasses are a compelling alternative to other mid-IR transparent materials (silicon, germanium or gallium arsenides…) to sustain this demand. Guided mid-IR praseodymium (Pr^{3+}) photoluminescence (PL) recorded between 3.5 and 5.5 µm using a continuous wave excitation at 1.55 µm in co-propagative configuration is presented in Fig. 2b. The incorporation of these efficient mid-IR emiters in micro-disk microcavities could enable the implementation of low-threshold on-chip mid-IR lasers with emission wavelength overlapping the strong characteristic vibrational transitions displayed by chemical molecules in the mid-IR. Mid-IR chemical detection has also been demonstrated by recording the transmitted power at 7.7 µm though chalcogenides spiral waveguides with different isopropanol concentrations deposited on the surface (Fig. 2c).

In conclusion, ridge waveguides were fabricated by RF magnetron sputtering and subsequent patterning using standard photolithographic steps. Different waveguiding structures (straight and spiral waveguides, micro-ring and micro-disk resonators) were processed and successfully tested for diverse applications in the near- and mid-IR.

References

[1] *Chalcogenide Glasses*, 1st Edition, Preparation, Properties and Applications, Editors: J.L. Adam & X.-H. Zhang, Woodhead Publishing, ISBN: 9780857093455 (2013).

[2] B. J. Eggleton, B. Luther-Davies, K. Richardson, *Chalcogenides photonics*, Nat. Photonics, 5, 141 (2011).

[3] M. Olivier, J.C. Tchahame, P. Němec, M. Chauvet, V. Besse, C. Cassagne, G. Boudebs, G. Renversez, R. Boidin, E. Baudet, V. Nazabal, *Structure, nonlinear properties, and photosensitivity of* $(GeSe_2)_{100-x}(Sb_2Se_3)_x$ *glasses*, Opt. Mater. Express, 4, 525 (2014).

[4] M. Sieger, B. Mizaikoff, *Toward on-chip mid-infrared sensors*, Anal. Chem., 88, 5562 (2016).

[5] A. Gutierrez-Arroyo, E. Baudet, L. Bodiou, J. Lemaitre, I. Hardy, F. Faijan, B. Bureau, V. Nazabal, J. Charrier, *Optical characterization at 7.7 µm of an integrated platform based on chalcogenide waveguides for sensing applications in the mid-InfraRed*, Opt. Express, 24, 23109 (2016).

Development of Inverted p-Substrate InP/AlGaInAs Lasers for Vertical Integration with Multiple Passive or Active Intrinsic Regions

Shane P. DUGGAN[1,2*], Niall P. KELLY[1,2], Ludovic CARO[1,2], Mohamad DERNAIKA[1,3], Maryam SHAYESTEH[1], Justin K. ALEXANDER[1,2], Hua YANG[1], Padraic E. MORRISSEY[1], Agnieszka GOCALINSKA[4], Kevin K. THOMAS[4], Emanuele PELUCCHI[4] and Frank H. PETERS[1,2]

[1]Integrated Photonics Group, Tyndall National Institute, Dyke Parade, Cork, T12R5CP, Ireland
[2]Physics Department, University College Cork, College Road, Cork, T12YN60, Ireland
[3]Electrical and Electronic Engineering Department, University College Cork, College Road, Cork, T12YN60, Ireland
[4]Epitaxy and Physics of Nanostructures Group, Tyndall National Institute, Dyke Parade, Cork, T12R5CP, Ireland
* shane.duggan@tyndall.ie

Photonic integrated circuits (PICs) often require separate active and passive optoelectronic devices on a single chip. Active devices generate and amplify light while passive devices are for lossless guiding and manipulation. Integration of the two types of optoelectronic devices is challenging as each requires different material. Monolithic vertical integration of passive and active devices allows separate material to be grown one above the other, while tapering of the different layers allows transitions between the now integrated devices.

Vertical integration of junctions requires every alternate device to be inverted from the traditional n-substrate layout to a p-substrate. For example for two devices vertically integrated the lower device may be p-i-n with an n-substrate, requiring the device above it to be n-i-p so that they can share the p-doped layer, resulting in an n-i-p-i-n structure.

Little work has been done on p-substrate semiconductor lasers. N-substrates have been preferred due to the instability of dopants in p-substrates. Typical Zn p-doping diffuses heavily during further growth at high temperatures with a risk of reducing optical efficiency if the intrinsic region is penetrated [4]. Diffusion can be restricted by placing a protecting undoped region between the p-doped and the intrinsic region [1]. It is also difficult to form a low resistance contact to p-doped InP [2], a fact avoided with n-substrate devices by using highly doped GaInAs(P) cap layers. However by using a broad p-substrate back contact the contact resistance is reduced, eliminating the requirement of additional layers, in addition to which the p-substrate should be highly doped and thinned to reduce its resistance as much as possible [2,3].

The p-substrate InP/AlGaInAs 1.5um lasers grown and tested here have a core of 5 quantum wells (QWs) and Figure 1 outlines the doping profiles of each revision used to increase device performance. While the first iteration included an undoped region between the intrinsic and p-doped layers, Figure 2 shows that the material failed to lase under CW operation and required high pulsed currents to work. However the peak wavelength was correctly centred at 1.5um, therefore a very similar epitaxial design was used for two subsequent growths where in one case the doping was pulled back further to absorb diffusion of Zn dopants, while the other case included a carbon doped layer as a stopping layer to prevent Zn diffusion, due to carbon being a more stable dopant [4]. The reason for the first failed growth is believed to have been diffusion into and through the QW core, as justified by ECVP measurement and CV measurements which determine the intrinsic region thickness, Figure 1.

Figure 1 shows that both revised editions had an increased intrinsic region and Figure 2 shows this allowed the samples to lase with thresholds below 40mA with wavelengths centred around 1.55um. These results indicate that either of these p-substrate InP/AlGaInAs lasers can be used for further vertical integration, and this work will present their development.

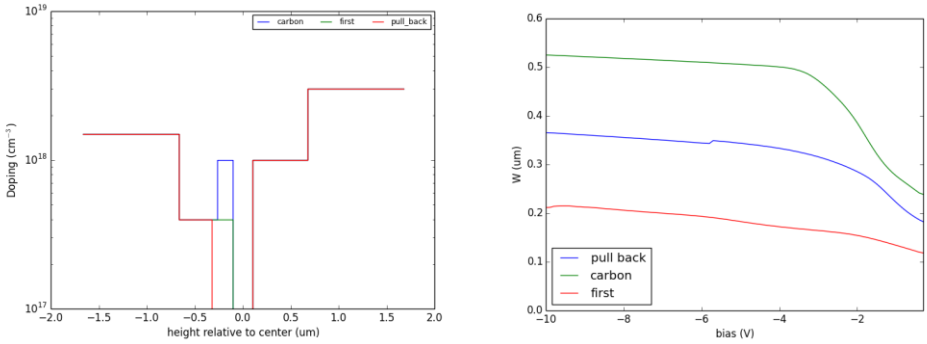


Fig. 1. Left: Doping profiles of the different epitaxial designs of the p-substrate material. The p-doping was pulled back on redesign to prevent diffusion into the core, while another iteration placed a carbon doped layer before the undoped region. Right: Capacitance-Voltage measurements were performed on circular diode structures on each of the different n-i-p wafers, from which the depletion width can be calculated from $C = \frac{\epsilon A}{W}$. The low depletion width W of the first sample was not sufficient to prevent diffusion into the core while the revised editions with the doping pulled back further and a carbon layer prevent diffusion into the core.

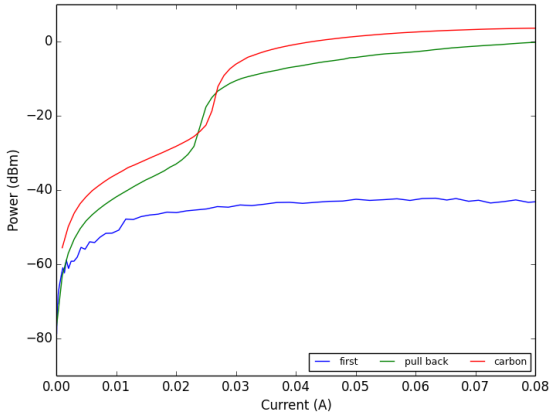


Fig. 2. Optical power vs injected current for Fabry-Perot lasers on each of the epitaxial designs: first iteration, with p-doping layers pulled back from the intrinsic region, and with a carbon doped blocking layer before the undoped region.

References

[1] S. Kakimoto, et al., *Threshold currents of 1.2-1.55um P-substrate buried crescent laser diodes,* IEEE Journal of Quantum Electronics, vol. 28, no. 7, pp. 1631-1635, 1992

[2] Y. Nakano, et al., *1.5um InGaAsP/InP BH Lasers on p-Type InP Substrates,* Japanese Journal of Applied Physics, vol. 19, no. 10, pp. L612, 1980

[3] D. Tauber, J.E. Bowers, *Dynamics of Wide Bandwidth Semiconductor Lasers,* International Journal of High Speed Electronics and Systems, vol. 8, no. 3, pp. 377-416, 1997

[4] M. Osiński, et al., *Vertical Cavity Lasers on P-Doped Substrates,* Electronic Letters, vol. 33, no. 9, pp. 783-784, 1997

EUROPEAN CONFERENCE ON INTEGRATED OPTICS

Ridge waveguide lasers based on fs-laser writing on rare-earth doped crystals

J. Martínez de Mendívil[1], G. Lifante[2*], E. Cantelar[2], J. del Hoyo[3], J. Solís[3], M.C. Pujol[4], M. Aguiló[4] and F. Díaz[4]

1 Departamento de Tratamiento de la Señal y Comunicaciones, Universidad de Mondragón, Arrasate-Mondragón, 20500, Gipuzkoa, Spain
2 Dept. de Física de Materiales, Universidad Autónoma de Madrid, Madrid, Spain
3 Laser Processing Group, Instituto de Óptica, CSIC, Madrid, Spain
4 Física i Cristalografia de Materials i Nanomaterials (FiCMA-FiCNA), Universitat Rovira i Virgili, Tarragona, Spain
* gines.lifante@uam.es

The fs-laser writing technique is an interesting and versatile approach to fabricate ridge optical structures in dielectrics, defining the so-called type-IV direct written waveguides [1]. The fs-laser ablation is used to remove the selected parts of the planar waveguide surface, constructing thus the ridges. This technology does not require the use of clean room facilities, and allows rapid prototyping of integrated photonic devices because it is a mask-less technology.

Among other integrated photonic devices, waveguide lasers in crystalline media are attractive to be used as miniaturized laser sources [2]. In particular doubles tungstates (KYW) and lithium niobate ($LiNbO_3$) are good candidates for laser hosts when doped with active rare earths, such as Yb or Nd, operating around 1 μm wavelength [3, 4].

In this work, we demonstrate laser operation is waveguide configuration based on Yb:KYW and Nd:$LiNbO_3$ fabricated by fs-laser written technology to create the ridges waveguides. The ridge waveguides are defined by structuring active planar waveguides with femtosecond laser machining. Here two types of planar waveguides have been using to design the waveguide lasers: step-index waveguides (by using liquid phase epitaxy on double-tugnstate crystals) and gradient index waveguides (by using metallic diffusion on lithium niobate crystals). A mirrorless Yb^{3+} doped $KY_{1-x-y}Gd_xLu_y(WO_4)_2$ waveguide laser with cw operation at 981.5 and 1001 nm, fabricated by liquid phase epitaxy and structured by femtosecond laser microstructuring, is first reported. The planar waveguide was fabricated by growing an Yb^{3+} doped $KY_{1-x-y}Gd_xLu_y(WO_4)_2$ epitaxial layer by liquid phase epitaxy over a $KY(WO_4)_2$ substrate. This planar waveguide was then microstructured by means of multiplexed beam femtosecond laser writing technique to define ridge waveguides. Mirrorless laser action is demonstrated in ridge waveguides with different fabrication parameters, obtaining maximum slope

efficiency above of 78% versus absorbed power (see figure 1), On the other hand, ridge waveguide lasers have been also fabricated on Nd^{3+} doped $LiNbO_3$ crystals. The fs-laser writing technique was used to define ridge structures on a gradient-index planar waveguide fabricated by Zn-diffusion. This planar waveguide was formed in a *z*-cut $LiNbO_3$ substrate homogeneously doped with a 0.23% of Nd^{3+} ions. By butting two mirrors at the waveguide end-facets, TM-polarized laser action at 1085 nm was achieved, which shows a threshold of 31 mW, with a 7% of slope efficiency, thus confirming the feasibility of this technique for the development of integrated laser devices.

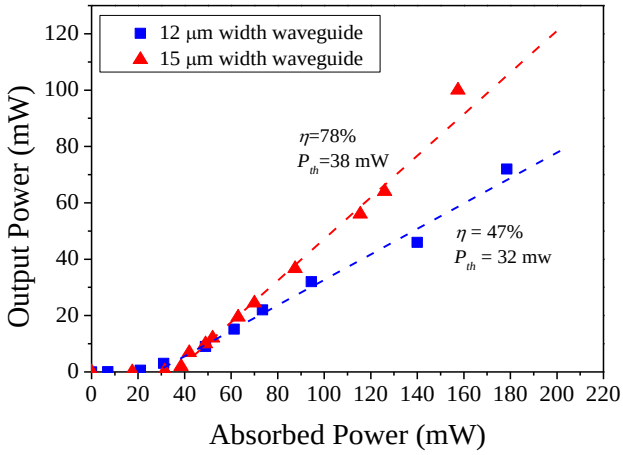


Fig. 1. Laser performance of a 12 and 15 μm width Yb:KYW ridge waveguide operating at 1001 nm.

References

[1] F. Cheng and J.R. Vázquez de Aldana, *Optical waveguides in crystalline dielectric materials produced by femtosecond-laser micromachining*. Laser Photonics Rev. **8**, 251-275 (2014).
[2] E. Cantelar, D. Jaque and G. Lifante, *Waveguide lasers based on dielectric materials*, Opt. Mater. **3** (2012) 555-571.
[3] J. Martínez de Mendívil, J. del Hoyo, J. Solís, M.C. Pujol, M. Aguiló, F. Díaz and G. Lifante, *Yb^{3+}-Doped Monoclinic Double Tungstate Waveguide Laser Combining Liquid Phase Epitaxy and Multiplexed Beam fs Laser Writing*. J. of Lightwave Technol. **33**, 4726-4730 (2015).
[4] J. Martínez de Mendívil, J. del Hoyo, J. Solís and G. Lifante, *Ridge waveguide laser in Nd:$LiNbO_3$ by Zn-diffusion and femtosecond-laser structuring*. Opt. Mat. **62**, 353-356 (2016).

PIC Fabrication Platforms for SOI and Si_3N_4 in a Flexible Photonic Foundry Concept

Anna Lena GIESECKE*, Jens BOLTEN, Thorsten WAHLBRINK, Piotr CEGIELSKI, Caroline PORSCHATIS, Daniel SCHALL, Bartos CHMIELAK, Andreas PRINZEN, Holger LERCH, Herbert KLEINJANS

AMO GmbH, Otto-Blumenthal-Str. 25, Aachen, 52074, Germany

* giesecke@amo.de

We provide unique highly flexible fabrication platforms for integrated photonic circuits based on SOI and Si_3N_4 from design to fabrication and characterization of the manufactured devices. The schematic in Fig. 1 depicts different options of our technology platforms. The accessibility of both platforms permits applications from telecom wavelengths to the NIR and visible range, hence the devices are suitable for communication as well as for sensing. AMO has been developing the SOI platform for photonic applications for more than one decade. Waveguide losses and grating couplers have been optimized for both telecom wavelength ranges around 1310 nm and 1550 nm. Critical passive structures such as directional couplers and ring resonators can be fabricated with high precision (Fig. 2b), g)). The passive platform is completed with efficient grating couplers (Fig. a)) (2.5 dB loss) and edge coupling through spot-size converters. In order to maximize the yield of our SOI-based photonic devices fabrication tolerances have been intensively studied and device design as well as processes both for the lithographic definition and for the pattern transfer via reactive ion etching have been optimized accordingly [1].

Active components in SOI such as modulators (Fig. 2f)-i)) and detectors [2] are enabled through ion implantation and optimized annealing steps. Furthermore, the co-integration of 2D-materials such as graphene into the photonic platform has been successfully demonstrated [3,4], enabling the fabrication of high speed photodetectors and heaters. The development of active SOI based components resulted in the fabrication of a transceiver module for an AOC (Fig. 2h)).

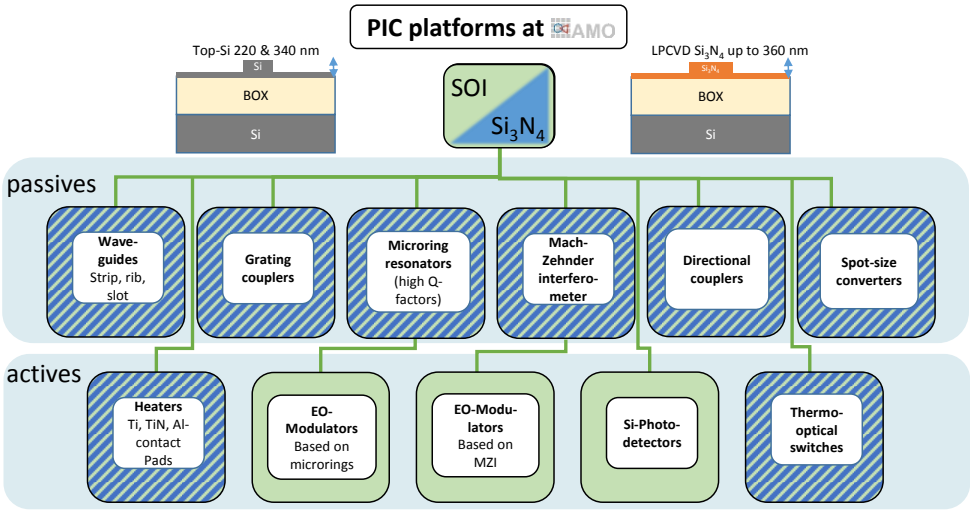


Fig. 1. PIC platforms at AMO. The hatched boxes show the components available for both SOI and Si_3N_4 platform. The green boxes show components only available for SOI.

To access an even broader wavelength range a second fabrication platform, based on silicon nitride on a thermally grown oxide on a Si substrate, has been developed.

Waveguides, directional couplers and grating couplers have been mainly designed for 1550 nm on a substrate with a thick 6 µm oxide layer and 100 nm thick Si_3N_4 layer. The corresponding waveguide losses for this platform do not exceed 0.1 dB/m. Thermal optical switches have been realized with Mach Zehnder interferometers with Ti-heaters [5]. A dedicated LPCVD silicon nitride process offers low stress layers. With this process also thicker waveguides with a height of 360 nm which offer better light confinement are feasible. These waveguide structures have a propagation loss of ~0.6dB/cm (@1550nm).

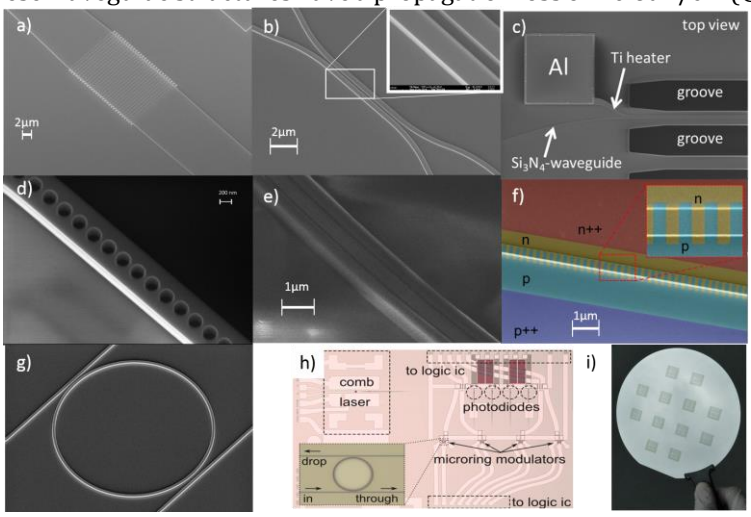


Fig. 2. Examples of fabricated components and devices with AMO's photonic platform. a) shallow-etched grating coupler, b) directional coupler, c) Si_3N_4 thermo-optical switch, d) photonic crystal waveguide, e) double slot ring resonator in Si_3N_4, f) interleaved phase shifter with pn-junction width of 150 nm, g) microring resonator, h) transceiver for active optical cable 56 Gbit/s [2], i) SOI wafer with transceiver chips

A Mix & Match approach of both highest resolution e-beam lithography and fast i-line stepper lithography is available for both the SOI- and the Si_3N_4-based fabrication platforms, combining flexibility and high precision with short turnaround times. In this way customized chip and wafer runs can be performed. Fabrication highlights of both photonic platforms as well as the implementation of new materials such as organics and perovskites towards the development of on-chip light sources will be presented.

Acknowledgement

We acknowledge our past and present projects funded by the European Union which are GAIA, PHOXTROT, PLASMOfab, Synchronics, and SPIRIT as well as the German national projects SHYWA and SASER funded by the BMBF.

References

[1] A. Prinzen, M. Waldow, H. Kurz, *Fabrication tolerances of SOI based directional couplers and ring resonators*, Optics Express, 21, 14, 17212-17220,

[2] H. Füser et al., *56 Gb/s WDM transmitter module based on silicon microrings using comb lasers*. CLEO: QELS Fundamental Science (pp. JTh2A-66). OSA, 2015

[3] D. Schall et al., *50 GBit/s photodetectors based on wafer-scale graphene for integrated silicon photonic communication systems*. ACS Photonics, 1(9), 781-784, 2014.

[4] D. Schall et al., *Infrared transparent graphene heater for silicon photonic integrated circuits.* Optics express, 24(8), 7871-7878, 2016.

[5] M. A. Piqueras et al., *Photonic Front-End for the next-generation of space SAR applications*. SPIE Remote Sensing (pp. 96391I-96391I). International Society for Optics and Photonics, 2015.

Energy consumption study of reverse-biased modulators in monolithic electronic-photonic technology

S. Hosseini[1]*, M. Cătuneanu[1], R. Henker[2], F. Ellinger[2], K. Jamshidi[1]
[1] Integrated Photonic Devices Lab, Technische Universität Dresden, 01069 Dresden, Germany
[2] Chair of Circuit Design and Network Theory, Technische Universität Dresden, Germany
* seyedreza.hosseini@tu-dresden.de

Electronic Photonic Integrated Circuits (EPIC) technology can be used to realize integrated photonic devices alongside with conventional electronic technology such as CMOS or BiCMOS. There is an alternative approach where photonic and electronic components are fabricated separately and then connected to each other using technologies such as wire bonding, flip-chip bump bonding or through silicon vias (TSV) [1]. The main challenge for the realization of high-speed devices is to realize energy-efficient devices [2, 3]. In this paper, the energy consumption of optical modulators as one of the main components of optical transceiver systems based on both pure photonic technology and EPIC technology are studied and compared. Modulator frequency response is simulated using 3D FDTD full wave commercial simulators (CST Studio). The characteristic impedance of modulator is later extracted using the scattering parameters. Furthermore, in order to avoid large computational processing time especially for longer lengths, a circuit model of modulator [3] is used and its results are compared with full wave simulations. Modulator transfer function and characteristic impedance predicted by circuit models are verified by those of full wave simulations as shown in Figs. 1a-1c. The energy consumption of optical modulator can be simply estimated as $E_c = \frac{1}{4}CV^2$ where C is modulator equivalent capacitance. C corresponds to dissipative capacitive elements of intrinsic and extrinsic parts and V is the voltage swing applied to modulator [3]. For pure photonic simulations, a 0.5 mm long traveling wave modulator (TWM) with GSG pads to apply bias voltage and RF signal as well as 50 Ω termination has been considered. Unlike pure photonic technology, the driver is monolithically integrated with modulator in EPIC technology. Thus the modulator needs no pads for external terminations and can also be connected to driver through metal routes in the first metal layers in order to avoid excess parasitic capacitances. Since the modulator parameters in the waveguide layer do not change for both technologies, the depletion capacitance and $V\pi$ are similar in both cases. Therefore, the difference of energy consumption between two technologies will be limited to the extrinsic capacitances. For example, full wave simulations result in the estimation of extrinsic capacitances of 61fF and 3fF for pure photonic and EPIC technologies for 0.5 mm length modulator, respectively. It represents about 95 %

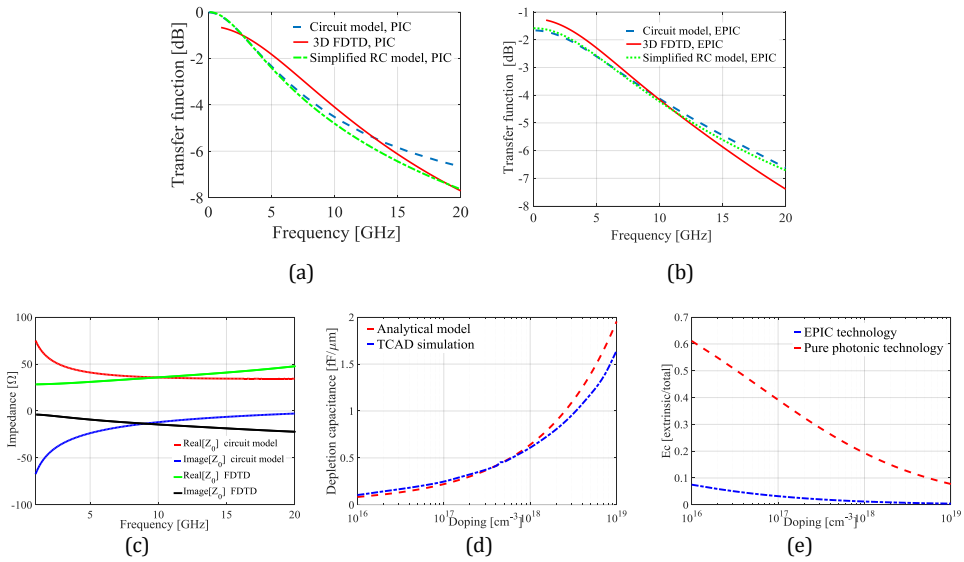


Fig. 1. Modulator transfer function simulations and comparison for a) pure photonic b) EPIC technologies. c) Modulator characteristic impedance. d) Intrinsic capacitance of modulator d) Extrinsic over total energy consumption of a standalone modulator.

enhancement of extrinsic energy consumption in EPIC rather than pure photonic. However, the main but constant energy term in both technologies is related to intrinsic capacitances. The intrinsic capacitance is obtained through our model which is validated by numerical simulations of electrical part (TCAD software) as illustrated in Fig. 1d. Total energy consumptions for both pure photonic and EPIC technology versus doping are obtained and shown in Fig 1e. As it can be seen, energy consumption difference is decreasing in high doping regions, which means common intrinsic energy consumption is a dominant term in both technologies. Extrinsic contribution of energy consumption will be higher if low doping levels are used. It means the EPIC technology would perform much better than pure photonic technology in terms of energy consumption if the low doping levels are used. Other important part of consumed energy in optical transmitters comes from driver's energy consumption. The driver's energy consumption mainly depends on, first the $V\pi$ and second the modulator length, i.e. how many segments the driver has to feed. By integrating the drivers with the modulators in EPIC technology less parasitics and also less energy consumption can be expected. It is shown that the energy consumption of a standalone modulator based on the EPIC technology (metals routed in bottom metal layer) is less than the similar modulator in pure photonic technology (metals routed in top metal layer) at fixed doping levels. It is shown that dominant term of modulators energy consumption in low and high doping levels corresponds to extrinsic and intrinsic consumed energy for both pure photonic and EPIC technologies, respectively.

This work is supported in part by the German Research Foundation (DFG) in the context of the collaborative research center, HAEC project.

References

[1] D. A. B. Miller, *Energy consumption in optical modulators for interconnects*, Opt. Express, no. 20, pp. A293-A308, 2012.

[2] S. Hosseini, K. Jamshidi, *Enhancement of bandwidth-energy consumption tradeoffs in reverse-biased modulators,* In Photonics Society Summer Topical Meeting Series *(SUM) IEEE,* pp. 94-95, 2016.

EUROPEAN CONFERENCE ON INTEGRATED OPTICS

Soft-proton exchange on Lithium Niobate substrates doped with Magnesium-oxide: route toward efficient and power-resistant nonlinear converters.

Tommaso LUNGHI[1*], Florent DOUTRE[1], Guillaume LEGOFF[1] , Getachew AYENEW[1] , Hervé TRONCHE[1] , Sébastien TANZILLI[1] , Pascal BALDI[1] and Marc DE MICHELI[1]

[1]Université Côte d'Azur, CNRS, Institut de Physique de Nice, France

[*] tlunghi@unice.fr

Wavelength nonlinear conversion is an attractive approach to coherently shift the wavelength of an optical beam in regions of the spectrum where sources, optical components and detectors are more reliable and practical. Among the different nonlinear materials congruent Lithium Niobate (CLN) is one of the most widely used thanks to its large nonlinear coefficient. Through quasi-phasematching technique, a wide set of three-wave mixing process can be addressed. In addition during these years several techniques have been developed in order to fabricate optical waveguide inside the substrate. However CLN suffers from Photo-Refractive Damage (PRD). The resistance to PRD can be improved by doping the lithium-niobate substrates with several dopants and Mangnesium-Oxide doped Lithium-Niobate substrates are the most accessible. Unfortunately, these substrates are less suitable for waveguide fabrication: the titanium indiffused process strongly reduces the benefit of Mg doping, while Annealed Proton Exchange (APE) waveguides show a nonlinear conversion less efficient than that of CLN. Several studies [1] reported that the crystallographic structure of Mg-doped LN crystals is more severely affected by the proton exchange than that of CLN.

An alternative to APE, Soft-Proton Exchange (SPE) [2] allows the increasing of refractive index without degrading the structural properties of the material. Technically SPE consists in a proton exchange performed at higher temperatures in a sealed ampoule with a diluted proton bath. When the proton concentration is sufficiently low, the exchange preserves both the crystal structure and the nonlinear coefficient.

In this work we report about the fabrication of waveguides starting from 5 mol% MgO-doped LN substrates using SPE. Through the measurement of the nonlinear coefficient by means of a scanning-SHG-microscopy setup [3] for different proton concentrations, we identified the threshold below which the original nonlinearity is preserved (see Fig.1(a)). We fabricate two photonic chips consisting of straight waveguides of 6 µm width. Transmission losses have been estimated respectively at 0.1 dB/cm and 0.8 dB/cm. The refractive-index profile is comparable to the one obtained for CLN substrates (see Fig.1(b)). Finally we qualitatively compare the resistance to the PRD between CLN and Mg-doped optical waveguides. Samples have been tested at 30°C by injecting an optical beam generated by a 76-MHz mode-locked laser with picosecond pulses at 710

nm. The total transmitted power is firstly measured with a power meter. Then the output beam is slightly defocalized so that only a portion of the beam is collected in the power meter. If the photorefractive effect takes place, the beam profile is distorted inducing a fluctuation in the power measured at the power meter. Figure 1 (c) compares the normalized optical power, $\frac{P-P_{avg}}{P_{avg}}$, measured by the power meter for the two waveguides. The label for each trace indicates the total power outcoming from the waveguide. Already at 100 µW we observed a strong fluctuations due to PRD in the CLN chip. On the contrary, in the Mg-doped waveguide this effect is still not measurable at 300 µW.

In conclusion, we fabricated for the first time waveguides starting from Mg-doped substrates using the SPE technique. Our results demonstrate that SPE provides clear advantages compared to other techniques to produce efficient and power-resistant nonlinear waveguide in this material.

We thank Prof. Liang Wanguo of the Fujian Institute of Research for providing us the Mg-doped crystals. This work was supported financially by the FP7 program of the European Commission through the Marie Curie ITN Picque project (grant agreement No. 608062), the Agence Nationale de la Recherche through the INQCA project (grant No. PN-II-ID-JRP-RO-FR-2014-0013).

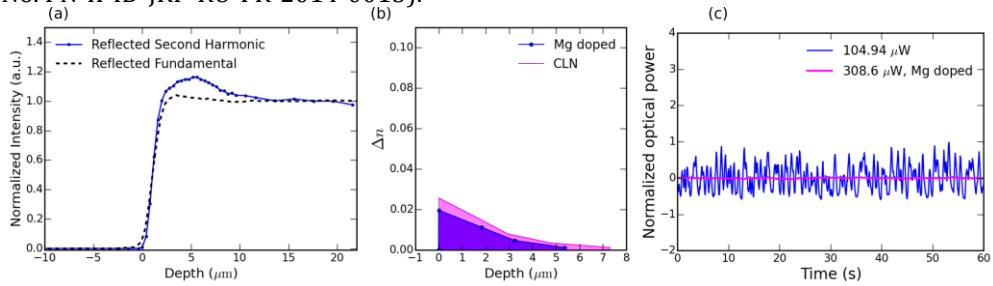


Fig. 1. (a) Reflected fundamental and Second Harmonic intensities versus depth for a slab waveguide based on MgO-doped substrates. (b) Refractive index profile measured at 633 nm for a SPE waveguide fabricated either on a MgO doped LN or on a CLN. (c) Normalized optical power transmitted trough a waveguide fabricated either on a CLN substrate or an Mg-doped substrate. The legend indicates the power outputting from the waveguide. The beam is slighty defocalized to collect only a portion on the power meter. The distortions induced by the PRD are directly translated in power fluctuations. The Mg-doped waveguide (magenta) is clearly more resistant to PRD.

References

[1] J. Sun and C. qing Xu, Journal of Applied Physics 117 (4), 043102 (2015).
[2] L. Chanvillard, P. Aschierri, P. Baldi, D. B. Ostrowsky, M. de Micheli, L. Huang, and D. J. Bamford, Applied Physics Letters 76, 1089 (2000).
[3] H. Åhlfeldt, Journal of Applied Physics 76 (6), 3255-3260 (1994).

Mid-Infrared chemical sensing using a chalcogenide integrated transducer

Aldo GUTIERREZ-ARROYO[1], Loïc BODIOU[1], Jonathan LEMAITRE[1], Emeline BAUDET[2], Marion BAILLIEUL[2], Isabelle HARDY[1], Virginie NAZABAL[2], Joël CHARRIER[1*].

[1]FOTON -UMR-CNRS 6082, ENSSAT BP80518, F-22305 Lannion Cedex, France
[2]ISCR, UMR-CNRS 6226, Glass and Ceramics Team, 35042 Rennes, France
[*] joel.charrier@univ-rennes1.fr

Mid-Infrared (2-20 µm) spectroscopic techniques are widely used to identify chemicals substances, allowing quantitative real-time measurements in gases, liquids and solids. The current trend heads to the miniaturization of optical sensors, replacing bulky laboratory instruments (FTIR, monochromators, ATR etc..) by lab-on-chip devices providing portability, mechanical stability, immunity to electromagnetic noise and the potential for batch production [1]. In recent years, optical integrated devices have been fabricated using different technologies such as GaAs, Si, Si_3N_4 and Ge. Chalcogenide glasses have also emerged as good candidates to manufacture Mid-Infrared photonic integrated circuits thanks to their ability to be deposited as thin films, their broad transparency (up to 20 µm), their potential to be doped with rare earth ions and their refractive index tunability obtained by varying glass composition [2].

In this paper, we present the optical detection of isopropanol solutions by evanescent field in the Mid Infrared using a chalcogenide single-mode ridge waveguide as integrated transducer. The optical absorption of isopropanol at 7.7 µm (Fig. 1) is detected through the variation of the transmitted optical power as a function of analyte concentration.

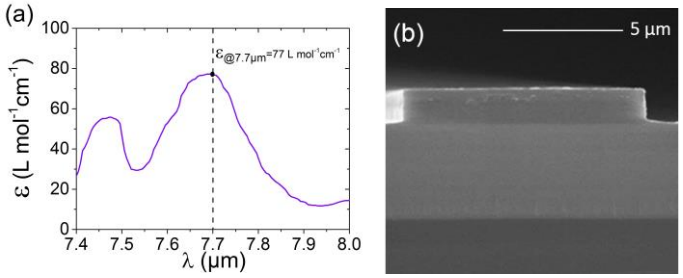


Fig. 1. (a) Molar absorption of isopropanol in the Mid-IR [3]. (b) Cross section of ridge waveguide (SEM image) made of two different compositions of chalcogenide glasses: $Ge_{12.5}Sb_{25}Se_{62.5}$ as guiding layer, $Ge_{28.1}Sb_{6.3}Se_{65.6}$ as confinement layer and the silicon substrate.

Chalcogenide multilayer structures were deposited on a silicon substrate by RF magnetron sputtering and processed as ridge waveguides using standard i-line photolithography and fluorine-based reactive ion etching (Fig. 1b) [2]. Refractive index values of 2.77 and 2.44 have been measured at λ=7.7 µm, respectively, for the guiding ($Ge_{12.5}Sb_{25}Se_{62.5}$) and confinement ($Ge_{28.1}Sb_{6.3}Se_{65.6}$) layers of the integrated transducer.

Optimal dimensions of the single-mode ridge waveguide (width=10 µm and height=1.7 µm) led to an evanescent power factor η=5%. Intrinsic propagation losses α= 2.5 dB/cm were measured by a cutback method from S-shape waveguides [2].
The sensitivity of the device is represented by the variation of output optical power *P* as a function of the solute concentration *C* [1] according to the expression 1.

$$S = \left|\frac{dP}{dC}\right| = \varepsilon\ \eta\ L\ P_0\ \exp\left(-\varepsilon\ \eta\ C\ L\ -\ \alpha_{prop} L\right) \qquad (1)$$

The evolution of the sensitivity *S* as a function of the waveguide length *L* was calculated and plotted in Fig. 2a taking into account the following parameters: ε=77 L mol^{-1}cm^{-1}, η=5 %, α=2.5 dB/cm, P_0= 0.5 mW. From this figure, it can be seen that the maximum transducer sensitivity *S* is obtained for a waveguide length L_{opt} equal to 0.63 cm.
Furthermore, the absorption of isopropanol at 7.7 µm is detected by measuring the attenuation of the transmitted power as a function of the analyte concentration. The performance of the evanescent optical integrated sensor was tested by depositing a droplet of 2 µL of the solution (isopropanol dissolved in cyclohexane) on the ridge waveguide surface. The intensity of guided mode, observed at the output of the waveguide by near-field at λ=7.7 µm, was measured by the Mid-IR camera for several concentrations between 2 and 10 v/v%, the results are displayed in Fig. 2b, 2c.

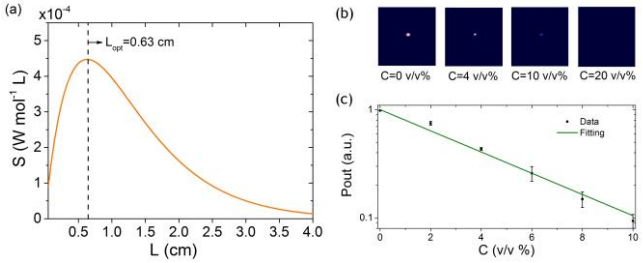


Fig. 2. (a) Evolution of the sensitivity *S* as a function of the waveguide length *L* for α=2.5 dB/cm. (b) Near field intensity of propagated light and (c) transmitted optical power at 7.7 µm for different concentrations of isopropanol.

The optical transmitted power decreases by increasing isopropanol concentration following Beer-Lambert law. These experimental results demonstrating on-chip real-time detection of isopropanol at 7.7 µm could be extended to other substances of interest and represent therefore an outstanding progress in lab-on-chip sensing schemes.

[1] A. Gutierrez-Arroyo, E. Baudet, L. Bodiou, V. Nazabal, E. Rinnert, K. Michel, B. Bureau, F. Colas, J. Charrier, *Theoretical study of an evanescent optical integrated sensor for multipurpose detection of gases and liquids in the Mid-Infrared*, Sens. Actuators B Chem, In press. DOI:10.1016/j.snb.2016.09.173 2017

[2] A. Gutierrez-Arroyo, E. Baudet, L. Bodiou, J. Lemaitre, I. Hardy, F. Faijan, B. Bureau, V. Nazabal, J. Charrier, *Optical characterization at 7.7 µm of an integrated platform based on chalcogenide waveguides for sensing applications in the mid-InfraRed*, Opt. Express, vol. 24, no. 20, pp. 23109-23117, 201

[3] See: *vpl.astro.washington.edu/spectra/allmoleculeslist.htm* for IR absorption cross-sections from PNNL (Last accessed December, 2016)

EUROPEAN CONFERENCE ON INTEGRATED OPTICS

Improving thermal performance of a UTC photodetector in the IMOS platform

Jorn P. VAN ENGELEN*, Longfei SHEN, Yuqing JIAO,
Meint K. SMIT, Jos J.G.M. VAN DER TOL
Photonic Integration Research Group, Eindhoven University of Technology, The Netherlands
* j.p.v.engelen@tue.nl

Recently a uni-traveling carrier photodetector (UTC-PD) with a 3 dB bandwidth beyond 67 GHz was presented [1]. The device shows good performance up to 3 mA of photocurrent but experiences thermal failure (see Fig. 1a) at higher currents due to the poor heat extraction in membrane-type devices. Improvements to the thermal design are proposed that promise to double the possible photocurrent before thermal failure, which makes the performance comparable with state-of-the-art SOI UTC-PDs [2].

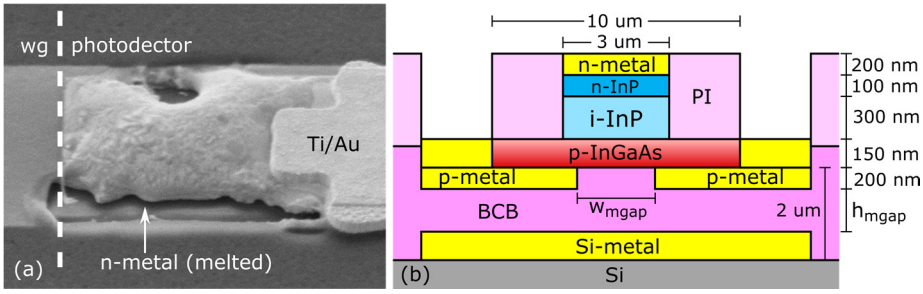


Fig. 1. SEM image (a) of the UTC-PD, the n-metal has melted due to high photocurrent. Schematic cross section (b) of the UTC-PD with the width of the p-metal opening (w_{mgap}) and the thickness of the BCB between the p-metal and Si-metal (h_{mgap}) indicated.

Extracting heat from the InP membrane is difficult as it is surrounded by air on top, and BCB below (see Fig. 1b). Currently the majority of the generated heat is extracted through the p-contacts as they have a large surface area compared to the device. Little heat is extracted through the silicon wafer due to the low thermal conductivity of BCB. The heat extraction through the p-metal can be improved by reducing w_{mgap}. This can be done without increasing the optical loss significantly if a solution like proposed in [3] is used to make low optical loss p-contacts. We can also improve heat extraction through the silicon wafer by replacing part of the BCB with metal, leaving a gap of h_{mgap} between the p-metal and Si-metal. The total thickness is kept the same so that changes to the processing are limited and the optical losses in passive waveguides can be kept low.

Commercial multiphysics simulation software is used to first find the fundamental optical mode in the device, which is used to determine the electron-hold pair generation for the semiconductor simulation. This gives the heat source term in the thermal simulation. Setting the photocurrent at 3 mA, the thermal conductivity to the surroundings is set so that the temperature at the n-metal alloy reaches its melting point of 360 °C. For different adjustments of the device the photocurrent is set again to reach the melting point.

In this way the maximum photocurrent before thermal failure is determined for different values of w_{mgap} and h_{mgap} (Fig. 2). Significant improvement can already be seen when w_{mgap} is reduced by only 500 nm. Introducing metal on top of the silicon also gives significant improvements, doubling the maximum current when the BCB gap is reduced to 10 nm. Choosing $w_{\mathrm{mgap}} = 2.5$ um, $h_{\mathrm{mgap}} = 10$ nm is expected to yield a maximum photocurrent of 7.5 mA. With a responsivity of 0.7 A/W, this leads to an UTC-PD with an optical input power of 10.3 dBm, which is comparable to state-of-the-art in SOI [2].

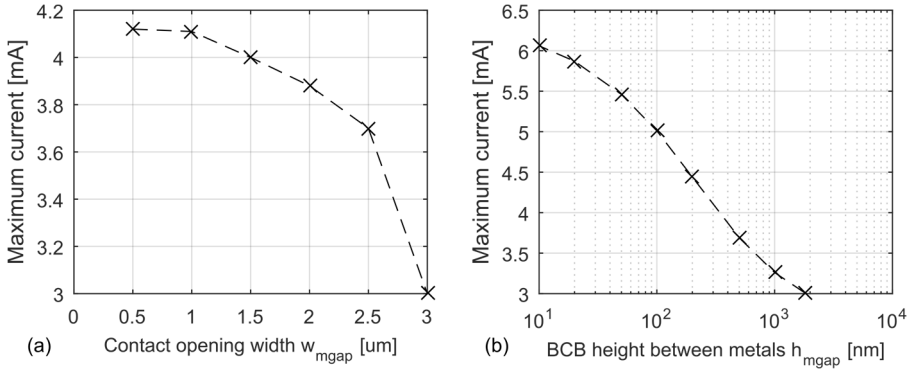


Fig. 2. The maximum current before reaching the temperature at which the top metal contact melts is shown as a function of a) the contact width opening w_{mgap} and b) the BCB height between the p-metal and the metal on top of the silicon.

Other improvements to obtain higher optical input power are 1) increasing responsivity by introducing an electron-block layer at the p-contact, and 2) introducing band-smoothing layers at the p-InGaAs / i-InP interface to operate the device at lower voltage.

We investigated improvements to the thermal design of a UTC-PD. Improving thermal conduction to the silicon wafer by means of a metal bridge doubles the maximum current before thermal failure. These ideas will be usable for other active membrane devices.

References

[1] L. Shen et al., *High-bandwidth uni-traveling carrier waveguide photodetector on an InP-membrane-on-silicon platform*, Optics Express, Vol. 24, No. 8, pp. 8290-8301, 2016

[2] X. Xie et al, *High-Power and High-Speed Heterogeneously Integrated Waveguide-Coupled Photodiodes on Silicon-on-Insulator*, J. of Lightwave Technology, Vol. 34, No. 1, pp. 73-78, 2016

[3] L. Shen et al., *Ohmic contacts with ultra-low optical loss on heavily doped n-type InGaAs and InGaAsP for InP-based photonic membranes*, IEEE Photonics Journal, Vol. 8, No. 1, 2016

Proton Exchanged Waveguides on Congruent Lithium Tantalate and MgO-doped Lithium Tantalate

Getachew T. AYENEW[1], Pascal BALDI[1*], Hervé TRONCHE[1], Florent DOUTRE[1], Marc DE MICHELI[1], Hoda KIANIRAD[2], Fredrik LAURELL[2]

[1]Université Côte d'Azur, CNRS, Institut de Physique de Nice, Parc Valrose, Nice, 06100, France
[2]Applied Physics Department, KTH, AlbaNova, Roslagstullsbacken 21, Stockholm, 106 91, Sweden
* Pascal.Baldi@unice.fr

Introduction: Lithium Tantalate (LT) has a shorter cut-off wavelength than Lithium Niobate (LN) which makes the material attractive for UV generation through nonlinear processes. While congruent LT (CLT) suffers strongly from photorefractive damage, MgO-doped LT (MgO:LT) is an interesting alternative as it was shown on LN that MgO reduces the photorefractive effects. On the other hand, fabricating highly confining, low-loss optical waveguides on LT while preserving its nonlinear properties is still an issue, as it was previously shown that the index variation obtained using proton exchange is one order of magnitude lower than that on LN and that direct Proton Exchange (PE) erases both nonlinear coefficient and periodic domains organization as on LN.

Proton Exchanged Planar Waveguides on CLT: A set of planar waveguides was fabricated on z-cut CLT samples from Crystal Tech and Roditi. As proton sources, we used benzoic acid (BA) melts buffered with amounts of lithium benzoate (LB) $\rho_{LB}=m(LB)/(m(LB)+m(BA))$ ranging from 0.5 to 3.5%. Based on our previous experience on LT [1], all the samples were processed at 330°C following the sealed ampules process. All samples are labelled CLTx.x, x.x referring to ρ_{LB}. The effective indices of the modes of the different waveguides have been measured using a two-prisms coupling technique in order to evaluate their propagation losses and to reconstruct their index profiles. On all the samples we tested, we were not able to observe scattering along the propagation, indicating that the propagation losses are low, typically lower than 1dB/cm according to our previous experience. The index reconstruction consists in using the IWKB method in order to evaluate the shape of the profile and the depth and δn_e of the different layers.

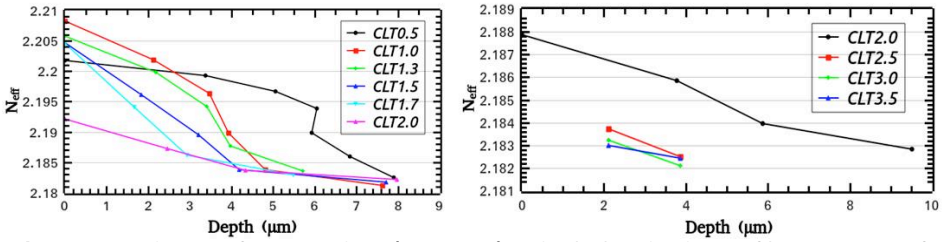


Fig. 1 Extraordinary refractive indices (@ 633nm) and calculated index profiles using IWKB for different ρLB. Waveguides were fabricated at 330°C and for 28hrs (left) and 72hrs (right).

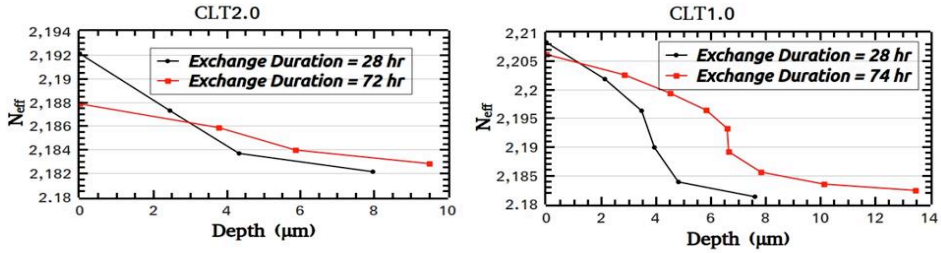


Fig. 2 Effect of the exchange time duration on the extraordinary refractive indices (@ 633nm) and calculated index profiles for 2% (left) and 1% (right) ρLB.

Figures 1 show the effective indices measured @ 633nm and the index profile for different ρ_{LB}. We note that for 2.5, 3.0 and 3.5% there are only two modes. According to [1] 3.5% should be SPE while those from 0.5 to 3.0% should be in the PE_{II} phase. The 2% seems particular as its surface index variation, while much larger than those obtained on SPE, is very different from the other PE_{II}. Figure 2 shows the effect of the exchange time duration on the index profile. While for CLT1.0, which exhibits a clear step-like profile near the surface, the depth is increased with time, CLT2.0 more likely seems to be annealed by the longer exchange duration. Focusing on ρ_{LB}=2%, the reproducibility was tested by fabricating three different samples in the same conditions and the measured effective indices were well in the measurements error bars. The local value of the second-order nonlinear coefficient was probed by SHG microscopy using the experimental set-up described in our previous works [2]. Figures 3 clearly show that 2% conserves the nonlinear coefficient in contrary to 1.7%. The 2% PE CLT planar waveguide more likely corresponds to the HiSoPE as already obtained on LN and is very attractive as it allows a relative good confinement while preserving the nonlinear properties [3].

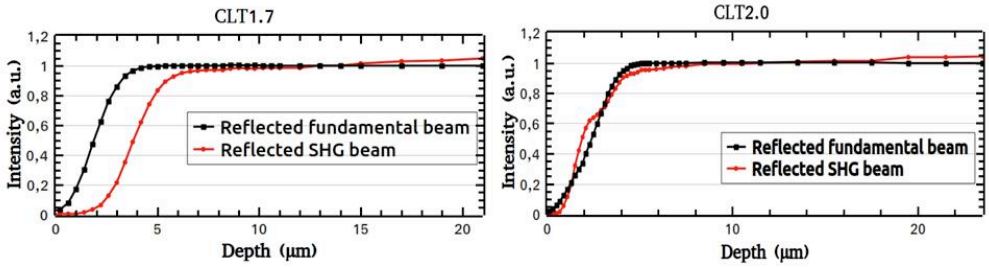


Fig. 3 Surface SHG for 1.7% (left) and 2% (right) ρ_{LB}. The superposition of SHG and IR signals (right) indicates that the nonlinear coefficient is preserved into the waveguide.

Proton Exchanged Channel Waveguides on CLT: Channel waveguides were processed using 2% LB for 28hrs at 330°C. At 1550nm, the resulting single-mode waveguides exhibit total insertion losses between two SMF28 fibres in a consistent 20 to 25% range. We also checked if hybrid modes were present or not and as expected no polarization conversion process was observed in contrary to LN [3] due to the positive birefringence of LT compared to the negative birefringence of LN. It thus seems that it is possible to obtain channel waveguides on CLT with good quality, good confinement and preserved nonlinear coefficient. We have now to study the effect of the PE process on poled CLT but we already started the study of PE exchanged planar waveguides on MgO:LT.

Proton Exchanged Planar Waveguides on 8% MgO:LT: We have started a similar study on 8% MgO:LT from Roditi. Figure 4 shows the effective indices measured @ 633nm and the index profile for ρ_{LB}=2% after 72hrs at 330°C. The comparison with Figure 2 indicates that MgO tends to slightly decrease the index variation. Similar results have been obtained for 1.0 and 1.5% and work is in progress to complete the study.

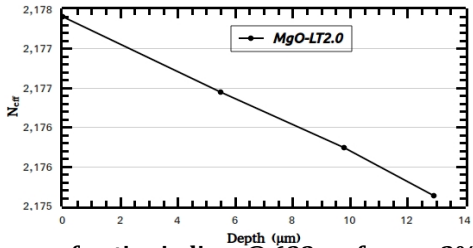


Fig. 4 Extraordinary refractive indices @ 633nm for ρ_{LB}=2% after 72hrs at 330°C.

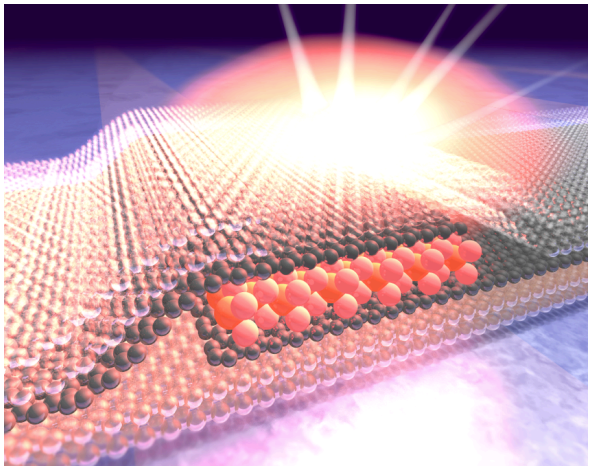
References

[1] V. Rastogi *et al.*, *Effect of proton exchange…*, Optical Materials, vol. 15, pp. 27-32, 2000
[2] K. El Hadi *et al.*, *Quasi-phase-matched…*, JOSA B, vol. 14, no. 11, pp. 3197-3203, 1997
[3] O. Stepanenko *et al.*, *Crystallographic and Optical…*, JLT, vol. 34, no. 9, pp. 2206-2212, 2016

Graphene opto-electronics for data communication, image sensing and plasmonics

Frank Koppens[1,2]
[1]*Institute of Science and Technology, 08860 Castelldefels (Barcelona), Spain*
[2]*ICREA – Institució Catalana de Recerça i Estudis Avancats, Barcelona, Spain.*
Frank.koppens@icfo.eu

Electrical control and detection of light and polaritons are at the heart of nano-photonics and opto-electronics. Two-dimensional materials have emerged as a toolbox for in-situ control of a wide range of polaritons: plasmons, excitons and phonons [1]. By stacking these materials on top of each other, heterostructures of these materials can be controlled at atomic scale, with extremely high quality and clean interfaces. In this talk, we will show several examples of 2d material heterostructure devices with novel ways of exciting, controlling and detecting polaritons [2,3].



We also show various types of ultra-fast and highly efficient photodetectors [4] and modulators for data communications applications. Graphene device promise a broadband response, high switching rates, small footprint and CMOS compatibility.

Finally, we show for the first time the monolithic integration of a CMOS integrated circuit with graphene, operating as a high mobility phototransistor. We demonstrate a high-resolution image sensor and operate it as a digital camera. 99.8% of the graphene pixels in the image sensor was successfully integrated with the read-out circuitry. The graphene was sensitized with colloidal quantum dots that make it sensitive to UV, visible and infrared light (300 – 2000 nm) [5].

References

[1] Polaritons in layered two-dimensional materials. Low et al., Nature Materials (2016).

[2] Thermoelectric detection and imaging of propagating graphene plasmons. Lundeberg et al., Nature Materials (2016)
[3] Ultra-confined acoustic THz graphene plasmons revealed by photocurrent nanoscopy. Alonso-Gonzalez et al., Nature Nanotechnology (2016)
[4] High-Responsivity Graphene–Boron Nitride Photodetector and Autocorrelator in a Silicon Photonic Integrated Circuit. Ren-Jye Shiue et al. Nano Letters, 15 (11), 2015.
[5] Image sensor array based on graphene-CMOS integration. Goossens et al., ArXiv 1701.03242 (2016).

The Germanium Zener-Emitter for Silicon Photonics

Roman Koerner,* Daniel Schwarz, Caterina Clausen, Michael Oehme, Inga A. Fischer, and Joerg Schulze
Institute of Semiconductor Engineering, University of Stuttgart
Pfaffenwaldring 47, Stuttgart, 70569 Germany.
*Email: koerner@iht.uni-stuttgart.de

Si-Photonic transceivers are classified by their operating wavelength, power consumption and integration in Si to sustain cost-effectiveness. Applying Ge as optical active material in a Zener-Emitter structure, has proven to provide a competitive solution for the integrated semiconductor optical amplifier (SOA) on Si [1].

We further exploit the usage of a Ge Zener tunnel diode for electrical pumping (Fig. 1), to achieve population inversion and stimulated emission in an indirect semiconductor material at room temperature by direct Zener band-to-band tunneling (BTBT) [2] (Fig. 2).

We conclude to present electrical pumped lasing in a 1 mm waveguide at 90 mA (5 kA/cm^2) and for the first time mono-mode lasing in a 3.2 mm waveguide at 110 mA (60 kA/cm^2) with maximum output power of the SOA of 1.65 mW (Fig. 3).

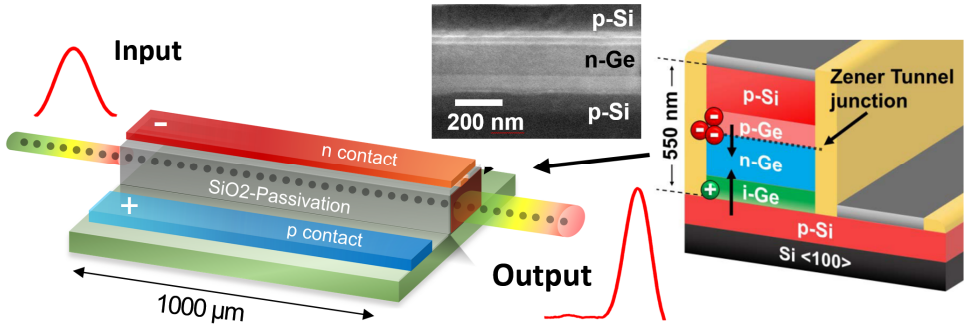


Fig. 1. (left) Two-terminal Zener-Emitter formed by cleaving the rip-waveguide. (middle) SEM-image of the Si-Ge-Si heterostructure with strained relaxed Ge by a SiGe virtual substrate. (right) MBE-Layer sequence with the Zener p-n tunnel diode for electron pumping and p-i-n diode for hole injection. The device provides complete state-of-the-art CMOS process integration by 550 nm device layer thickness.

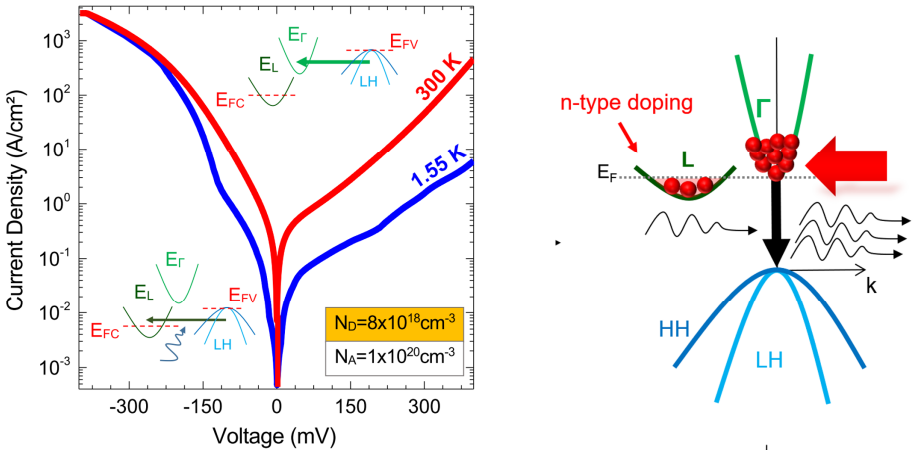


Fig. 2. (left) Ge tunnel diode for direct Zener-BTBT injection. The direct onset is visible by a small kink under reverse bias. (right) Schematic Ge bandstructure with tunnel injection and n-type doping. Stimulated emission is possible with wavelength defined by doping.

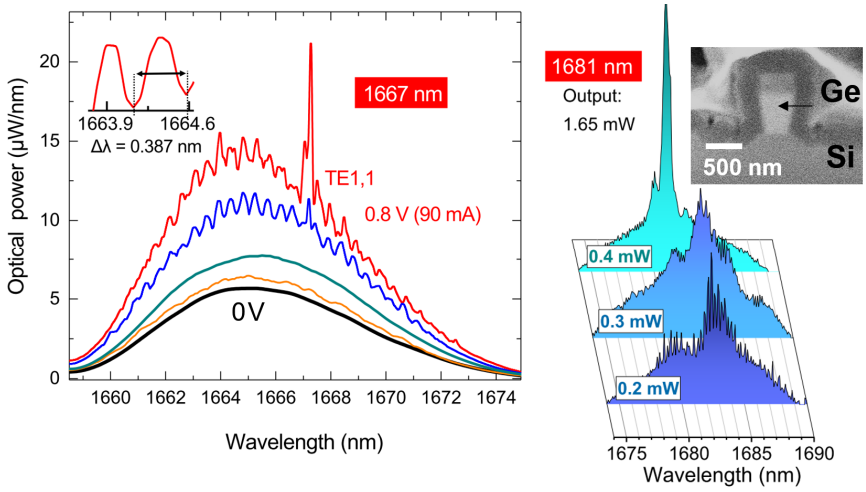


Fig. 3. (left) Optical amplification by the Zener-Emitter under electrical pumping. (right) Mono-mode lasing at 0.4 mW optical signal input, 110 mA electrical pumping (3.2 mm length) and 1.65 mW output power at room temperature.

The authors gratefully acknowledge the funding by DFG Grants no. OE 520/5-1, KI 561/5 and FI 1511/2-1.

References

[1] R. Koerner et al., *The Zener-Emitter: A Novel Superluminescent Ge Optical Waveguide-Amplifier with 4.7 dB Gain at 92 mA Based on Free-Carrier Modulation by Direct Zener Tunneling Monolithically Integrated on Si*, in Proceedings of the International Electron Devices Meeting (IEDM), pp. 22.5, 2016.

[2] K.-H. Kao et al., *Direct and Indirect Band-to-Band Tunneling in Germanium-Based TFETs*, IEEE Transactions on Electron Devices, vol. 59, no. 2, pp. 292–301, 2012.



Hybrid integration of carbon nanotubes in silicon photonic resonators

Elena DURAN-VALDEIGLESIAS[1*], Weiwei ZHANG[1], Carlos ALONSO-RAMOS[1], Xavier LE ROUX[1], Samuel SERNA[1], Thi-Hong-Cam HOANG[1], Matteo BALESTRIERI[2], Delphine MARRIS-MORINI[1], Eric CASSAN[1], Francesca INTONTI[2], Francesco SARTI[2], Niccolò CASELLI[2], Federico LA CHINA[2], Massimo GURIOLI[2], Arianna FILORAMO[3], Laurent VIVIEN[1]

[1] Centre de Nanosciences et de Nanotechnologies, Univ. Paris Sud, CNRS, Université Paris Saclay, 91405 Orsay, France

[2] Department of Physics, University of Florence European Laboratory for Non-linear Spectroscopy, 50019 Sesto Fiorentino (FI), Italy

[3] LICSEN, NIMBE, CEA, CNRS, Université Paris-Saclay, CEA Saclay 91191 Gif-sur-Yvette Cedex, France

[*] elena.duran@u-psud.fr

On-chip integration of all photonic components in the silicon platform is an important goal to accomplish high efficiency, low energy consumption, low cost and device miniaturization. However, silicon does not have efficient light emission or detection in the telecommunication wavelength range (close to 1.3µm and 1.55µm). Hence, hybrid integration of III-V materials or germanium is commonly adopted for the implementation of lasers and photodetectors. Nevertheless, these heterogeneous integration schemes compromise the low cost of using silicon [1].

Carbon nanotubes (CNTs) have recently been proposed as an attractive one-dimensional light emitting material [2]. Interestingly, semiconducting single wall carbon nanotubes (SWNTs) are a versatile material with room temperature light detection and emission in the near-infrared. SWNTs also exhibit intrinsic room temperature optical gain [3], which makes them a very interesting candidate for the realization of lasers in Si photonics. In addition, SWNTs have shown compatibility with Si CMOS process. Furthermore, recent advances in polymer-assisted selection of semiconducting SWNT and deposition techniques, poise this solution-processed approach to deliver a high quality material produced at large volumes and low cost.

Here, we report on the development of a new integration scheme to couple the light emission from SWNTs into Si photonic resonators. In this scheme, Si structures are protected with an HSQ (Hydrogen Silses Quioxane) layer, defining specific interaction regions, and polymer-sorted SWNTs are drop casted on top. The SWNT photo-luminescence (PL) enhancement achievable in a micro-ring resonator is directly proportional to the overlap between the SWNTs layer and the evanescent field of the waveguide mode and inversely proportional to the propagation loss [4, 5]. By defining small interaction windows with the size of the illumination spot of our Ti:Sapphire pump, we ensure that all SWNTs in contact with the waveguide are excited. This way

we obviate unwanted absorption arising from non-excited SWNTs, thereby improving the emission enhancement in our Si micro-ring resonators.

As an illustrative example, Fig. 1 shows the collected PL spectrum for two Si micro-resonators, one with the interaction window in the ring-to-bus coupling region (blue line and SEM on the left), and another with the interaction region within the ring (green line and SEM on the right). The micro-ring with the interaction window in the ring-to-bus coupling region exhibits two wideband lobes, around 1.2μm and 1.3μm wavelength, that correspond with the emission of our polymer-sorted SWNTs solution [6]. On top of this emission, we observe a set of remarkably sharp resonance enhancement peaks produced in the Si micro-ring. Interestingly, when we place the interaction window within the ring is possible to remove the SWNT background emission, substantially improving the signal-to-noise ratio.

These results pave the way for the realization of integrated sources with high spectral purity operating within the O Datacom band, based on the combination of SWNTs and Si micro-resonators.

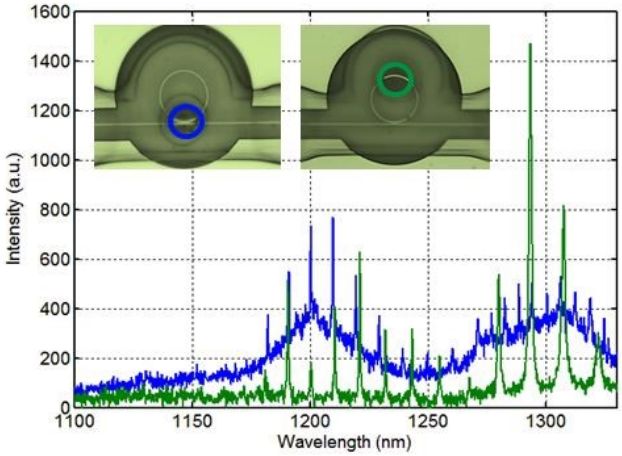


Fig. 1. PL intensity as a function of the wavelength for two different scenarios. In blue line when the interaction region is in the coupler between ring and bus waveguide. In green line when the interaction area is placed within the ring.

This work has been supported by the European project FET CARTOON.

References

[1] Vivien, L. and Pavesi, L., *Handbook of silicon photonics*, Taylor & Francis, 2013.
[2] Saito, R., Dresselhaus, G. and Dresselhaus, M. S., *Physical Properties of Carbon Nanotubes*, Imperial College Press, 1998.
[3] Gaufrès, E., Izard, N., Le Roux, X., Marris-Morini, D., Kazaoui, S., Cassan, E. and Vivien, L., *Optical gain in carbon nanotubes*, Appl. Phys. Lett. Vol. 96, no. 23, pp. 231105-231108, 2010.
[4] Noury, A., Le Roux, X., Vivien, L., and Izard, N., *Controlling carbon nanotube photoluminescence using silicon microring resonators*, Nanotechnology, Vol. 25, no. 21, pp. 215201, 2014.
[5] Noury, A., Le Roux, X., Vivien, L., and Izard, N., *Enhanced light emission from carbon nanotubes integrated in silicon micro-resonator*, Nanotechnology, Vol. 26, no. 34, p. 345201, 2015.
[6] Izard, N., Kazaoui, S., Hata, K., Okazaki, T., Saito, T., Iijima, S., and Minami, N., *Semiconductor-enriched single wall carbon nanotube networks applied to field effect transistors*, Appl. Phys. Lett., Vol. 92, no. 24, p. 243112, 2008.

Integrated magneto-plasmonics for non-reciprocal optical devices

Giovanni MAGNO, Vy YAM, Béatrice DAGENS*
C2N, Orsay site, Université Paris-Sud, bâtiment 220, 91405 Orsay cedex, France
*beatrice.dagens@c2n.upsaclay.fr

Integration of optical isolators and circulators has remained for many years a crucial technological issue which makes difficult the insertion of active components in photonic circuits (PICs). More generally, use of non-reciprocal (NR) transmission in photonic systems could considerably enrich possible architectures. The design of optical guided structure with NR functionality requires simultaneous spatial and time-reversal symmetry breakings in the waveguide (WG). Whereas spatial symmetry breaking is easy to obtain by suitable geometrical design, time-symmetry breaking requires non-linear interaction of the propagative wave with the medium. Magneto-optical materials can provide this non-linearity. Especially the transverse magneto-optical Kerr effect (TMOKE) is well-adapted to guiding configurations and thus to integration in PICs. The main magneto-optical materials exploited for TMOKE induced non-reciprocal transmission at telecom wavelengths are garnet oxides like Bi or Ce substituted Ytrium iron garnets (Bi:YIG, Ce:YIG), and ferromagnetic metals like FeCo.

Garnet interferometer lead to the demonstration of 21 dB of isolation at 1550nm in a nonreciprocal SOI device made of a directly wafer bonded Ce-YIG bulk layer [1], with a large footprint. For miniaturization, MO strength can be enhanced using the light confinement and deceleration concepts from garnet photonic crystal [2,3]. A fundamentally different approach consists in using metallic MO cladding layers, like FeCo, and exploit the imaginary part of the TMOKE effect, i.e. the non-reciprocal dichroic loss [4,5]. A TM semiconductor optical amplifier including 50 nm thick FeCo layer deposited on WG, reached isolation ratio of 12 dB without insertion losses [6]. However, the compromise between metal induced losses and TMOKE strength (related to mode confinement in FeCo layer) was never really solved, to reach application compatible performance. One aspect of this work was the special role played by the surface plasmon polariton (SPP) excitation at the ferromagnetic metal interface which causes a concentration of the light near the magneto-optically active interface.

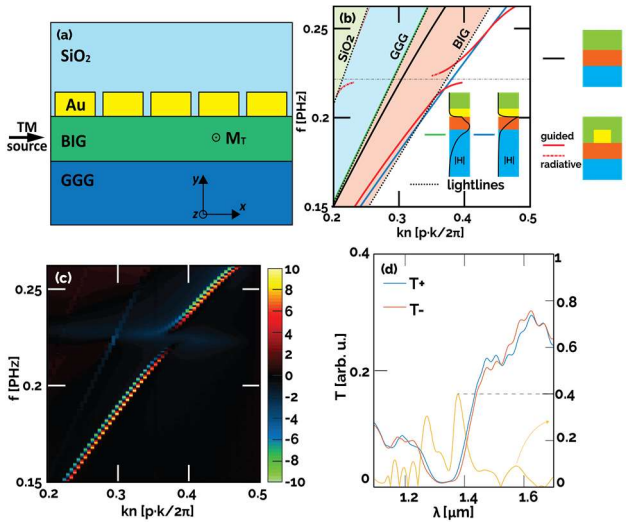


Fig. 1. (a) 1D periodic Au grating on BIG waveguide covered by SiO_2. (b) FDTD calculated band structure of the magneto-plasmonic. (c) Superposition of band structures for $+M_T^{sat}$ and $-M_T^{sat}$. (d) WG transmittance T and isolation ratio parameter Δ.

With the same idea, huge enhancement of TMOKE with a metallic grating on a MO substrate [7] was demonstrated, in non-guided structures. One significant improvement with respect to the use of FeCo layer comes from the separation here of plasmonic and

MO effects in two different materials (plasmonic metal and MO oxide), allowing the mode energy concentration in the MO and less lossy one. More recently, sign inversion of the non-reciprocal dichroism for a given magnetization direction was also obtained with gold grating deposited on MO garnet thick layer [8], by only grating shape modification. Sign inversion is induced by resonant modes coupling involving both the Fabry-Perot (FP) mode generated in the grating slits, and the SPP mode at the garnet/Au interface, and could be suitably used in a push-pull configuration.

This property is the starting point for a renewal of the integrated isolator design. In this paper we propose to extend it to the TM waveguide configuration with a 1D periodic Au grating on BIG (Bismuth Iron Garnet) waveguide in TMOKE configuration (Fig. 1(a)).

The optical response of the waveguide has been calculated using commercial software based on finite difference time domain (FDTD) method extended to the instance of gyrotropic materials. The magnetic film permittivity tensor has the following non zero components: $\varepsilon_{xx} = \varepsilon_{yy} = \varepsilon_{zz} = 2.51^2$ and $\varepsilon_{xy} = -\varepsilon_{yx} = ig(M_T)$, where $g(M_T)$ is the gyrotropy of the BIG material. BIG dispersion is negligible in the study wavelength range and $g(M_T^{sat}) = 0.1$ at the saturation magnetization [9]. The gold permittivity is described by a Drude model fitting of ellipsometric data. The non-MO GGG substrate and the SiO_2 superstrate permittivities are equal to 1.97^2 and 1.45^2, respectively.

Figure 1(b) represents the band diagram of the proposed structure when the height, period and slits of the grating respectively are h =130 nm, p = 200 nm and s = 20 nm. The grating period is shorter than the 1rst order Bragg condition in order to avoid back reflection. Dash-dotted black lines correspond to BIG, GGG and SiO_2 lightlines. Full and dash-dotted red curves correspond to dispersion curves of the magneto-plasmonic WG. The presence of 1D periodic slits of 20 nm in the gold film introduces the formation of a bandgap at 1.33 µm. This bandgap is attributed to the coupling between Fabry-Perot like slits modes (independent of the waveguide mode k-vector) and the SPP mode (interrupted by the grating slits) related to the blue dispersion curve. Fig. 1(c) presents the superimposition of the band structures for $+M_T^{sat}$ and $-M_T^{sat}$. We clearly observe a shift of the SPP dispersion curves, which highlights the existence of a difference between the wave vectors for waves propagating in forward and backward directions. The corresponding WG transmittances T^+ and T^- are represented in Fig. 1(d), together with the isolation parameter $\Delta = abs(T^+ - T^-)/\max(T^+, T^-)$. Two maxima can be distinguished at 1.38 µm, and 1.27 µm on the Δ curve. This shows that, for this specific grating geometry, the NR transmission is enhanced in the vicinity of the bandgap.

To conclude, we have numerically shown that when a magneto-optical bismuth iron garnet waveguide is coupled to a gold grating on its top, surface plasmon polaritons may strongly enhance transverse magnetic-optical Kerr effect especially when guided modes interact with grating slit modes. The TMOKE effect can be tuned by optimization of grating geometry and opens the prospect of achieving an improved integrated isolator.

This work was partially funded by Optoelectronic and Photonic chair of Paris-Sud University, supported by PSA.

References

[1] Y. Shoji et al. Appl. Phys. Lett., 92 (2008).
[2] M. Vanwolleghem et al, Physical Review Rapid Comm., Vol.80, No.12, 121102(R), 2009
[3] W. Smigaj, et al, Optics Letters, 35 (4), pp 568-570, 2010
[4] M. Takenaka, et al. in Proc. 11th IPRM, Davos, Switzerland, pp. 298-292 (1999)
[5] W. Zaets et al. IEEE Photon. Technol. Lett., 11(8), pp.1012-1014 (1999)
[6] W. Van Parys et al, Appl. Phys. Lett., 88, 071115 (2006)
[7] V. I. Belotelov et al. (PIERS 2009), Moscow, Russia, 18-21 August 2009
[8] L. Halagacka et al, Optics Express Vol. 21, Iss. 19, pp. 21741–21755 (2013)
[9] B. Vertruyen, et al, Phys. Rev. B 78, 094429 (2008)

EUROPEAN CONFERENCE ON INTEGRATED OPTICS

Novel Sampled Grating Design for High Precision, Multiple Wavelength DFB Laser Arrays

Song TANG[1], Lianping HOU[1], Iain EDDIE[2], Xiangfei CHEN[3], John H. MARSH[1*]
[1]University of Glasgow, School of Engineering, Glasgow, G12 8QQ, U.K.
[2]CST Global Ltd., 4 Stanley Blvd, Blantyre, Glasgow, G72 0BN U.K.
[3]Nanjing University, College of Engineering and Applied Sciences, Nanjing, 210093, China
[*]john.marsh@glasgow.ac.uk

Distributed feedback (DFB) semiconductor laser arrays are important components for wavelength division multiplexing networks. Recently, the reconstruction-equivalent-chirp (REC) technique, based on sampled Bragg gratings (SBGs), has been applied to DFB laser arrays to give precise wavelength control [1]. Rather than operating at the 0^{th}-order reflection of the Bragg grating, the lasers make use of either the $+1^{st}$- or -1^{st}-order reflections. However, the effective coupling coefficient, κ, of a sampled grating is reduced substantially from that of a uniform grating, because of the reduced duty cycle of the grating and because the effective index modulation seen by $\pm1^{st}$-order reflections is only $1/\pi$ times that of the 0^{th}-order reflection. To overcome this, designs of SBGs with phase shifted grating sections have been proposed and demonstrated in fibre lasers. In these structures, the (not required) 0^{th}-order mode is suppressed while the index modulation experienced by reflection orders is enhanced [2]. Here we have designed gratings using the REC technique with π-phase shifted gratings for DFB diode lasers.

The device layout, fabricated devices and a fabricated grating are shown in Fig. 1. Three different gratings were studied: a uniform 0^{th}-order grating, a conventional SBG (C-SBG), and a π-phase shifted SBG (PPS-SBG) shown in Figures 2(a), (b), (c) respectively. The largest κ for a C-SBG is obtained with a duty cycle of 0.5, which reduces the effective κ of the $\pm1^{st}$-order reflections by a factor of π relative to that of the 0^{th}-order refection from a uniform grating [2]. The effective κ of the $\pm1^{st}$-order reflections from the PPS-SBG should therefore be $2/\pi$ times that of a uniform grating.

For the uniform 0^{th}-order gratings, the period was 243 nm; for the SBG structures, the grating and sampling periods were 260 nm and 3.712 μm respectively. Figure 3(a) shows the spectrum just below threshold for the three structures of Fig.2; the stop bands can be clearly seen and their widths are listed in Table 1. Also shown in Table 1 are the stop band widths, calculated using a simple transfer matrix approach, for uniform passive waveguides for three different values of κ (Fig. 3(b)). Stop bands of active structures are significantly smaller than for passive waveguides because of the effect of the laser gain. In order to relate the measurements on active devices with the modelling results for passive waveguides, we have calculated the ratio of the stop bands for active and passive structures and shown it is almost constant (0.6 ± 0.03). Based on this simple approach, we conclude the effective coupling coefficients are

approximately in the expected ratios of 1 : 1/π : 2/π for uniform : C-SBG : PPS-SBG.

We have also fabricated an eight-wavelength laser array using PPS-SBG whose lasing spectra are shown in Fig. 3(c). The channel spacing is designed to be 100 GHz. By linear fitting, the average wavelength spacing is 0.837 nm with a residual of 0.059 nm.

Table 1. Properties of modelled and measured gratings

Grating type	C-SBG	PPS-SBG	Uniform
Measured stop band / nm	0.405	0.454	0.475
Uniform grating equivalent κ / cm^{-1}	7.4	14.8	23.2
Uniform grating passive stop band / nm	0.645	0.719	0.835
Ratio of {measured/passive stop band}	0.63	0.63	0.57

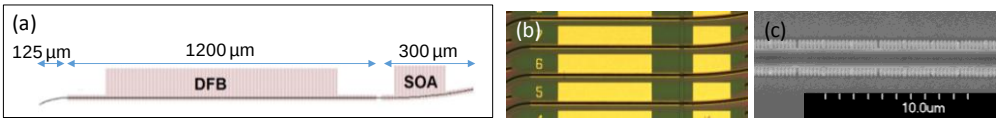


Fig. 1. (a) Device schematic, (b) micrograph of fabricated device, and (c) π-phase shifted sampled Bragg grating (PPS-SBG) in DFB section.

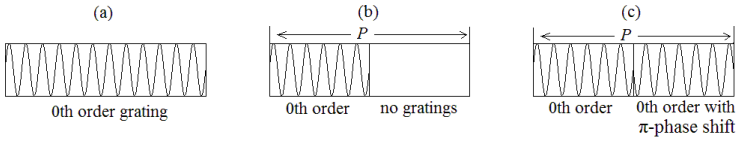


Fig. 2. Grating structures of (a) uniform 0th order grating (b) conventional sampled Bragg grating (C-SBG) (c) π-phase-shifted SBG (PPS-SBG). *P* is the sampling period.

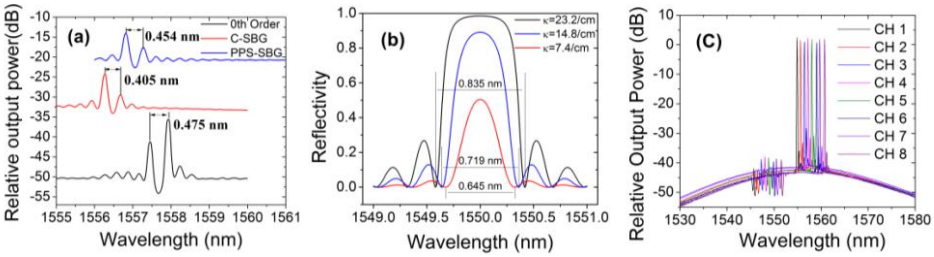


Fig. 3. (a) Spectra of lasers just below threshold (50 mA) with uniform 0th order grating, C-SBG, and PPS-SBG, (b) calculated stop bands of passive laser waveguides, and (c) optical spectra of the laser array.

References

[1] Y. Shi, S. Li, X. Chen, L. Li, J. Li, T. Zhang, J. Zheng, Y. Zhang, S. Tang, L. Hou, J. H. Marsh, B. Qiu, *High channel count and high precision channel spacing multi-wavelength laser array for future PICs*, Scientific Reports, vol. 4, article 7377,2014

[2] J. Li, Y. Cheng, Z. Yin, L. Jia, X. Chen, S. Liu, S. Li and Y. Lu, *A multiexposure technology for sampled Bragg gratings and its applications in dual-wavelength lasing generation and OCDMA en/decoding*, IEEE Photon. Technol. Lett., vol. 21, pp. 1639-1641, 2009

[3] L. Hou, M. Haji, J. Akbar, J. H. Marsh, and A. C. Bryce, *AlGaInAs/InP monolithically integrated DFB laser array*, IEEE J. Quantum Electron., vol. 48, pp. 137-143, 2012

Tunable Deeply Etched V-notch Reflectors

Mohamad Dernaika[1,2*], Ludovic Caro[1,3], Niall P. Kelly[1,3], Maryam Shayesteh[1] and Frank H. Peters[1,3]

[1]Tyndall National Institute, Lee Maltings, Cork, Ireland
[2]Departement of Electrical and Electronic Engineering, University College Cork, College Road, Cork, Ireland
[3]Physics Department, University College Cork, College Road, Cork, Ireland
* Mohamad.dernaika@tyndall.ie

Monolithically integrated and tunable semiconductor lasers are of great interest for dense wavelength division multiplexing (DWDM) and conventional (WDM) networks. Distributed Bragg reflector and Distributed feedback lasers have demonstrated excellent performance in terms of supplying a single mode output with high stability. However, Bragg based lasers require high resolution lithography and multiple epitaxial growth steps, which adds to the fabrication complexity, time and cost.

Regrowth free, monolithically integrated single mode lasers that use standard UV lithography with relatively simple fabrication processes have drawn a lot of interest. One such laser is the slotted Fabry Perot (SFP) [1], which exploits mini inter-cavity reflections by using index perturbation along the ridge in a form of slots. Also, slots can be used as mirrors to create a monolithically integrated facet-less or single-facet lasers [2,3]. A single slot etched just above the active region provide a maximum of around 2-3% reflection. Therefore, to create sufficient reflection to replace a cleaved facet, 9 slots are often used to build an effective mirror [2]. For example, to achieve a facet-less SFP laser with a 400 GHz discrete tuning step requires 2 mirrors each, with a length of approximately 900 μm.

A limitation of the slot is that its reflection is highly sensitive to the etch depth [4], and this reflection strength governs both the laser performance and the consistency across the wafer. Therefore, a wet etch is often used in conjunction with a dry etch to reach the intended depth. The effect of crystal orientation on the wet chemical etching [5] limits the cavity design flexibility across the chip.

In this paper, we demonstrate a novel V-notch reflector that uses lithography to control reflectance instead of depth. Moreover, by lithographically manipulating the V-notch dimensions, flexible control over the reflected power and loss is possible. The deeply etched V-notch reflector overcome the depth sensitivity of the slot, allowing various reflection options without the need of additional fabrication steps, accurate depth control or a wet etch. Fig.1 show an illustration and a SEM image of the V-notch

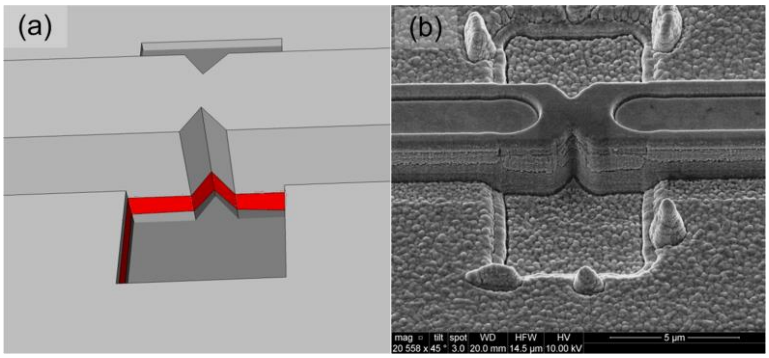
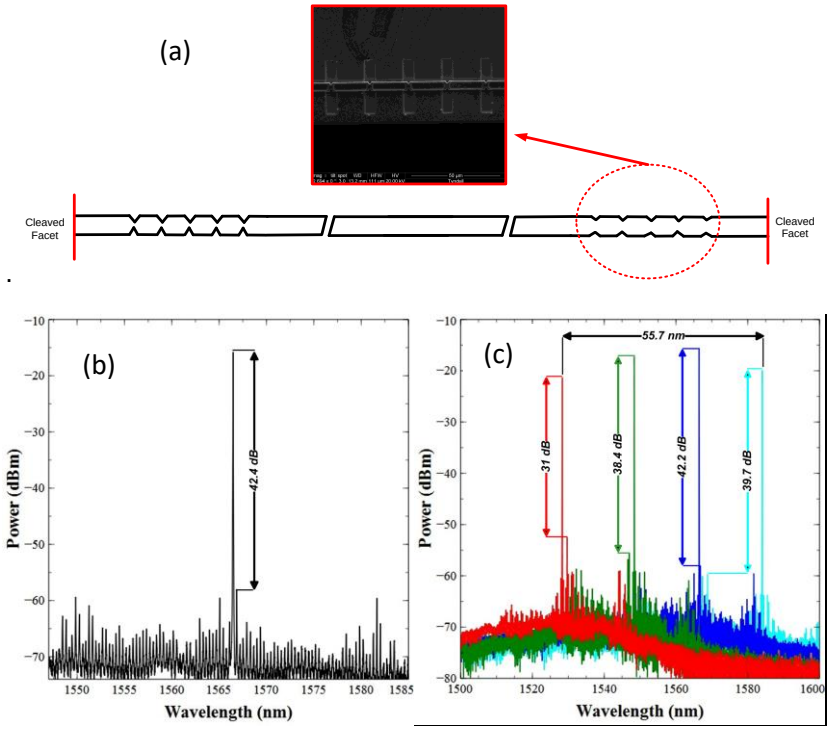


Fig.1 (a)V-notch illustration showing the active region in red(b) V-notch SEM

These lithographically controlled V-notches can be valuable in generic fabrication foundries where the depth options are limited or only deep etch ridges are used. Some of the V-notch structures have higher reflectivities than the slots, which reduces the mirror size compared to the slotted mirrors used in conventional SFP. By measuring the modulation depth and L-I curves of various V notch structures it was possible to estimate their reflection and loss. Simulation results using commercial Eigen mode expansion (EEM) software ModePROP from RSOFT agrees well with the experimental data. Finally, a V-notch laser cavity that exhibits an SMSR up to 42 dB and tuning range across 55 nm using V-notch with various dimensions will be presented (Fig.2)



Fig,2 (a)cavity Design (b) single mode with a SMSR of 42.4 dB (c) Tuning across 55.7 nm with SMSR>31 dB

References

[1] C. Herbert, D. Jones, A. Kaszubowska-Anandarajah, B. Kelly, M. Rensing, J. O'Carroll, R. Phelan, P. Anandarajah, P. Perry, J. O'Gorman et al., "Discrete mode lasers for communication applications," IET optoelectronics, vol. 3, no. 1, pp. 1–17, 2009.

[2] D. C. Byrne, J. P. Engelstaedter, W.-H. Guo, Q. Y. Lu, B. Corbett, B. Roycroft, J. O'Callaghan, F. Peters, and J. F. Donegan, "Discretely tunable semiconductor lasers suitable for photonic integration," IEEE Journal of Selected Topics in Quantum Electronics, vol. 15, no. 3, pp. 482–487, 2009.

[3] Yang, Hua, et al. "Monolithic integration of single facet slotted laser, SOA, and MMI coupler." IEEE Photonics Technology Letters 25.3 (2013): 257-260.

[4] Q. Lu, W. Guo, R. Phelan, D. Byrne, J. Donegan, P. Lambkin, and B. Corbett, "Analysis of slot characteristics in slotted single-mode semiconductor lasers using the 2-d scattering matrix method," IEEE photonics technology letters, vol. 18, no. 24, pp. 2605–2607, 2006.

[5] N. Siwak, X. Fan, and R. Ghodssi, "Fabrication challenges for indium phosphide microsystems," Journal of Micromechanics and Microengineering, vol. 25, no. 4, p. 043001, 2015

EUROPEAN CONFERENCE ON INTEGRATED OPTICS

Latest Developments in Low-Cost Integrated WDM Transceivers for Telecom Applications

Karen SOLIS-TRAPALA[1*], Boudewijn DOCTER[1]
[1]Effect Photonics, Torenallee 20, Eindhoven, 5617 BC, The Netherlands
[*] karensolis@effectphotonics.nl

The need to support the ever-increasing data traffic demands has accelerated the development of the underlying network technology. Pluggable transceivers have now become a norm and industry has acknowledged that Photonic Integration, regardless of the material platform, is vital to the continuous scaling of optical networks. Indium phosphide (InP) based photonic integrated circuit (PIC) technology offers high performance and cost advantages when applied in Dense Wavelength Division Multiplexing–(DWDM) long haul communication systems [1] - both in highly parallel systems as well as in single wavelength, high bit-rate systems. However, for short and medium reach applications, the cost and integration challenges become increasingly stringent. In this paper, we review technology aspects and trade-offs for the application of InP-based PICs in mid-range (10-100 km) pluggable transceivers. Latest results on integrated high-speed modulators will be presented, together with the innovations that are required to cost-effectively apply PIC technology into commercial products.

The fact that the main optical system components (lasers, modulators, (de-)multiplexers, and photodetectors) can all be made in different alloys of InP makes this integration platform highly attractive. A whole system can be monolithically integrated on a chip, including wavelength locking, power monitoring and equalization; we therefore call this System-on-Chip (SoC) technology. The SoC technology enables several powerful, cost-cutting features. First, the whole circuit can be readily tested at the wafer level, helping design refinement and to identify defective samples early in the process, well before being packaged. And second, the monolithic integration reduces overall complexity at the packaging level, as there is no need for complex flip-chip bonding of different materials or cumbersome alignment of micro free-space components. This enables the co-packaging of electronics and optics in a non-hermetic form that eliminates the need for the traditional and expensive gold boxes. This way, low-cost, high-performance transceivers with increased functionality can be realised in standard form factors. For example, based on this technology, a 10x10 Gb/s NRZ DWDM transmitter optical sub-assembly (TOSA) designed for application into standard form factor transceivers has been developed. The multi-channel PIC comprises 10 distributed Bragg reflector (DBR) lasers (see spectrum in Fig. 1(a)) each modulated via a Mach-Zehnder modulator (MZM) and combined with an arrayed waveguide grating (AWG) for multiplexing, and several

monitoring functions all in a chip occupying a small area of 4x6 mm. This is less than the amount of InP needed for 10 individual channels, and therefore the AWG and monitors come almost for free, on top of the reduced handling complexity in the packaging process.

In the 10-100 km transmission range the use of MZMs is appealing because, in contrast to electro-absorption modulators, they offer better chirp management and extinction ratio control over a wide wavelength range without incurring additional loss [2]. To meet the performance requirements within the power budget, high-efficiency MZMs are combined with cost-effective off-the-shelf electronics. The inset in Fig. 1(a) shows a representative eye diagram of the 10x10 Gb/s TOSA in which the MZMs were negatively pre-chirped. Pre-chirping is known to reduce the power penalty induced by fibre nonlinearity both in normal and anomalous dispersion fibres, enabling longer transmission distances [3]. RF extinction ratio higher than 12 dB with the peak to peak modulation voltage (Vpp) of 1.5V is obtained, using low-cost drivers.

The next generation transceivers will require higher bit rates per channel. In this context, up to 5-times channel throughput increase (i.e. 50 Gb/s/λ) of the 10x10G-class TOSA has been demonstrated when paired with simple digital signal processing techniques and using PAM-4 signals. Figure 1(b) illustrates how the MZM chirp is exploited to enable the PAM-4 WDM dispersion tolerant direct-detection based transmission up to 25 km without dispersion compensating fibre (DCF) and 75 km with DCF. Figure 1(c) shows the frequency response characteristics of the MZM used in this experiment. The traveling-wave InP modulator has a 3-dB bandwidth in excess of 25 GHz, with a modulation voltage of only 1.6 Vpp. Overall, this technology is a compelling candidate for the realisation of high-speed-high-efficiency pluggable transceivers.

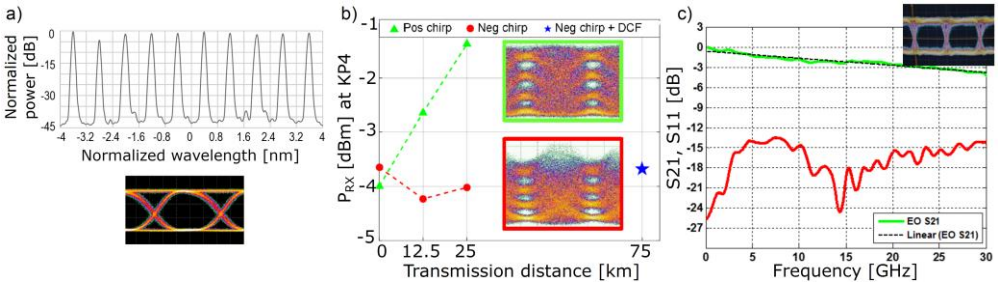


Fig. 1. a) Output spectrum and typical eye diagram of a 10x10 Gb/s NRZ DWDM TOSA based on the SoC technology. b) Chirp impact on PAM-4 WDM transmission at 25 Gb/s/λ using 10x10G-class TOSA. c) MZM frequency response.

The authors greatly acknowledge the technical contributions of Saeed Tahvili, Muhammad Usman Sadiq, and Aaron Albores-Mejia from Effect Photonics, and John van Weerdenburg, Sjoerd van der Heide, and Chigo Okonkwo from the Eindhoven University of Technology.

References

[1] V. Lal *et al.*, *Full C-band tunable coherent transmitter and receiver InP photonic integrated circuits*, Proc. ECOC, PDP Th.3.A.4, 2016.

[2] J.S. Barton *et al.*, *Tailorable chirp using integrated Mach-Zehnder modulators with tunable sampled grating distributed Bragg reflector lasers*, Proc. IEEE 18th International Semiconductor Laser Conference, pp. 49-50, 2002.

[3] A. Sano *et al.*, *A 40-Gb/s/ch WDM transmission with SPM/XPM suppression through prechirping and Dispersion Management,* J. Lightw. Technol., vol. 18, no. 11, pp. 1519–1527, 2000.

Optical Frequency Domain Reflectometry for Characterization of Distributed Bragg Reflectors

Dan Zhao[1*], Dzmitry Pustakhod[1], Luc Augustin[1,2], Jeroen Bolk[1], Kevin Williams[1] and Xaveer Leijtens[1]

[1]Eindhoven University of Technology, Den Dolech 2, 5612 AZ, Eindhoven, the Netherlands

[2]Smart Photonics, Horsten 1, 5612 AX, Eindhoven, the Netherlands *d.zhao@tue.nl

Abstract: We present the characterization of the reflection spectra of distributed Bragg reflectors (DBRs) created using DUV scanner lithography in indium-phosphide (InP) with the optical frequency domain reflectometry (OFDR) method.

Introduction: The Distributed Bragg Reflector (DBR) is an important waveguide component for achieving wavelength selective filter functions. To enable the DBR as a standard building block in the COBRA platform [1], a main challenge is the development of a high precision lithography technology on indium-phosphide (InP) wafers. Recently, we have successfully used the 193 nm DUV scanner to fabricate DBRs on InP wafers, for the first time [2]. Another challenge is to characterize the reflection spectra of fabricated buried DBRs. With a direct measurement of reflections from anti-reflection coated chips, the coupling loss between the fibre and sample is hard to be estimated. With cleaved chips, which enable self-referenced analysis, the coupling loss can be estimated. However, the contribution of the Fabry–Pérot cavity introduced by the facets need to be de-embedded to separate the pure grating reflection. In the optical frequency domain reflectometry (OFDR) method, we can separate the facet reflections from the grating response in the spatial domain [3].

The OFDR system: The schematic diagram of the OFDR system used for the characterization of DBRs on a cleaved chip is shown in Fig. 1. The sample has a 1950 μm long waveguide with a DBR positioned at 1000 μm from the front facet. The intensity modulation resulting from the interference of reflections from the cleaved facets and the DBR (green arrows) are recorded by the power meter when sweeping the wavelength of the tunable laser. Taking the Fast Fourier transform (FFT) of the recorded signal, it is then possible to spatially map the reflection distribution.

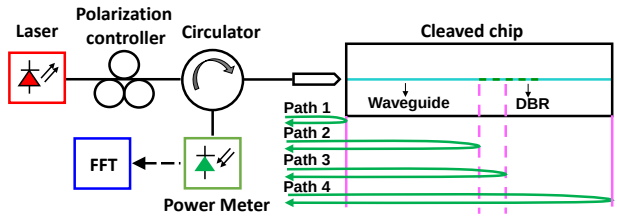


Fig. 1. The schematic diagram of the OFDR system.

The reconstruction of the DBR reflection is carried out in the following steps: first, remove those reflections in the spatial domain that correspond to a path difference longer than the DBR length, in this way we keep only interference between paths 2 and 3. Second, correct the magnitude of the FFT by eliminating the coupling and propagation losses. The coupling loss can be calculated from the average loss in the wavelength range outside the grating reflection peak. Third, apply an inverse Fourier Transform to the corrected FFT signal. Simulations have been done in our optical extensions implemented in Agilent's Advanced Design System (ADS) to demonstrate the accuracy of the method. Fig. 2(a) shows the comparison of the FFT results between the reference DBR (blue) and the sample with cleaved facets (red). It shows that the sample with cleaved facets has extra reflection peaks and extra losses compared to the reference. The reconstructed FFT

signal of the sample, shown as the light blue curve in Fig. 2(b), matches well with the reference. By applying an inverse FFT, the extracted grating reflection matches well with the reference reflection (Fig. 2(c)).

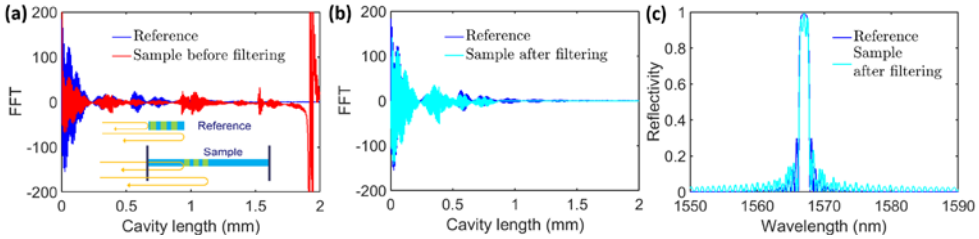


Fig. 2. FFT of simulated reflection from the reference and the sample (a) before and (b) after filtering. (c) Reference and reconstructed grating reflection spectrum.

Measurement results and discussions: A set of DBRs fabricated in the COBRA platform with periods of 236.3, 237.8, 238.5, 239.9 and 240.1 nm and lengths of 200, 400, 500, and 600 µm were characterized. Fig. 3(a) and (b) show the measured and extracted reflection spectra for DBRs with a fixed period of 240.1 nm. The DBR reflection spectrum is not directly visible in the measurements due to the losses induced by coupling, waveguide propagation and Fabry–Pérot interference. The extracted results show the reflection spectra of the DBRs. It shows that the same grating period results in the same Bragg wavelength and that a longer length of grating results in higher peak reflectivity. The Bragg wavelength of in total 40 different samples over a wafer has been analyzed. The mean values at 5 periods are shown as blue dots in Fig. 3(c). The standard deviation at each period is smaller than 0.7 nm, which is sufficient to target the wavelength for tunable DBR gratings. The Bragg wavelength increases linearly as the period increases, which indicates the reproducibility of the lithography process over a large area.

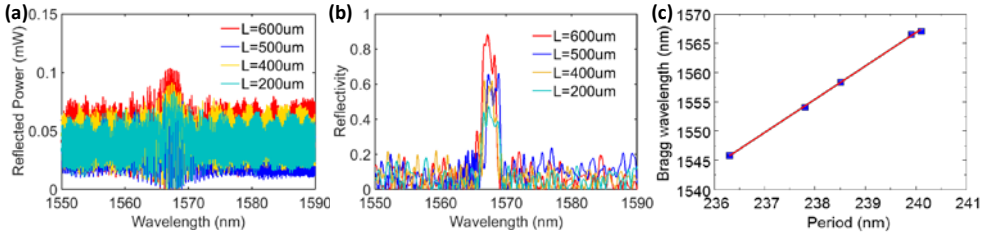


Fig. 3. (a) Measured and (b) extracted reflections of DBRs at different length, (c) Measured Bragg wavelength (blue spots) as a function of period and its linear fit (red line).

Conclusion and acknowledgement: We have developed a method based on OFDR with a subsequent filtering in the spatial domain to extract the pure power reflectivity of DBRs. The fabrication with 193 nm DUV technology is demonstrated to be reproducible over a large area. We acknowledge support by the Dutch Technology Foundation STW for project 13538.

References

[1] M. Smit et al., *An introduction to InP-based generic integration technology*, Semiconductor Science and Technology, vol. 29, no. 8, pp. 083001, 2014

[2] D. Zhao et.al., *Distributed Bragg reflectors on InP platform fabricated with deep-UV technology*, Proceedings of the 21th Annual Symposium of the IEEE Photonics Benelux Chapter, pp. 231-234, 2016

[3] B. J. Soller et. al, *High resolution optical frequency domain reflectometry for characterization of components and assemblies*, Optics Express, vol. 13, no. 2, pp. 666-674, 2005

Fully Integrated Optical Frequency Domain Reflectometry

Luis A. BRU[1], Gloria MICÓ[1], Daniel PASTOR[1*], B. GARGALLO[2], David DOMENECH[2], Ana M. SÁNCHEZ[3], Josep M. CIRERA[3], Javier SANCHEZ[3], Carlos DOMÍNGUEZ[3] and Pascual MUÑOZ[1,2]

[1]Photonic-IC group @ Photonic Research Labs, Universitat Politècnica de Valencia, Spain
[2]VLC Photonics S.L., Ed9B-UPV, c/ Camino de Vera s/n, Valencia, Spain
[3]IMB-CNM-CSIC, Campus Belaterra UAB, Barcelona, Spain
[*]dpastor@dcom.upv.es

Optical Frequency Domain Reflectometry (OFDR) [1-5] provides valuable complex information (modulus and phase) in the time and optical frequency domains for characterization of new technologies and integrated devices. The standard approach employing fiber based Mach-Zehnder Interferometers (MZI) [1-5] requires dedicated bulky set-ups, subject to demanding stabilization conditions, in order to preserve the light polarization states and the optical phase variations due to temperature changes over long fiber MZIs (>4-5 meters in some cases due to the required fiber pigtails couple light to/from the photonic chip). Here we propose for the first time to our knowledge a fully Integrated OFDR (IOFDR) approach, where all the required MZI structures are co-integrated with the Device Under Test (DUT). The device was fabricated on a 100mm Si wafer, composed of a SiO_2 buffer (2.5µm thick, n=1.464) grown by thermal, following a LPCVD Si_3N_4 layer with thickness 300nm (n= 2.01) and a 2.0µm thick SiO_2 (n=1.45) deposited by PECVD.

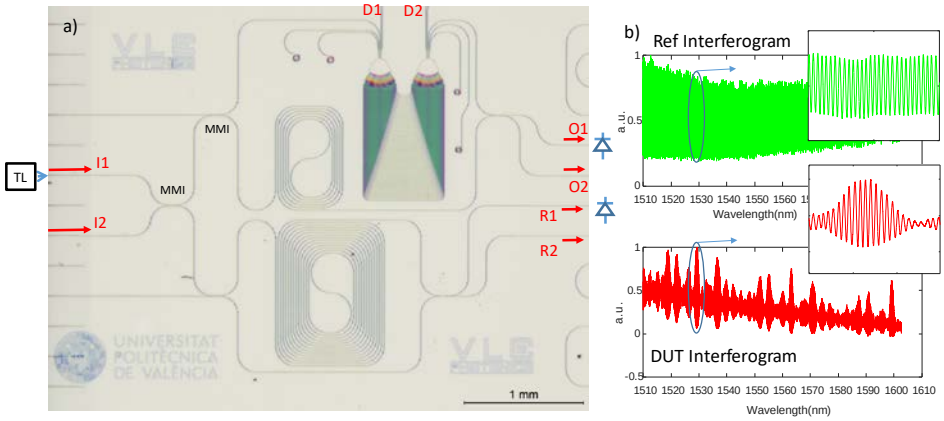


Fig. 1. a) Fully Integrated OFDR layout. b) DUT and Ref interferograms

The IOFDR set up is composed of two on-chip imbalanced MZIs, fed by a scanning Tunable Laser (TL), Fig. 1. The upper MZI embraces the DUT (a 5x5 Array Waveguide Grating (AWG) design as a proof of concept). The lower MZI is used to obtain the reference (or trigger) for the phase error correction due to imperfections during the TL scanning. In both MZIs we employ spirals to adjust the optical path differences ($\Delta L_{DUT}, \Delta L_{ref}$) according to the DUT characteristics. The objective is to ensure that the triggering interferogram provides sampling points of the DUT interferogram subject to the Nyquist criterion, in order to avoid aliasing of the DUT temporal response. We employ 50:50 MMIs for all the MZIs and also at the input signal splitting on the left hand side of the design. Finally, for the IOFDR assessment the TL signal, swept along 100nm (speed 40nm/s), is injected at input port I1 or I2, and the signals from one of the MZI-DUT outputs (O1 or O2), and one of the reference MZI outputs (R1 or R2) are collected and driven to two PIN detectors connected to, Fig.1.

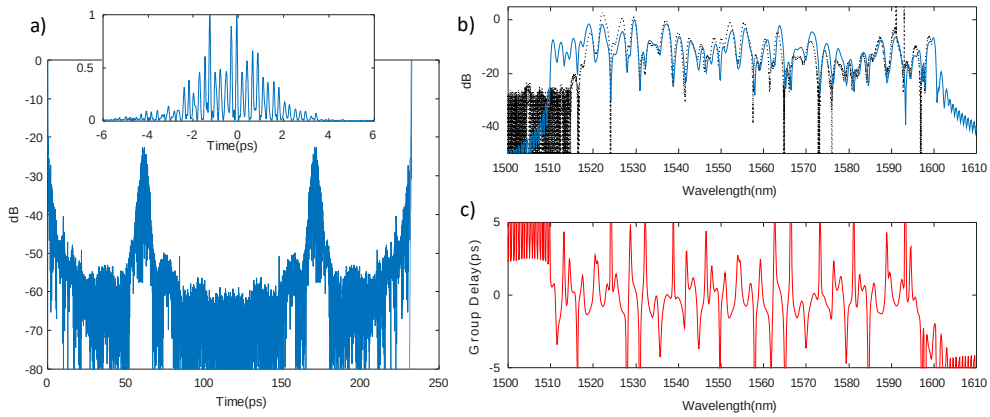


Fig. 2. a) DUT time response, b) Spectral amplitude: Dotted line standard measurement, Cont. line IOFDR, c) Group Delay response from IOFDR data.

After detection, the interferograms, Fig. 1(b), are sampled and acquired (5e4 samples/s per channel) and the DUT interferogram is re-sampled numerically in the reference zero-crossings to perform the correction for scanning errors. Finally, the Fast Fourier Transform (FFT) is employed to obtain the DUT time response $h(t)$, Fig. 2(a). Notice that we are representing the complete transformed signal in time domain ranging from 0 to 232 ps, that corresponds with the designed $\Delta L_{ref} = 36.9\,mm$ ($n_{eff} \approx 1.89$). Time response $h(t)$ appears symmetrically at $\sim 62\,ps$ and $\sim(232-62)\,ps$ corresponding with the $\Delta L_{DUT} = 0.984\,mm$ (calculated for the central AWG waveguide). The AWG was designed with 59 waveguides in the array and a Free Spectral Range (FSR) of 32 nm (4.0THz), so the expected impulsive response is composed by a train of short pulses spaced 0.24 ps, with length 14.5 ps. See Fig. 2(a) and inset showing $|h(t)|^2$ in dB and natural units. We can see on $|h(t)|^2$ the power distribution in the AWG arms, as well as a strong power fluctuation in some waveguides of the array, due to fabrication imperfections. Notice that phase propagation errors between waveguides can be obtained also [3]. Additionally the spectral response in IOFDR was obtained by slicing the $h(t)$ around the 62 ps band along ±6ps and performing the Inverse FFT. Amplitude and the group delay responses are shown in Fig. 2(a) and (b). In order to verify the IOFDR results we took a standard spectral amplitude measurement with an ASE source and an Optical Spectrum Analyzer. For this, we employed available direct ports on the AWG (D1 and D2 in Fig. 1(a)). The amplitude responses from the IOFDR setup and the standard measure are compared in Fig. 2 (b), with the required manual wavelength shift since we are using a different in/out combination. Overall, the IOFRD chip provides a very good agreement with the classic measurement, but it provides full-field information of the DUT in the time and optical frequency domains.

References

[1] U. Glombitza and E. Brinkmeyer, J. Lightwave Technol. 11 1377–1384 (1993)
[2] K. Takada and T. Hirose, Optics Letters 34, 24, 3914-3916 (2009)
[3] L. A. Bru, B. Gargallo, e.a., in Proc. ECIO, paper ecio-o–08, 2016.
[4] B. J. Soller, D. K. Gifford, e. a., Optics Express 13, 2, 666-674 (2005)
[5] D. K. Gifford, B. J. Soller, e. a., Applied Optics 44, 34, 7282-7286 (2005)



Active Plasmonics

Anatoly V Zayats[1*]
[1]Department of Physics, King's College London, London, WC2R 2LS, United Kingdom
[*]anatoly.zayats@kcl.ac.uk

Strong light-matter intercations can be realised in plasmonic nanostructures openning up opportunities to control electromagnetic signals on subwavelength scales. In this talk we will discuss various plasmonic and metamaterial-based approaches for achieving active nanophotonic functionalities. All-optical and electro-optical effects as well polarisation and dispersion management with plasmonic nanostructures and their sensing applications will be overviewed.

Plasmonics makes use of coupling between electromagnetic waves and free-electron excitations at the interface of good conductors. The electromagnetic field enhancement effects associated with surface plasmons and specific to them field confinement result in a strong sensitivity of plasmonic modes to dielectric surroundings, thus facilitating all-optical and electronic control of their propagation [1,2]. These properties are especially suitable for development of active integrated componnets which can be used within purely plasmonic circuits or incorporated into photonic, e.g., Si-based, circuitry to achive desired functionality which is difficult to achive by other means [3]. Going beyond conventional plasmonic materials, such as Au and Ag, new material platfoms based on CMOC compatible metals such as Al and Cu, highly doped semiconductors, transparent conductive oxides and metamaterials have been developed. In particular, by controlling arrangements of plasmonic nanostructures withing metamaterials, complete control over surface plasmonic dispersion and field enhancement can be achieved [4-6]. Combining plasmonic nanostructures with electro-optical materials or using their free-electron nonlinearities, various types modulators and switches can be demosntrted operating at very low powers.

In this paper, we will overview active nanophotonic functionalities based plasmonic and metamaterial waveguides and discuss integrated and free standing componets for signal modulation, and polarisation and dispersion [7-13]. With a strong refctive index sensetivity diue to the field confinement and enhancement, intgrated plasmonic and meamaterial circuitry can also be used for high-performance sensing applications.

References

[1] A. V. Zayats, S. A. Maier, Eds., *Active plasmonics and tuneable plasmonic metamaterials*, Wiley, New York, 2013

[2] A. V. Krasavin, A. V. Zayats, *Active nanophotonic circuitry based on dielectric-loaded plasmonic waveguides: a review*, Adv. Opt. Mat., vol. 3, pp. 1652-1799, 2015.

[3] A. V. Krasavin, A. V. Zayats, *Benchmarking system-level performance of passive and active plasmonic components: integrated circuits approach*, Proc. IEEE, vol. 104, pp. 2338-2348, 2016.

[4] W. Dickson, S. Beckett, Ch. McClatchey, A. Murphy, D. O'Connor, G. A. Wurtz, R. Pollard, A. V. Zayats, *Hyperbolic polaritonic crystals based on nanostructured nanorod metamaterials*, Adv. Mat., vol. 27, pp. 5974-5980, 2015.

[5] N. Vasilantonakis, M. Nasir, W. Dickson, G. A. Wurtz, A. V. Zayats, *Bulk plasmon-polaritons in hyperbolic nanorod metamaterial waveguides*, Laser Phot. Rev., vol. 9, pp. 345-353, 2015.

[6] A. Neira, G. A. Wurtz, A. V. Zayats, *Superluminal and stopped light due to mode coupling in confined hyperbolic metamaterial waveguides*, Sci. Rep., vol. 5, 17678, 2015.

[7] C. P. T. McPolin, J.-S. Bouillard, S. Vilain, A. V. Krasavin, W. Dickson, D. O'Connor, G. A. Wurtz, J. Justice, B. Corbett, and A. V. Zayats, *Integrated plasmonic circuitry on a vertical-cavity surface-emitting semiconductor laser platform*, Nat. Comm., vol. 7, 12409, 2016.

[8] C. McPolin, N. Olivier, J.-S. Bouillard, D. O'Connor, A. V. Krasavin, W. Dickson, G. A. Wurtz, and A. V. Zayats, *Universal switching of plasmonic signals using optical resonator modes*, Light: Sci. Appl., vol. 6, e16237, 2017.

[9] O. Lysenko, M. Bache, N. Olivier, A. V. Zayats, A. Lavrinenko, *Nonlinear dynamics of ultrashort long-range surface plasmon polariton pulses in gold strip waveguides*, ACS Photonics, vol. 3, pp. 2324–2329, 2016.

[10] A. Neira, N. Olivier, M. E. Nasir, W. Dickson, G. A. Wurtz, A. V. Zayats, *Eliminating material constraints for nonlinearity with plasmonic metamaterials*, Nat. Comm. vol. 6, 7757, 2015.

[11] A. D. Neira, G. A. Wurtz, P. Ginzburg, A. V. Zayats, *Ultrafast all-optical modulation with hyperbolic metamaterial integrated in Si photonic circuitry*, Opt. Exp., vol. 22, pp. 10987-10994, 2014.

[12] J.-S. Bouillard, S. Vilain, W. Dickson, G. A. Wurtz, A. V. Zayats, *Broadband and broadangle optical antennas based on plasmonic crystals with linear chirp*, Sci. Rep., vol. 2, 829, 2012.

[13] A. S. Shalin, P. Ginzburg, P. A. Belov, Yu. S. Kivshar, A. V. Zayats, *Nano-opto-mechanical effects in plasmonic waveguides*, Laser Phot. Rev., vol. 8, pp. 131-136, 2014.

Subwavelength waveguide devices for Near and Mid-Infrared applications

Alejandro ORTEGA-MOÑUX[1*], Robert HALIR[1], J. Darío SARMIENTO-MERENGUEL[1], Alejandro SÁNCHEZ-POSTIGO[1], José M. LUQUE-GONZÁLEZ[1], J. Gonzalo WANGÜEMERT-PÉREZ[1], Jens SCHMID[2], Dan-Xia XU[2], Siegfried JANZ[2], Jean LAPOINTE[2], Jordi SOLER-PENADES[3], Milos NEDELJKOVIC[3], Goran Z. MASHANOVICH[3], Carlos ALONSO-RAMOS[4], Diego PÉREZ-GALACHO[4], Daniel BENEDIKOVIC[4], Jiří ČTYROKÝ[5], Íñigo MOLINA-FERNÁNDEZ[1] and Pavel CHEBEN[2]

[1]Universidad de Málaga, ETSI Telecomunicación, Campus de Teatinos s/n, 29071 Málaga, Spain
[2]National Research Council of Canada, Ottawa, Ontario K1A0R6, Canada
[3] Optoelectronics Research Centre, University of Southampton, SO17 1BJ, United Kingdom
[4]Centre de Nanosciences et de Nanotechnologies, CNRS, Univ. Paris-Sud, Université Paris-Saclay, 91405 Orsay cedex, France
[5] Institute of Photonics and Electronics AS CR, v.v.i., Chaberska 57, 18251 Prague 8, Czech Republic
[*] aom@ic.uma.es

Subwavelength gratings (SWGs) are periodic structures with a pitch (Λ) smaller than half the wavelength of the propagating wave (λ_m), so diffraction effects are suppressed. SWGs behave as artificial birefringent metamaterials with optical properties which depend on the geometry of the structure [1, 2]. They have found a myriad of applications in the field of integrated optics [3], most of them implemented in the silicon-on-insulator platform (SOI). Refractive index engineering based on SWGs has contributed to significant improvements in the performance of fiber-to-chip couplers, which is known as one of the major challenges in integrated optics. The same technique has been applied to design low loss waveguide crossings, integrated planar lens and evanescent field sensors. A refinement of the design technique enables engineering not only the refractive index, but also the dispersion profile of the SWG structure, thus paving the way toward ultra-broadband integrated optical components, such as directional couplers or multimode interference (MMI) devices. If the designer takes advantage of the inherent birefringence of SWGs, these structures can be used to implement high performance integrated polarization beam splitters, polarization rotators and polarizers. Currently, most of the practical devices based on SWG waveguides have been proposed for near-infrared (NIR) telecom wavelengths. For the designer, the main limitation is the minimum feature size that can be reliably fabricated (~100 nm), which constrains the SWG structures to periods larger than 200 nm. This is very close to the Bragg period at telecom wavelengths ($\Lambda_B = \lambda_m /2 \sim 280$ nm for the SOI platform), so the degrees of freedom for the design are often quite limited. Nevertheless, it is worth to note that the subwavelength condition ($\Lambda < \lambda_m /2$) is much easier to meet for mid-infrared (MIR) wavelengths than for the comparatively shorter near-infrared wavelengths, so it can be expected that SWG techniques will have a relevant impact in the design of MIR integrated optical devices in the near future. In this talk we give an overview of some of our recent advances in the development of high performance subwavelength waveguide devices for near and mid-infrared applications [4-15] (see Fig. 1). Practical issues of the design process, such as the relevance of substrate leakage losses and the effects of the random jitter, inherent to any fabrication process, will be also covered [16, 17].

We acknowledge funding from the Ministerio de Economía y Competitividad, Programa Estatal de Investigación, Desarrollo e Innovación Orientada a los Retos de la Sociedad (cofinanciado FEDER), Proyecto TEC2013-46917-C2-1-R, Proyecto TEC2016-80718-R, and the Universidad de Málaga.

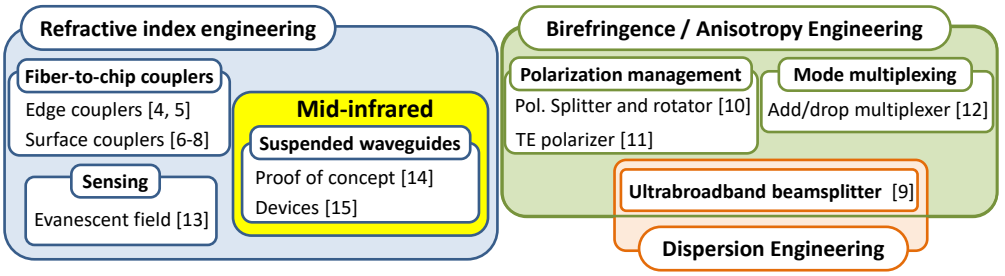


Fig. 1. Classification of our recent work in subwavelength grating waveguide devices.

References

[1] S. M. Rytov, *The electromagnetic properties of finely layered medium*, Sov. Phys. JETP, vol. 2, pp. 466, 1956.

[2] P. Cheben *et al.*, *Refractive index engineering with subwavelength gratings for efficient microphotonic couplers and planar waveguide multiplexers*, Opt. Lett., vol. 35, pp. 2526-2528, 2010.

[3] R. Halir *et al.*, *Waveguide sub-wavelength structures: a review of principles and applications,* Laser Photonics Rev., vol. 9, no. 1, pp. 25-49, 2015.

[4] P. Cheben et al. *Broadband polarization independent nanophotonic coupler for silicon waveguides with ultra-high efficiency*, Opt. Express vol. 23, pp. 22553–22563, 2015.

[5] M. Papes, *et al., Fiber-chip edge coupler with large mode size for silicon photonic wire waveguides*, Opt. Express, vol. 24, pp. 5026-5038, 2016.

[6] D. Benedikovic, *et al., Subwavelength index engineered surface grating coupler with sub-decibel efficiency for 220-nm silicon-on-insulator waveguides,* Opt. Express, vol. 23, pp. 22628-22635, 2015.

[7] D. Benedikovic, *et al., Single-etch subwavelength engineered fiber-chip grating couplers for 1.3 μm datacom wavelength band*, Opt. Express, vol. 24, pp. 12893-12904, 2016.

[8] A. Sánchez-Postigo et al., *Broadband fiber-chip zero-order surface grating coupler with 0.4 dB efficiency,* Opt.Lett., vol. 41, pp. 3013-3016, 2016.

[9] R. Halir *et al.*, *Ultra-broadband nanophotonic beamsplitter using an anisotropic sub-wavelength metamaterial,* Laser Photonics Rev., vol. 10, pp. 1039-1046, 2016.

[10] Y. Xiong, et al., *Polarization splitter and rotator with subwavelength grating for enhanced fabrication tolerance*, Opt. Lett. Vol. 39, pp. 6931-6934, 2014.

[11] Y. Xiong, *et al., High extinction ratio and broadband silicon TE-pass polarizer using subwavelength grating index engineering*, IEEE Photon. J., vol. 7, pp. 1-7, 2015

[12] D. Pérez-Galacho *et al.*, *Add/Drop Mode-Division Multiplexer Based on a Mach–Zehnder Interferometer and Periodic Waveguides*, IEEE Photon. J., vol. 7, pp. 1-7, 2015.

[13] J. G. Wangüemert-Pérez *et al., Evanescent field waveguide sensing with subwavelength grating structures in silicon-on-insulator*, Opt. Lett., vol. 39, pp. 4442-4445, 2014.

[14] J. Soler Penadés, *et al., Suspended SOI waveguide with sub-wavelength grating cladding for mid-infrared*, Opt. Lett. Vol. 39, pp. 5661-5664, 2014.

[15] J. Soler Penadés *et al.*, *Suspended silicon mid-infrared waveguide devices with subwavelength grating metamaterial cladding*, Opt. Express 24, pp. 22908-22916, 2016.

[16] J. D. Sarmiento-Merenguel *et al.*, *Controlling leakage losses in subwavelength grating silicon metamaterial waveguides,* Opt. Lett., vol. 41, pp. 3443-3446, 2016.

[17] A. Ortega-Moñux, *et. al, Disorder in sub-wavelength metamaterial waveguides*, to be published.

Ultra-broadband Silicon Photonic Multimode Interference Coupler

Robert HALIR[1*], Pavel CHEBEN[2], Jose M. LUQUE-GONZÁLEZ[2], Jose D. SARMIENTO-MERENGUEL[1], Jens H. SCHMID[2], Gonzalo Wangüemert-Pérez[1], Dan-Xia XU[2], Shurui WANG[2], Alejandro ORTEGA-MOÑUX[1], and Íñigo MOLINA-FERNÁNDEZ[1]

[1]Universidad de Málaga, ETSI Telecomunicación, Campus de Teatinos s/n, 29071 Málaga, Spain
[2]National Research Council of Canada, Ottawa, Ontario K1A0R6, Canada
[*] robert.halir@ic.uma.es

In integrated optics, multimode interference couplers (MMIs) are used as light-wave splitters and combiners in a wide variety of devices ranging from spectrometers to sensors and coherent optical receivers. While their design and operation is generally well understood [1], the operational bandwidth remains limited. Here we present a sub-wavelength structured MMI, shown in Fig. 1(a), that overcomes this limitation and experimentally demonstrate a bandwidth exceeding 300nm at telecom wavelength, with more than 500nm bandwidth potentially attainable (as per 3D-FDTD simulations).

Referring to Fig. 1(b), in a MMI a light-wave with mode profile f_{in} is launched into the multimode region, exciting several higher order modes φ_i. These modes propagate with different phase constants β_i forming images of the input field f_{in}. A two-fold image is formed at the position $z = (3/2)\, L_\pi$, with $L_\pi = \pi/(\beta_1 - \beta_2)$ the beat-length of the two lowest order modes. By placing the output waveguides at this position a 3 dB coupler is obtained. However, the beat-length L_π is wavelength dependent, so the position of the images moves as wavelength is tuned, limiting the device bandwidth [1].

We use a sub-wavelength grating (SWG) metamaterial to overcome this limitation. SWGs behave as equivalent homogenous media with controllable refractive index, and have found widespread application in silicon photonics [2]-[5]. Broadband 3 dB couplers based on SWG directional couplers [6]-[7] and SWG adiabatic couplers [8] have been recently demonstrated, with bandwidths between 100 nm and 130 nm. In our SWG MMI [Fig. 1(a)], we exploit the anisotropy of the SWG to experimentally demonstrate a 3 dB coupler that covers 300nm of bandwidth around a wavelength of 1.55 µm. 3D FDTD simulations show that more than 500nm can be achieved.

The anisotropy of the SWG medium is analogous to that of a uniaxial crystal: two waves polarized along the x axis (electric field parallel to the silicon segments) and z axis (electric field perpendicular to the silicon segments) experience different equivalent indexes, n_{xx} and n_{zz} [Fig. 1(a)]. The device can thus be modelled as a conventional MMI composed of a homogenous anisotropic material [Fig. 1(b)]. The beat length of such an anisotropic MMI is given by $L_\pi \approx (4\mathrm{W}^2)/3\lambda \cdot n_{zz}^2/n_{xx}$, and is significantly shorter and less wavelength dependent compared to a conventional MMI [9].

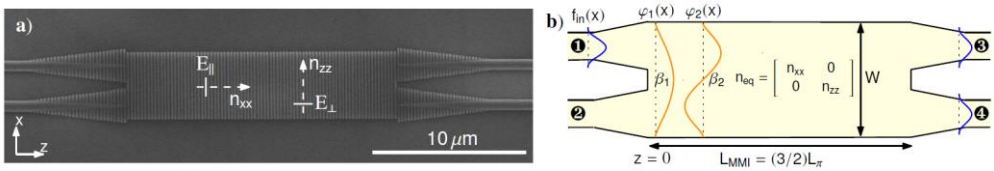


Fig. 1. (a) Scanning electron microscope image of a sub-wavelength patterned multimode interference coupler engineered for ultra-broadband operation. (b) Schematic top view of a 2×2 multimode interference coupler.

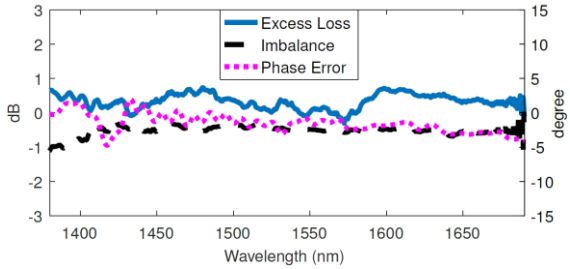


Fig. 2. Measured performance of the device shown in Fig. 1(a), revealing high-performance operation over a bandwidth in excess of 300nm, actually limited by the setup wavelength scanning range.

Figure 2 shows the performance of the sub-wavelength patterned MMI, measured using a broadband source and an optical spectrum analyser. Both imbalance (power difference between the two outputs) and excess loss (power lost in the device) are below 1 dB over the full measurement range (1380nm – 1700nm). The phase error (deviation from the ideal 90° phase shift between the outputs) is smaller than 5°. Even an ideal (simulated) conventional MMI device only exhibits a comparable performance over a limited bandwidth of 200nm.

We believe that such ultra-broadband MMI devices will pave the way towards broadband on-chip systems for diverse applications ranging from optical sensing to data communications.

We acknowledge funding from the Ministerio de Economía y Competitividad, Programa Estatal de Investigación, Desarrollo e Innovación Orientada a los Retos de la Sociedad (cofinanciado FEDER), Proyecto TEC2013-46917-C2-1-R, Proyecto TEC2016-80718-R, and the Universidad de Málaga.

References

[1] L. B. Soldano, and E. C. Pennings, *Optical multi-mode interference devices based on self-imaging: principles and applications,* J. Lightw. Technol., vol. 13, pp. 615-627, 1995.

[2] P. Cheben *et al.*, *Refractive index engineering with subwavelength gratings for efficient microphotonic couplers and planar waveguide multiplexers*, Opt. Lett., vol. 35, pp. 2526-2528, 2010.

[3] R. Halir *et al.*, *Waveguide sub-wavelength structures: a review of principles and applications,* Laser Photonics Rev., vol. 9, no. 1, pp. 25-49, 2015.

[4] J. D. Sarmiento-Merenguel *et al.*, *Controlling leakage losses in subwavelength grating silicon metamaterial waveguides,* Opt. Lett., vol. 41, pp. 3443-3446, 2016.

[5] A. Sánchez-Postigo et al., *Broadband fiber-chip zero-order surface grating coupler with 0.4 dB efficiency,* Opt.Lett., vol. 41, pp. 3013-3016, 2016.

[6] R. Halir *et al.*, *Colorless directional coupler with dispersion engineered sub-wavelength structure,* Opt. Express, vol. 20, pp. 13470-13477, 2012.

[7] Y. Wang *et al.*, *Compact Broadband Directional Couplers Using Subwavelength Gratings,* IEEE Photon. J., vol. 8, pp. 1-8, June 2016.

[8] H. Yun *et al., Broadband 2 × 2 adiabatic 3 dB coupler using silicon-on-insulator sub-wavelength grating waveguides,* Opt. Lett., vol. 41, pp. 3041-3044, 2016.

[9] R. Halir *et al.*, *Ultra-broadband nanophotonic beamsplitter using an anisotropic sub-wavelength metamaterial,* Laser Photonics Rev., vol. 10, pp. 1039-1046, 2016.

EUROPEAN CONFERENCE ON INTEGRATED OPTICS

Fully suspended slot waveguide racetrack resonators

Wen Zhou[1*], Zhenzhou Cheng[2], Yun Gao[1], Xinru Wu[1], Xiankai Sun[1], Hon Ki Tsang[1]
[1] Department of Electronic Engineering, The Chinese University of Hong Kong, Shatin, Hong Kong
[2] Department of Chemistry, The University of Tokyo, Tokyo, 113-0033, Japan
[*] wzhou@ee.cuhk.edu.hk

A fully suspended slot waveguide (FSSW) racetrack resonator is experimentally demonstrated for the first time. The suspended slotted waveguide core is mechanically supported by lateral subwavelength grating (SWG) bridges. The measured loaded optical *Q* factor is 1650 at a resonant wavelength of 2326.20 nm, with extinction ratio of 18.1 dB.

Optical slot waveguides fabricated on the silicon-on-insulator (SOI) platform enables direct light–matter interaction [1]. Its ring resonators are promising for trace-gas sensing [2], microparticle trapping [3], and nano-optomechanical mass and displacement measurements [4]. To date, slot ring/racetrack structures on buried oxide (BOX) have been adopted in the above applications. However, their operation wavelength is limited below 4.0 μm in the mid-infrared (MIR) regime due to the strong absorption of BOX [1].

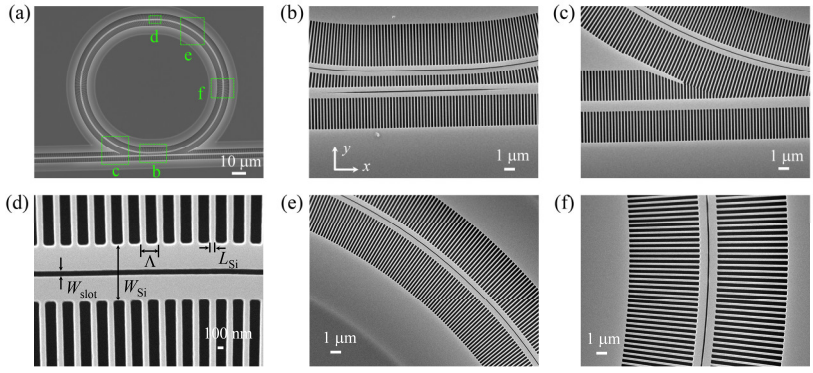


Fig. 1. Top-view SEM images of a FSSW racetrack resonator. (a) Overview of a complete racetrack resonator. (b–f) Zoomed-in areas of the waveguide coupler and bends.

In order to achieve a broad spectral range of transparency in the MIR regime, we propose and demonstrate a FSSW racetrack resonator fabricated on a 340-nm SOI wafer, where the BOX is removed finally. As shown in Fig. 1(a), a curved slotted waveguide core is mechanically supported by lateral subwavelength grating bridges. The bus waveguide is a suspended strip waveguide [5] with two strip-to-slot mode

converters and a section of slotted waveguide in the middle, as shown in Fig. 1(b). We define the bus-to-racetrack coupling length as L_c and the centre-to-centre separation of the coupling region as d. The waveguide bends shown in Fig. 1(c), (e), (f) have a same radius of R. A zoomed-in slot waveguide structure is shown in Fig. 1(d). Widths of the waveguide core and slot are W_{Si} and W_{slot}, and the period and length in the x direction of the periodic anchoring pillars in a SWG cladding are Λ and L_{Si}.

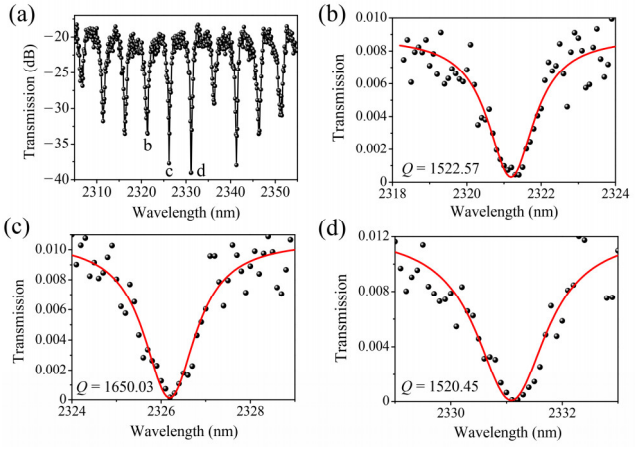


Fig. 2. (a) Transmission spectrum of a FSSW racetrack resonator. (b–d) Zoomed-in spectra of the labeled modes with fitted loaded *Q* factors.

Fig. 2(a) shows a measured transmission spectrum with a resolution 0.1 nm for a racetrack resonator with (L_c, d, R) = (6.00, 1.80, 47.75) μm and (W_{Si}, W_{slot}, Λ, L_{Si}) = (955.18, 87.48, 299.94, 102.07) nm. Regimes of under, critical, and over coupling can be seen from changes in the extinction ratios in the wavelength range from 2305 to 2355 nm with increased coupling coefficient. Three pronounced transmission dips are selected for analyzing the loaded optical Q factors. Their resonant wavelength, loaded Q factor, and extinction ratio are (2321.40 nm, 1522, 13.11 dB), (2326.20 nm, 1650, 18.14 dB), and (2331.10 nm, 1520, 19.62 dB), respectively. The loaded Q factor may be improved by optimizing L_c and d, in order to minimize the coupling loss.

In summary, we have experimentally demonstrated FSSW racetrack resonators with their loaded optical Q factors above 1500. They could be used for applications where enhancement of direct light–matter interaction is desired, such as spectroscopy, sensing, and optical tweezers.

References

[1] J. S. Penadés, A. Z. Khokhar, M. Nedeljkovic, and G. Z. Mashanovich, *Low-Loss Mid-Infrared SOI Slot Waveguides*, IEEE Photon. Technol. Lett., vol. 27, no. 11, pp. 1197-1199, 2015

[2] J. T. Robinson, L. Chen, and M. Lipson, *On-chip gas detection in silicon optical microcavities*, Opt. Express, vol. 16, no. 6, pp. 4296-4301, 2008

[3] J. Witzens and M. Hochberg, *Optical detection of target molecule induced aggregation of nanoparticles by means of high-Q resonators*, Opt. Express, vol. 19, no. 8, pp. 7034-7061, 2011

[4] M. Li, W. H. P. Pernice, and H. X. Tang, *Ultrahigh-frequency nano-optomechanical resonators in slot waveguide ring cavities*, Appl. Phys. Lett., vol. 97, no. 18, pp. 183110, 2010

[5] J. S. Penadés, C. Alonso-Ramos, A. Z. Khokhar, M. Nedeljkovic, L. A. Boodhoo, A. Ortega-Moñux, I. Molina-Fernández, P. Cheben, and G. Z. Mashanovich, *Suspended SOI waveguide with sub-wavelength grating cladding for mid-infrared*, Opt. Lett., vol. 39, no. 19, pp. 5661-5664, 2014



The effect of photonic integration on the evolution of communication systems

Hercules AVRAMOPOULOS[1*]
[1]ICCS/NTUA, Zografou, 15780, Greece
[*]hav@mail.ntua.gr

Over the last decades, the ubiquitous necessity for high-bandwidth and low-cost has instigated the penetration of photonic integrated circuits (PICs) though all the major application areas of Photonics, providing the speed, cost and integration density credentials required for preventing the imminent capacity crunch. Ranging from the high-speed low-cost IM/DD links of datacenter networks to the spectrally-efficient flexible coherent systems of the metro and core, the industry is seeking PIC-based solutions offering extensive functionalities, low cost and manufacturability. In this context, III-V materials present their inherent competence to provide a complete set of functionalities, such as light emission, modulation and detection while Silicon Photonics (SiPh) bear the promise of capitalizing on the enormous investments and progresses in CMOS fabs. In addition, dielectric integration platforms based on Silicon Nitride (SiN) and Polymers have made their appearance enabling seamless coupling to optical fibers, significantly reduced propagation losses as well as valuable sensing attributes through enhanced light-matter interaction. This vast set of technology and material options has profoundly extended the capabilities of communication systems, paving the inroad towards next generation Datacom, Telecom and Sensing implementations and future applications, as signified by the most recent technological breakthroughs and developments. In [1] Luxtera presents a 4x26Gb/s transceiver packaged in a QSFP28 module, while in [2] the 300nm wafer-based Si-photonics platform of STMicroelectonics and Luxtera is discussed and in [3] a 3-mode multiplexing and de-multiplexing integrated silicon photonic circuit supporting 240 Gb/s data rate is demonstrated by Intel. Recent advancements in InP photonic integration platforms targeting beyond-telecom applications were recently presented by TU/e [4], whereas a comb-based programmable radio-frequency photonic filter, utilizing an InP arrayed waveguide grating pulse shaper was also demonstrated by Infinera [5]. HP Labs and UC Santa Barbara have proposed a compact, low power consumption and high direct modulation speed hybrid III/V on silicon microring laser [6] while a novel 3D integrated tunable hybrid silicon laser has been experimentally demonstrated in [7]. Hybrid 25Gb/s III-V/silicon transmitters relying on a co-integration scheme were presented in [8] by CEA-LETI and STMicroelectronics. A brief technology description of the TriPleX integration platform is presented in [9], together with some application examples ranging from visible light implementations to photonic (bio-) sensing [10] and microwave photonics, while the building blocks of three mid-IR silicon photonics material platforms suitable for communications and sensing are discussed in [11]. IBM has recently proposed and demonstrated a Polymer-to-SiPh flip-chip adiabatic coupling interface, compatible with

the company's large area capable single-mode polymer waveguide technology [12], whereas the photonic components of HHI's Polyboard platform are summarized in [13] and a 3D integration scheme is proposed enabling 1Tb/s data-center connectivity.
In the following figure, our recent highlights on the field of photonic integration, carried out within the frames of collaborative research projects co-funded by the European Commission, are summarized. Figure 1(a) shows a fully re-configurable 16x1 SiPh MUX/DEMUX device for flex-grid applications, fabricated and packaged within ICT-SPIRIT, while figure 1(b) presents a 40Gbps PAM4 transmitter (top) and a 64Gbps PAM4 linear optical receiver (bottom) developed within ICT-MIRAGE. An assembled and packaged 50Gbaud single polarization coherent receiver relying on HHI's Polyboard, realized during the third year of the ICT-PANTHER project, is demonstrated in Fig. 1(c), whereas photonic ring resonator bio-sensors based on Triplex integration platform, developed within the ICT-BIOFOS project, are depicted in Fig. 1(d).

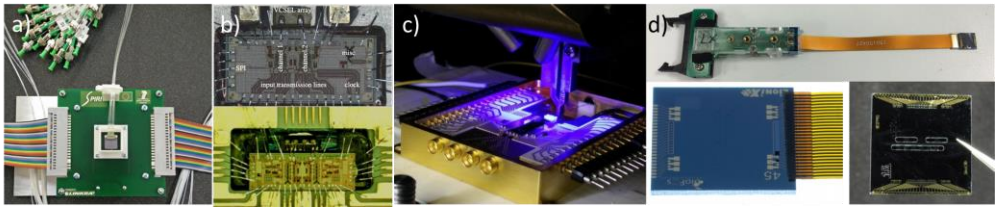


Fig. 1. (a) 16x1 fully-reconfigurable MUX/DEMUX, (b) 40Gbps PAM4 Tx and 64Gbps PAM4 linear optical Rx, (c) 50Gbaud single polarization Polyboard coherent receiver and (d) photonic ring resonator bio-sensors based on Triplex integration platform

References

[1] De Dobbelaere, P., et al. "Deployment of silicon photonics technology in data communication applications." Optical MEMS and Nanophotonics (OMN), 2016.
[2] Boeuf, Frédéric, et al. "Silicon photonics R&D and manufacturing on 300-mm wafer platform." Journal of Lightwave Technology 34.2 (2016): 286-295.
[3] Chen, Christine P., et al. "240 Gb/s mode and wavelength division multiplexed data transmission in Si photonics." IEEE Optical Interconnects Conference (OI), 2016. IEEE, 2016.
[4] Jiao, Yuqing, et al. "III–V photonic integrated circuits for beyond-telecom applications." Wireless and Optical Communication Conference (WOCC), 2016 25th. IEEE, 2016.
[5] Kim, H-J., et al. "Comb-based programmable RF photonic filter with an InP arrayed waveguide grating pulse shaper." Lasers and Electro-Optics (CLEO), 2016 Conference on. IEEE, 2016.
[6] Zhang, Chong, et al. "High-speed hybrid silicon microring lasers." Circuits and Systems (MWSCAS), 2015 IEEE 58th International Midwest Symposium on. IEEE, 2015.
[7] Song, Bowen, et al. "3D integrated hybrid silicon laser." Op. Ex. 24.10 (2016): 10435-10444.
[8] Ferrotti, Thomas, et al. "Co-integrated 1.3 μm hybrid III-V/silicon tunable laser and silicon Mach-Zehnder modulator operating at 25Gb/s." Optics Express 24.26 (2016): 30379-30401.
[9] Heideman, R. G., et al. "TriPleX™: The low loss passive photonics platform: Industrial applications through Multi Project Wafer runs." Phot. Conf. (IPC), 2014 IEEE. IEEE, 2014.
[10] Besselink, G. A. J., et al. "Performance of Arrayed Microring Resonator Sensors with the TriPleX Platform." J. Biosens. Bioelectron 7.209 (2016).
[11] Mashanovich, G. Z., et al. "Mid IR Applications of Si Photonics", OECC/PS2016.
[12] Dangel, Roger, et al. "Polymer waveguides for electro-optical integration in data centers and high-performance computers." Optics express 23.4 (2015): 4736-4750.
[13] Keil, Norbert, et al. "Novel Integration Technologies for Disruptive Capacity Upgrade in Data Centre Systems." Optical Fiber Communication Conference. Optical Society of America, 2016.

Heterogeneously Integrated III-V/SOI DBR Laser with Over 7 nm Continuous Wavelength Tuning Range

Sören DHOORE[1, 2*], Gunther ROELKENS[1, 2], Geert MORTHIER[1, 2]
[1]Photonics Research Group, INTEC, Ghent University - imec, Ghent, 9000, Belgium
[2]Center for Nano- and Biophotonics (NB-Photonics), Ghent University, Ghent, 9000, Belgium
* Soren.Dhoore@UGent.be

Many tele- and datacom applications require single-wavelength tunable lasers with easy wavelength control and sufficient tuning range. Such lasers can for instance be used in WDM-based optical networks or to replace fixed wavelength distributed feedback (DFB) lasers. In recent years there has been a lot of interest in tunable lasers heterogeneously integrated on the silicon-on-insulator (SOI) platform. Several heterogeneously integrated III-V/SOI tunable distributed Bragg reflector (DBR) and DFB lasers have already been demonstrated. DBR-types typically employ a single [1] or double silicon ring [2] with heaters as wavelength-selective and tunable element. In recent work we demonstrated a discretely tunable sampled grating (SG)-DFB laser with a discontinuous tuning range of more than 55 nm [3].

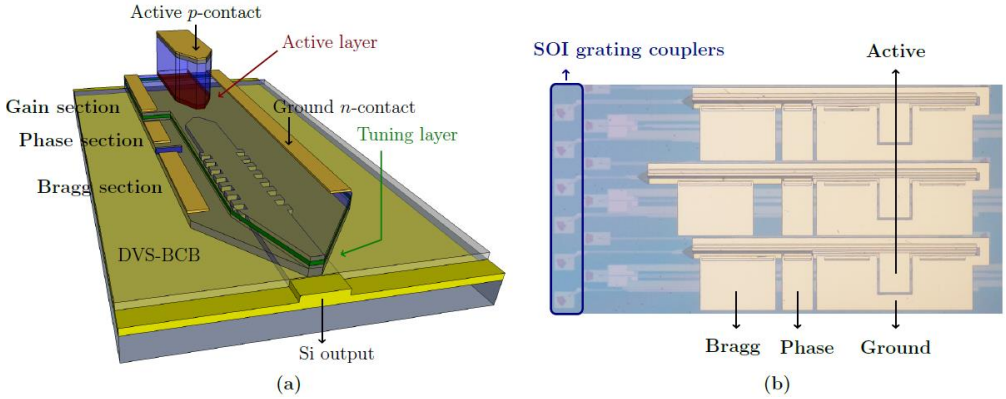


Fig. 1. III-V/SOI tunable DBR laser. (a) Schematic; (b) Microscope image.

Here we demonstrate over 7 nm continuous wavelength tuning with a novel III-V/SOI DBR laser. The laser structure consists of an SOI waveguide circuit on which a III-V tunable twin-guide (TTG) membrane is heterogeneously integrated by means of adhesive DVS-BCB bonding. The TTG membrane comprises an active layer (with 6 InGaAsP quantum wells, bandgap wavelength 1550 nm) and a tuning layer (InGaAsP, bandgap wavelength 1400 nm) in which carriers can be injected to provide gain and phase tuning respectively. The laser cavity is formed by a broadband reflecting facet and a DBR mirror. The latter is implemented as a first-order sidewall-corrugated waveguide grating [4] defined in the 400 nm silicon device layer. The weak sidewall-corrugation provides a narrowband spectral reflection characteristic to ensure single-mode lasing operation. It also provides an additional advantage over ring resonator configurations as for the latter a large free spectral range (FSR) is more difficult to obtain due to minimum bend radii requirements. Fig.1 (a) and (b) show a schematic and microscope image of the laser device respectively. Three laser sections can be discerned: a gain, phase and Bragg section. In the gain section current is injected into the active layer to provide optical gain. The tuning layer is left unbiased. In the phase and Bragg section the active layer is etched

away and current is injected into the tuning layer. Upon current injection the effective index of the waveguide mode is modified through the free-carrier plasma dispersion effect and Joule heating. Simultaneous adjustment of the phase and Bragg current allows for continuous tuning of the lasing wavelength.

Device characterisation is carried out on a temperature-controlled stage at 10°C. Light is couped out from the silicon waveguide to a single-mode optical fiber (SMF) through a reflectionless SOI grating coupler [5]. Fig.2 (a) shows the LI curve of the laser. The threshold current is 60 mA and a maximum waveguide-coupled output power of about −4 dBm is obtained. The superimposed lasing spectra at different tuning currents (Bragg and phase) are shown in Fig.2 (b). The wavelength tuning range is larger than 7 nm. The redshift of the lasing wavelength indicates a dominant heating effect. By improving the heat sinking and a modification of the epitaxial layer stack (by e.g. using a thicker tuning and surrounding cladding layer) in future designs, we expect to significantly increase the optical confinement factor in the tuning layer, resulting in a stronger electronic effect and hence faster tuning (~ns). In that case an adiabatic tapered III-V/SOI coupler similar to one of the couplers reported in [6] can be used.

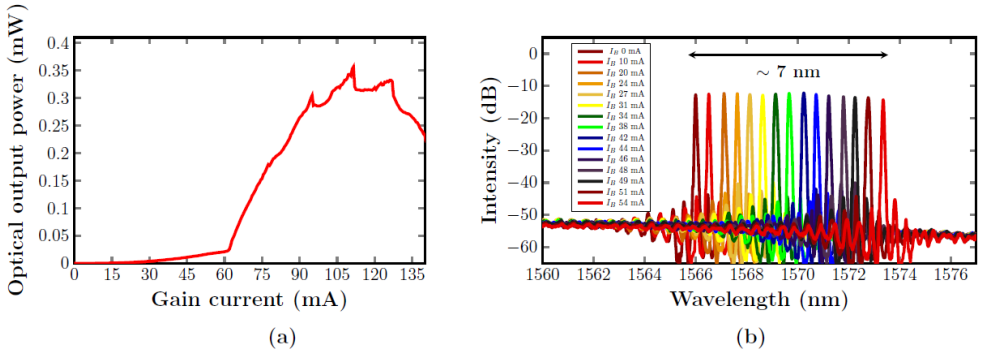


Fig. 2. Static characterization results. (a) LI curve; (b) Superimposed lasing spectra.

References

[1] S. Keyvaninia et al., *Demonstration of a heterogeneously integrated III-V/SOI single wavelength tunable laser*, Opt. Express, vol. 21, no. 3, 3784-3792, 2013.

[2] J.C. Hulme et al., *Widely tunable Vernier ring laser on hybrid silicon*, Opt. Express, vol. 21, no. 17, 19718-19722, 2013.

[3] S. Dhoore et al., *Demonstration of a discretely tunable III-V-on-silicon sampled grating DFB laser*, IEEE Photon. Technol. Lett., vol. 28, no. 21, pp. 2343-2346, 2016.

[4] X. Wang et al., *Narrowband waveguide Bragg gratings on SOI wafers with CMOS-compatible fabrication process,* Opt. Express, vol. 20, no. 14, 15547-15558, 2012.

[5] D. Vermeulen et al., *Reflectionless grating couplers for SOI photonic integrated circuits*, Opt. Express, vol. 20, no. 20, 22278-22283, 2012.

[6] S. Dhoore et al., *Novel adiabatic tapered couplers for active III-V/SOI devices fabricated through transfer printing*, Opt. Express, vol. 24, no. 12, pp. 12976-12990, 2016.

De-multiplexing coherent optical combs within Photonic Integrated Circuits

Maryam SHAYESTEH[1*], Kevin SHORTISS[1], William COTTER[2], Padraic E. MORRISEY[1], Alison. H. PERROT[1,2], Niall. P. KELLY[1], Frank. H. PETERS[1,2]

[1]Tyndall National Institute, Lee Maltings, Dyke Parade, Cork, T12R5CP, IRELAND

[2]University College Cork, Cork, T12 YN60, IRELAND

[*] Maryam.shayesteh@tyndall.ie

Significant research effort has been directed towards successfully demultiplexing the coherent optical combs for use in Coherent Wavelength Division Multiplexing (CoWDM) technologies. Photonic Integrated Circuits (PICs) are a low cost and energy efficient solution. The selective amplification attainable of a target optical comb line via injection locking has already been demonstrated [1]. Here, we investigate the effect device gain has on the amplification of the target and neighbouring comb lines, in an attempt to maximize the side mode suppression ratio (SMSR) achievable using a MMI and slotted Fabry-Perot device. The schematic of the setup consisting of Tunable laser source (TLS), Mach-Zehender Modulator (MZM), Polarization controller (PC), Erbium doped fibre amplifier (EDFA), Photonic integrated circuit (PIC), and the optical spectrum analyzer (OSA) as well as the device under test are presented in Fig. 1. The slave SFP laser was biased to slightly above threshold where it was operating as a multimode laser diode. MMI is biased so that it is transparent and not absorbing the light.

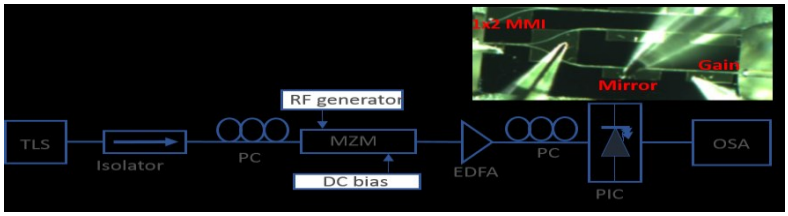


Fig 1: Schematic of the test setup. The inset shows the actual picture of the device which consists of 1x2 MMI, and 2 laser arms.

Initially the wavelength was swept across the resonance of the slave laser. The signal was generated by modulating single wavelength output from TLS. RF frequency was set to 12.5 GHz, and MZM was biased at the null so that the main carrier was suppressed and a 2 line coherent optical comb was generated. This created 12.5 GHz sidebands on each side of the carrier (see Fig. 2a), and would make observations relatively easier on the OSA when the injection locking happened. This is an ongoing experiment and the following step is investigating the de-multiplexing behavior of a comb with 3 lines of equal power. Traces of the OSA recorded for each injected wavelength were used to generate a two dimensional plot which can be seen in Fig. 2b. In this case the three injection locking regions are observed at injection wavelengths of 1551.65, 1551.7, and 1551.85 nm. Interestingly the suppressed mode was able to injection lock as well although with the SMSR less than 15 dB. An SMSR greater that 25 dB was maintained between either of the side bands while the other comb line was injection locked. Also, an SMSR greater than 20 dB is observed for the slave laser side modes.

In another experiment, the effect of driving current in the gain section was examined in order to optimize the SMSR of the slave laser as well as the gain for the filtered subcarriers in the comb. The gain current was increased from 55 to 80 mA, resulting in a higher SMSR and better filtering of each subcarriers of the comb (> 20 dB). However, increasing the current made it more difficult to injection lock the slave laser at some point: e.g. at 80 mA drive current injection locking did not happen. Due to page restrictions, the data is not presented.

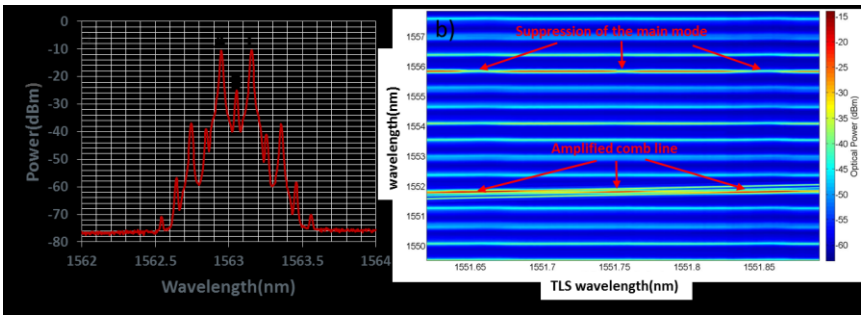


Fig 2: a) Example of the comb signal used for injection. B is the carrier, and A, and C are side bands generated with 25 GHz spacing. b) Intensity plot presenting the optical spectrum of the slave laser as the comb is injected. Each of the subcarriers are injection locked to a laser side mode. Here the laser main mode is suppressed with SMSR bigger that 20 dB. The gain for any of the filtered subcarriers is in excess of 25 dB.

A rate equation model is used to model the comb frequency suppression as the internal gain of the PIC was varied. The model assumes the MMI introduces coupling losses and a phase change to the frequency comb, and the slotted Fabry-Perot device is assumed to be single mode. From Ref. [1], the field within the device is assumed to vary as:

$$\frac{d}{dt}E_s(t) = \frac{1}{2}\left[2i\omega(N) + G(N) - \frac{1}{\tau_p}\right]E_s(t) + \frac{K}{\tau_{in}}E_c(t) \qquad (1)$$

where E_s and E_c are the slave and comb electric fields, ω and G are the optical frequency and differential gain of the slotted Fabry-Perot device, and are dependent on N, the carrier density in the gain section of the device. G_N is assumed to be constant across the frequencies in the model. τ_p and τ_{in} define the photon lifetime and round trip time within the device, and K includes the coupling losses and phase change due to the MMI. As in [4], the rate equations are modified from Ref. [2,3] to include the multiple comb frequencies, by assuming that $E_c(t) = \sum_j E_{inj} e^{i(w_j t + \psi)}$, where ω_j are the frequencies of the comb lines. The rate equations are then modelled as:

$$\frac{d}{dt}E_s(t) = \frac{1}{2}G_N(N(t) - N_{th})E_s(t) + E_{inj}\sum_j \cos\left(\delta\omega_j t - \phi_s(t)\right) \qquad (2)$$

$$\frac{d}{dt}\phi_s(t) = \frac{1}{2}\alpha_H G_N[N(t) - N_{th}] + \frac{E_{inj}}{E_s(t)}\sum_j \sin\left(\delta\omega_j t - \phi_s(t)\right) \qquad (3)$$

$$\frac{d}{dt}N(t) = R_p - \frac{N(t)}{\tau_s} - G_N[N(t) - N_{th}]E_s(t)^2 - \frac{1}{\tau_p}E_s(t)^2 \qquad (4)$$

where $\delta\omega_j$ is the detuning between each comb line and the slotted Fabry-Perot laser's frequency. The numerical simulations will be compared with the experimental results, as the gain of the slave laser is adjusted.

References

[1] W. Cotter, et. al, OSA Applied Optics, Vol. 51, Issue 30,
[2] R. Lang, IEEE J. Quantum Electron. QE-18, 976 1982).
[3] F. Mogensen, H. Olesen, G. Jacobsen, IEEE J. Quantum Electron, QE-21 7 (1985)
[4] D. S. Wu, D. J. Richardson, R. Slavík, Proc. SPIE 8781, Integrated Optics: Physics and Simulations, 87810J (May, 2013)

EUROPEAN CONFERENCE ON INTEGRATED OPTICS

Monolithic tunable lasers for low cost DWDM networks

Jian-Jun He[1,2*], Sen Zhang[1], Jianjun Meng[1], Xiaohai Xiong[1], Huabin Xing[2], Hushan Jin[2], Di Zhong[2], Jiasheng Zhao[2]

[1]State Key Laboratory of Modern Optical Instrumentation, Centre for Integrated Optoelectronics, College of Optical Science and Engineering, Zhejiang University, Hangzhou 310027, China

[2]Lightip Technologies, Co. Ltd., 11. Xi-Yuan Eighth Road, Hangzhou 310030, China

[*]jjhe@zju.edu.cn

Low-cost tunable lasers are key enablers for next-generation dense wavelength division multiplexing (DWDM) based access and metro networks. At present, tunable lasers are mostly deployed in long-haul optical transmission systems due to their high cost resulting from fabrication and operation complexity for structures such as sampled grating distributed Bragg reflector (SGDBR) [1,2]. For wide deployment of the WDM technology in metro, access, and data center networks, the cost reduction of tunable lasers has become a key issue. Recently, a simple and compact tunable V-cavity laser (VCL) has been proposed and demonstrated [3-4]. By using a specially designed half-wave coupler between two Fabry-Perot lasers, a widely-tunable single-mode laser with high side mode suppression ratio (SMSR) is achieved without requiring complex gratings. Discrete wavelength tuning up to 50 channels at 100 GHz spacing has been demonstrated experimentally with a simple tuning algorithm [5]. Single-electrode controlled fast wavelength tuning in the order of ~10ns has also been achieved by using a quantum well intermixed tuning section [6].

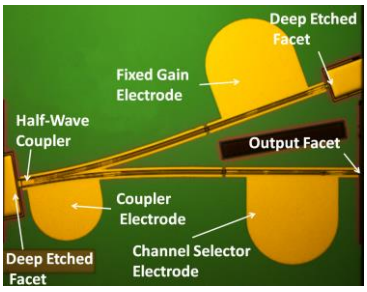


Fig. 1. Photograph of the VCL chip

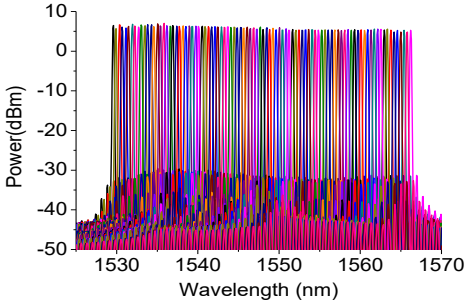


Fig.2. Measured spectra of 93 channels with 50GHz spacing.

Figure 1 shows the top-view photograph of the V-Cavity laser chip. It consists of two Fabry-Perot cavities with slightly different optical path lengths. The length of the fixed gain cavity is designed to be 450μm to match its resonant wavelengths to the ITU grid of 100 GHz spacing. The channel selector cavity is 5% longer so that the Vernier effect

can be used to achieve a wide tuning range. The two cavities are coupled through a half-wave coupler which has a π-phase difference between the bar-coupling and cross-coupling coefficients to achieve high SMSR. In order to control the cavity lengths precisely, three deep etched facets are used as cavity mirrors. The output is emitted from the etched facet of the channel selector cavity. The back facets on the coupler and on the fixed gain cavity are coated with high-reflective Au film after surface passivation. Three electrodes are deposited on the top surface while a common ground electrode is deposited on the back side. The channel selector electrode on the long cavity is used for wavelength tuning through current injection and the other two electrodes provide the gain. The coupler electrode is also used for direct modulation. Standard fabrication process for ridge waveguide Fabry-Perot lasers is used with an additional step of deep etching for making the reflective mirrors. The chip size is only about 500μm × 350μm.

Figure 2 shows the measured spectra for 93-channels on the ITU grid with 50GHz spacing. A dynamic SMSR of about 37dB is achieved when the laser is directly modulated at 2.5Gbps. The static SMSRs without the modulation signal are typically 2~3dB higher. The fiber coupled power is about 6dBm. By adjusting the current of the channel selector electrode and the TEC temperature control, we can obtain 47 channels from 1529.55nm to 1566.31nm of the ITU grid in 100GHz spacing, covering the full C band. To access the 50GHz spacing grid, we change the TEC temperature by about 4-5°C to tune to 46 channels from 1529.94nm to 1565.9nm, which are shifted by 50GHz from the previous grid. By slightly adjusting the current of the coupler electrode, the output power of the channels can be balanced.

Tunable transmitter optical sub-assembly (TOSA) and SFP transceiver modules have been developed based on the V-cavity laser. For data rate at 2.5Gbps, error free transmission over 50km is achieved with excellent eye diagrams. The receiver sensitivity penalty is less than 0.5dB for 25km transmission and less than 1dB for 50km transmission. Error free transmissions are also achieved for 25km at 5Gbps and 10km at 10Gbps. Thanks to the built-in Fabry-Perot etalons in the laser, excellent wavelength stability is achieved even though no wavelength locker is used. The frequency variation over a 10-day period is about 0.5GHz under reliability test at 70°C ambient temperature. Since the VCL is much simpler and more compact compared to other widely tunable lasers, the VCL-based tunable TOSA and SFP modules have great potential for low-cost mass deployment in metro and access networks.

References

[1] B. Mason, G. A. Fish, S. P DenBaars, and L. A. Coldren, *Widely tunable sampled grating DBR laser with integrated electroabsorption modulator*, IEEE Photon. Technol. Lett. 11, 638-640, 1999

[2] L. A. Coldren, *Monolithic Tunable Diode Lasers*, IEEE J. Sel. Topics in Quantum Electron. 6, 988, 2000

[3] J.-J. He and D. Liu, *Wavelength switchable semiconductor laser using half-wave V-coupled cavities*, Opt. Express 16, 3896-3911, 2008

[4] J. Jin, L. Wang, Y. Wang, T. Yu, and J.-J. He. *Widely wavelength switchable V-coupled-cavity semiconductor laser with ~40 dB side-mode suppression ratio*, Opt. Lett. 36, pp. 4230-4232, 2011

[5] S. Zhang, J. Meng, S. Guo, L. Wang and J.-J. He, *Simple and compact V-cavity semiconductor laser with 50x100 GHz wavelength tuning*, Optics Express 21, 13564, 2013

[6] X. Zhang, J.-J. He, N. Liu, and J. J. Dubowski, *Carrier-induced fast wavelength switching in tunable V-cavity laser with quantum well intermixed tuning section*, Optics Express 23, 26336, 2015

EUROPEAN CONFERENCE ON INTEGRATED OPTICS

Microwave and RF Photonic Applications of Micro-Combs

Xingyuan Xu,[1] Jiayang Wu,[1] Mehrdad Shoeiby,[2] Sai T. Chu,[3] Brent E. Little,[4] Roberto Morandotti,[5], Arnan Mitchell,[2] and David J. Moss[1,*]

[1]*Centre for Micro-Photonics, Swinburne University of Technology, Hawthorn, VIC 3122 Australia*
[2]*School of Engineering, RMIT University, Melbourne, VIC 3000, Australia*
[3]*Department of Physics and Material Science, City University of Hong Kong, Hong Kong, China.*
[4]*Xi'an Institute of Optics and Precision Mechanics Precision Mechanics of CAS, Xi'an, China.*
[5]*INRS –Énergie, Matériaux et Télécommunications, Varennes, Québec, J3X 1S2, Canada.*
*dmoss@swin.edu.au

Photonic integrated circuits that exploit nonlinear optics for all-optical signal processing have been demonstrated, particularly in silicon, including all-optical logic [1], demultiplexing from 160Gb/s [2] to over 1Tb/s [3], to optical performance monitoring using slow light at speeds of up to 640Gb/s [4-5], all-optical regeneration [6], and many others. The efficiency of all-optical devices depends on the waveguide nonlinear parameter, $\gamma = \omega n_2 / c A_{eff}$. Although silicon can achieve extremely high values of γ, it suffers from high nonlinear losses due to two-photon absorption (TPA) and the resulting free carriers. Even if the free carriers are eliminated by p-i-n junctions, silicon's poor intrinsic nonlinear figure of merit (FOM = $n_2 / (\beta \lambda)$, where β is the TPA) of around 0.3 in the telecom band is far too low to achieve high performance. While TPA can be turned to advantage for all-optical functions [7-9], for the most part silicon's low FOM in the telecom band is a limitation.

In 2008-2010, new CMOS compatible platforms for nonlinear optics were introduced, including Hydex [8-18] and silicon nitride [19]. These platforms exhibit negligible nonlinear absorption in the telecom band, and have revolutionized micro-resonator optical frequency combs. The first integrated CMOS compatible integrated optical parametric oscillators were reported in 2010 [11,19], showing that Kerr frequency comb sources could be realised in chip form by using ring resonators with relatively modest Q-factors. Following this, a stable modelocked laser with pulse repetition rates from 200GHz to 800GHz was reported [12]. The success of this platform arises from its very low linear loss, its moderate nonlinearity ($\gamma \cong 233 W^{-1}km^{-1}$) and negligible nonlinear loss (TPA) [18].

Here, we review radio-frequency (RF) and microwave photonics applications of micro-combs. Optical frequency combs, and microcombs in particular, are ideal sources with which to base microwave and RF transversal filters on [20]. Many RF applications, including radar mapping, measurement, imaging as well as the realization of advanced modulation formats for digital communications, require the generation, analysis and processing of analogue RF signals where both the amplitude and phase of the signals are important. In-phase and quadrature-phase components of a signal can be obtained via a photonic based Hilbert transform [21]. Figure 1 shows a schematic of our ring resonator, with a Q factor of 1.2 million and FSR of 200GHz [11]. The comb spectrum has a spacing corresponding to the FSR of the microring, and was a "Type II" comb [22] with limited coherence between the comb lines. For the photonic Hilbert transformer demonstrated here, however, this was more than adequate. Figure 1 shows the output of the Hilbert transformer [21], displaying an RF range of over 5

octaves, and a high quality output. We review a wide range of novel RF functions based on microcombs. These devices have significant potential for applications in telecommunications and on-chip WDM optical interconnects for computing and many other applications.

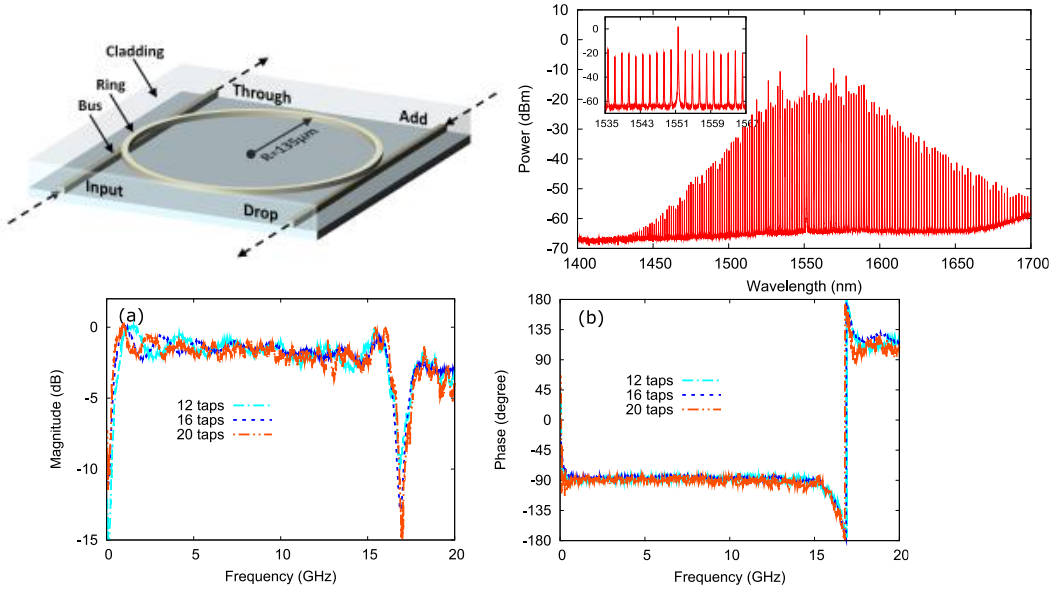


Fig. 1. Integrated ring resonator (top left), output comb spectrum (top right), Hilbert transform output (bottom) for both amplitude and phase.

References

[1] Li, F. et al., Optics Express **19**, 20364-20371 (2011). DOI: 10.1364/OE.19.020364.

[2] Li, F. et al., Optics Express **18**, 3905-3910 (2010). DOI: 10.1364/OE.18.003905.

[3] H.Ji, *et.al.*, Photonics Technology Letters **22** 1762 (2010).

[4] Monat, C. et al., Optics express 18 (7), 6831-6840 (2010). DOI: 10.1364/OE.18.006831.

[5] Corcoran, B., et. al., Optics Express **18**, (8) 7770-7781 (2010). DOI: 10.1364/OE.18.007770.

[6] V.G. Ta'eed, et al., Optics Letters **30** 2900 (2005). DOI: 10.1364/OL.30.002900.

[7] Moss, D.J., et al., "Electronics Letters **41** 320 (2005). DOI: DOI: 10.1049/el:20058051.

[8] M. Lamont, et al., Photonics Technology Letters **18** 1185 (2006). DOI:10.1109/LPT.2006.874718.

[9] A.Tuniz, G.Brawley, D.J.Moss, B.J.Eggleton,, Optics Express **16** 18524 (2008). DOI: 10.1364/OE.16.018524.

[10] Ferrera, M., *et al.*, *Nature Photonics* **2** 737 (2008). doi:10.1038/nphoton.2008.228.

[11] L. Razzari et al., *Nature Photonics* **4** 41 (2010). doi:10.1038/nphoton.2009.236.

[12] M.Peccianti, et al., *Nature Communications* **3** 765 (2012). doi:10.1038/ncomms1762

[13] A. Pasquazi; et al., Optics Express **20** (24) 27355 – 27362 (2012). DOI: 10.1364/OE.20.027355.

[14] A.Pasquazi; et al., Optics Express **21** (11) 13333-13341 (2013). DOI: 10.1364/OE.21.013333.

[15] A.Pasquazi, et al., Optics Express **18**, (8) 7634-7641 (2010). DOI: 10.1364/OE.18.007634.

[16] D. J. Moss, et al., Nature Photonics **7** (8) 597-607 (2013). doi:10.1038/nphoton.2013.183.

[17] M.Peccianti, et al., Optics Express **18**, (8) 7625-7633 (2010). DOI: 10.1364/OE.18.007625.

[18] D.Duchesne, et al., Optics Express **18**, 923-930 (2010). DOI: 10.1364/OE.18.000923.

[19] Levy, J. S., et al., *Nature Photonics* **4**, 37-40 (2010).

[20] V. R. Supradeepa, et al., Nat. Photonics 6 (3), 186–194 (2012).

[21] T.G .Nguyen, et al., Optics Express 23 (17) 22087 (2015). DOI:10.1364/OE.23.022087

[22] Ferdous, F., et al., *Nature Photonics* **5** 770-776 (2011).

EUROPEAN CONFERENCE ON INTEGRATED OPTICS

Efficient nonlinear interactions in GaN waveguides

Maksym GROMOVYI[1*], Fabrice SEMOND[1], Julien BRAULT[1], Aimeric COURVILLE[1], Pascal BALDI[2], Jean-Yves DUBOZ[1], Marc P. DE MICHELI[2]

[1]Université Côte d'Azur, CNRS, CRHEA, rue Bernard Grégory, 06560 Valbonne, France
[2]Université Côte d'Azur, CNRS, INΦNI, Parc Valrose, 06100 Nice, France
[*] Maksym.Gromovyi@crhea.cnrs.fr

Abstract: We have been able to fabricate low loss GaN planar waveguides designed for efficient second harmonic generation. By using modal phase matching we reached 2% power conversion between the TM0 pump and the TM2 harmonic modes.

1. State of the art

Nonlinear interactions in AlGaN semiconductors recently generated considerable research interest [1-3]. Indeed, the combination in these materials of a relatively high nonlinear coefficient 10pm/V, a large transparency window 200nm-5µm and a direct band gap can lead to novel applications in the future.

Although a lot of progress has been done for the sputtered AlN films [3], mono-crystalline AlGaN layers mainly grown by epitaxy on Si or Sapphire substrates still show poor photonic quality [1,4]. In this paper we present an approach, which allows us to fabricate low loss GaN waveguides epitaxially grown on Sapphire substrate. Low propagation losses allow NIR to visible power conversion with 2% efficiency, which to our best knowledge is the highest value reported so far for the GaN waveguides.

2. Fabrication of low loss waveguides for efficient nonlinear interactions

Modal phase matching which is crucial for the efficient nonlinear interactions can be realized in AlGaN waveguides due to the high refractive index difference between GaN and AlN. We exploit this difference to compensate the material dispersion by the modal dispersion in a multi-modal waveguide.

Low propagation losses is a major requirement to obtain efficient SHG. Here we perform a careful study to identify the main sources of propagation losses. We demonstrate that about 1µm thick AlGaN buffer layer is sufficient to isolate all the modes confined in the GaN layer from the substrate and the perturbed nucleation layers. This buffer layer allows us to improve drastically the waveguide performance although the propagation losses still remain to high for SHG (10dB/cm at 630nm).

An important discovery was made during this study when we realised that the so-called kinetic surface roughness associated with the epitaxial growth has a major impact on the waveguide losses. The amplitude of the kinetic roughness depends on the layer

thickness and the growth temperature determines its spatial frequency. As MBE and MOVPE growths, take place at different temperatures, respectively 800°C and 1050°C the surface aspect of the layer depends very much on the chosen process. Combining them, we were able to reduce the amplitude and the spatial frequency of the surface roughness in such a way that the propagation losses drop down from 10 to 1dB/cm.

3. Second harmonic generation

Those low propagation losses allowed us to study second harmonic generation using modal phase matching with the setup shown on Fig. 1. Using the prism-coupling technique we inject the pump at 1260nm in the TM0 mode. The pump propagates about 3mm in the waveguide and generates the harmonic in the TM2 mode at 630nm. Both are collected and separated by a second prism and send on appropriate detectors.

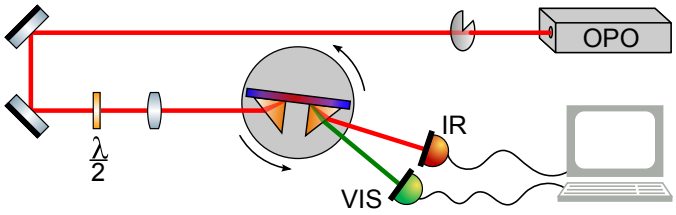


Fig. 1. Experimental setup. Prism coupling is used for the planar waveguide.

In Fig. 2 a) we plot the harmonic signal as a function on the pump wavelength and observe a sharp phase matching curve as predicted by the theory. In Fig. 2 b) we plots the SH intensity as a function of pump energy. The conversion efficiency reaches 2% for 400nJ pump pulses.

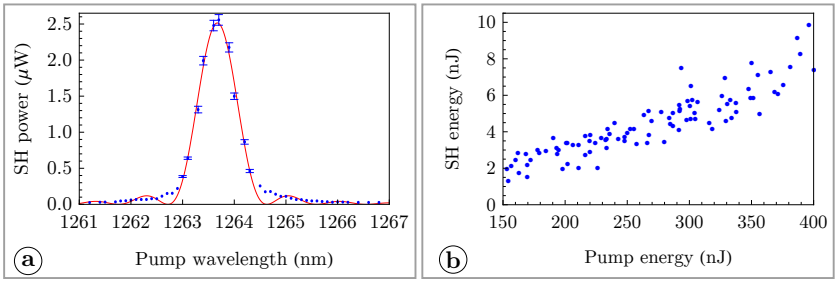


Fig. 2. a) Acceptance curve. b) Harmonic energy as a function of pump energy.

To further improve these state of art results, we plan to fabricate ridge waveguides to reach higher power densities and to use polarity inversion to increase the TM0/TM2 modal overlap.

References

[1] C. Xiong, et al. *Integrated GaN photonic circuits on silicon(100) for second harmonic generation*, Optics Express, vol. 19, no. 11, pp. 10462-10470, 2011

[2] T. Troha, et al. *UV second harmonic generation in AlN waveguides with modal phase matching*, Optical Materials Express, vol. 6, no. 6, pp. 2014-2023, 2016

[3] X. Guo, et al. *Second-harmonic generation in aluminum nitride microrings with 2500%/W conversion efficiency*, Optica, vol. 3, no. 10, pp. 1126-11131, 2016

[4] A. Stolz, et al. *Optical waveguide loss minimized into gallium nitride based structures grown by metal organic vapor phase epitaxy*, Applied Physics Letters, vol. 98, no. 16, pp. 161903, 2011

Hybrid Integrated Photonics for On-Chip Heralded Photon-Number States

Panagiotis VERGYRIS[1*], Thomas MEANY[2], Tommaso LUNGHI[1], Gregory SAUDER[1], James DOWNES[2], M. J. Steel[2], Michael J. Withford[2], Olivier ALIBART[1], Sébastien TANZILLI[1]

1 Université Côte d'Azur, CNRS, Laboratoire de Physique de la Matière Condensée (LPMC), Nice, 06108 Nice cedex 2, France

2 Centre for Ultrahigh bandwidth Devices for Optical Systems (CUDOS), Department of Physics and Astronomy, Macquarie University, North Ryde, 2109 NSW, Australia

* panagiotis.vergyris@unice.fr

Abstract: We show the potential of a hybrid technology for realizing highly complex circuits for quantum photonic applications. We demonstrate the most advanced chip enabling four photon generation and manipulation for heralding tunable two-photon states.

Integrated photonics plays a remarkable role in investigating fundamental quantum phenomena as well as a variety of disruptive quantum technologies [1]. More specifically, the ability of realizing complex and scalable quantum circuits finds repercussions in quantum sensing, secure communication, as well as in quantum computation and simulation, that would be otherwise inaccessible using bulk-optic approaches. Despite this attractive potential, only a few examples of on-chip multi-photon generation and manipulation based on monolithic platforms have been reported to date, due to fabrication challenges [2–4]. Currently, more complex devices are being considered exploiting hybridization of complementary technologies [5]. Following such a strategy, we demonstrate, for the first time, an integrated optical four-photon generator enabling the on-chip engineering of heralded two-photon states thanks to real-time manipulation capabilities.

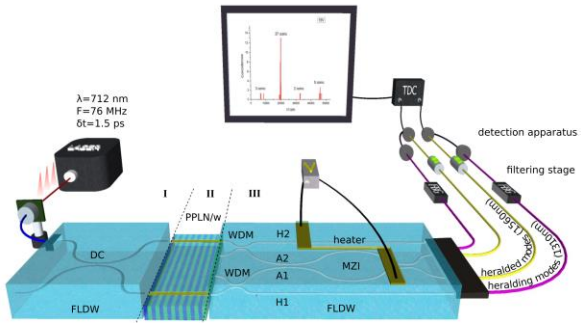


Fig. 1. Configurable two-photon state generator based on the hybridization of two complementary integrated optical technologies.

Lithium niobate (LN) stands as a key plateform for integrated quantum photonics mostly for its optical nonlinear properties. LN's optical-optical nonlinearity allows to efficiently produce photon pairs in low-loss waveguides, while its electro-optical nonlinearity permits to actively route the photons in desired spatial modes [4]. However, the fabrication steps are delicate, therefore limiting the complexity of the considered devices. On the other hand, the femto-second laser direct-writing (FLDW) technique on glass (SiO2) has recently emerged for its fast prototyping of 3D low-loss circuits, despite the lack of efficient optical nonlinearities for photon-pair generation. In our realization, we combine those two complementary platforms for exploiting the best features of both technologies and to demonstrate an advanced photonic device [5].

Our demonstration enables on-chip manipulation of four photons for the generation of configurable two-photon states, for the first time in a heralded fashion. The heralding feature is an important functionality for next generation quantum systems, making it possible to implement efficiently series of quantum operations. More specifically, our device permits producing a variety of path-coded heralded two-photon states, ranging from product to entangled states, thanks to real-time configuration capabilities.

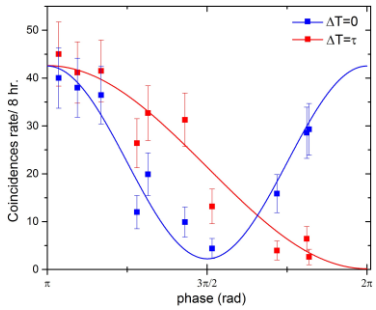


Fig. 2. 4-fold coincidences for single-(red) and two-(blue) photons interference.

Our realization consists of three photonic chips fabricated on either LN for photon generation or on SiO2 substrates for photon manipulation purposes (Figure 1). The input chip routes the pump laser pulses in two spatial modes coupled to two identical periodically poled lithium niobate waveguides (PPLN/w) allowing the simultaneous generation of paired photons spectrally distinguishable (at 1560 nm and 1310 nm) via the process of spontaneous parametric down-conversion. Integrated optical functions ensure the splitting of the photons of each pair and, thanks to an integrated, thermally tunable, Mach-Zehnder interferometer, the manipulation of heralded photon-number states is achieved. Coincidence detection of the two 1310 nm photons in the outer modes heralds the arrival of the two photons at 1560 nm in the inner modes, encoded in the following quantum state:

$$|\psi\rangle \sim \left(1 - e^{i2\varphi(V)}\right)(|20\rangle - |02\rangle)/\sqrt{2} + 2i\left(1 + e^{i2\varphi(V)}\right)|11\rangle, \qquad (1)$$

where the phase $\varphi(V)$ from the interferometer can be tuned by adjusting the temperature gradient between the two arms thanks to the 3D capabilities of the FLDW waveguides. Therefore, the source can prepare on demand, either a two-photon N00N or a product state. By exploiting the capabilities of the time-to-digital converter (TDC) for coincidence counting, we can trace simultaneously the single-photon (red) as well as the two-photon (blue) interference fringes (Figure 2). Both the double phase sensitivity of the two-photon state and the absence of 4-fold coincidences for a given phase $\varphi(V) = 3\pi/2$, confirm the generation of the N00N state and prove that the states are engineered with high levels of purity. This elementary device is opening the route towards merging several key functionalities on a single chip for achieving more complex circuits dedicated to advanced quantum protocols.

References

[1] S. Tanzilli et al., *On the genesis and evolution of integrated quantum optics*, Laser Photon. Rev., vol. 6, pp. 115-143, 2012

[2] B. J. Metcal et al., *Multiphoton quantum interference in a multiport integrated photonic device*, Nat. Commun., vol. 4, pp. 1356, 2013

[3] J. Silverstone et al., *On-chip quantum interference between silicon photon-pair sources,* Nat. Phot., vol. 8, pp. 104–108, 2014

[4] H. Jin et al., *On-Chip Generation and Manipulation of Entangled Photons Based on Reconfigurable Lithium-Niobate Waveguide Circuits*, Phys. Rev. Lett., vol 113, pp. 103601, 2014

[5] T. Meany et al., *Hybrid photonic circuit for multiplexed heralded single photons*, Laser Photon. Rev., vol. 8, pp 42-46, 2014

Integrated Quantum Optics with Electrically Driven Quantum Dot - Micropillars

Pierce MUNNELLY[1*], Tobias HEINDEL[1], Martin KAMP[2], Sven HÖFLING[2,3], Christian SCHNEIDER[2] and Stephan REITZENSTEIN[1]

[1] Institut für Festkörperphysik, Technische Universität Berlin, Berlin 10623, Germany
[2] Technische Physik, Universität Würzburg, Würzburg 97074, Germany
[3] School of Physics and Astronomy, University of St Andrews, St Andrews KY16 9SS, United Kingdom
[*] munnelpb@physik.tu-berlin.de

Abstract

We report on results in the field of integrated quantum optics using a novel integrated photonic device consisting of electrically contacted InGaAs quantum dot-micropillar cavities. Whispering gallery modes support single-mode lasing and radiate within the plane of the active material towards neighbouring, separately contacted micropillars, which are monolithically integrated and can be used for a range of purposes including on-demand single photon generation and investigating opto-electronic feedback.

Device Layout: The micropillars are fabricated on a GaAs substrate and their composition can be seen in Fig. 1 (a). A single micropillar 6-10 microns in diameter is surrounded by a group of five smaller micropillars (diameters ~ 2 microns, see Fig. 1 (b)). The peripheral pillars share one contact with apertures above each pillar for the vertical emission of single photons. The larger central micropillar supports single mode lasing of laterally emitting whispering gallery modes (WGMs); this laser light excites the quantum dots (QDs) in the peripheral pillars, whose spontaneous emission is enhanced by cQED effects. The lasers themselves have high β-factors on the order of 10% on account of their low mode volumes resulting in threshold currents as low as 8 μA [1].

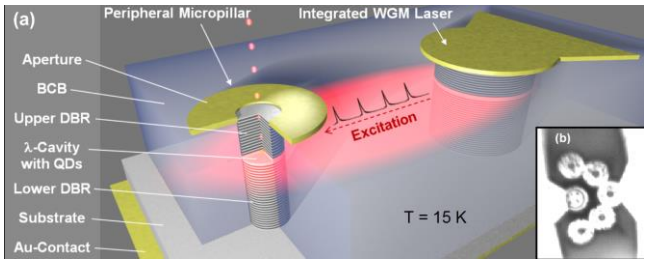


Fig. 1. Sample layout based on pin-doped semiconductor QD-micropillars. a) GaAs/AlAs distributed Bragg reflectors form the top and bottom parts of the micropillars. The central micropillar is an electrically pumped single mode WGM laser which excites the neighboring QD-micropillars. (b) A CMOS camera image of the sample. Pillar-laser separation is 15 μm.

Experimental Setup and Results: The sample is analyzed with a micro-photoluminescence spectroscopy setup at cryogenic temperatures. Purcell factors of between 2 and 4 have been observed in the external pillars [2] as well as single-photon purities of as low as $g^{(2)}(0) = 0.07$ during integrated microlaser excitation, as shown in Fig. 2(c). The emission of these single photons can be spectrally tuned by up to 1.1 meV via the Stark effect as demonstrated in Fig. 2(b). Alternatively, if the bias is negative, the micropillars serve as photodetectors, converting laser light into photocurrent which has been used to determine the laser threshold using a lock-in technique [3], and this photocurrent has been also used in a feedback experiment to generate self-sustained pulses in the laser output, opening possible routes to chaos in the laser emission (c.f. Fig. 2(d)). Further work will focus on on-chip resonant excitation to generate highly indistinguishable photons under pulsed electrical excitation.

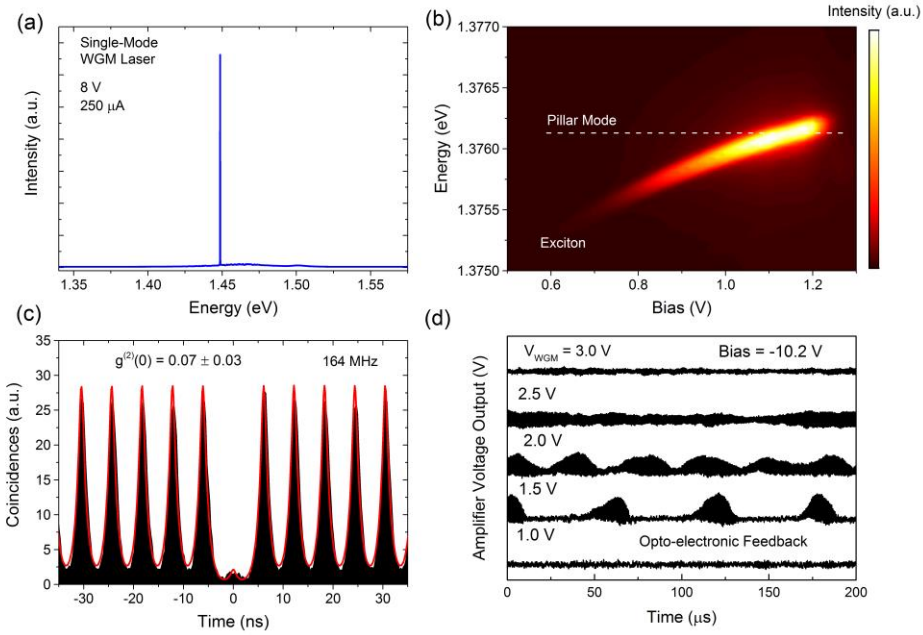


Fig. 2. Experimental results. (a) Single mode lasing from a central WGM microlaser. (b) Electro-optical tuning of a single QD exciton via the Stark effect. (c) Pulsed second order autocorrelation function measured on a QD pumped via the integrated microlaser. (d) Opto-electronic feedback between a microlaser and surrounding micropillars acting as photodetectors, with increasing laser bias V_{WGM}.

References

[1] E. Stock et al., *On-chip quantum optics with quantum dot microcavities,* Adv. Mater. 25, 707, 2013

[2] P. Munnelly et al., *A pulsed nonclassical light source driven by an integrated electrically triggered quantum dot microlaser,* IEEE J. Sel. Top. Quantum Electron. 21, 681, 2015

[3] M. M. Karow et al., *On-chip light detection using monolithically integrated quantum dot micropillars,* Appl. Phys. Lett. 108, 081110, 2016



EUROPEAN CONFERENCE ON INTEGRATED OPTICS

Sub-Wavelength engineered waveguide Bragg filter for optical pump-rejection

Diego PEREZ-GALACHO[1*], Carlos ALONSO-RAMOS[1], Florent MAZEAS[2], Xavier Le ROUX[1], Dorian OSER[1], Weiwei ZHANG[1], Delphine MARRIS-MORINI[1], Laurent LABONTE[2], Sébastien TANZILLI[2], Eric CASSAN[1], Laurent VIVIEN[1]

[1]Centre for Nanoscience and Nanotechnology, CNRS, Univ. Paris-Sud, 91405 Orsay, France
[2]Université Nice Sophia Antipolis, Laboratoire de Physique de la Matière Condensée, CNRS UMR 7336, Parc Valrose, 06108 Nice cedex 2, France
* diego.perez-galacho@u-psud.fr

Silicon photonics has become a major technology in the recent years. Its development has been driven mainly by datacom and sensing applications. However it can also be used for generating and manipulating entangled photon pairs [1]. This paves the way to the envisioned monolithic integration of quantum-processing circuits. On-chip photon pairs generation has been already demonstrated using spontaneous four wave mixing in Si microresonators [1]. Due to huge difference in terms of power between the pump signal and the photon pair signal, on-chip pump-rejection filters are required in order to use this kind of nonlinear sources. The requirements for these filters comprise not only high rejection but also narrow bandwidth (typically around 1nm). Implementing on-chip filters with those characteristics is nowadays a real challenge. Architectures based on contradirectional couplers [2] and rings and reflectors [3] have been reported with sub-nanometer bandwidth, however they lack the appropriate rejection levels. Ultra high rejection can be obtained with Mach-Zehnder interferometer based filters [4], but they need active tuning and often exhibit broader bandwidth. Bragg filters can be used just properly designing the modulation of the waveguide width, but in order to meet the bandwidth demands corrugations width below 10nm can be required [5], complicating its fabrication. In this work, we present a Bragg filter based on Sub-Wavelength Grating (SWG) waveguides overcoming these fabrication constraints. Its schematic representation is shown in Fig. 1 (a), it is based on dividing the Bragg period (Λ_B) into two SWG periods (Λ_1, Λ_2). The widest part of each SWG period are slightly different (ΔW), implementing an effective Bragg grating width corrugation. Using this approach the minimum width corrugation is no longer limited by the minimum feature size (as in conventional Bragg filters), but its limitation arises from the resolution of the lithography process. This resolution is normally in the order of just a few nanometers, therefore our approach enables the use of very small modulation widths leading to very narrow filters.

In order to evaluate experimentally the proposed filtering structure, the SWG based Bragg filters were fabricated. We used a 220 nm thick SOI platform with 2µm thick BOX. Since the resolution of our electron-beam lithography process is 5nm, we used that

value as modulating width (ΔW=5nm). SEM pictures of the fabricated filter are shown in Fig (b) and (d).

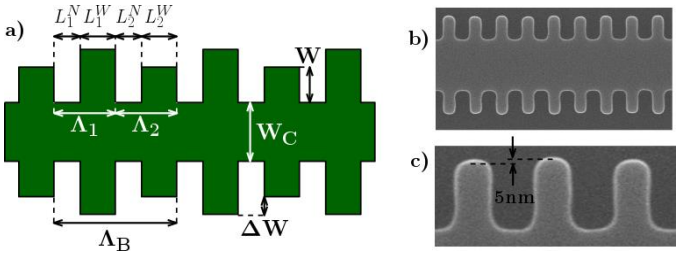


Fig. 1. SWG based Bragg filter: schematic view (a) and SEM pictures (b) and (c).

In order to characterize the device, TE-polarized light was injected and extracted of the chip by means of grating couplers. In Fig. 2 the experimental results of the SWG based Bragg filter are shown for three different lengths, alongside with the results of a straight waveguide. As expected, the longer the filter the higher the rejection. It can be seen that the transmission outside the rejection band is comparable to the reference waveguide in the three cases and it is within the alignment precision of our setup. From Fig. 2, we see that the 1000μm long filter exhibits an outstanding performance with a bandwidth as narrow as 1.1nm and a rejection exceeding 40dB. This represents an improvement close to 30dB in rejection compared to previously reported Si Bragg filters based on SWG engineering [6]. These results are an important step towards the realization of Si pump-rejection filters for on-chip photon-pair sources and quantum processing applications.

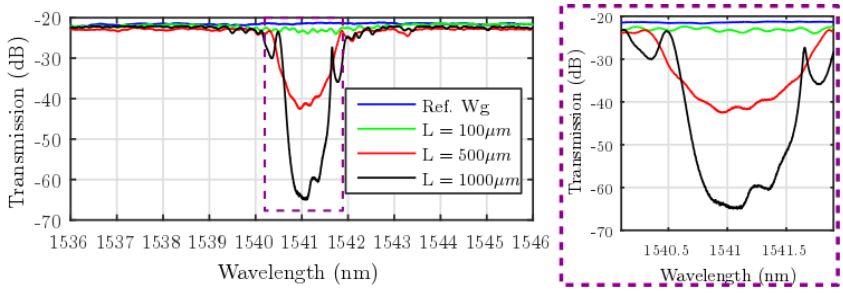


Fig. 2. Experimental results of the fabricated filter for three different lengths.

This work has been supported by the French National project ANR-SITQOM

References

[1] F. Mazeas, M. Traetta, M. Bentivegna, F. Kaiser, D. Aktas, W. Zhang, C. A. Ramos, L. A. Ngah, T. Lunghi, E. Picholle, N. Belabas-Plougonven, X. Le Roux, E. Cassan, D. Marris-Morini, L. Vivien, G. Sauder, L. Labonté, and S. Tanzilli, Opt. Express 24, 28731 (2016).
[2] R. Boeck, M. Caverley, L. Chrostowski, and N. A. F. Jaeger, Opt. Express 23, 25509 (2015).
[3] C. Alonso-Ramos, A. Ortega-Moñux, I. Molina-Fernández, A. Annoni, A. Melloni, M. Strain, M. Sorel, P. Orlandi, P. Bassi, and F. Morichetti, in IEEE 11th International Conference on Group IV Photonics (GFP) (IEEE, 2014), pp. 219–220.
[4] C. M. Wilkes, X. Qiang, J. Wang, R. Santagati, S. Paesani, X. Zhou, D. A. B. Miller, G. D. Marshall, M. G. Thompson, and J. L. O'Brien, Opt. Lett. 41, 5318 (2016).
[5] X. Wang, W. Shi, R. Vafaei, N. A. F. Jaeger, and L. Chrostowski, IEEE Photon. Technol. Lett. 23, 290 (2011).
[6] J. Wang, I. Glesk, and L. R. Chen, Electron. Lett. 51(9), 712 (2015).

Silicon Photonic Transceiver Array based on the Transfer Printing of III-V O-band Photodetectors

Jing ZHANG*[,1], Amin ABASSI[1], Andreas DE GROOTE[1], Ruggero LOI[2], James O'CALLAGHAN[2], Brian CORBETT[2], António José TRINDADE[3], Christopher A. BOWER[3] and Gunther ROELKENS[1]

[1]Photonics Research Group, Ghent University – imec, Technologiepark 15, 9052 Gent, Belgium
[2]Tyndall National Institute, University College Cork, Lee Maltings, Cork, Ireland
[3] X-Celeprint Limited, Cork, Ireland
* jingzhan.zhang@ugent.be

Silicon photonics is emerging as a promising platform for the integration of high-speed optical transceivers and transceiver arrays. The technology allows for the realization of compact optical circuits integrating devices with low power consumption and high bandwidth. In this paper we elaborate on the realization of a 4-channel silicon photonic transceiver array for point-to-point Fiber-To-The-Home (FTTH) optical networks, operating at 10 Gbit/s per channel. In point-to-point optical networks every subscriber has its own transceiver at the central office side. In order to keep size and power consumption of such a central office manageable for a large number of subscribers, the realization of integrated, low power consumption transceiver arrays is of paramount importance. This is exactly the focus of this paper. Figure 1a shows the schematic layout of the 4-channel central office transceiver, while Figure 1b shows the realized chip. A 1550 nm CW laser is coupled to the silicon photonic transceiver, where it is split in 4 channels, each of which has a 10Gbit/s silicon ring modulator to imprint the downstream data on the carrier. For the upstream O-band data signal sent through the same fiber, polarization independent detection is required. In order to achieve the duplexing of the O-band and C-band signal and the polarization independent detection of the O-band signal, O-band III-V photodetectors are integrated on top of the output fiber-to-chip grating couplers of the different channels, as shown in Fig. 2. While allowing polarization independent detection of the upstream O-band signal, the photodetectors are transparent for the C-band downstream signal, by selecting the cut-off wavelength of the III-V absorbing material to be 1.37um. This enables the realization of transceiver arrays for the central office.

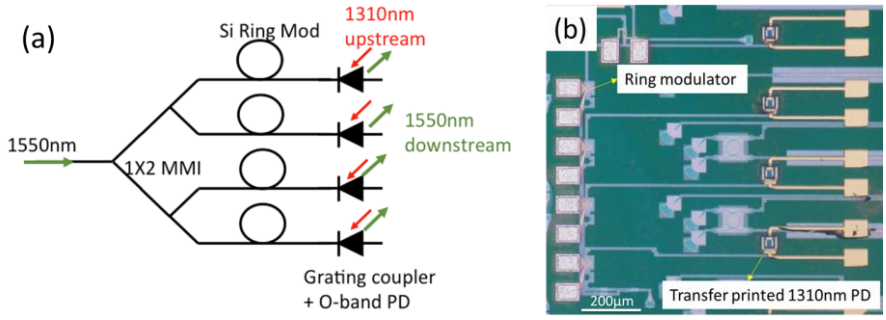


Fig. 1: (a) Schematic of the III-V-on-silicon FTTH central office transceiver array; (b) microscope image of the realized chip

The integration of the III-V photodetectors was realized using a transfer printing approach [1,2], allowing for an efficient use of III-V semiconductor material and enabling the low-cost, 200mm or 300mm wafer-scale integration of the O-band photodetectors on a silicon photonic wafer.

The photodetectors have an aperture of approximately 30 x 40um resulting in a 3dB bandwidth (at -3 V bias) of 11 GHz. Of key importance for the operation of the transceiver is the transparency of the photodetector for the downstream C-band signal. This was verified under CW conditions, as shown in Fig. 2. The responsivity for the O-band signal is 0.4-0.5 A/W, while that for the C-band signal was 0.025-0.03 mA/W, resulting in more than 40dB suppression of the C-band signal. The dark current of the photodetectors varied between 0.6-1.1 uA at -3V bias.

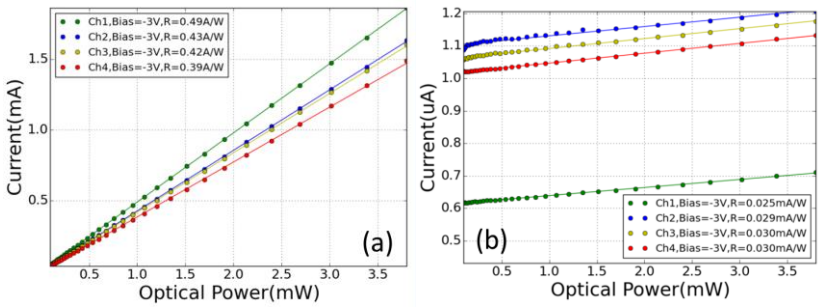


Fig. 2: (a) Photocurrent as a function of optical input power for the O-band signal; (b) Photodetector current as a function of optical input power for the C-band signal (-3V bias)

The ring resonator modulators had a 3dB bandwidth of 15 GHz, easily enabling 10 Gbit/s operation. A 2.5 Vpp voltage swing allows 12 dB extinction ratio of the 1550 nm carrier. Using this circuit we successfully demonstrated the operation at 10Gbit/s of all 4 channels, both upstream and downstream. Upstream wavelengths spanning from 1270 nm to 1350 nm were successfully used. Almost no polarization dependent loss was observed. Error-free operation for the upstream signal is obtained at 0dBm optical input power (due to the lack of an integrated transimpedance amplifier). The downstream signal quality was evaluated using a commercial C-band receiver, showing error free operation at a received power of -11 dBm. The overlayed 10G eye diagrams of the upstream and downstream signal are shown in Fig. 3.

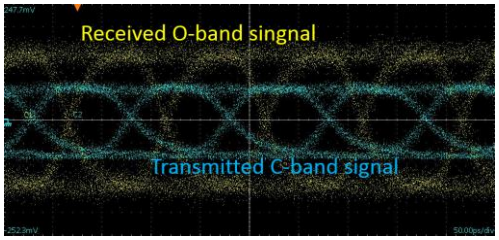


Fig. 3: Overlaid 10G eye diagrams of the upstream (O-band) data signal and downstream (C-band) data signal

Part of the work was supported by the H2020 project TOPHIT under the ICT2-2014 Smart System Integration program.

References

[1] J. Justice , C. Bower, M. Meitl, M. Mooney, M. Gubbins, B. Corbett, *Wafer-scale integration of group III-V lasers on silicon using transfer printing of epitaxial layers*, Nat. Phot. 6, 610-614 (2012)

[2] A. De Groote, A. De Groote, P. Cardile, A. Subramanian, A. Fecioru, C. Bower, D. Delbeke, R. Baets, G. Roelkens, *Transfer-printing-based integration of single-mode waveguide-coupled III-V-on-silicon broadband light emitters*, Opt. Express, 24(13), p.13754-13762 (2016)

Balanced Waveguide Avalanche Photodetector Chip

Tobias BECKERWERTH, Gan ZHOU, Sten SEIFERT, Angela SEEGER, Patrick RUNGE, Martin SCHELL
Fraunhofer Heinrich Hertz-Institute, Einsteinufer 37, 10587 Berlin

Abstract: We demonstrate a balanced waveguide avalanche photodiode chip with high bandwidth, sensitivity, linearity and low polarization dependence over the entire C-band. Moreover, we emphasize the integration with a homodyne coherent receiver for coherent transmission in data-centers.

1. Introduction

The worldwide internet traffic is still growing and short-haul transmission in intra- (0.5 to 2km) and inter-data center (<80 km) traffic covers more than 70% of overall traffic volume [1]. This raises the demand of optical-networks and therefore photodetectors which fulfill high sensitivity reducing the power consumption and also linearity for operation at higher modulation formats has to be achieved. For these specifications balanced avalanche photodetectors in a homodyne setup seem a suitable solution since avalanche photodiodes have proved to fulfil the requirements even for 100-Gb/s ethernet applications [2].

The presented balanced avalanche photodiode realizes good linearity as well as high output power and bandwidth above 20 GHz. This shows the potential for 28 Gbaud transmission systems. A conceptual setup of a homodyne receiver using two balanced APD chips is presented.

2. Design and Fabrication

The fabricated balanced APD is designed by using a SACM structure including a partially p-doped absorber region. The absorbing region consists of InGaAs while the multiplication and charge layer material is InAlAs [3,4]. The layer structure was grown on a waveguide lattice matched to InP using MOVPE on a 3-inch wafer. Furthermore, the balanced photodetector chip includes two single mode fibre spot-size converters and an integrated electrical bias network consisting of integrated capacitors and resistors.

3. Measurement Results

The photodetector chip is characterized by measuring the DC performance including gain and intrinsic responsivity but also the RF performance in terms of bias dependent bandwidth and linearity independently for each photodiode. In Fig.1 the measured dark current, photocurrent and resulting gain characteristics are presented. It shows a gain up to M=14 while the reverse bias voltage is not higher than 16 V. At unity gain voltage U_{M1}= 8.5 V the responsivity is higher than R > 0.60 A/W over the entire C-Band with a dark current lower than 10 nA (Fig.1). Additionally, the PD shows low polarization dependency where the PDL is

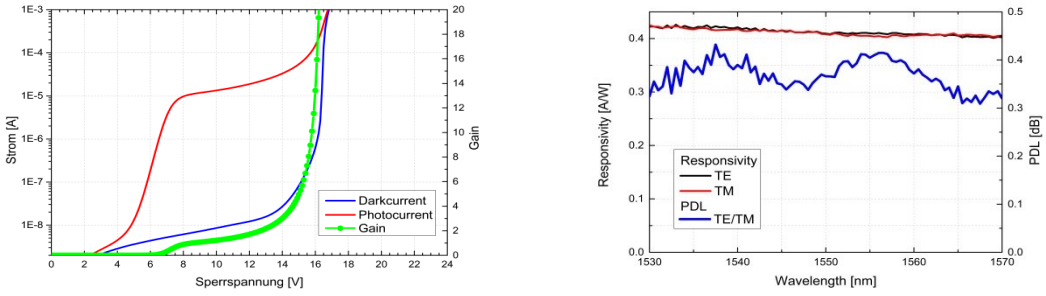


Fig. 1 UI-characteristics (left) and responsivity (right) of fabricated APD chip

below 0.5 dB. The f_{3dB} bandwidth as well as the linearity was measured separately on chip level applying different bias voltages U corresponding to different gains. The bandwidth (Fig.2) is up to f_{3dB}=24 GHz for low

gain at U=12 V and decreases with increasing bias voltage. For a gain up to M=5.5 at an operation voltage of U=15V the resulting bandwidth is still f_{3dB}=20 GHz for both APDs being sufficient for 28 Gb/s. At a higher gain up to M=14 a f_{3dB} bandwidth of 17 GHz is obtained.

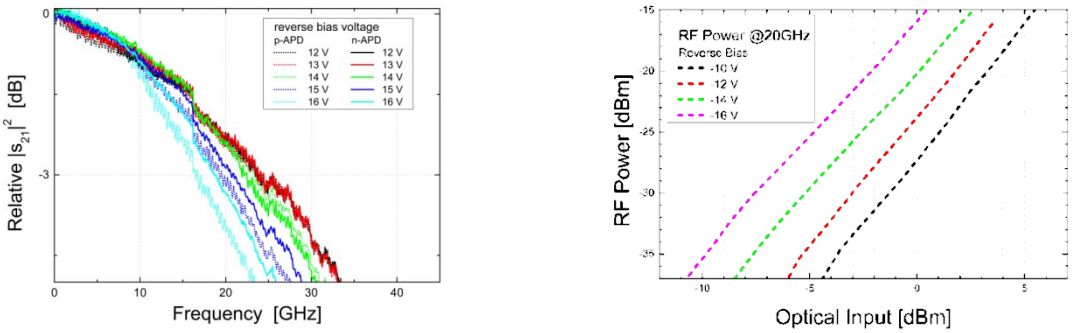


Fig.2 bias dependent bandwidth (left) and linearity measurement (right) of balanced APD chip

This results in a maximum gain-bandwidth-product of GBP = 238 GHz and responsivity-bandwidth product of 147 A/W GHz. The linearity of the chip was determined by varying the input power and measuring the RF ouput power at 20 GHz of frequency (Fig.2). A good linear behavior for input powers in the range of -10 to 5 dBm can be observed. As a result, the chip can detect higher modulation formats. A possible setup to use the chip for homodyne detection is proposed in Fig.3. Therefore, the same platform as in [5] can be used and the local oscillator (LO) is replaced by a delayed input signal. Due to the use of balanced photodiodes the difference of photocurrents can be obtained directly. In that way the overall power consumption of the receiver circuit is additionally reduced.

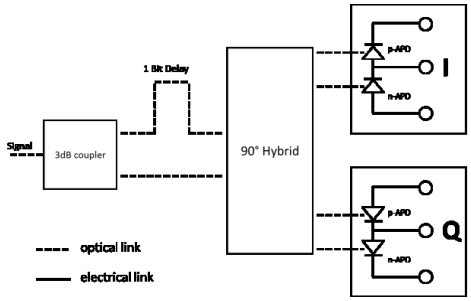


Fig. 3 Conceptual circuit model of homodyne receiver using balanced APD chips

4. Conclusion

A waveguide integrated balanced APD chip with high sensitivity and good linearity was demonstrated showing a bandwidth of 20 GHz at an overall responsivity of R=3.2 A/W and a SNR above 100. The high sensitivity, output power and linearity fulfill all demands for coherent receiver at 28Gb/s. With a homodyne setup the LO can be eliminated and when biasing the detector below U=16V even power consumption and heating can be reduced. First results on for O-band show low polarization dependence and even higher responsivity than in the C-band which all in all makes it a good candidate for data center applications.

[1] C. Xie, "Optical Interconnects for Data Centers",2016 IEEE PHOTONICS CONFERENCE, 29th Conf. of the IEEE Photonics Society (Waikoloa Village, USA, Octobre 2-6, 2016)

[2] M. Nada, "Vertical illumination InAlAs avalanche photodiode for 50-Gbit/s applications", 26th Int. Conf. on Indium Phosphide and Related Materials (Montpellier, France, May 11-15, 2014)

[3] J. C. Campbell, *Fellow, IEEE*, *Recent Advances in Avalanche Photodiodes,* JOURNAL OF LIGHTWAVE TECHNOLOGY, VOL. 34, NO. 2, JANUARY 15, 2016

[4] S. Shimizu, K. Shiba, T. Nakata, K. Kasahara and K. Makita, "40 Gbit/s waveguide avalanche photodiodewith p-type absorption layer and thin InAlAs multiplication layer", ELECTRONICS LETTERS 12th April 2007 Vol. 43 No. 8

[5] P. Runge, "80 GHz Balanced Photodetector Chip for Next Generation Optical Networks" ,Optical Fiber Communication Conference 2014**,** (San Francisco, USA, 9-13 March, 2014)

EUROPEAN CONFERENCE ON INTEGRATED OPTICS

Noise Insensitive Transparent Light Monitoring on a Silicon Photonics Chip

Douglas O. M. de AGUIAR, Andrea ANNONI, Emanuele GUGLIELMI, Francesco ZANETTO, Francesco MORICHETTI, Marco SAMPIETRO, Andrea MELLONI*
Dipartimento di Elettronica, Informazione e Bioingegneria, Politecnico di Milano,
Via Ponzio 34/5, Milano, 20133, Italy
* andrea.melloni@polimi.it

The complexity scaling up of photonic integrated circuits (PICs) enables the manipulation of many optical signals on a photonic chip, to perform operation like channel (de)multiplexing, routing, and switching. For these applications, it is useful to be able to identify each data channel inside the PIC, regardless of the presence of other concurrent channels and optical noise. In this work, we report on the optical signal to noise (OSNR) tolerance of on-chip channel monitoring performed with a transparent detector, namely ContactLess Integrated Photonic Probe (CLIPP) [1], which is integrated in a silicon photonics (SiP) waveguide. We show that, regardless of noise, the CLIPP can measure the power of optical channels that are suitably labelled through a weak modulation tone. An accuracy as high as 0.2 dB is demonstrated for an on-chip OSNR as low as 5 dB/0.1nm, with a power sensitivity of about -28 dBm.

The CLIPP device used in the experiment is shown in Fig. 1a. The CLIPP consists of two metal electrodes (20 µm × 50 µm size, 50 µm spacing) deposited on top of a straight SiP channel waveguide, with a 480 nm × 220 nm Si core buried in a SiO_2 cladding. The light intensity in the waveguide is monitored by measuring the change of the Si resistivity R_{wg} (Fig 1b) induced by surface state absorption at the core-cladding interface [1]. For the CLIPP read-out, one electrode of the CLIPP is driven with a voltage V_e = 2 V (at 100 kHz), while at the second electrode a current signal i_e providing information on the light intensity in the waveguide is detected with a low-noise lock-in system [1].

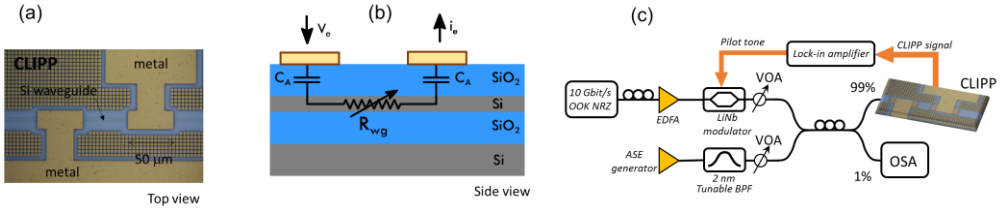


Fig. 1. (a) Top view photograph of a CLIPP integrated on a straight SiP waveguide; (b) Side view sketch of the CLIPP device; (c) experimental setup used in the experiment.

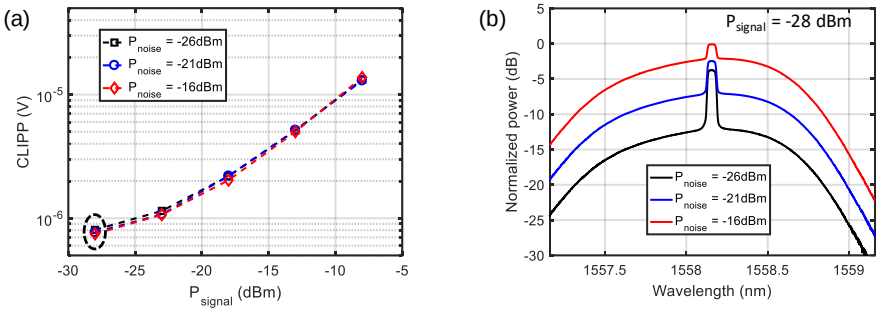


Fig. 2. (a) CLIPP signal vs on-chip signal power (P_{signal}) for different levels of noise power. (b) Spectra of the noisy signal measured when P_{signal} = -28 dBm, for different level of noise.

The experimental setup used in the experiment is shown in Fig. 1c. A pilot tone with a low modulation index at 3 kHz is superimposed to a 10 Gbps OOK signal generated by a commercial $LiNbO_3$ modulator. An ASE noise source (not labelled with tones) is coupled to this signal via a 90/10 fiber coupler, after being filtered by a 2 nm tuneable filter. Variable optical attenuators (VOAs) are used to control the *off-chip* OSNR level between 2 dB (worst case, on-chip signal power P_{signal} = -8 dBm) and 32 dB (best case, P_{signal} = -28 dBm), evaluated over a 0.1 nm bandwidth. Since the noisy signal is coupled to the SiP through polarization selective grating couplers working on TE polarization, the *on-chip* OSNR level is 3dB higher than the off-chip OSNR monitored with the optical spectrum analyser (OSA). As the ASE signal is not labelled with a tone, demodulation of the CLIPP at the frequency of the pilot tone can provide direct information on the signal power [2].

Figure 2a shows that, the electrical signal provided by the CLIPP (after demodulation at the tone frequency) is insensitive to the noise level, whose on-chip total power P_{noise} is increased from -26 dBm (black squares) to -16 dBm (red diamonds). Accurate signal monitoring is achieved even when the on-chip signal power drops to -28 dBm, at this level the noise power being more than 10 dB higher than the signal power. The spectra in Fig. 2b show that when P_{signal} = -28 dBm, the off-chip OSNR is as low as 2 dB (5 dB on-chip OSNR). From the horizontal drift of the curves in Fig. 2a, we estimate an accuracy of about 0.5 dB in the signal power monitoring, regardless of the noise power level.

Our results demonstrate the possibility to perform accurate on-chip monitoring of a noisy signal through a transparent detector. We demonstrated power measurement of signals with on-chip OSNR as low as 5 dB/0.1 nm with an accuracy of 0.5 dB, a sensitivity of -28 dBm and a dynamic range of 20 dB. Applications of the proposed technique to the on-chip monitoring of the OSNR are also expected. This could be particularly useful in III-V platforms, where the CLIPP concept has been demonstrated, to monitor the noise level of integrated amplifiers.

This work has been supported in part by the European Commission through the H2020 project ICT-STREAMS (Contract No. 688172).

[1] F. Morichetti, et al., "Non-invasive on-chip light observation by contactless waveguide conductivity monitoring," IEEE J. Sel. Topics Quantum Electron. 20, 292-301 (2014).

[2] S. Grillanda, et al. "Non-Invasive Monitoring of Mode-Division Multiplexed Channels on a Silicon Photonic Chip," J. Lightwave Technol. 33, 1197-1201 (2015).

Demonstration of Silicon-On-Insulator Coherent receiver for Radio-Over-Fiber applications

Jose D. SARMIENTO-MERENGUEL[1*], Jochem VERBIST[3], Jing ZHANG[2,4], Bart MOENECLAEY[3], Johan Bauwelinck[3], Xin Yin[3], Robert HALIR[1], Alejandro ORTEGA-MOÑUX[1], Íñigo MOLINA-FERNÁNDEZ[1], Gunther ROELKENS[2,4].

[1]Universidad de Málaga, Dept. de Ingeniería de Comunicaciones, ETSI Telecomunicación, Campus de Teatinos s/n, Málaga, 29071, Spain

[2]Photonics Research Group, Dep. INTEC, UGent-imec, 9052 Ghent, Belgium

[3]IDLab, Dep. INTEC, UGent-imec, 9052 Ghent, Belgium

[4]Center for Nano- and Biophotonics, Ghent University, 9000 Ghent, Belgium

[*]jdsm@ic.uma.es

Radio-Over-Fiber transmission has emerged during the last years as a promising technology allowing the seamless integration of optical and wireless technologies. One of the most relevant applications of RoF systems is found in mobile networks, specifically in the transmission of RF signals from the base station (BS) to the central office (CO), as shown in figure 1 (a). Most of the current approaches are based on intensity-modulation/direct-detection (IM-DD) systems [1]. On the other hand, schemes based on complex modulation formats, i.e. phase modulation and coherent detection (PM-CD), have also been proposed, overcoming the limited dynamic range of the IM-DD systems, and offering the coherent detection advantages, such as mitigation of fiber transmission impairments through signal processing, coherent gain, etc. [2]. Moreover, in coherent reception schemes, by properly tuning the local oscillator, down-conversion of the RF signal can also be performed, thus relaxing the electronics. Furthermore, taking advantage of the coherent gain, the RF amplifier usually located at the base station can be theoretically omitted, reducing the operation costs. In this contribution, a Silicon-On-Insulator (SOI) coherent receiver with low power consumption [3] is demonstrated, shown in Figure 1(b), for the reception of RoF signals in the uplink, from the BS to the CO, for the first time. In this proof of concept, coherent gain and improved error magnitude (EVM) compared to IM-DD is demonstrated.

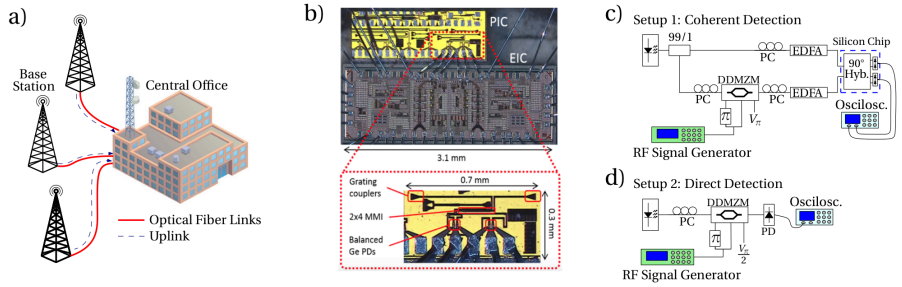


Fig. 1. a) Application of RoF transmission in the mobile access network; b) Microscope picture of the silicon photonic coherent receiver with integrated transimpedance amplifier; c) Setup 1, used for coherent reception of RoF signals; d) Setup 2, used for direct-detection reception of RoF signals.

Figure 1 (c) and (d) show the two different setups employed for the demonstration. Setup 1, shown in Fig. 1 (c), has been used for the demonstration of RoF coherent reception. In this setup light from a laser source is split, in a 1/99 power divider. The smaller fraction is used for the local oscillator signal, and the rest is sent to a dual drive Mach-Zehnder modulator (DDMZM). The modulated RF signal is generated at 3.5GHz using a vector signal generator. This RF signal is divided in two branches, introducing a 180º phase shift in one of them.

The bias point of the DDMZM is set to V_π so that the RF signal linearly modulates the optical field. Due to the insertion losses of the grating couplers in the coherent receiver ($IL \approx 15\ dB$) it has been necessary to employ an EDFA amplifier in each of the optical coherent receiver inputs. Setup 2, shown in Fig. 1 (d), is used to evaluate the operation of an IM-DD scheme, in order to compare the performances of both scenarios. In this case the MZM is biased in its quadrature point, pursuing intensity modulation.

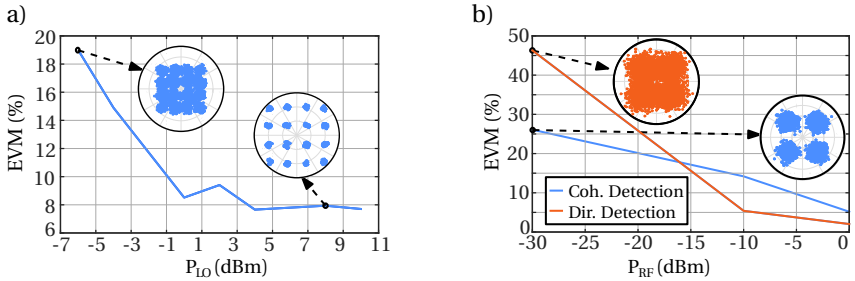


Fig. 2. a) EVM as a function of the on-chip LO power (P_{LO}). Representative received constellations are shown (P_{RF} is set to 0 dBm); b) EVM for coherent vs. direct detection. At low P_{RF} coherent detection, (on-chip P_{LO} of 10 dBm), exhibits better performance.

In a first experiment, the performance improvement due to the coherent gain is demonstrated in setup 1, using a 160 Mbps 16QAM as baseband signal. The error vector magnitude (EVM) of the received constellation was measured as a function of the power of the local oscillator. Figure 2 a) shows the result of this experiment, where the on-chip power of the local oscillator is swept from -6 to 10 dBm. It can be observed that as the LO power increases, the EVM becomes smaller, thus demonstrating the improvement in the performance. The second experiment consists in demonstrating that in similar conditions, for low RF signal power (as it happens in real scenarios), coherent reception presents better performance than direct detection. In this case, a 160 Mbps QPSK baseband signal is employed in both setups. In order to fairly compare both schemes, measurements are done for the same optical signal power at the input of the receivers. Figure 2 b) shows the measured EVM in both cases, as a function of the RF signal power. It can be seen how for lower RF signal power the direct detection exhibits higher EVM than the coherent detection, demonstrating that coherent reception can be a better alternative. In summary, the results presented in this work demonstrate the operation of a SOI integrated coherent receiver for RoF signal reception. Coherent gain is demonstrated, which can imply the substitution of the RF amplifier located in the base stations. Furthermore, the operation of the coherent receiver has been compared with a direct detection scheme, showing better performance for low power RF signals.

We acknowledge funding from the Ministerio de Economía y Competitividad, Programa Estatal de Investigación, Desarrollo e Innovación Orientada a los Retos de la Sociedad (cofinanciado FEDER), Proyecto TEC2013-46917-C2-1-R, Proyecto TEC2016-80718-R, and the Universidad de Málaga. The contribution of the IDLab members was partly supported by the iMinds IoT research program and the H2020 project Flex5Gware.

References

[1] D. Novak *et al., Radio-Over-Fiber Technologies for Emerging Wireless Systems*, IEEE J. Quant. Electron., vol. 52, no. 1, pp. 1-11, 2016

[2] T.R. Clark *et al., Coherent optical phase-modulation link*, IEEE Photon. Technol. Lett., vol. 19, no. 16, pp. 1206-1208, 2007.

[3] J. Zhang *et al., Compact Low-Power-Consumption 28-Gbaud QPSK/16-QAM Integrated Silicon Photonic/Electronic Coherent Receiver*. IEEE Photon. J., vol. 8, no. 1, pp. 1-10, 2016.



Photonic ICs
for Ultrahigh Speed and Coherent Systems

Andreas UMBACH
Finisar Germany, Reuchlinstraße 10-11, 10553 Berlin, Germany
andreas.umbach@finisar.com

Abstract: Photonic Integrated Circuits both in the InP and SiP material systems are becoming more and more popular as they provide solutions to the challenges of more and more miniaturization, optical and rf interconnects and the increasing cost pressure for optical components. Optical coherent transmission systems and photonic microwave photonics are application areas for highly complex and high speed PICs. Receiver PICs and transmitter PICs will be presented and discussed.

Introduction: The ever-growing demand of communication bandwidth driven by increasing use of video in social networks as well as the fast growing number of devices communicating with each other (IoT, Internet of Things) requires the highest possible aggregation of data transmission on single fibers. Gridless wavelength multiplexing is introduced to achieve high spectral density in the available EDFA-spectrum. Polarization multiplexing and complex modulation formats such as DQPSK, 16 QAM or even 64 QAM are applied to increase the number of bits per symbol for an intended reach. The highest possible symbol rates up to 64 GBaud is utilized to achieve the optimum throughput in each wavelength channel. At the same time, faceplate density of internet switches drives the miniaturization of space and power consumption of the very same components and CFP2 and CFP4 pluggable coherent modules are envisaged.

PICs: Photonic ICs comprising a multitude of functionalities are already used in the market and will be further developed. These can range from a parallel array of ultrafast photodiodes connected to a multimode interference coupler serving as an optical power splitter [1] to increase the power handling capability of photodetectors e.g. for millimeter-wave photonic applications, as depicted in Fig.1, to monolithically integrated dual polarization coherent receivers [2] with a set of 4 photodiodes per polarization to detect the differential encoded I and Q signals of the coherent transmission, see Fig.2. Nested Mach-Zehnder-Modulators [3] are used to encode phase and intensity information either to generate radio signals or coherent communication signals. On the transmit side as well as for local oscillators on the receive side narrow line width lasers

[e.g. 4] are required and present an opportunity for further integration on InP or for hybrid integration, if Silicon photonics is the chosen PIC technology.

The performance of these and related PICs on InP will be presented and opportunities for further photonic integration will be discussed.

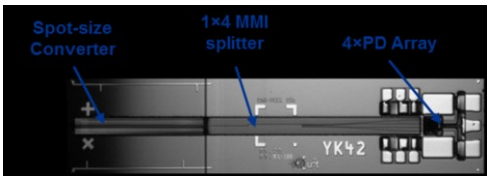


Fig. 1. Four waveguide integrated photodiodes coupled to a 1x4 MMI power splitter and recombined at the electrical rf-output.

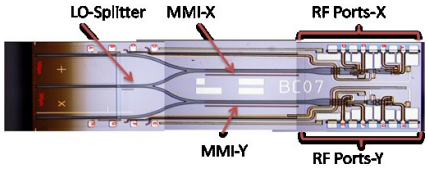


Fig. 2. Dual polarization coherent receiver chip on InP comprising spot-size converters, power splitters and optical mixers and 8 photodiodes.

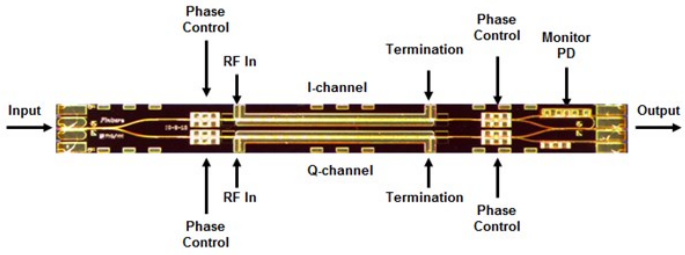


Fig. 3. I-Q modulator PIC on InP, comprising two nested MZMs, monitor PDs, phase control sections and electrical termination.

References

[1] E.Rouvalis, P.Müller, S.Fedderwitz, D.Trommer, J.Stephan, A.Steffan, G.Unterbörsch; "A high-power and high-linearity 50 GHz waveguide photodiode module", Optical Fiber Communication Conference (OFC), paper M2G.1, (2014).

[2] P. Runge, G. Zhou, F. Ganzer, S. Seifert, S. Mutschall and A. Seeger, "Polarisation insensitive coherent receiver PIC for 100Gbaud communication," 2016 Optical Fiber Communications Conference and Exhibition (OFC), Anaheim, CA, 2016, pp. 1-3.

[3] K. Prosyk, T. Brast, M. Gruner, M. Hamacher, D. Hoffmann, R. Millett, and K. Velthaus, "Tunable InP-based Optical IQ Modulator for 160 Gb/s," in 37th European Conference and Exposition on Optical Communications, OSA Technical Digest (CD) (Optical Society of America, 2011), paper Th.13.A.5

[4] U. Eriksson et al., "High performance narrow linewidth thermally tuned semiconductor laser," 2015 European Conference on Optical Communication (ECOC), Valencia, 2015, pp. 1-3.

EUROPEAN CONFERENCE ON INTEGRATED OPTICS

Robust and energy efficient heterogeneous light sources in silicon

Di LIANG*, Geza KURCZVEIL, Xue HUANG, Marco FIORENTINO, Raymond G. BEAUSOLEIL
Hewlett Packard Labs, 1501 Page Mill Road, Palo Alto, 94304, USA
* di.liang@hpe.com

Bandwidth and power consumption are two primary physical and practical obstacles in conventional metal interconnect to keep Moore's Law valid in complimentary metal-oxide semiconductor (CMOS) circuits. Silicon (Si)-based photonics have been heavily studied to provide an highly integrated, low-cost and volume photonic interconnect solution. We review our effort to develop a new laser control mechanism and employee advanced III-V epitaxial materials in the promising heterogeneous laser platform.

Fig. 1(a) shows the schematic of a three-terminal heterogeneous microring laser which can be cascaded easily to be a CWDM multi-wavelength source. Unlike the typical two-terminal pin diode lasers, the third terminal P2 here is placed on silicon to control a heterogeneous MOS capacitor which is naturally formed by sandwiching a thin layer of dielectric at the III-V/Si bonding interface (Fig. 1(b)). When a voltage is applied to the terminals N and P2, the electric field can accumulate or deplete a large amount of free carriers at the dielectric/semiconductor interface as shown in Fig. 1(c). This results in the useful plasma dispersion effect to tune laser threshold, power and wavelength.

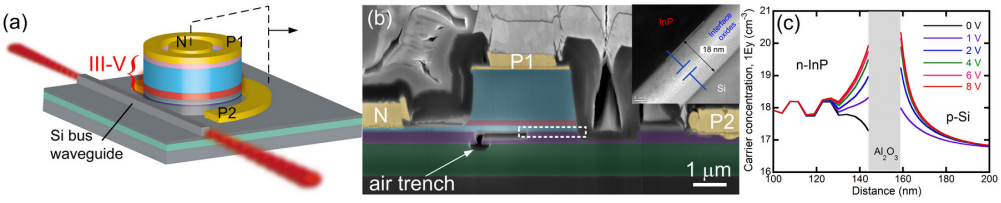


Fig. 1. (a) Schematic and (b) SEM image of a heterogeneous microring laser; inset: TEM image of a MOS capacitor, and (c) its simulated carrier profile at different bias voltages.

Fig. 2(a) shows the continuous-wave (cw) light-current-voltage (LIV) characteristic of a 40 μm-diameter laser at room temperature (RT). When the MOS bias rises from 0 to 4 V, a threshold increase from 8 to 10 mA and a reduction of over 50% in output power i.e., measured detector current, are observed. The lasing wavelength blue-shifts over 0.3 nm, indicating a result of the plasma dispersion rather than heating. The extremely low capacitor leakage current density down to few μA/cm^2 (Fig. 4c inset) translates an ultra-high wavelength tuning efficiency up to 6 nm/nW, a factor of ten millions improvement over conventional thermal or carrier injection approach.

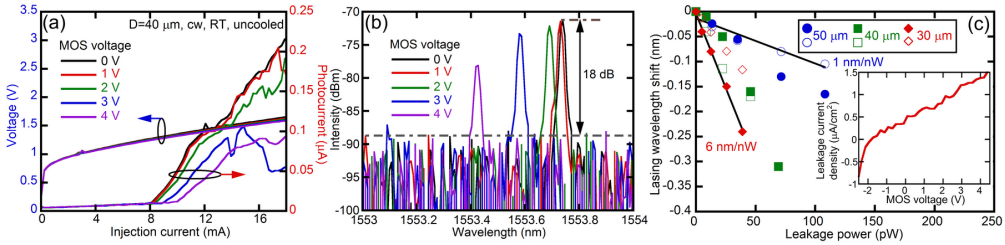


Fig. 2. (a) LIV, (b) spectrum and (c) wavelength shift vs. capacitor leakage power of a MOS-type heterogeneous microring laser

In addition to a new control freedom from the integrated MOS capacitor, we have largely improved the robustness of the heterogeneous laser operation by adopting the advanced quantum dot (QD) material. Compared with conventional quantum well laser active region, QD materials have distinct advantages in better temperature stability, lower threshold current density and better immunity to defects, etc. Figs. 3(a) and (b) show the schematic and SEM cross-sectional images of a Fabry-Perot (FP) heterogeneous with an InAs QD active region.

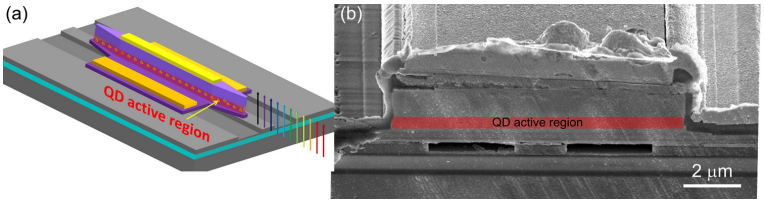


Fig. 3. (a) Schematic and (b) SEM image of a heterogeneous FP laser with QD active region

Fig. 4(a) shows the temperature-dependent LIs for a 3 mm-long device. Decent lasing up to 12 mW with minimum threshold current density <230 A/cm^2 and no thermal roll-over is seen up to 100 °C stage temperature. In Fig. 4(b), device characteristic temperature T_0 is 333, 125 and 61K in 20-40, 40-60 and 60-100 °C regions, respectively. The typical RT spectra below and above threshold are exhibited by Fig. 4(b), indicating multiple lasing peaks due to the broad gain band from QD ground state even at 90 °C (data not shown). These data proves it an ideal device structure to build a (mode-lock) comb laser for DWDM applications. It is straightforward to integrate the MOS capacitor here to fine tune/lock the wavelength grid with nearly zero power consumption.

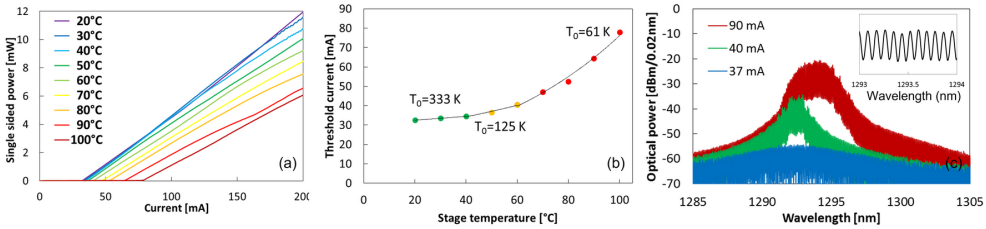


Fig. 4. (a) LIs and (b) characteristic temperatures at different stage temperature, and (c) laser spectra at different injection current levels

[1] D. Liang, X. Huang, G. Kurczveil, M. Fiorentino, R. G. Beausoleil, *Integrated finely tunable microring laser on silicon*, Nature Photonics, vol. 10, pp. 719-722, 2016.

[2] G. Kurczveil, D. Liang, M. Fiorentino, and R. G. Beausoleil, *Robust hybrid quantum dot laser for integrated silicon photonics*, Optics Express, vol. 24, pp. 16167-16174, 2016.



Integrated photonic systems on silicon

Jason S. ORCUTT*
IBM T. J. Watson Research Center, 1101 Kitchawan Rd, Yorktown Heights, NY 10598, USA
* jsorcutt@us.ibm.com

Monolithic CMOS silicon photonics technology enables functional system on chip integration of complete electro-optic subsystems and single-chip transceivers. A complete set of building block components has been designed and integrated within a single manufacturing process that targets O-band data communication standards including direct-detect and 4x25 Gb/s WDM transceivers [1]; however, the nanophotonic building blocks and diverse process features can be utilized for a wide variety of applications, including environmental trace gas sensing [2], medical diagnostics, and quantum interconnects. Automation, simulation and verification support for the optoelectronic elements in industry standard CAD tools enables small teams to reliably design complex systems.

References

[1] J. S. Orcutt, D. M. Gill, J. E. Proesel, J. Ellis-Monaghan, F. Horst, T. Barwicz, C. Xiong, F. G. Anderson, A. Agrawal, Y. Martin, C. W. Baks, M. Khater, J. C. Rosenberg, W. D. Sacher, J. Hofrichter, E. Kiewra, A. D. Stricker, F. Libsch, B. J. Offrein, M. Meghelli, N. B. Feilchenfeld, W. Haensch, W. M. Green, *Monolithic silicon photonics at 25 Gb/s*, Optical Fiber Conference, paper Th4H.1, 2016.

[2] E. J. Zhang, L. Tombez, J. S. Orcutt, S. Kamlapurkar, G. Wysocki, W. M. Green, *Silicon photonic on-chip trace-gas spectroscopy of methane*, Conference on Lasers and Electro-Optics: Science and Innovations, paper SF2H.1, 2016.

InP PICs for Coherent Optical Transmission

Rob GRIFFIN
Oclaro, Caswell, Towcester NN12 6RA, UK
robert.griffin@oclaro.com

The widespread deployment of digital coherent optics has been underpinned by the development of sophisticated optical components to provide functionality for transmit and local oscillator (LO) laser, dual-polarisation (DP) in-phase and quadrature (I&Q) modulator, and integrated coherent receiver (ICR). Working together with CMOS digital signal processing (DSP), digital optics has transformed long-haul optical transmission over the last few years, and is increasingly attractive for metro and data-centre applications.

A strong trend for recent deployment of digital coherent optics has been the utilisation of analog coherent optics (ACO) – optical functionality is implemented in a standardised pluggable module, while the DSP and other electronics resides on a host board. InP photonic integrated circuits (PICs) are well suited to this application, fulfilling requirements for demanding optical performance together with small size and suitability for volume manufacturing. Building on the development of an InP platform over several decades, Oclaro's PIC technology has enabled early commercial deployment of ACO-CFP2 modules capable of operation beyond 200Gb/s. The first generation of coherent PICs comprise:

- A DSDBR laser PIC providing fullband flexible tuning, narrow linewidth suitable for 16QAM operation, high optical output power and low electrical power dissipation [1]
- A DP I&Q modulator PIC combining an array of 4 Mach-Zehnder modulators together with integrated functionality for monitor and control. Additionally, semiconductor optical amplifier elements are integrated on the PIC to compensate for substantial modulation losses associated with generation of 'Nyquist shaped' optical formats [2]
- A pair of receiver PICs, each combining an MMI-based optical hybrid with 4 integrated waveguide photodetectors, providing high responsivity, close matching and wide bandwidth [3]

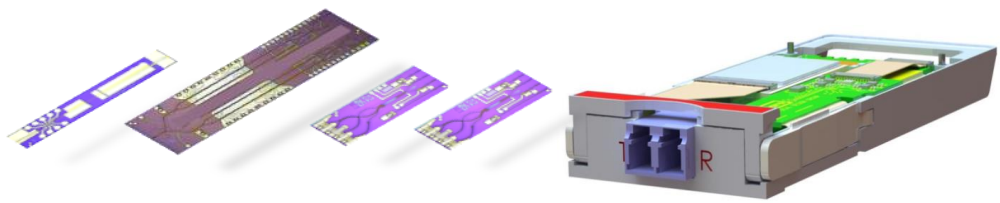


Fig.1. An InP 'chipset' of optical PICs enables implementation of high-performance ACO-CFP2 pluggable modules for 32 GBaud operation

The next generation of InP PICs will further extend capabilities, allowing operation at higher Baud rates, higher constellation density, and with reduced footprint. In conjunction with advances in CMOS technology – which provide greater functionality and reduced power dissipation – these InP PICs will provide improvements in cost/bit and W/bit for optical transmission, and are likely to find ever wider application throughout the optical network.

References

[1] S. C. Davies, R. A. Griffin, A. J. Ward, N. D. Whitbread, I. Davies, L. Langley, S. Fourte, J. Mo, Y. Xu and A. Carter "*Narrow linewidth, high power, high operating temperature digital supermode distributed Bragg reflector laser*" in Proceedings of 39th European Conference and on Optical Communication, Th.1.B.3, 2013.

[2] R. A. Griffin, N. I. Whitbread, S. K. Jones, S. C. Heck, P. Firth, D. Govan and T. Goodall, "*InP coherent optical modulator with integrated amplification for high capacity transmission*", in Proceedings of the Optical Fiber Communication Conference, Th4E-2, 2015.

[3] S. Farwell, P. Aivaliotis, Y. Qian, P. Bromley, R. Griggs, J. N. Y. Hoe, C. Smith, and S. Jones, "*InP coherent receiver chip with high performance and manufacturability for CFP2 modules*", in Proceedings of the Optical Fiber Communication Conference, W1I-6, 2014.

Heterogeneously Integrated III-V/SOI DBR Laser with Over 7 nm Continuous Wavelength Tuning Range

Sören DHOORE[1, 2*], Gunther ROELKENS[1, 2], Geert MORTHIER[1, 2]
[1]Photonics Research Group, INTEC, Ghent University - imec, Ghent, 9000, Belgium
[2]Center for Nano- and Biophotonics (NB-Photonics), Ghent University, Ghent, 9000, Belgium
* Soren.Dhoore@UGent.be

Many tele- and datacom applications require single-wavelength tunable lasers with easy wavelength control and sufficient tuning range. Such lasers can for instance be used in WDM-based optical networks or to replace fixed wavelength distributed feedback (DFB) lasers. In recent years there has been a lot of interest in tunable lasers heterogeneously integrated on the silicon-on-insulator (SOI) platform. Several heterogeneously integrated III-V/SOI tunable distributed Bragg reflector (DBR) and DFB lasers have already been demonstrated. DBR-types typically employ a single [1] or double silicon ring [2] with heaters as wavelength-selective and tunable element. In recent work we demonstrated a discretely tunable sampled grating (SG)-DFB laser with a discontinuous tuning range of more than 55 nm [3].

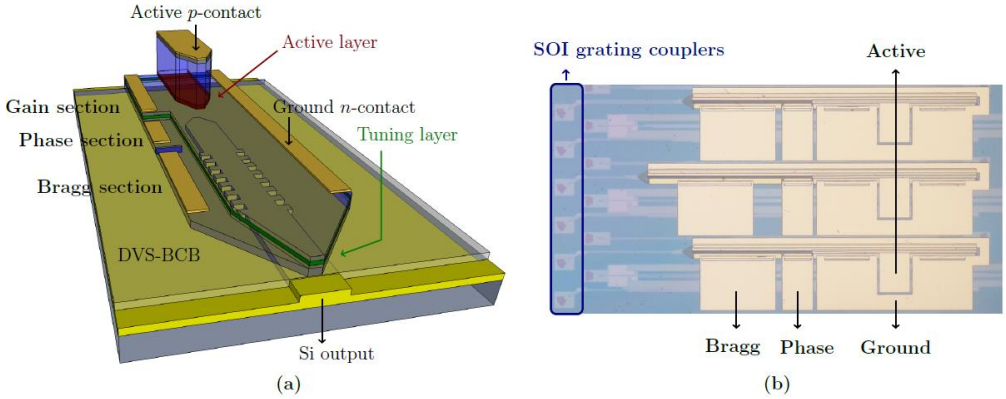


Fig. 1. III-V/SOI tunable DBR laser. (a) Schematic; (b) Microscope image.

Here we demonstrate over 7 nm continuous wavelength tuning with a novel III-V/SOI DBR laser. The laser structure consists of an SOI waveguide circuit on which a III-V tunable twin-guide (TTG) membrane is heterogeneously integrated by means of adhesive DVS-BCB bonding. The TTG membrane comprises an active layer (with 6 InGaAsP quantum wells, bandgap wavelength 1550 nm) and a tuning layer (InGaAsP, bandgap wavelength 1400 nm) in which carriers can be injected to provide gain and phase tuning respectively. The laser cavity is formed by a broadband reflecting facet and a DBR mirror. The latter is implemented as a first-order sidewall-corrugated waveguide grating [4] defined in the 400 nm silicon device layer. The weak sidewall-corrugation provides a narrowband spectral reflection characteristic to ensure single-mode lasing operation. It also provides an additional advantage over ring resonator configurations as for the latter a large free spectral range (FSR) is more difficult to obtain due to minimum bend radii requirements. Fig.1 (a) and (b) show a schematic and microscope image of the laser device respectively. Three laser sections can be discerned: a gain, phase and Bragg section. In the gain section current is injected into the active layer to provide optical gain. The tuning layer is left unbiased. In the phase and Bragg section the active layer is etched

away and current is injected into the tuning layer. Upon current injection the effective index of the waveguide mode is modified through the free-carrier plasma dispersion effect and Joule heating. Simultaneous adjustment of the phase and Bragg current allows for continuous tuning of the lasing wavelength.

Device characterisation is carried out on a temperature-controlled stage at 10°C. Light is couped out from the silicon waveguide to a single-mode optical fiber (SMF) through a reflectionless SOI grating coupler [5]. Fig.2 (a) shows the LI curve of the laser. The threshold current is 60 mA and a maximum waveguide-coupled output power of about −4 dBm is obtained. The superimposed lasing spectra at different tuning currents (Bragg and phase) are shown in Fig.2 (b). The wavelength tuning range is larger than 7 nm. The redshift of the lasing wavelength indicates a dominant heating effect. By improving the heat sinking and a modification of the epitaxial layer stack (by e.g. using a thicker tuning and surrounding cladding layer) in future designs, we expect to significantly increase the optical confinement factor in the tuning layer, resulting in a stronger electronic effect and hence faster tuning (~ns). In that case an adiabatic tapered III-V/SOI coupler similar to one of the couplers reported in [6] can be used.

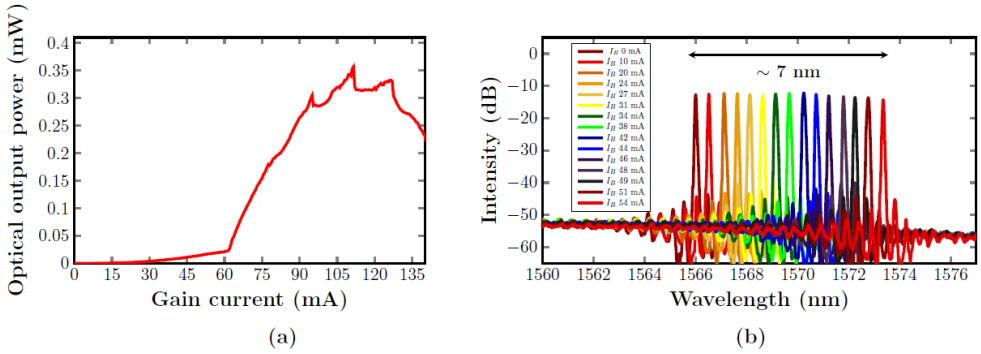


Fig. 2. Static characterization results. (a) LI curve; (b) Superimposed lasing spectra.

References

[1] S. Keyvaninia et al., *Demonstration of a heterogeneously integrated III-V/SOI single wavelength tunable laser*, Opt. Express, vol. 21, no. 3, 3784-3792, 2013.

[2] J.C. Hulme et al., *Widely tunable Vernier ring laser on hybrid silicon*, Opt. Express, vol. 21, no. 17, 19718-19722, 2013.

[3] S. Dhoore et al., *Demonstration of a discretely tunable III-V-on-silicon sampled grating DFB laser*, IEEE Photon. Technol. Lett., vol. 28, no. 21, pp. 2343-2346, 2016.

[4] X. Wang et al., *Narrowband waveguide Bragg gratings on SOI wafers with CMOS-compatible fabrication process,* Opt. Express, vol. 20, no. 14, 15547-15558, 2012.

[5] D. Vermeulen et al., *Reflectionless grating couplers for SOI photonic integrated circuits*, Opt. Express, vol. 20, no. 20, 22278-22283, 2012.

[6] S. Dhoore et al., *Novel adiabatic tapered couplers for active III-V/SOI devices fabricated through transfer printing*, Opt. Express, vol. 24, no. 12, pp. 12976-12990, 2016.

Development of a SiGe Arrayed Waveguide Grating in the 2185-2285 cm^{-1} range

Julien Favreau, Jean-Michel Hartmann, Pierre Labeye, Jean-Marc Fedeli,

CEA-LETI, MINATEC Campus, 17 Rue des Martyrs - 38054 GRENOBLE Cedex 9, France

*jean-marc.fedeli@cea.fr

***Abstract*: In this paper, we present the design, process and characterization of an AWG based on a SiGe step index waveguide platform, operating at 4.5 µm (2185-2285 cm^{-1}). A transmission of -1.6 dB and a crosstalk below -12 dB are demonstrated.**

Keywords— AWG, silicon photonics, multiplexer, gas sensing, MIR.

I. INTRODUCTION

Many gases present strong absorption lines in the mid IR (2-10 µm) giving much interest for spectroscopic gas sensing. Moreover, the advent of new Mid-IR laser sources such as Quantum Cascade Laser (QCL) eases the highly specific detection of these gases by a simple absorption measurement. Unfortunately, QCL are weakly tunable (typically over 3 cm^{-1}), thus limiting the use of one laser for one gas. Nevertheless, a promising way for broadening the tunability of this spectroscopic solution is to use an array of QCL, with different emission wavelengths in conjunction with a wavelength multiplexer. A particularly promising one is the Arrayed Waveguide Grating (AWG). Indeed, AWG have been extensively studied in the Telecom wavelength range and different technical solutions have been proposed to transfer these AWG to the Mid-IR range [1]. For instance, AWG based on SOI waveguides have been proposed by Muneeb *et.al.* [2] who demonstrated an AWG working at 3.8 µm. Nevertheless, this technical solution, due to the absorption of the SiO2 buffer layer is limited to wavelength below 4 µm. Malik *et.al.* [3] proposed a solution based on Ge-On-Silicon waveguides with a demonstration at 5 µm.
In a recent paper [4], we proposed a new waveguide platform based on SiGe graded index waveguides. This material presents an important transparency range from 3 µm to 8 µm as well as a full compatibility with CMOS fabrication tools. However in order to increase the compactness of this kind of multiplexer, a new platform based on step index SiGe has been developed. We present, in this paper, the design, process and characterization of an AWG working at around 4.5 µm.

II. AWG DESIGN

In order to explore the possibilities of the SiGe/Si waveguides platform over the whole 3-8µm spectral band, we have developed a fast AWG design tool based on Gaussian approximation of waveguide fundamental mode and Fourier diffraction optics. A precise description of AWG working principle can be found in literature [5]. Fig. 1 shows the basic principle of an AWG working in the de-multiplexing way.

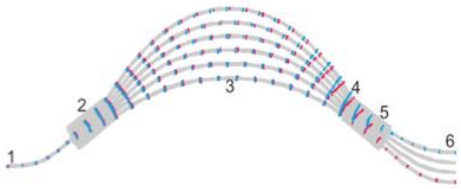


Fig. 1. Sketch of an AWG. Principle of operation in the de-multiplexing way. (1) Single mode waveguide. (2) Planar waveguide. (3) Arrayed Waveguide. (4, 5) Recombination area. (6) Single mode output waveguides.

In order to improve the spectral response of the AWG, especially between two adjacent channels, we introduced a MMI coupler. The effect of the MMI [6] is to flatten the spectral response of each AWG channel in order to obtain a higher intensity output over the entire spectral range. Fig. 2 shows the influence of the MMI on the spectral response of the central channel.

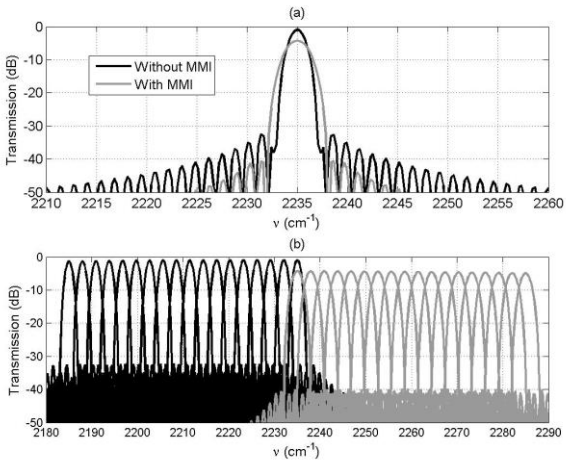


Fig. 2. (a) Influence of the MMI coupler on the spectral response of the central channel of the AWG. (b) Spectral response of the AWG with and without MMI.

III. AWG PROCESS

To make array waveguide grating devices, SiGe/Si waveguides technology have been preferred. This technology is developed in the 200 mm fabrication platform at CEA-LETI with microelectronics equipment. Those low loss and

large bandwidth waveguides have been specially designed for integrated gas sensing applications. The core layer of the waveguide is constituted of a step index $Si_{60}Ge_{40}$ layer grown by reduced pressure epitaxy with 2.7 µm thickness. The core is structured to define all the passive functions by DUV photolithography and SiGe deep reactive ion etching processes. To complete the fabrication, the patterns are fully embedded in a 4.2 µm thick epitaxial Si layer deposited by reduced pressure-CVD. This layer constitutes the cladding layer for the waveguides and is thick enough to ensure a complete optical isolation of the AWG from ambient atmosphere. This is of primary importance as those devices are specially developed for gas sensing applications. Fig. 3a shows a view of the final 200mm wafer and Fig.3b a SEM image of a cleaved output of a waveguide. No void and good cleaved surfaces are noticeable. The initial spacing pitch of 100 µm between adjacent waveguides, i.e. compatible with DFB QCL arrays geometry, is progressively decreased down to few microns as required by the design at the entrance of the first diffractive area of the AWG. From the technology point of view, the minimum spacing size is limited by the subsequent gap filling with Si epitaxial cladding layer which impose a trench not larger than 2 µm. Due to technological uncertainties sixteen additional exit waveguides have been added to compensate eventual refractive index discrepancies. Note that in this AWG type, MMI structures have been added at the output waveguide junction.

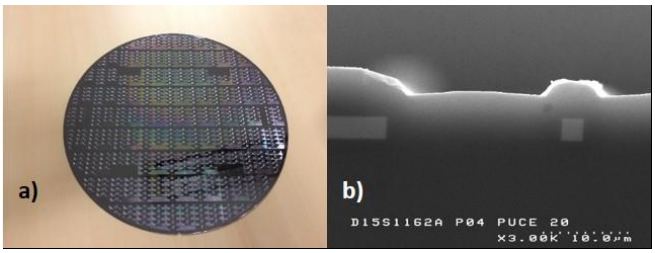


Fig. 3. (a) 200mm wafer with compact AWG. (b) Details of a SiGe input waveguide.

IV. AWG CHARACTERIZATION

Basic passive devices (lines, bends, and splitters with MMI) were first characterized in order to verify the quality of fabrication and to calibrate the testing apparatus. The AWG were characterized in the de-multiplexing way with a Fabry-Perot QCL working in pulsed mode. A broadband QCL light is injected in one of the 17 outputs and the light coming out of the 35 input waveguides is spectrally analyzed with a FTIR spectrometer. The AWG presents a low loss normalized transmission (-1.6 dB) with a cross talk below -12 dB (see Fig. 4). The whole transmission spectrum appeared to be spectrally shifted by +7.14 cm^{-1}. This can be explained by the SiGe refractive index value not sufficiently accurate at the time of the design. Technological discrepancies may also introduce phase errors [7]. The maximum shift from channel spacing measured for the AWG central output is $\Delta\sigma_{Input22}$=0.13 cm^{-1}, which is a 4 % variation from the designed 2.94 cm^{-1} channel spacing.

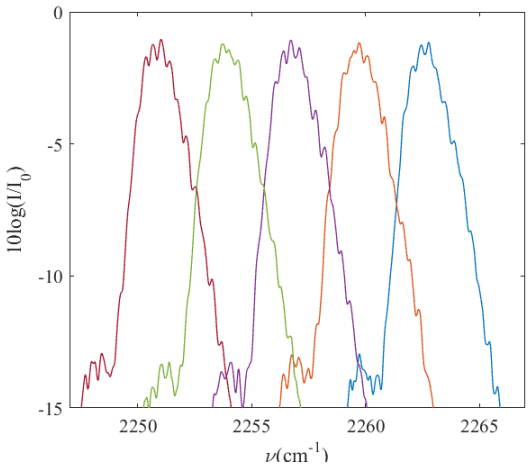


Fig. 4. Normalized spectra measured for 5 outputs of the AWG.

V. CONCLUSION

So we will present the design, process and characterization of a 17x35 AWG working in the 4.5 µm range. The normalized transmission of the AWG is around -1.6 dB with a cross talk below -12 dB. This technology can be extended to other MIR wavelength range till the absorption of the Si cladding reach a too high level.

Acknowledgement:

The research leading to these results has received funding from the European Community's H2020 under MIRPHAB project: **www.mirphab.eu**

REFERENCES

[1] G. Roelkens, U. Dave, A. Gassenq, N. Hattasan, C. Hu, B. Kuyken, F. Leo, A. Malik and M. Muneeb, IEEE J. Sel. Top. Quantum Electron, **20**, 394-404 (2014).

[2] M. Muneeb, X. Chen, P. Verheyen, G. Lepage, S. Pathak, E. Ryckeboer, A. Malik, B. Kuyken, M. Nedeljkovic, J. V. Campenhout, G. Z. Mashanovich and G. Roelkens , Opt. Express **21**, 11659–11669 (2013).

[3] A. Malik, M. Muneeb, S. Pathak, Y. Shimura, J. Van Campenhout, R. Loo and G. Roelkens , Photonics Technology Letters, IEEE **25**, 1805-1808 (2013).

[4] Design, fabrication and characterization of an AWG at 4.5 µm - P. Barritault et Al., Optics express 23 (20), 26168-26181

[5] M. K. Smit and C. Van Dam, IEEE J. Sel. Top. Quantum Electron. **2**(2), 236–250 (1996).

[6] S. Pathak, M. Vanslembrouck, P. Dumon, D. Van Thourhout, W. Bogaerts, J. Light Tech. **31**, 87-93 (2013).

[7] Impact of Non-Central Input in N x M Mid-IR Arrayed Waveguide Gratings Integrated on Si - A. Koshkinbayeva et Al. IEEE Photonics Technology Letters 28(20):1-1 · October 2016 DOI: 10.1109/LPT.2016.2587386

C-band linear propagation characteristics for a 300 nm film height Silicon Nitride photonics platform

Gloria MICÓ[1], Luis BRU[1], Daniel PASTOR[1], Daniel PÉREZ[1], David DOMENECH[2], Ana M. SÁNCHEZ[3], Josep M. CIRERA[3], Javier SANCHEZ[3], Carlos DOMÍNGUEZ[3] and Pascual MUÑOZ[1,2*]

[1]Photonic-IC group @ Photonic Research Labs, Universitat Politècnica de Valencia, Spain
[2]VLC Photonics S.L., Ed9B-UPV, c/ Camino de Vera s/n, Valencia, Spain
[3]IMB-CNM-CSIC, Campus Belaterra UAB, Barcelona, Spain
[*]pascual@ieee.org

Silicon Nitride (Si_3N_4) material is widely used in the fabrication of microelectronic circuits, as a basic material for developing the electronic devices mainly due to its electronic, structural and chemical properties [1]. For photonics, the first fabrication of Si_3N_4 films on a SiO_2 buffer on Silicon wafers, for propagation of red visible light was reported early in 1977 [2]. After similar works during the 1980s, a fully integrated Mach-Zehnder Interferometer (MZI) sensor was reported a few years latter [3]. Renewed interests on this material platform started again back in 2005 [4,5] with developed processes and applications in the NIR. They were followed developments of SiONx waveguides [6], whereas [7-9] developed Si_3N_4 waveguides (2008-2011). Up to 2011 the demonstrations by telecom related groups were for NIR C-Band at 1550 nm, with waveguide cross-sections for moderate confinement (film heights h>100nm), despite other researchers [8] reported by 2011 low confinement waveguides (film h<100 nm). In 2013 some groups [10,11] set new paths of Si_3N_4 technology for visible light applications. In parallel since 2011, there is a growing interest on high confinement (h>400 nm) waveguides for NIR+ (λ>2000nm), [12-15], whereas very recently new moderate confinement platforms appear [16-18]. In general, medium film height, 100-400nm, provides moderate propagation loss, confinement and non-linear effects with comparatively simpler fabrication processes. For the NIR, moderate confinement waveguides (h=150-400nm) have been demonstrated by several groups [4,17]. LPCVD Si_3N_4 guiding film heights of 150-200nm, with waveguide widths 0.8-2.0μm resulted into propagation losses of 0.11-1.45 dB/cm at 1550 nm, for BOX heights up to 5.0μm. Other groups as [19] have reported 3D integration on top of SOI, employing LPCVD Si_3N_4 guiding film heights 300-400nm, with waveguide widths 0.8-1.0μm, resulting into propagation loss of 1.30-2.10 dB/cm at 1550 nm for BOX heights in between 2.0-5.0μm.

In this paper we present the characterization of the linear propagation properties (loss, group index, dispersion, birefringence, thermo-optic phase shift) for Si_3N_4 strip waveguides with guiding film height of 300nm. The devices were fabricated on a 100mm Si wafer, composed of a SiO_2 buffer (2.5μm thick, n=1.464) grown by thermal oxidation of the silicon substrate, following a LPCVD Si_3N_4 layer with thickness 300nm (n= 2.01) and a 2.0μm thick SiO_2 (n=1.45) deposited by PECVD. The metal layer stack is 30nm Cr and 100nm Au. In some wafers of the batch, additional process steps were deployed to improve the optical quality of the structures (cf. [4]). A set of test structures, MZIs, spiral waveguides and ring resonators (RRs), Fig. 1, was deployed for strip waveguides of width 1.0μm. The MZI layout was devised so as to have the length difference only in straight sections of the width of interest, with a bend radius of 50μm

to reduce the footprint. The RRs and spiral waveguides (radius 150µm for negligible bend loss) were deployed to perform full-field time resolved measurements using optical frequency domain reflectometry (OFDR) [20], in transmission and reflection mode respectively.

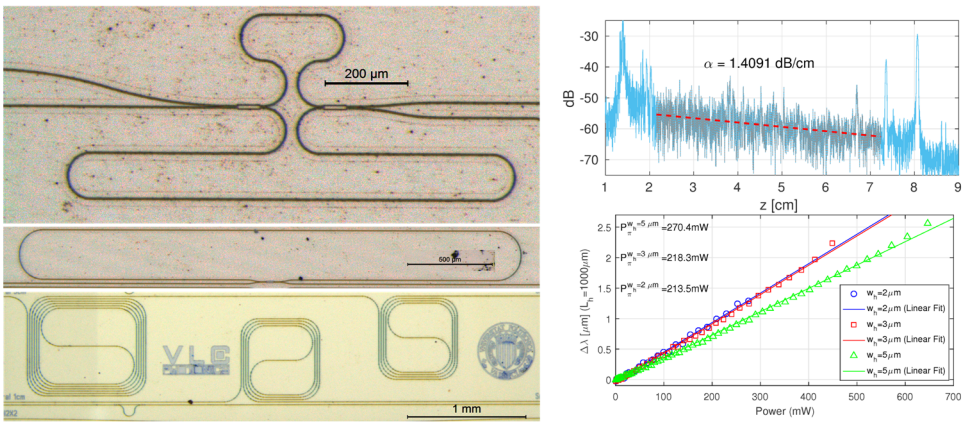


Fig. 1. Test structures (left), MZI, RR and spirals, and measurements (right), OFDR backscattering and thermo-optic tuners switching power Δλ=1 nm corresponds to P_π).

The propagation loss was derived both from the transmission spectrum of MZIs [21] and the backscattering of spiral waveguides, Fig. 1. Values in the range of 1.2-1.6 dB/cm were obtained for devices in the wafers without oxidation and annealing, so further loss reduction can be expected [4]. From the relative positions of the nulls in the transmission spectra of MZIs, n_g=1.90-1.92 was inferred. The dispersion was derived from transmission OFDR measurements of RRs, yielding [-0.7,-1.0] ps/nm·m, that match those from the second derivative of the simulated effective index (-0.75 ps/nm·m). Time resolved OFDR measurements provided the TE and TM propagation delay difference leading to birefringence of 0.168. Finally, thermal tuners of different lengths and widths were characterized, with P_π in [213,270] mW as shown in Fig. 1.

[1] E.F. Krimmel & R. Hezel, Si_3N_4 in Microelectronics and Solar Cells, Springer-Verlag 1991.
[2] W. Stutius and W. Streifer, Applied Optics, vol. 16, no. 12, pp. 3218-3222, 1977.
[3] E. F. Schipper e.a. Sensors and Actuators B: Chemical, vol. 40, no. 2-3, pp. 147–153, 1997.
[4] M. J. Shaw e.a., Proc. SPIE 5720, pp. 109–118, 2005.
[5] M. Melchiorri e.a., Applied Physics Letters, vol. 86, no. 12, pp. 121111, 2005.
[6] K. Worhoff e.a., in Proc. ICTON, vol. 3, pp. 266–269, 2008.
[7] S. C. Mao, e.a., Optics Express, vol. 16, no. 25, pp. 20809-20816, 2008.
[8] J.F. Bauters e.a., Optics Express vol. 19, pp. 3163-3174, 2011.
[9] J. F. Bauters e.a, Optics Express, vol. 19, no. 24, pp. 24090–24101, 2011.
[10] S. Romero-García e.a., Optics Express, vol. 21, no. 12, pp. 14036–14046, 2013.
[11] A. Z. Subramanian e.a., IEEE Photonics Journal, vol. 5, no. 6, p. 2202809, 2013.
[12] T. J. Kippenberg e.a., Science, vol. 332, no. 6029, pp. 555–559, Apr. 2011.
[13] K. Luke e.a., Optics Letters, vol. 40, no. 21, pp. 4823-4826, 2015.
[14] C. J. Krückel e.a, Optics Express, vol. 23, no. 20, pp. 25827-25837, 2015.
[15] K. Luke e.a., Optics Express, vol. 21, no. 19, pp. 22829–22833, 2013.
[16] D. Doménech e.a., in Proc. OPTOEL, PO-SII-27, 2015.
[17] K. Shang e.a., Optics Express, vol. 23, no. 16, pp. 21334-21342, 2015.
[18] P. Muellner e.a., in Proc. ECIO, paper ecio-o–19, 2016.
[19] W. D. Sacher e.a., J. of Lightwave Technol., vol. 33, no. 4, pp. 901–910, 2015.
[20] U. Glombitza and E. Brinkmeyer, J. of Lightwave Technol., vol. 11, no. 8, pp. 1377-1384, 1993.
[21] M. A. Tran e.a., IEEE Photonics Technology Letters, vol. 28, no. 14, pp. 1517-1520, 2016.

A Fiber-to-Chip Grating Coupler for the Ge-on-Si Platform at 5µm wavelength

Sanja Radosavljevic*, Bart Kuyken, Gunther Roelkens
Photonics Research Group, Ghent University - imec, Technologiepark 15, 9052 Ghent, Belgium
Center for Nano- and Biophotonics, Technologiepark 15, 9052 Ghent, Belgium
* sanja.radosavljevic@ugent.be

Abstract: We present efficient TM fiber-to-chip grating couplers that couple light between a single mode InF fiber and Germanium-on-Silicon (Ge-on-Si) waveguides in the 5 µm wavelength range. In recent years, Ge-on-Si has emerged as a platform of interest for sensing applications beyond 4 µm [1, 2]. Ge has low losses for light in the 4-12 µm range, which makes it suitable for the realization of mid-infrared (midIR) photonic integrated circuit gas and liquid sensors.

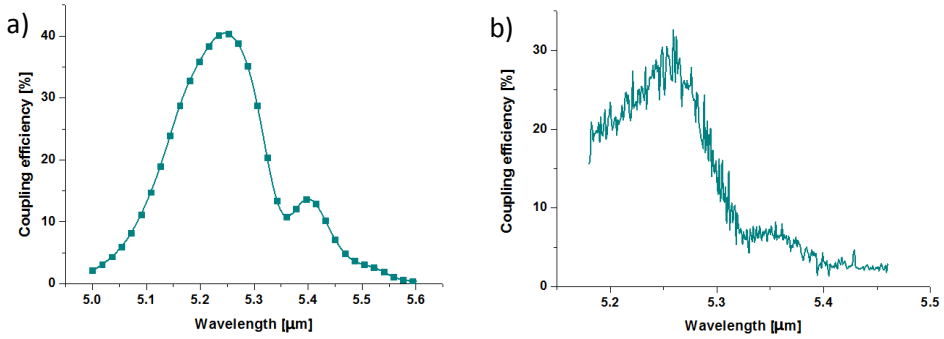


Fig 1. Simulated fiber-to-chip coupling efficiency as a function of wavelength (a) and the measured couping efficiency of the grating (b)

Grating coupler design: Since for a number of midIR applications QCL sources are used, emitting TM polarized light, we have opted to design fiber-chip interfaces for TM polarization. The couplers are designed in a 2 µm thick Ge waveguide layer on a silicon substrate. The TM grating coupler for the Ge-on-Si platform has a period of 1.42 µm, a 80% duty cycle (defined as the ratio of the width of the unetched tooth and the grating period) and an etch depth of 0.9 µm. The waveguides are partially etched with the same etch depth. The simulated coupling efficiency is 40% with a 3dB bandwidth of 180 nm at a central wavelength around 5.22 µm (Fig. 1a), for a fiber angle of $\theta = 5°$. The simulated reflectivity of the grating is below 1%, as calculated by 2D FDTD.

Fabrication and measurement: The grating and the waveguide are both defined with e-beam lithography and etched in one step using a chromium mask and a CF_4/H_2 plasma. Due to the fabrication imperfections the duty cycle of the fabricated device is 0.82, while the period and the etch depth is close to the targeted value. The best overlap of the fiber mode and the fundamental TM grating mode was achieved for a 27.5 µm wide grating. The top view and cross-section of the characterized device is shown in Fig. 2. The measurement system is schematically shown in Fig. 3b. Light from the free-space external cavity QCL operating in CW is coupled to the InF fiber by a ZnS lens. Between the laser and the lens we have a chopper and a Babinet-Soleil polarization control element.

The chopper turns the CW light into 50% duty cycle pulses and hence allows us to detect light on an InSb detector in combination with a pre-amplifier and lock-in system. The polarization control element is used to maximize transmission through the device at the central wavelength. Since the polarization at the fiber output facet is wavelength dependent we have measured the TE/TM ratio as a function of wavelength at the fiber facet by placing a wire grid polarizer and a thermal detector directly under the input fiber and comparing this power with measurement on the thermal detector without the grid polarizer (Fig. 3a). This ratio we took into account when measuring the total laser power in CW mode on the InSb detector (dashed line in Fig. 3b). The loss caused by the difference in length of the fiber when measuring the chip (full line in Fig. 3b) and when measuring the QCL power directly (dashed line in Fig. 3b) is not negligible in the wavelength range of interest and is evaluated from [3].

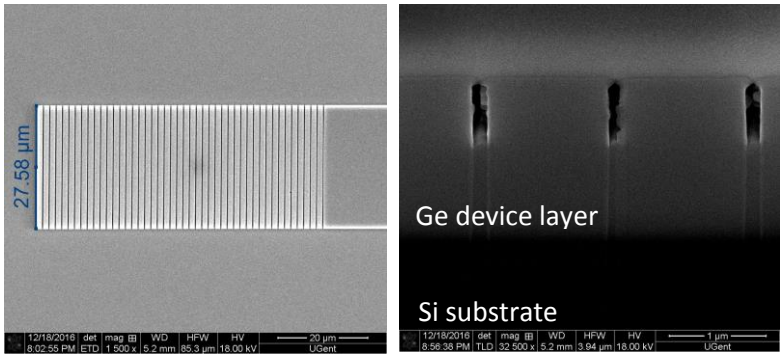


Fig. 2. Top view (left) and cross-section (right) of the Ge-on-Si grating coupler

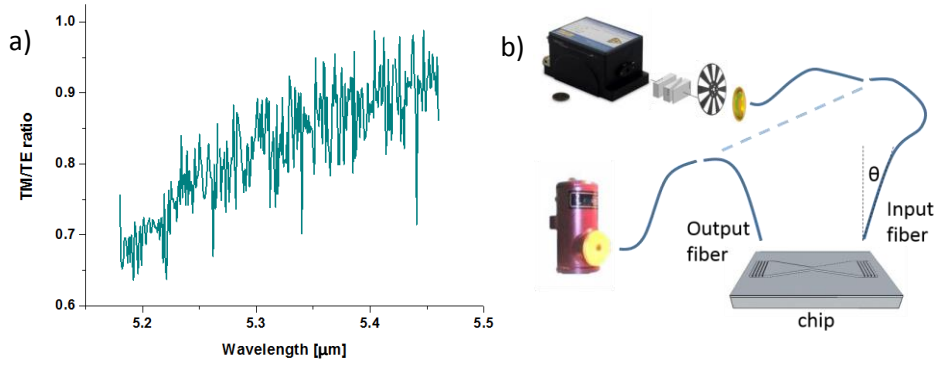


Fig 3. The TM to TE ratio vs. wavelength (a) and the measurement setup (b)

The experimentally characterized grating coupler shows -5dB (30%) coupling efficiency and a 3 dB bandwidth of 150 nm (Fig. 1b). The variations in the coupling efficiency are attributed to variations in the laser output power and measurement system and not to grating reflections.

References

[1] G. Roelkens et al., ``Silicon-based heterogeneous photonic integrated circuits for the mid-infrared,'' IEEE Journal of Selected Topics in Quantum Electronics, vol. 20, issue 4, 2014

[2] A. Malik et al., ``Silicon-based photonic integrated circuits for the mid-infrared,'' Proceedings of 8th International Conference on Materials for Advanced Technologies, 2015

[3] https://www.thorlabs.com/newgrouppage9.cfm?objectgroup_id=7062

EUROPEAN CONFERENCE ON INTEGRATED OPTICS

Mid-infrared integrated photonics in silicon and germanium

Goran Z. MASHANOVICH[1*], Wei CAO[1], Zhibo QU[1], Ahmed OSMAN[1], Yangbo WU[1], Taintian LI[1,2], Jordi Soler PENADES[1], Stevan STANKOVIC[1], Radan SLAVIK[1], Frederic Y. GARDES[1], Vinita MITTAL[1], Ganapathy S. MURUGAN[1], James S. WILKINSON[1], David J. THOMSON[1], Callum G. LITTLEJOHNS[1], Milos NEDELJKOVIC[1]

[1]Optoelectronic Research Centre, University of Southampton, Southampton, SO17 1BJ, UK
[2]Silicon Photonics and Microsystems Lab, Peking University, 00871 Beijing, P.R. China
[*] g.mashanovich@soton.ac.uk

Mid-infrared (MIR) silicon and germanium photonic devices and systems could be useful in a range of applications [1]. Silicon and germanium are transparent in the MIR, have large refractive indices and are dominant materials in microelectronics. Germainum is particularly interesting photonic material that has larger transparency range, refractive index, optical modulation, non-linear effects and carrier mobility compared to silicon. As such, both Si and Ge devices can be very compact (Fig. 1).

We have demonstrated a range of MIR devices and integrated circuits in Si, such as low loss passive devices, large bandwidth detectors, on-chip Fourier-transform spectrometers, and optical modulators [2-7]. For waveguides longer than 4 μm, a suspended Si platform can be used [8,9].

Recently, we have focused our work on the Ge-on-Si platform and have demonstrated low loss waveguides and other passive devices [10], couplers [11], cascaded ring resonators [12] fast all-optical modulation [13,14], modulators and sensors [15]. We have reached wavelengths up to ~9 μm and our future work will address the extension of the spectral range for Ge-based platforms and further reduction of the loss.

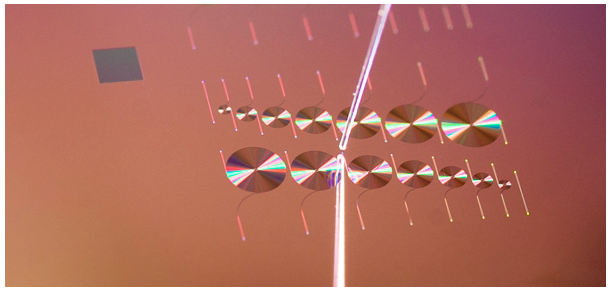


Fig. 1. Mid-infrared light coupling from an optical fibre to long spiral waveguides (up to 40cm in length)

References

[1] R. Soref, "Mid-infrared photonics in silicon and germanium," *Nat Photon,* vol. 4, pp. 495-497, 2010.

[2] M. Nedeljkovic, A. Z. Khokhar, Y. Hu, X. Chen, J. Soler Penades, S. Stankovic, D. J. Thomson, F. Y. Gardes, H. M. H. Chong, G. T. Reed, and G. Z. Mashanovich, "Silicon photonic devices and platforms for the mid-infrared" *Opt. Mat. Express*, vol. 3, pp. 1205–1214, 2013.

[3] J. Soler Penades, A. Z. Khokhar, M. Nedeljkovic, and G. Z. Mashanovich, "Low loss mid-infrared SOI slot waveguides," *IEEE Photon. Technol. Lett.*, vol. 27, pp. 1197-1199, 2015.

[4] G. Z. Mashanovich, F. Y. Gardes, D. J. Thomson, Y. Hu, K. Li, M. Nedeljkovic, J. Soler Penades, A. Z. Khokhar, C. J. Mitchell, S. Stankovic, R. Topley, S. A. Reynolds, Y. Wang, B. Troia, V. M. N. Passaro, C. G. Littlejohns, T. Dominguez Bucio, P. R. Wilson, and G. T. Reed, "Silicon photonic waveguides and devices for near- and mid-IR applications," *J. Sel. Top. Quantum Electron.*, vol. 21, 8200112, 2015.

[5] B. Troia, A. Z. Khokhar, M. Nedeljkovic, J. Soler Penades, V. M. N. Passaro, and G. Z. Mashanovich, "Cascade-coupled racetrack resonators based on the Vernier effect in mid-infrared," *Opt. Express*, vol. 22, pp. 23990-24003, 2014.

[6] M. Nedeljkovic, S. Stanković, C. Mitchell, A. Z. Khokhar, S. Reynolds, D. J. Thomson, F. Y. Gardes, C. Littlejohns, G. T. Reed, and G. Z. Mashanovich, "Mid-infrared thermo-optic modulators in SOI," *IEEE Photon. Technol. Lett.*, vol. 26, pp. 1352-1355, 2014.

[7] Y. Hu, T. Li, D. J. Thomson, X. Chen, J. Soler Penades, A. Z. Khokhar, C. J. Mitchell, G. T. Reed, and G. Z. Mashanovich, "Wavelength division (de)multiplexing in mid-infrared wavelength range using interleaved angled multimode interferometer on the silicon-on-insulator platform," *Opt. Lett.*, vol. 39, pp. 1406–1409, 2014.

[8] J. Soler Penades, A. Ortega-Moñux, M. Nedeljkovic, J. G. Wangüemert-Pérez, R. Halir, A.Z. Khokhar, C. Alonso-Ramos, Z. Qu, I. Molina-Fernández, P. Cheben and G. Z. Mashanovich, "Suspended silicon mid-infrared waveguide devices with subwavelength grating metamaterial cladding," *Optics Express,* vol. 24, pp. 22908-22916, 2016.

[9] J. Soler Penades, C. Alonso-Ramos, A. Z. Khokhar, M. Nedeljkovic, L. A. Boodhoo, A. Ortega-Monux, I. Molina-Fernandez, P. Cheben, and G. Z. Mashanovich, "Suspended SOI waveguide with sub-wavelength grating cladding for mid-infrared," *Opt. Lett.*, vol. 39, pp. 5661-5664, 2014.

[10] M. Nedeljkovic, J. Soler Penades, C. J. Mitchell, T. Dominquez Bucio, A. Z. Khokhar, C. Littlejohns, F. Y. Gardes, and G. Z. Mashanovich, "Surface grating coupled low loss Ge-on-Si rib waveguides and multimode interferometers," *IEEE Photon. Technol. Lett.*, vol. 27, pp. 1040-1043, 2015.

[11] C. Alonso-Ramos, M. Nedeljkovic, D. Benedikovic, J. Soler Penadés, C. Littlejohns, D. Pérez-Galacho, L. Vivien, P. Cheben, and G. Z. Mashanovich, "Germanium-on-silicon mid-infrared grating couplers with low-reflectivity inverse taper excitation," *Opt. Lett.,* vol. 41, pp. 4324-4327, 2016.

[12] B. Troia, J. Soler Penades, A. K. Khokhar, M. Nedeljkovic, C. Alonso-Ramos, V. M. N. Passaro, and G. Z. Mashanovich, "Germanium-on-silicon Vernier-effect photonic microcavities for the mid-infrared," *Opt. Lett.*, vol. 41, pp. 610-613, 2016.

[13] L. Shen, N. Healy, C. J. Mitchell, J. Soler Penades, M. Nedeljkovic, G. Z. Mashanovich, and A. C. Peacock, "Mid-infrared all-optical modulation in low loss germanium-on-silicon waveguides," *Opt. Lett.*, vol. 40, pp. 268–271, 2015.

[14] L. Shen, N. Healy, C. J. Mitchell, J. Solar Penades, M. Nedeljkovic, G. Z. Mashanovich, and A. C. Peacock, "Two-photon absorption and all-optical modulation in germanium-on-silicon waveguides for the mid-infrared," *Opt. Lett.*, vol. 40, pp. 2213-2216, 2015.

[15] G. Z. Mashanovich, C. J. Mitchell, A. Z. Khokhar, C. G. Littlejohns, J. Soler Penades, W. Cao, Z. Qu, L. Shen, N. Healy, A. C. Peacock, F. Y. Gardes, V. Mittal, G. Senthil Murugan, J. S. Wilkinson and M. Nedeljkovic, "Germanium mid-infrared photonic devices," *J. Lightwave Technol.* (in press)

Integrated Microwave Photonics: The evolution from ASICs to Universal Processors

Daniel PEREZ[1*], Ivana GASULLA[1], José CAPMANY[1]
[1]Universitat Politécnica de Valencia, Camino de Vera s/n, Valencia, 46022, Spain

[*] jcapmany@iteam.upv.es

Integrated microwave photonics (IMWP) deals with the application of integrated photonics technologies to microwave photonics (MWP) systems [1,2]. During the last 5 years, IMWP has become probably the most active area of current research and development in the discipline of MWP [3], capitalizing upon the outstanding progress of integrated photonics in various material platforms such as indium phosphide (InP), Silicon on Insulator (SOI) and silicon nitride (Si_3N_4). In this paper, we will first introduce this topic with special emphasis on its relevant application fields to the community briefly outlining the salient characteristics of available material platforms that can be employed for the implementation of IMWP chips. We will compare the features of more mature material platforms such as InP [4], SOI [5] and Si3N4 [6].

The core part of the paper will be devoted to describe the two salient approaches that are available for the implementation of IMWP chips from a functional point of view. On one hand, we will review the recent progress in Application-Specific Photonic Integrated Circuits (ASPICs), where a particular circuit and chip configuration is designed to optimally perform a particular MWP functionality [2]. Examples on different functionalities recently reported will be presented, including tunable filtering, optoelectronic oscillation, instantaneous frequency measurement, frequency up and down conversion, etc. On another hand, recent progress will be reported on a radically different approach, the universal MWP signal processor architecture that can be integrated on a chip and is capable of performing all the main functionalities by suitable software programming of its control signals [7-9]. This last approach is inspired by the flexibility of digital signal processors, where a common hardware is shared by multiple functionalities through a software-defined approach (or programmability), leading to significant cost reduction in the hardware fabrication. Figure 1 shows a picture of such concept, where the central element is a reconfigurable optical core included after external modulation (represented as an E/O device) and prior to detection (represented as an O/E device). The role of the optical core is to provide the required routing/switching functionalities and also the implementation of reconfigurable processing elements such as FIR/IIR filtering, delay lines and phase shifting operations either in standalone or in cascade configuration.

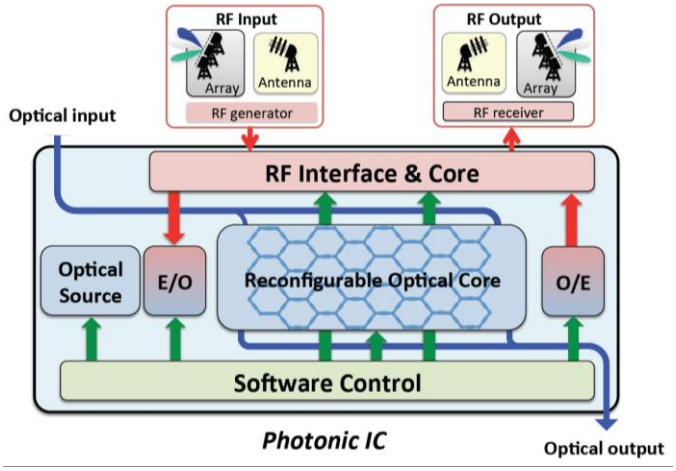


Fig. 1. Reconfigurable Universal MWP signal processor architecture.

The flexible implementation of the optical core requires a design approach based on interconnected waveguide meshes. In particular, we shall address the recent theoretical and experimental progress achieved in our group in Silicon based reconfigurable hexagonal [10] lattices.

References

[1] S. Ezekiel, M. Burla, J. Klamkin, D. Mrapung and J. Capmany, "RD engineering meets optoelectronics," IEEE Microwave Journal, pp. 28-45, (2015).
[2] D. Marpaung, C. Roeloffzen, R. Heideman, A. Leinse, S. Sales, and J. Capmany, "Integrated microwave photonics," Laser Photon. Rev., vol. 7, no. 4, pp. 506–538, (2013).
[3] J. Capmany and D. Novak, "Microwave photonics combines two worlds," Nat. Photonics, vol. 1, no. 6, pp. 319–330, (2007).
[4] J. Sancho, J. Bourderionnet, J. Lloret, S. Combrié, I. Gasulla, S. Xavier, S. Sales, P. Colman, G. Lehoucq, D. Dolfi, J. Capmany, and A. de Rossi, "Integrable microwave filter based on a photonic crystal delay line," Nature Commun., vol. 3, p. 1075, Sept. (2012).
[5] W. Zhang and J. P. Yao, "Silicon-based integrated microwave photonics, " IEEE J. Quantum Electron., vol. 52, 0600412 (2016).
[6] C. Roeloffzen, L. Zhuang, C. Taddei, A. Leinse, R. Heideman, P.van Dijk, R. Oldenbeuving, D. Marpaung, M. Burla, and K. Boller, "Silicon nitride microwave photonic circuits," Opt. Express, vol. 21, no. 19, pp. 22937–22961, (2013).
[7] "Birth of the programmable optical chip," Nature Photon., vol. 10, p. 1 (2016).
[8] J. Capmany, et al., "Microwave photonics: The programmable processor," Nature Photon., vol. 10, pp. 6-8 (2016).
[9] L. Zhuang et al., "Programmable photonic signal processor chip for radiofrequency applications," Optica, vol. 2, no. 8, p. 54, (2015).
[10] D. Pérez, I. Gasulla, J. Capmany and R.A. Soref, "Reconfigurable latttice mesh designs for programmable photonic processors," Opt. Express, vol. 24, no. XX, pp.YY-ZZ, (2016).



Recent development in integrated photonic solutions for THz systems

Cyril C. Renaud[1*], Katarzyna Balakier[1], Luis Gonzalez-Guerrero[1], James P. Seddon[1], Ahmad Mohammad[1], Martyn J. Fice[1], Alwyn J. Seeds[1]

[1]University College London, Torrington Place, London WC1E 7JE, United Kingdom

[*] c.renaud@ucl.ac.uk

THz technologies are continuing to develop for a wide set of applications and photonic is seen as a key technology for their development [1,2]. This is mostly due to their relatively high power, coherence and tuneability as well as, through through the development of optical communication, high speed modulation. However, despite these advantages it is clear that for many application and the development of THz technology a smaller footprint and lower power consumption will also be essential. While photonic solutions using discrete components have shown promising results [3], it remains essential to solve these remaining problems. To do so will require integrated photonic solutions as it will naturally offer smaller footprint while some of the losses within a discrete element system could be better managed thus enabling lower power consumption.

In this presentation we will discuss mainly integrated solutions for photomixing and review the different photonic integration techniques and their advantages. In particular we will show details of an integrated source that could be controlled to offer high frequency stability in the range up to 1 THz, as well as solutions based photonic intgrated chips foundries [4].

In more details the typical heterodyne coherent system that we are discussing is shown in figure 1. While dual laser source can offer tuneability of several THz in order to abtain high frequency stabilitiy across the range one would use an optical frequency comb generator (OFCG) used to lock the heterodyne source on a microwave reference. Finally the photomixer or potentially photoreceiver are essential part of the system. The discussion will thus concentrate on the integration of these different components.

We will then present solutions as sources and receivers for frequencies up to 1THz with a source frequency linewidth better than 10 Hz in the range. In particular we will look at a foundry based dual laser source that could be locked on a comb for frequency up to a THz and a fully integrated chip including two lasers and a uni-travelling carrier photodiode that has been used both as an emitter and receiver for frequencies up to 100 GHz. As an other essential part of the system would be an integrated comb generator we will also discussed a set of solution and in particular the use of FM lasers and recirculating loops to offer a compact and efficient wide comb source.

We will finally discussed different demonstrations of applications of these integrated technologies in particular for THz spectroscopy and wireless communication.

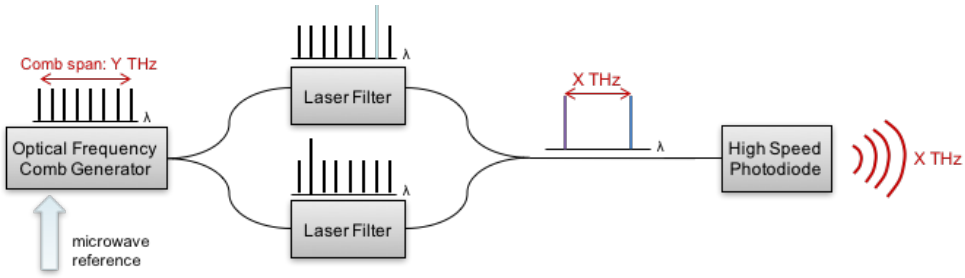


Fig. 1: Schematic of a typical heterodyne THz source.

ACKNOWLEDGMENT

This work was supported by Engineering and Physical Sciences Research Council grants for coherent terahertz system (COTS) (EP/J017671/1), and by the European Commission through the European project iPHOS (grant agreement no: 257539).

References

[1] M. Tonouchi, "Cutting-edge terahertz technology," Nature Photonics, **1**, pp. 97-105, 2007
[2] A. J. Seeds and K. J. Williams, "Microwave photonics," Journal of Lightwave Technology, vol. 24, pp. 4628-4641, Dec 2006.
[3] A. J. Seeds, M. J. Fice, K. Balakier, M. Natrella, O. Mitrofanov, M. Lamponi, et al., "Coherent terahertz photonics," Optics Express, vol. 21, pp. 22988-23000, Sep 23 2013.
[4] 56. Smit, M. et al., "Generic foundry model for InP-based photonics," IET Optoelectronics, **5**5), 187-194, 2011

Monolithically Integrated 1GHz Extended Cavity Linear Mode-Locked Laser

Robinson GUZMÁN[1*], Guillermo CARPINTERO[1], Carlos GORDON[1], Luis J. ORBE[2]
[1]Department of Electronic Technology, Avenida de la Universidad 30, Leganés, Madrid, 28911, Spain
[2] PhoeniX Software, Hengelosestraat 705, 7521 PA Enschede, The Netherlands
[*] rcguzman@ing.uc3m.es

We report a monolithically integrated 42 mm long cavity linear mode-locked laser at 1541 nm, with a low repetition rate at 1 GHz. The device uses InP-based active-passive integration technology and integrated multimode interference reflectors. Passive (PML) and hybrid mode-locked (HML) regime operation are experimentally demonstrated. The device exhibits a very narrow RF linewidth of the beat note of few KHz and Hz for both regimes.

Nowadays, several photonic or electronics techniques for generating of microwave signals used for short-range high data rate communication systems, frequency combs generators, metrology among other applications, are available to satisfy the needs of the customer. However, the use of optic fibre to carry signal long distances with a very low propagation loss, is one of the advantages that photonic techniques have over electronic. Moreover, photonic techniques have other additional advantages such as the quality of the signal generated (low phase noise), the tuning range of the generated frequency and bandwidth modulation [1]. Two of the most common photonic signal generation techniques used for the microwave carrier signals generation are based on optical heterodyning (Dual Wavelength Laser Source), or pulsed lasers (Mode-Locked Laser Source). Each of the techniques has its own quality features and tuning range [2]. The main advantage of the solution provided by the pulsed lasers is that they offer stable signal generation, directly yielding a frequency comb. There are extensive references on integrated mode-locked lasers [3]. However, few solutions operating within the frequency range of our interest (10 MHz to 14 GHz). One of the easiest ways to decrease the repetition rate is increasing the length of the resonator cavity. However, due to the propagation loss in the InP platform, they must be performed by hybrid integration. The most recent reference is an on-chip III-V-on-silicon mode locked laser with a repetition rate of 1 GHz. The length cavity is 37.4 mm [4].One of the characteristics in the use of photonic integration technologies circuits is to reduce system size. We aim to develop photonic integrated circuits (PICs) for the generation and distribution of frequency standards and calibration signals of very high quality by photonic techniques.

The PIC was designed using standardized building blocks and fabricated within a commercial MPW run through an InP active-passive integration foundry service. The mask manufacturing carried shown in figure 1 (a), where we have the linear laser structure. A photograph of the extended cavity made in a spiral-shaped structure is shown in figure 1 (b).

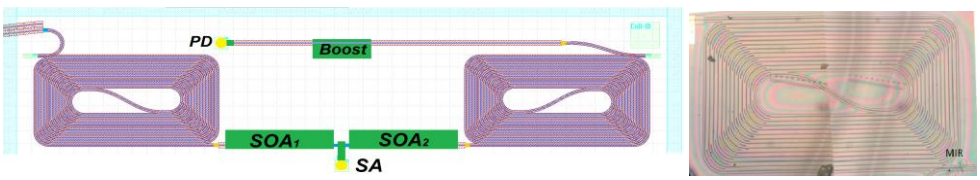
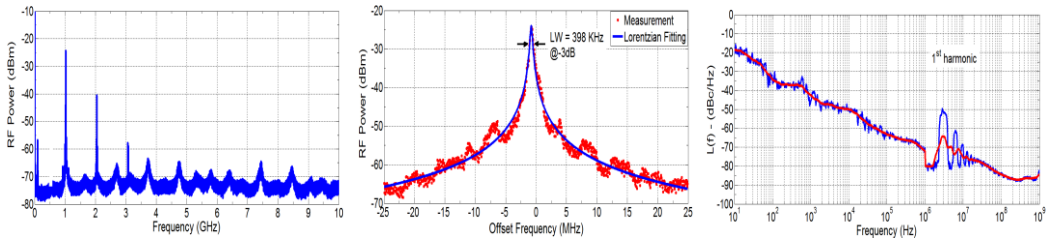


Fig. 1. (a) Layout of the photonic integrated circuit. (b) Microscope photograph of the extended cavity made in a spiral-shaped structure

The linear laser structure has a cavity length of 42 mm, corresponding to a frequency spacing of 1 GHz. It has two 750 µm semiconductor optical amplifiers (SOA) with a 50 µm

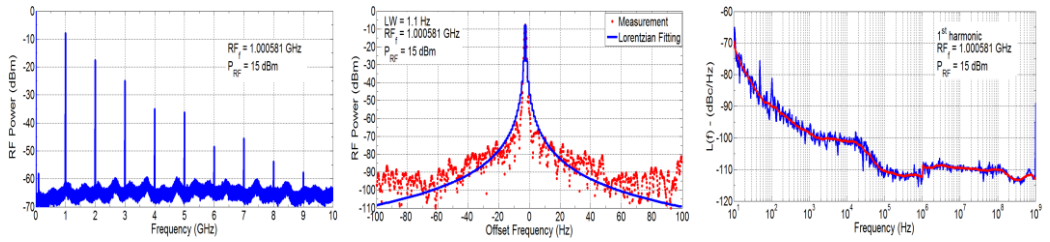
saturable absorber (SA) placed between them. The saturable absorber is located in the middle of the whole linear laser structure. At both ends of the SOA, we designed a waveguide passive, whose length is generated by a spiral-shaped structure. Both spiral-shaped structures on each side of the amplifiers are connected to individual multimode interference reflector (MIR) mirrors to form the Fabry-Perot cavity. At one of the linear laser structure outputs, we placed another SOA (booster) in order to amplify the optical signal launched into the photodiode (PD). Regarding the other output, a 7º angled waveguide to carry light out of the chip is used. An antireflective (AR) coating to avoid light back-reflections is used on the chip facets.

The extended cavity linear mode-locked laser was characterized by choosing the bias conditions which exhibit both passive and hybrid regime of the mode-locked laser. The chosen bias condition to get both regimes is setting a total forward bias current of 110 mA and a reverse bias voltage of -2.8 V for the gain sections and saturable absorber, respectively. These results are presented in figure 2 and figure 3. Electrical spectrums generate an electrical frequency comb, where the fundamental frequency tone appears at the repetition frequency (1 GHz) of the device, with higher harmonics. The fundamental frequency tone appears in detail being clearly hybrid mode in which the device is more stable. The device yields a very narrow RF linewidth of the beat note, 398 KHz and 1.1 Hz @-3dB, both for PML and HML, respectively.



(a) (b) (c)

Fig. 2. Mode-locked laser characterization in passive regime. (a) Electrical spectrum response. (b) Linewidth measurement of the fundamental frequency tone. The achieved beat note was about 398 KHz at -3dB using a Lorentzian shape fitting (blue line). (c) Phase noise measurement of the fundamental frequency tone.



(a) (b) (c)

Fig. 2. Mode-locked laser characterization in hybrid regime. (a) Electrical spectrum response. (b) Linewidth measurement of the fundamental frequency tone. The achieved beat note was about 1.1 Hz at -3dB using a Lorentzian shape fitting (blue line). (c) Phase noise measurement of the fundamental frequency tone.

References

[1] G. Carpintero et al, "Photonic Integrated Circuits for Radio-frequency signal generation", Journal of Lightwave Technology, VOL.34, No. 2, pp. 508-515, 2016.

[2] T. Nagatsuma and G. Carpintero, "Recent progress and Future Prospect of Photonics-Enabled Terahertz Communication Research", IEICE Trans. Electron., VOL.E98-C, No. 12, pp. 1060-1070, 2015.

[3] K A Williams et al, "Long-wavelength monolithic mode-locked diode lasers", New Journal of Physics 6 (2004) 179.

[4] K. Van Gasse, et al, "Passively mode-locked III-V-on-silicon laser with 1 GHz repetition rate", ISLC, , September 12, 2016.

26 GHz Carrier Frequency 10 Gbit/s Radio-over-Fiber Link based on a Directly Modulated III-V/Si DFB Laser

Kasper VAN GASSE[1*], Joris VAN KERREBROUCK[2], Amin ABBASI[1], Geert MORTHIER[1], Guy TORFS[2], Gunther ROELKENS[1]

[1]Photonics Research Group, INTEC, Ghent University -imec, Gent, 9000, Belgium

[2]IDLab, INTEC, Ghent University - imec, Gent, 9000, Belgium

[*] kasper.vangasse@ugent.be

Worldwide mobile data traffic is expected to increase an eightfold by 2020 compared to 2015, reaching 30.6 exabytes per month [1]. To keep up with this increasing demand providers will need to use new technologies and network architectures, generally referred to as the 5th generation mobile network or 5G. Current mobile networks have pushed the link spectrum efficiency close to the Shannon limit by using complex modulation formats such as 64-QAM OFDM, leaving little room for improvement. To further improve connectivity and increase bandwidth more spectrum will be needed. This can be achieved through the use of currently unused bands and shrinking cell size to maximize spectrum re-use. To enable this, Radio-over-Fiber (RoF) links will be an important technology. When using higher carrier frequencies, it is beneficial to move the signal processing and signal up-conversion from the cell site to a central office. This greatly reduces deployment and operations cost, while enabling centralized control [2]. This is definitely the case for small cell architectures, where central control and low cost are essential. In many RoF links a Mach-Zehnder Modulator (MZM) is used to imprint the RF signal on an optical carrier, as the MZM provides good linearity and high bandwidth. However, in recent years directly modulated semiconductor lasers (DMLs) have shown rivalling performance in digital transmission [3]. Also as transmitter in RoF links DMLs have been demonstrated as good transmitters [4]. The great advantage of using directly modulated lasers is the lower complexity, cost and insertion loss (defining the link gain) compared to using external modulation. Since deployment and operation costs are essential in 5G scenarios, DMLs are ideally suited as transmitters.

In this work we demonstrate a RoF link where the transmitter is a directly modulated III-V-on-Silicon DFB laser. The hybrid silicon technology offers many advantages, such as the possibility to integrate it with high bandwidth Si-Ge PDs and passive optical functions such as wavelength multiplexing. The III-V-on-Silicon DFB laser was fabricated by adhesive wafer bonding of an InP epitaxial grown material with a multiple quantum well gain section on a SOI photonic integrated circuit as illustrated in Fig. 1(a). The photonic integrated circuit was fabricated by imec on a 400 nm thick top Si wafer with deep UV lithography. The DFB grating was defined in the Si rib waveguide with a 180 nm dry-etch and has a period of 245 nm with a 50% duty cycle. The laser is a quarter-wave shifted DFB with a length of 340 µm. A detailed description of the fabrication process can be found in [5]. The laser has an output of 5 mW in the Si waveguide for a driving current of 100 mA at a wavelength of 1571 nm. The bandwidth of the laser was determined using a 67 GHz Keysight PNA-X 67, and the result for different bias currents can be found in Fig. 1(b). More details about the laser characterization and digital transmission demonstration can be found in [3]. The high bandwidth characteristics of the device enable its use for high carrier frequency Radio-over-Fiber transmission. An overview of the measurement set-up is shown in Fig 1(c). For the experiment the III-V-on-silicon laser (DUT) was placed on a temperature-controlled stage and kept at 20°C. The laser was biased at 100 mA corresponding to the

maximum small signal bandwidth. The DUT was driven with a Keysight M8195A AWG, the output of the AWG was amplified with a 50 GHz SHF RF amplifier. The laser was coupled to standard single mode fiber (SMF) using an on-chip grating coupler. The output was amplified to 1 dBm with an EDFA to compensate for the chip-to-SMF coupling losses.

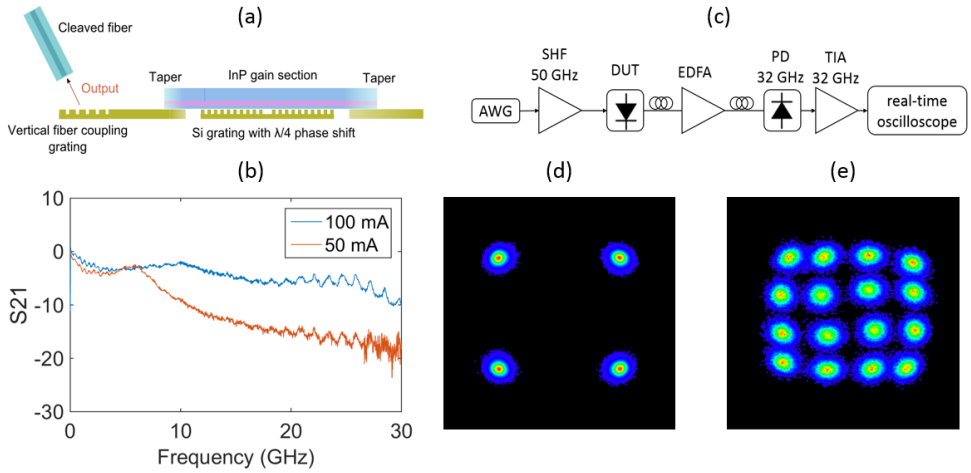


Figure 1: (a) Side view of the III-V-on-silicon DFB laser (b) S21 of the III-V-on-silicon DFB laser for different currents. (c) Overview of the measurement set-up. (d) Constellation of 1 Gbaud QPSK transmission on a 26 GHz carrier. (e) 2.5 Gbaud 16-QAM on a 26 GHz carrier

The optical output is then transmitted over 2 km of standard SMF. The receiver is a 32 GHz Discovery Semiconductor PD with TIA, and the output signal is analysed with a Keysight DSOZ634A real-time oscilloscope with 63 GHz bandwidth. We transmitted QPSK and 16-QAM signals at 1 and 2.5 Gbaud. This was done on a 26 GHz carrier frequency as will be used in 5G wireless networks. Transmission at 1 GBaud symbol rate gave an rms error vector magnitude (EVM) of 7-8% rms, independent of the modulation format. Such an EVM translates in error-free operation for QPSK modulation. Constellation diagrams of 2 Gbit/s QPSK and 10 Gbit/s 16-QAM on a 26 GHz carrier over 2 km of standard SMF is shown in Fig. 1(d)-(e). These experiments demonstrate that the III-V-on-Silicon DML is suited for high bit rate radio-over-fiber transmitters using high carrier frequencies to be used in 5G wireless access networks.

References

[1] Cisco, *Cisco Visual Networking Index: Global Mobile Data Traffic Forecast Update, 2015–2020 (white paper)*, Cisco System Inc., San Jose, 2016

[2] D C. Liu, J. Wang, L. Cheng, M. Zhu and G. K. Chang, *Key Microwave-Photonics Technologies for Next-Generation Cloud-Based Radio Access Networks*, Journal of Lightwave Technology, vol. 32, no. 20, pp. 3452-3460, 2014.

[3] A. Abbasi et al., *Enhanced modulation bandwidth of heterogeneously integrated III–V-on-silicon DFB laser for 40 Gb/s NRZ-OOK direct modulation*, 2016 International Semiconductor Laser Conference (ISLC), Kobe, Japan, pp. 1-2, 2016

[4] P. Hartmann, Xin Qian, A. Wonfor, R. V. Penty and I. H. White, *1-20 GHz Directly Modulated Radio over MMF Link*, 2005 International Topical Meeting on Microwave Photonics, pp. 95-98, 2005

[5] G. Roelkens et al., *III-V-on-silicon photonic devices for optical communication and sensing*, Photonics (invited), 2(3), p.969-1004, 2015

Photonic Integration in Converged Data Centre Systems

Richard PITWON[1*]
[1]Seagate, 1000 Langstone Technology Park, Havant, Hampshire PO9 1SA, United Kingdom
[*]richard.pitwon@seagate.com

System embedded photonic interconnect has been a strong area of focus in the European funding programmes for collaborative research and technological development over the past 15 years. This is particularly evident in projects from the Sixth Framework Programme (FP6), which ran from 2002 – 2006 [1], the Seventh Framework Programme (FP7), which ran from 2007 – 2013 [2] and the current Horizon2020 programme, which started in 2014 and is due to end in 2020 [3].

The PhoxTroT project [4] is a four year project, with a large consortium of 18 European organisations led by Fraunhofer IZM as project coordinator. PhoxTroT is an acronym of the full project title: "Photonics for High-Performance, Low-Cost & Low-Energy Data Centers, High Performance Computing Systems: Terabit/s Optical Interconnect Technologies for On-Board, Board-to-Board, Rack-to-Rack data links".

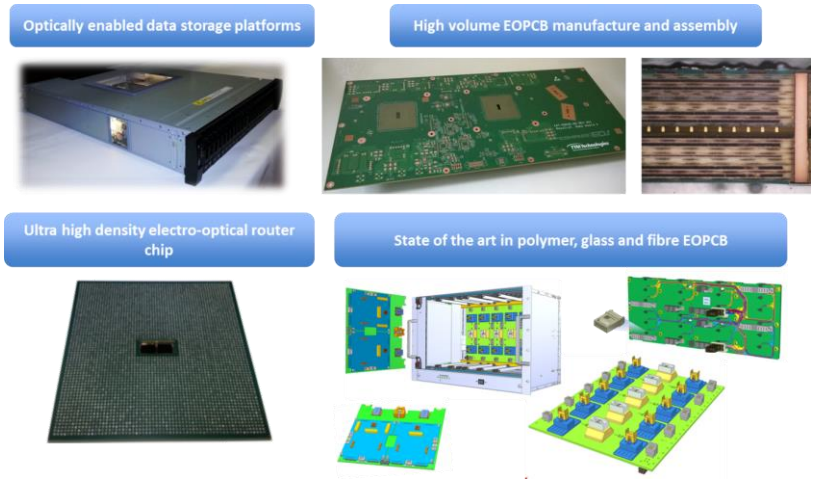


Fig. 1. PhoxTrot vision: On-chip, chip-to-chip, board-to-board and rack-to-rack optical interconnect solutions deployed in PhoxTrot demonstration platform

The vision of this large scale "Integrated Project" is to develop an entire technology portfolio of cost- and energy-efficient Tb/s-scale on-chip, chip-to-chip, board-to-board and rack-to-rack level photonic interconnect solutions within data centre and HPC

architectures. COSMICC ("CMOS Solutions for Mid-board Integrated transceivers with breakthrough Connectivity at ultra-low Cost") is a three year research project, supported by the Horizon2020 Framework Programme and led by CEA-LETI, which brings together key industrial and research partners partners including ST-Microelectronics, Finisar and Seagate [5]. The purpose of the project is to enable mass-commercialisation of silicon photonics based transceivers by enhancing the existing photonic integration platforms ST-Microelectronics and to ultimately deploy in data centre systems. The COSMICC transceiver technologies will be mounted in a series of optical interconnect test platforms, one of which is shown in Fig. 2.

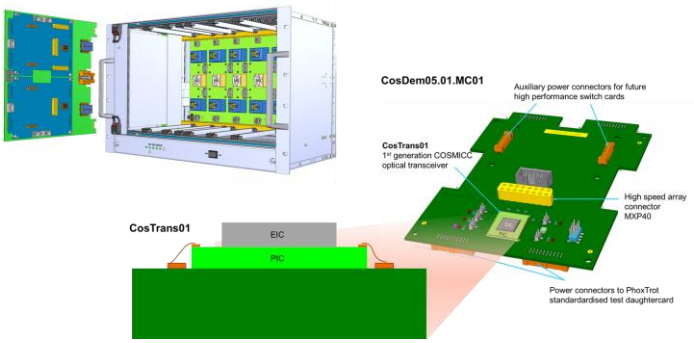


Fig. 2. COSMICC transceiver test platform

Seagate is developing a cross-project initiative called "PhoxLab", which will allow advanced technologies and demonstration platforms from different international projects to be tested with respect to one another. Phoxlab defines sub-system card form factors, which can be disseminated to allow other projects to design test board platforms enabling advanced optical transceivers or switches (such as silicon photonics devices), optical circuit boards and connectors to be mounted into different systems of varying complexity and Technology Readiness Levels (TRLs).

It is envisaged that COSMICC and other European, as well as international projects developing technologies in this sphere will be able to vastly expand their performance evaluation by participating in the initiative. This work was supported by the European Commission through the Horizon2020 COSMICC project.

References

[1] European Commission, "Sixth Framework Programme." [Online]. Available: https://ec.europa.eu/research/fp6/index_en.cfm.
[2] European Commission, "Seventh Framework Programme." [Online]. Available: http://cordis.europa.eu/fp7.
[3] European Commission, "Horizon 2020." [Online]. Available: https://ec.europa.eu/programmes/horizon2020.
[4] Tolga Tekin, "PhoxTrot project." [Online]. Available: http://www.phoxtrot.eu/. [Accessed: 16-Nov-2015].
[5] CEA-LETI, "Horizon 2020 COSMICC project." [Online]. Available: http://www.h2020-cosmicc.com.

Silicon Photonics based WDM Systems: Chip and Module Level Integration

Jeremy WITZENS[1*], Alvaro MOSCOSO-MARTÍR[1], Juliana MÜLLER[1], Florian MERGET[1], Johannes HAUCK[1], Sebastian ROMERO-GARCÍA[1], Bin SHEN[1], François LELARGE[2], Romain BRENOT[3], Alexandre GARREAU[3], Elad MENTOVICH[4], Daniel E. RASMUSSEN[4], Avner BADIHI[4], Anna SANDOMIRSKY[4], Rony SETTER[4]

[1]RWTH Aachen University, Institute of Integrated Photonics, Sommerfeldstr. 24, Aachen, 52074 Germany

[2]Almae Technologies SAS, Route de Nozay, Marcoussis, 91460, France

[3]III-V Lab, Campus de Polytechnique, 1 av. Augustin Fresnel, Palaiseau, 91767, France

[4]Mellanox Technologies, Hakidma 26, Ofer Industrial Park, Yokneam, Israel

[*] jwitzens@iph.rwth-aachen.de

The implementation of compact, dense WDM transceivers in Silicon Photonics (SiP), that are sufficiently cost and power efficient for Data Centre applications, is a notably challenging endeavour. Semiconductor Mode Locked Lasers (MLL) [1] and Resonant Ring Modulators (RRM) [2, 3] have been proposed as key devices for an elegant and efficient transceiver architecture. In recent works, we have shown that single section passively mode-locked MLLs can generate adequate optical carriers for 14 Gbps and 25 Gbps serial communications with on-off keying modulation [4]. A systematic analysis of the optical power budget of a solution comprising a MLL, an array of RRMs driven by hybridly integrated chip-scale electronics, and a Semiconductor Optical Amplifier (SOA) has also been reported [5]. At the 2017 European Conf. on Integrated Optics we will be reporting on recent progress towards integration of this transceiver architecture.

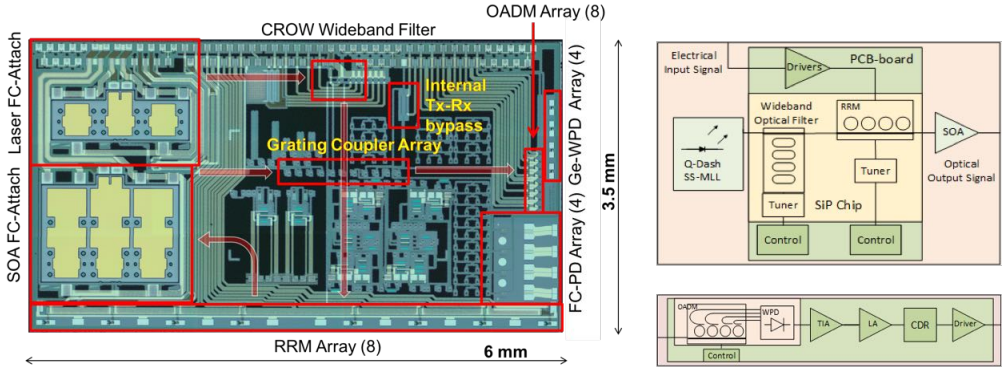


Fig. 1. Micrograph of the system chip and diagram of system architecture.

Fig. 1 shows a micrograph of the system chip as well as a block-diagram of the system architecture. A wideband optical filter implemented with coupled ring resonators in Coupled Resonators Optical Waveguides (CROW) configuration selects the highest

power lines of the MLL as optical carriers for downstream modulation. Extinction of unused lines is essential to limit SOA saturation and the ensuing data distortion.

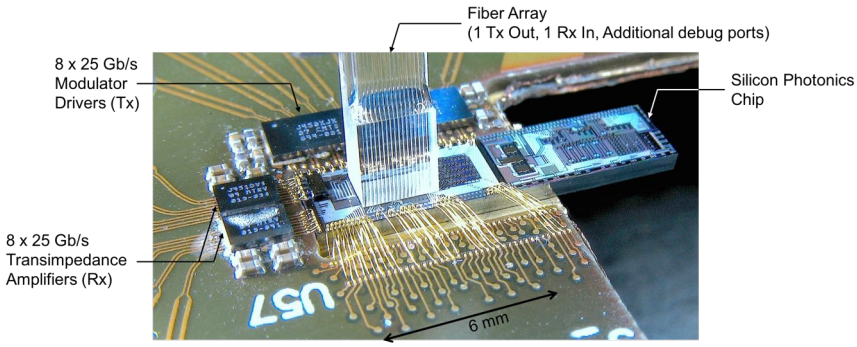
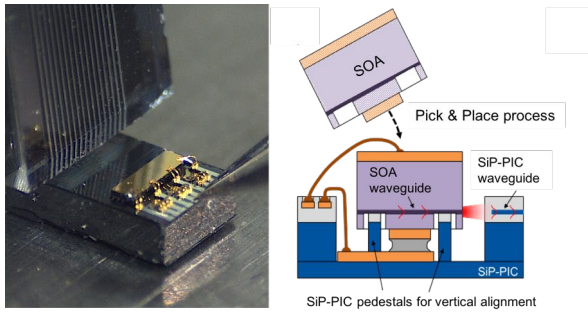


Fig. 2. Photograph of the SiP chip wire bonded to chip scale driver and receiver electronics. The MLL is coupled in by means of a lensed fibre edge coupled to the chip (not shown). The SOA is an external commercial device interposed between the Tx Out and Rx In ports.

Fig. 2 shows the currently evaluated transceiver, in which MLL and SOA remain external devices. We are currently building a demonstrator packaged as a module with flip-chip integrated MLL and SOA. To this end, we have developed a flip-chip integration process (Fig. 3) in which the vertical alignment is guaranteed by a mechanical contact between pedestals defined in a recess etched into the SiP chip and the laser or SOA [6]. We have introduced the extra refinement that the pedestal height is defined by selectively removing the SiP waveguide layer on top of the pedestals, and that corresponding mechanical contact areas are defined on the III-V chips by a selective wet etch stopping on top of the III-V waveguide layer. This way, the accuracy of vertical alignment is independent on the process control exerted on layer thicknesses during SiP or III-V chip fabrication. Horizontal alignment tolerances can be further relaxed with suitable edge couplers [6,7].



[1] D. Yin et al., *Laser Diode Comb Spectrum Amplification preserving low RIN for WDM application*, in Proc. SPIE, vol. 7631, 76311R, 2009.

[2] Q. Xu et al., *Micrometre-scale silicon electro-optic modulator*, Nat., vol. 435, pp. 325-327, 2005.

[3] J. Müller et al., *Optical Peaking Enhancement in High-Speed Ring Modulators,* Sci. Rep., vol. 4, 6310, 2014.

[4] J. Müller et al., *High Speed WDM Interconnect Using Silicon Photonics Ring Modulators,* in Proc. Europ. Conf. on Opt. Comm. (ECOC), Valencia, Spain, 2015.

[5] A. Moscoso-Mártir et al., *Silicon Photonics WDM Transceiver with SOA and Semiconductor Mode-Locked Laser,* arXiv:1605.08668.

[6] T. Shimizu et al., Photon. Res., vol. 2, no. 3, pp. A19-A24, 2014.

[7] S. Romero-García et al., J. Sel. Top. Quant. Electron., vol. 20, no. 4, 8200611, 2014.

Dilated 4×4 Hybrid MZI-SOA Switch with Relaxed Active Bias Control

M. Ding[1*], A. Wonfor[1], Q. Cheng[1], R. V. Penty[1], I. H. White[1]
[1] Centre for Photonic Systems, University of Cambridge, CB3 0FA, United Kingdom
[*] md613@cam.ac.uk

Increasingly complex and high capacity optical switch fabrics are being proposed and demonstrated for high-bandwidth data streams in datacentres [1]. Mach-Zehnder interferometer (MZI) and semiconductor optical amplifier (SOA) based switches have received much attention owing to their nanosecond response time which is essential for packet switching [2]. However, the scalability of MZI switches is inherently limited by insertion loss and accumulated crosstalk, whilst the scalability of SOA switches is restricted by accumulated noise and distortion.

We therefore have proposed a hybrid MZI-SOA approach, where MZIs are implemented as 1×2 or 2×1 low-loss switching elements, minimising crosstalk by using a single input, and where short SOAs are included as gain or absorption units, offering either loss compensation or crosstalk suppression though adding only minimal noise and distortion [3]. Using this approach, a 2×2 hybrid building block has been built by connecting four MZIs and eight SOAs in a dilated Beneš structure. This exhibited a -40dB extinction/crosstalk ratio and lossless operation [4]. The schematic of a 4×4 switch based on this approach and consisting of four 2×2 dilated hybrid building blocks is shown Fig. 1(a). For multi-stage networks such as this, it has been shown that active power monitoring and bias control can be employed to maintain constant output power and extend the input power dynamic range (IPDR) [5]. In this paper, we demonstrate the first current controlled operation of this 4×4 hybrid switch and investigate the control tolerance.

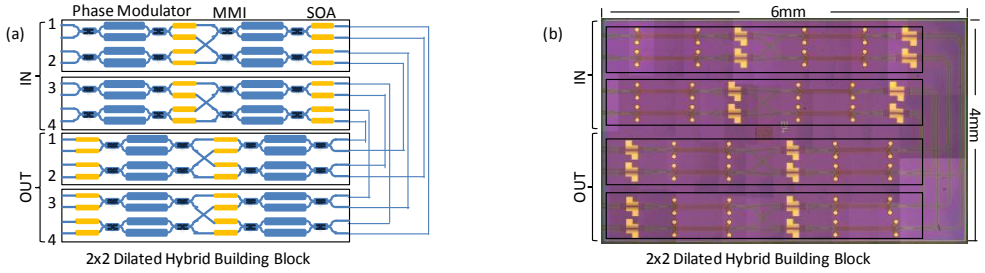


Fig. 1. (a).Schematic of 4×4 switch (b) Photograph of the fabricated hybrid switch

The switch was designed and fabricated on a multi-project wafer using a generic foundry within the EU FP7 PARADIGM project [6] with a sector size of 4mm×6mm. 1000/900μm long MZIs are used as 1×2 or 2×1 switching elements and 230/250μm long SOAs provide 5/6.3dB gain with 15mA/17mA bias currents to compensate loss from passive components. The slightly longer SOAs (250μm) are placed before the folded shuffle network to compensate for excess loss.

Power variation at the input causes fluctuation in the output power which in turn requires more demanding receiver performance levels or which leads to signal degradation in the following active components. It is therefore highly desirable to maintain a constant output power for a range of input powers. The first and second

stage SOAs are therefore calibrated to select the optimum bias condition for various input powers. The calibration is performed with a 10 Gb/s NRZ signal at a wavelength of 1535.9nm. Lensed fibres are used to couple light in and out of the switch chip. The switch chip is mounted on a thermo-electric cooler and operated at 20^0C. The optical transfer function is evaluated for a broad range of currents and input powers. Fig. 2(a) shows the optical transfer function as the first and second stage SOA currents are varied, all other SOAs being biased at 15mA. Also shown is the transfer function for the controlled condition whereby the output power is fixed at -6dBm for a 10dB range of input power by varying the first and second stage SOA currents.

The IPDR with constant (15mA/17mA) and controlled current operation is shown in Fig. 2(b). At lower input power, it is not possible to achieve the desired constant output power owing to the limited gain from SOAs. The optimised bias current for first and second stage SOAs is selected here to minimise power penalty. The IPDR for a penalty of less than 0.2dB has been extended from 4dB to 8dB by implementing the active bias control. The power penalty improvement is significant at high powers because there is less amplifier-induced distortion as the SOA bias currents are lower. The tolerance of the bias control depends on the input power. Fig. 2(c) show a detailed penalty map for the active bias control as a function of both input power and bias variation. A 5mA bias current range is shown to maintain the power penalty below 0.2dB, this being a relatively relaxed tolerance in terms of the necessary current control.

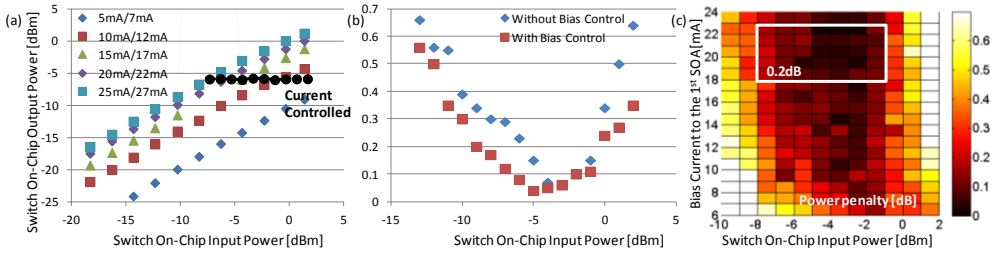


Fig. 2. (a) Static transfer function of the switch for varied and controlled current (b) Input dynamic range for the switch with fixed and controlled current operation (c)Penalty map as a function of input power and bias current.

In conclusion, this paper presents the active bias control for the 4×4 hybrid MZI-SOA switch chip. By controlling the injection current of the first and second stage SOAs, the fixed output power is achieved for a 10dB range of input power, and IPDR for a penalty less than 0.2 dB is extended from 4dB to 8dB with 5mA control current tolerance. This extended IPDR enables the scalability of the hybrid optical switch.

The authors wish to acknowledge funding from the UK EPSRC SwiTching And tRansmission (STAR) project EP/K018116/1 and FP7 PARADIGM project. Additional data related to this publication is available at http://www.repository.cam.ac.uk/.

References

[1] A. Wonfor, et al, *J. Opt. Commun. Netw*., vol. 3, p. A32, (2011).
[2] M. Crovella, et al, Internet Measurement: Infrastructure,Traffic and Applications. New York, NY, USA: Wiley, (2006)
[3] Q. Cheng, et.al, *J. Lightw. Technol*., 18, pp. 3077- 3084, (2013).
[4] Q. Cheng, et al, *Optics Letters*, vol. 39, no. 6, (2014)
[5] I.H. White et al, *J. Opt. Commun. Netw*., vol. 6, p. 180, (2007).
[6] M. Smit, et.al, *Semiconductor Science and Technology,* vol. 29, p. 083001, (2014).

Flexible Multimode Polymer Waveguides for High-Speed Optical Interconnects

Fengyuan SHI, Nikos BAMIEDAKIS, Richard V. PENTY, Ian H. WHITE, Daping CHU*

Electrical Engineering Division, Engineering Department, University of Cambridge,
9 JJ Thomson Avenue, Cambridge, CB3 0FA, United Kingdom
* dpc31@cam.ac.uk

Abstract: Flexible multimode polymer waveguides are shown to maintain bandwidth length products > 300 GHz×m for bend radii as low as 3 mm under restricted launch, with < 0.7 dB excess bend loss.

Introduction: Recently, multimode polymer waveguides have attracted increased interest for use in short-reach optical interconnections and optical backplanes. These waveguides can be formed and directly integrated on standard printed circuit boards (PCBs) owing to their favourable material properties [1]. Bandwidth studies have shown that the waveguides have the potential to support 100 Gb/s data transmission despite their highly-multimoded nature [1], and 40 Gb/s data transmission over a 1 m long multimode polymer waveguide has been demonstrated recently [2]. These waveguides can also be fabricated on flexible substrates enabling additional applications. Although studies on flexible multimode polymer waveguides have been reported [3, 4], there has been particular concern about the bend loss of waveguides required to provide high bandwidth. This work therefore reports the waveguide bend loss alongside bandwidth as a function of curvature and bending angle under restricted launch. The measured results indicate a bending and twisting loss of less than 0.7 dB for a curvature R > 3mm, despite allowing bandwidth-length products (BLP) of at least 300 GHz×m under restricted excitation. Further studies are underway combining loss and bandwidth measurements with near- and far-field measurements to reveal their mode loss and coupling behaviour and therefore, enable the design of optimised flexible waveguides and related components.

Bend loss measurement: The polymer waveguide samples are fabricated from siloxane materials [Dow Corning® OE-4140 (core) and OE-4141 (cladding) Cured Optical Elastomers] with a standard photolithographic method on flexible 125 μm-thick polyimide substrates. The waveguide cross section is ~50×50 μm^2 and samples of 10 and 24 cm in length are used for the measurements. An 850 nm vertical-cavity surface-emitting laser (VCSEL) is employed as the light source, while a cleaved fibre is used to couple the light. The waveguide sample is wrapped round a cylindrical mandrel and the output light is focused with a microscope objective onto a broad area detector (Fig. 1a). Mandrels with different diameters and different wrapping angles (from 0º to 180º) are employed. Moreover, the samples are twisted a variable number of turns and their insertion loss is recorded (Fig. 1b-d). Two different launch conditions are employed by using different types of cleaved fibres: a 4/125 μm single mode fibre (SMF) and a standard 50/125 μm multimode fibre (MMF), at the waveguide input in order to assess their loss performance under different types of excitation. For each launch condition and setup, 12 waveguides are measured and the average insertion loss value is obtained. The average insertion loss of the waveguide samples when not bent (R=∞) is also measured and used as a reference to obtain the excess bend loss. This is found to be 1.4 and 1.5 dB for the 10 cm-long samples under the SMF and 50 μm MMF inputs, respectively. Fig. 1e and 1f show the excess loss as a function of bending radius and angle (R = 5 mm), respectively, while Fig. 1g shows the excess loss when the sample is twisted (1 twist turn = 360º). The samples can be bent down to a radius of 2 mm without any cracks and with excess bend losses of below 1.5 and 3.7 dB for the SMF and 50 μm MMF inputs, respectively. The variation of bend loss with bending angle (Fig. 1f)

indicates that the majority of the optical power is lost in the first 90º of the curvature. After that, lower order modes, which exhibit lower attenuation along the bend, are left to propagate in the waveguide. Twisting the samples more than 1 full turn (360º) however results in additional loss, mainly due to the acute twisting nodes (Fig. 1c) occurring in the flexible samples. Applying more than 2 turns, does not significantly further increase the loss as only the low order modes are left to propagate. Excess twisting losses of less than 0.6 and 2 dB are recorded for up to 4 full turns under the SMF and 50 µm MMF input, respectively. Similar bend loss performance is observed from the longer samples.

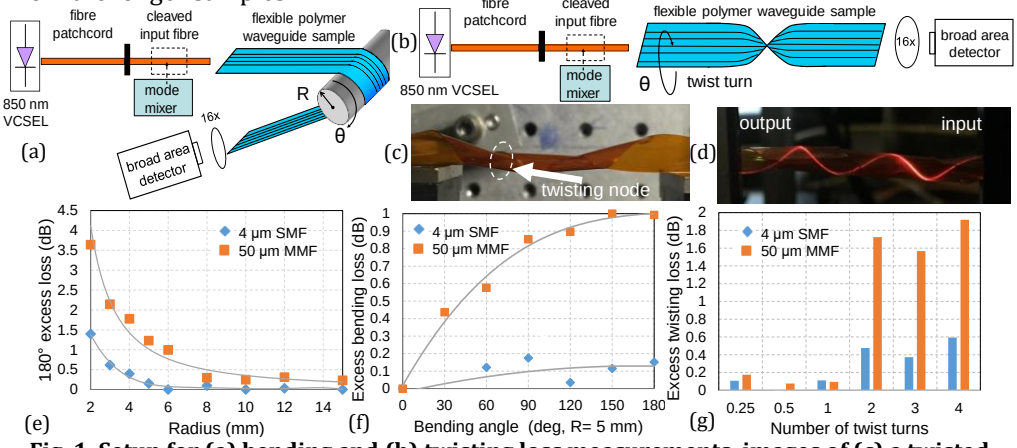


Fig. 1. Setup for (a) bending and (b) twisting loss measurements, images of (c) a twisted flexible waveguide sample (2 full twists) (d)with light, and excess bend loss as a function of (e) radius of curvature, (f) bending angle (R = 5 mm) and (g) number of full twist turns.

Bandwidth measurement: The bandwidth of the 24 cm-long waveguides is obtained using pulse broadening measurement. A setup similar to the one described in [1] is employed, while a 10× microscope objective with a numerical aperture (NA) of 0.2 is used at the waveguide input to emulate a SMF input. A short pulse (~400 fs FWHM) is launched into the flexed samples and the pulse broadening due to the waveguide dispersion is recorded for different bending radii. The waveguide BLP can then be extracted and it is found to be >300 GHz×m for all radii ≥ 3 mm under a restricted launch (Fig. 2). The results indicate that, under a restricted launch, tighter bends enhance mode coupling (rather than mode loss) in the waveguide and result in a slight reduction of bandwidth. This view can be confirmed by the increased NA of waveguides as measured (Fig. 2). Bandwidth measurements under different launch conditions are underway and the results will be presented at the conference.

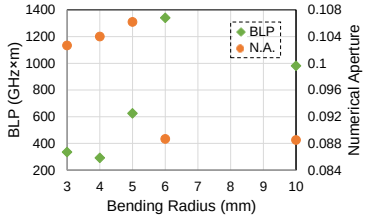


Fig. 2. BLP and NA as a function of bending radius

Conclusion: The loss and bandwidth of flexible multimode polymer waveguides are investigated under different launch conditions, providing an understanding of mode propagation in these waveguides. Excess bend and twisting losses as low as 0.7 and 0.6 dB, respectively, are demonstrated for radii greater than 3 mm while maintaining BLP of greater than 300 GHz×m under a restricted launch.

References

[1] J. Chen, et al., JLT, vol. 34, no. 12, pp. 2934–2940, 2015.
[2] N. Bamiedakis, et al., JLT, vol. 33, pp. 882-888, 2015.
[3] R. Dangel, et al., JLT, vol. 31, pp. 3915-3926, 2013.
[4] T. Chen, et al., JLT, vol. 33, pp. 2032-2037, 2015

High-gain waveguide amplifiers based on potassium rare-earth double tungstates

Yean-Sheng YONG[1*], Sergio A. VÁZQUEZ-CÓRDOVA[1], Shanmugam ARAVAZHI[2], Christos GRIVAS[3], Jennifer L. HEREK[1], Sonia M. GARCÍA-BLANCO[1], and Markus POLLNAU[2,4]

[1]Optical Sciences Group, MESA+ Institute for Nanotechnology, University of Twente, P.O. Box 217, 7500 AE Enschede, Netherlands

[2]Integrated Optical Microsystems Group, MESA+ Institute for Nanotechnology, University of Twente, P.O. Box 217, 7500 AE Enschede, Netherlands

[3]School of Physics and Astronomy, University of Southampton, Southampton SO17 1BJ, UK

[4]Department of Materials and Nano Physics, School of Information and Communication Technology, KTH–Royal Institute of Technology, Electrum 229, Isafjordsgatan 22–24, 16440 Kista, Sweden

[*] y.s.yong@utwente.nl

The down-scaling of the rare-earth-doped amplifier to chip-scale device length is beneficial for signal amplification within short-reach interconnects such as optical backplanes [1, 2] and for the realization of novel active/passive integrated optical chips. Thus far, with the demonstration of 20 dB net gain [3], high bit-rate operation at 170 Gb/s [4], and gain bandwidth over 80 nm [5] in the C-band, as well as 14.4 dB net gain at 1064 nm wavelength [6], rare-earth-doped amorphous Al_2O_3 is a very promising material for waveguide amplifiers. The corresponding peak gain per unit length of Er^{3+}- and Nd^{3+}-doped Al_2O_3 are ~2.0 dB/cm [5] and 6.3 dB/cm [6], respectively. To further increase the gain per unit length, a host material with higher transition cross-sections and higher active-ion solubility is needed. In this work, it is shown that highly Yb^{3+}-doped and Er^{3+}-doped monoclinic potassium rare-earth double tungstate, $KRE(WO_4)_2$ epitaxial layers match these two conditions and produce higher gain per unit length.

Yb^{3+}-doped and Er^{3+}-doped $KRE(WO_4)_2$ layers were grown on undoped potassium yttrium double tungstate, $KY(WO_4)_2$, substrates with the dimension of 1 mm × 10 mm × 10 mm by liquid phase epitaxy [7]. Optically inert Lu^{3+} and Gd^{3+} are included in the epitaxial layer for: i) maintaining lattice matching conditions with respect to the substrate, ii) increasing the refractive index contrast between active layer and substrate, and iii) maximizing the active ion concentration. The index of refraction of the substrate at $E||n_m$ is ~2.0 for the wavelength range of 1000-1550 nm and the refractive index contrast between the active layer and the substrate is ~0.012.

Figure 1(a) shows the absorption and emission cross-sections of the $KYb_{0.57}Gd_{0.43}(WO_4)_2$ layer determined with the procedure described in [8]. The 57 at.% Yb^{3+} in the epitaxial layer corresponds to an active ion density of $\sim 3.8\times10^{21}$ cm^{-3}. The peak absorption and emission cross-sections are 13.1×10^{-20} cm^2 and 16.2×10^{-20} cm^2, respectively, at ~981 nm, which is about an order of magnitude higher than those of Al_2O_3:Yb^{3+} [9]. The transition cross-sections of Er^{3+}-doped $KRE(WO_4)_2$ layers are displayed in Fig. 1(b). The luminescence spectra and luminescence lifetime measurements were performed on a layer with the lowest available Er^{3+} concentration of 0.75 at.% ($\sim 0.47\times10^{20}$ cm^{-3}) to avoid reabsorption effects, while the reciprocity theorem was used to calculate the absorption cross-section. The Er^{3+} peak transition

cross-sections are ~4.3× higher in potassium double tungstates than in Al_2O_3.

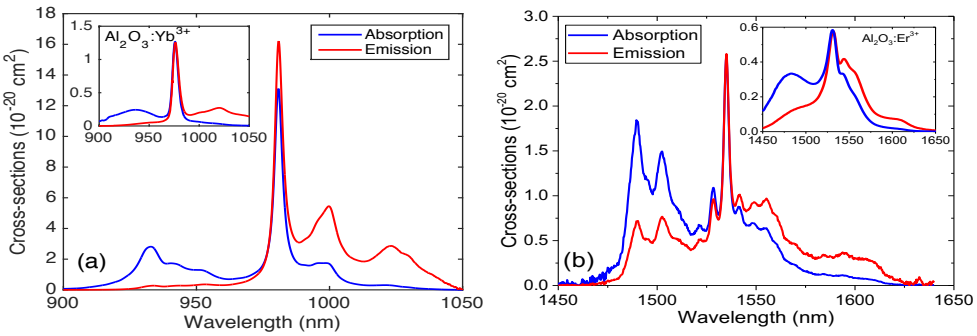


Fig. 1. Transition cross-sections of (a) Yb^{3+}-doped and (b) Er^{3+}-doped potassium rare-earth double tungstate epitaxial layers. The insets show the corresponding transition cross-sections for the same active ion doped into Al_2O_3 [5, 9] for comparison purpose.

The luminescence lifetime measured from $KYb_{0.57}Gd_{0.43}(WO_4)_2$ is merely ~7% less than the lifetime from low-doped (1.2 at.% Yb^{3+}) sample (245 µs), indicating a very weak lifetime quenching. The averaged lifetime of the first excited state ($^4I_{13/2}$) for the samples with 0.75-10 at.% Er^{3+} is ~3.05 ms. No sign of lifetime quenching was observed for the samples within the range of Er^{3+} concentrations investigated. However, like in many Er^{3+}-doped materials, excitation-density-dependent energy-transfer upconversion significantly shortens the luminescence-decay time.

Pump-probe measurements are conducted to determine the optical gain. By launching both optical beams perpendicular to the 32 µm-thick $KYb_{0.57}Gd_{0.43}(WO_4)_2$ layer, a net gain of >900 dB/cm is determined at the 981 nm signal wavelength by pumping at 932 nm wavelength. The reduction of transition cross-sections at elevated temperatures [8] due to pump-induced heating may be the gain-limiting mechanism. The 6 at.% Er^{3+}-doped $KRE(WO_4)_2$ channel waveguides, micro-structured using ion-beam etching, produce gain >10 dB/cm at the 1534.75 nm signal wavelength by pumping at 984.5 nm, which is much higher than most of the singly Er^{3+}-doped materials. The gain of the Er^{3+}-doped $KRE(WO_4)_2$ waveguides is limited by energy-transfer upconversion and excited-state absorption processes. As a result, higher Er^{3+} concentration does not lead to better gain.

In summary, Yb^{3+}- or Er^{3+}-doped $KRE(WO_4)_2$ epitaxial layers exhibit large transition cross-sections and limited luminescence lifetime quenching at high doping concentrations. High optical gain of >900 dB/cm for highly Yb^{3+}-doped layers (57 at.%) at 981 nm wavelength and >10 dB/cm for the Er^{3+}-doped layers (6 at.%) at 1534.75 nm wavelength were demonstrated.

References

[1] R. Dangel et al., Opt. Express **23**, 4736-4750, 2015.
[2] F. E. Doany et al., IEEE Trans. Adv. Packag. **32**, 345-359, 2009.
[3] S. A. Vázquez-Córdova et al., Opt. Express **22**, 25993-26004, 2014.
[4] J. D. B. Bradley et al., Opt. Express **24**, 22201-22208, 2009.
[5] J. D. B. Bradley et al., J. Opt. Soc. Am. B **27**, 187-196, 2010.
[6] J. Yang et al., Appl. Phys. B **101**, 119-127, 2010.
[7] S. Aravazhi et al., Appl. Phys. B **111**, 433-446, 2013.
[8] Y. S. Yong et al., Opt. Express **24**, 26825-26837, 2016.
[9] L. Agazzi, Ph.D. thesis, University of Twente, Enschede, The Netherlands, p. 35, 2012.

Optically integrated InP-Si_3N_4 hybrid laser

Youwen FAN[1*], Jörn P. EPPING[2,3], Ruud M. OLDENBEUVING[2,3], Chris G. H. ROELOFFZEN[2,3], Marcel HOEKMAN[3], Ronald DEKKER[4], René G. HEIDEMAN[3], Peter J. M. VAN DER SLOT[1], and Klaus-J. BOLLER[1]

[1]University of Twente, MESA+ Institute for Nanotechnology, Laser Physics and Nonlinear Optics Group, Enschede 7500 AE, The Netherlands
[2]SatraX B.V., Enschede 7500 AL, The Netherlands
[3]LioniX B.V., Enschede 7500 AL, The Netherlands
[4]XiO Photonics B.V., Enschede 7500 BG, The Netherlands
[*] corresponding author e-mail: y.fan@utwente.nl

Abstract—We present the first demonstration of an optically integrated InP-Si_3N_4 hybrid laser. The feasibility and viability of facet-to-facet, butt-coupled integration is proven by single-frequency operation, tunability across a wide range of 43 nm (including the entire telecom C-band) with spectral linewidths as narrow as 87 kHz.

I. Introduction

Narrow linewidth semiconductor lasers are of interest for a wide range of applications [1], [2]. Specifically when looking for narrow spectral linewidths, monolithic semiconductor lasers in which all the components are made of the same material approach their limits. This is the reason why so-called hybrid lasers are currently receiving considerable interest. In such lasers, the semiconductor amplifier is optically coupled to a low-loss waveguide circuit made from another material, and this is known to decrease the Schawlow-Townes linewidth of a laser [3]. In this paper, we demonstrate an optically integrated InP-Si_3N_4 laser for the first time. For providing a strong margin of tolerable losses and cavity designs, we utilize a high-gain reflective semiconductor optical amplifier (RSOA).

2. Integration processes

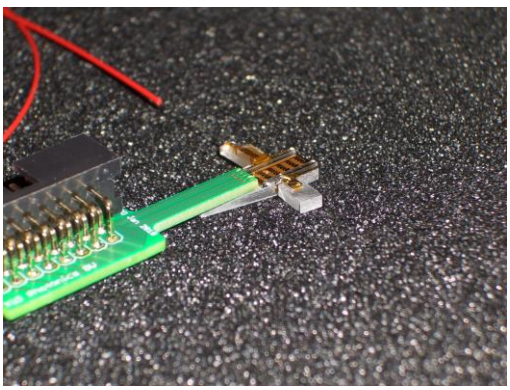


Fig. 1. Photograph of the integrated hybrid laser

A picture of the integrated laser is shown in Fig. 1. The RSOA and the feedback circuit were fixed on separate submounts and all the electric contact pads were wire-bonded to a fan-out printed circuit board (PCB) which was connected to a dedicated designed controlling board. The output waveguide facet was first aligned and assembled with a high numerical aperture (NA) polarization maintaining (PM) fiber that has a specified 1/e field strength mode field diameter (MFD) of 6 μm in both directions to minimize the output coupling loss. Optically transparent UV curable adhesive was applied to the InP-Si_3N_4 interface. After fiber-chip assembly, the InP section and Si_3N_4 circuit were aligned using translational stages under monitoring of the output power and optical spectrum until the glue was cured by UV light. Afterwards, the whole laser was mounted on top of a copper heat sink using thermally conductive silver-filled epoxy.

3. Characteristics of the integrated hybrid laser and discussion

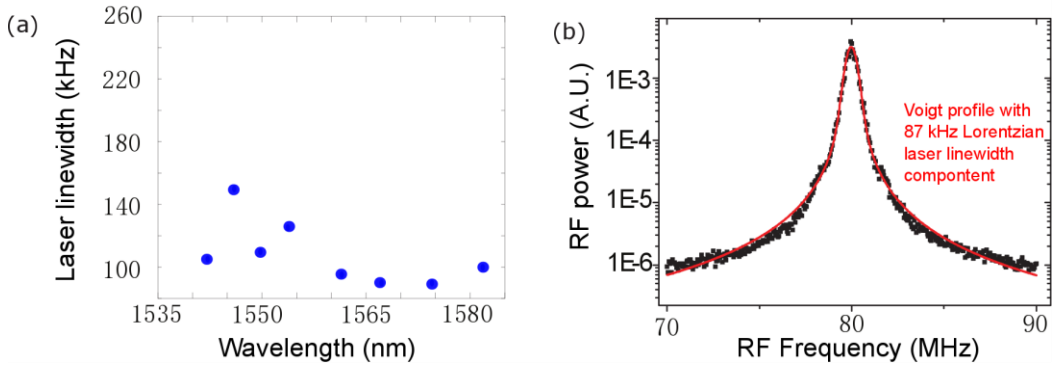


Fig. 2. (a) Laser linewidth measured at various wavelength within the tuning range; (b) Recorded beat signal (black) at a driving current of 196 mA and a laser output wavelength of 1578.12 nm

The fiber-coupled output power of the laser is about 1.7 mW at a 200 mA pump current at a threshold current of 35 mA. A first step of spectral characterization was thermo-optic wavelength tuning of the single-frequency laser output. A wide tuning range of 43 nm was achieved by thermally tuning the MRRs. The typical side mode suppression ratio (SMSR) ranges from 35 dB to 40 dB over the 43 nm tuning range and the relative intensity noise (RIN) is measured to be -135 dBc/Hz. Next we systematically measured the linewidths at various laser wavelengths as is shown in Fig. 2, while the output power was kept to around 1 mW,. The measurements clearly indicate that the laser exhibits linewidths smaller than 150 kHz over the entire tuning range, and exhibit a narrowest linewidth of 87 kHz.

Bearing in mind that the linewidth is inversely proportional to the output power [6] and also drops with the optical length of the external waveguide feedback circuit and its frequency selectivity, we expect that the laser linewidth can be reduced by a factor of 10 straightforwardly.

4. Conclusion

In this paper, an optically integrated InP-Si_3N_4 hybrid laser is presented for the first time. A wide range operation of more than 43 nm is achieved with a typical side mode suppression ratio (SMSR) of 35 dB. The laser shows good noise performance with relative intensity noise less than -135 dBc/Hz and a very narrow linewidth as low as 87 kHz. Such properties make InP-Si_3N_4 hybrid lasers promising for advanced quadrature amplitude modulation (QAM) [1].

References

[1] S. Zhang, P. Y. Kam, C. Yu, and J. Chen, *Laser linewidth tolerance of decision-aided maximum likelihood phase estimation in coherent optical M-ary PSK and QAM systems*, IEEE Photon. Technol. Lett., vol. 21, no. 15, pp. 1075–1077, 2009.

[2] J. E. Koroshetz, *Fiber lasers for lidar*, in Optical Fiber Communication Conference and Exposition and The National Fiber Optic Engineers Conference. Optical Society of America, 2005, p. OFJ4.

[3] C. Henry, *Theory of the linewidth of semiconductor lasers*, IEEE J. Quant. Electron., vol. 18, no. 2, pp. 259–264, 1982.

[4] R. M. Oldenbeuving, E. J. Klein, H. L. Offerhaus, C. J. Lee, H. Song, and K.-J. Boller, *25 kHz narrow spectral bandwidth of a wavelength tunable diode laser with a short waveguide-based external cavity*, Laser. Phys. Lett., vol. 10, no. 1, p. 015804, 2013.

[5] A. J. Zilkie, P. Seddighian, B. J. Bijlani, W. Qian, D. C. Lee, S. Fathololoumi, J. Fong, R. Shafiiha, D. Feng, B. J. Luff, X. Zheng, J. E. Cunningham, A. V. Krishnamoorthy, and M. Asghari, *Power-efficient III-V/Silicon external cavity DBR lasers*, Opt. Express, vol. 20, no. 21, pp. 23 456–23 462, 2012.

[6] K. Dridi, A. Benhsaien, J. Zhang, and T. J. Hall, *Narrow linewidth 1550 nm corrugated ridge waveguide DFB lasers*, IEEE Photon. Technol. Lett., vol. 26, no. 12, pp. 1192–1195, 2014.



EUROPEAN CONFERENCE ON INTEGRATED OPTICS

Electro-Optic Modulation in Silicon Nitride Photonic Integrated Circuits by means of ALD ZnO Overlays

Artur HERMANS[1,2,*], Michiel VAN DAELE[3], Jolien DENDOOVEN[3], Stéphane CLEMMEN[1,2], Christophe DETAVERNIER[3], Roel BAETS[1,2]

[1]Photonics Research Group, Ghent University - imec, 9052 Ghent, Belgium

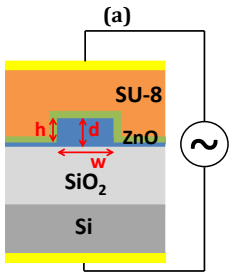
[2]Center for Nano- and Biophotonics (NB-Photonics), Ghent University, 9052 Ghent, Belgium

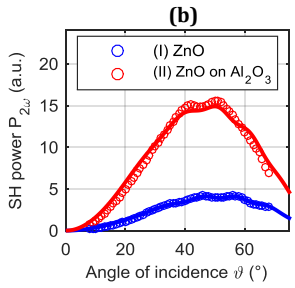
[3]Department of Solid State Sciences, Faculty of Sciences, Ghent University, 9000 Ghent, Belgium

[*] artur.hermans@ugent.be

Second-order nonlinear optical ($\chi^{(2)}$) effects are at the basis of many applications such as fast electro-optic modulators (EOMs) and optical parametric oscillators. But most of these $\chi^{(2)}$ devices make use of bulk materials or low-contrast waveguides. By integrating $\chi^{(2)}$ effects on a chip and exploiting the advancements in nanophotonic circuit design, cheaper, smaller and more efficient $\chi^{(2)}$ devices could be realized. The CMOS-compatible Si and SiN platform have proven to be well-suited for photonic integration, however, they lack significant $\chi^{(2)}$ nonlinearity. We propose using atomic layer deposited (ALD) zinc oxide to fill this need. ALD lends itself well to photonic integration as it is a low-temperature, conformal deposition technique that provides thickness precision at the monolayer level. ZnO is a wide band gap material (~3.3 eV) that crystallizes preferably in the hexagonal wurtzite structure, point group 6mm [1]. We report on strong second-harmonic generation (SHG) in polycrystalline plasma-enhanced ALD (PE-ALD) ZnO thin films deposited on glass substrates. Furthermore, we have observed the linear electro-optic (EO) effect in SiN waveguides coated with PE-ALD ZnO. To the best of our knowledge, this is the first demonstration of the linear EO effect in a waveguide with a $\chi^{(2)}$ active ALD overlay.

For thin film deposition a homebuilt ALD reactor with a base pressure of 10^{-6} mbar is used. In the SHG experiments we have studied two samples: (I) 39.1 nm ZnO on glass, and (II) 36.7 nm ZnO on 6 nm Al_2O_3 on glass. An Al_2O_3 seed layer is used in sample (II) because it has been shown to promote (002) orientation of the ZnO crystallites and therefore improve $\chi^{(2)}$ nonlinearity [2]. The Al_2O_3 layer is deposited via thermal ALD at a substrate temperature of 120°C (from trimethylaluminium and H_2O, both for 5 s at 5×10^{-3} mbar). ZnO deposition is done at 300°C by PE-ALD (5 s diethyl zinc at 5×10^{-3} mbar and 10 s O_2 plasma at 10^{-2} mbar). For the EOM, we started from air-cladded SiN waveguides fabricated in a CMOS-fab on which we deposited 87 nm ZnO (there is no Al_2O_3 seed layer in this first sample). This was followed by spin coating of a 3 µm SU-8 cladding and electrode fabrication. A cross-section of the structure is depicted in Fig. 1a. The electric field is applied vertically. This allows to access χ_{zzz} and χ_{xxz} (or r_{333} and r_{113}) in the ZnO layer on top using the TM_{00} and TE_{00} mode respectively. The chip is cleaved at both waveguide ends for edge coupling.





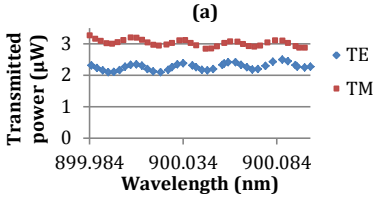
(c)

$\chi^{(2)}$ values obtained from fitting SHG data	(I) ZnO	(II) ZnO on Al_2O_3
χ_{zzz} (pm/V)	-4 ± 2	-14 ± 5
$2\chi_{xxz}+\chi_{zxx}$ (pm/V)	5.9 ± 0.5	13.1 ± 0.9

Fig. 1. (a) Schematic device cross-section of EOM (d = 300 nm, h = 270 nm, w = 650 nm). (b) SHG measurements (circles) and fitted curves (full lines). (c) $\chi^{(2)}$ fitting results.

For the SHG experiments we use a femtosecond laser at a wavelength of 980 nm. The laser light (p-polarized) is focused onto the samples and the transmitted SH power is measured as a function of the angle of incidence. More details about the setup and modelling can be found in [3]. The results for both samples are shown in Fig. 1b/c. Using an Al_2O_3 seed layer increases the main tensor element $|\chi_{zzz}|$ from 4 pm/V to 14 pm/V.

The EOM measurements are done with a fiber-coupled tunable CW laser (890-910 nm). A fiber polarization controller is used to select TE or TM polarization. As the waveguide with cleaved facets forms a Fabry-Pérot cavity, the phase modulation will be converted into amplitude modulation. This makes the EO effect observable by measuring the transmitted power while applying a voltage. Fig. 2a shows the Fabry-Pérot fringes in a transmission measurement (for a waveguide length of 7.5 mm). For the EOM measurement we set the wavelength to a slope of the fringes to maximize modulation. Then, an AC voltage is applied and the RF output of the photodetector is connected to an electrical spectrum analyzer. In the RF spectrum a peak appears at the frequency of the applied voltage indicating a linear EO effect (not Kerr or thermal). As expected the peak height varies linearly with the amplitude of the applied voltage (Fig. 2b). From these measurements, we estimate χ_{zzz} and χ_{xxz} of ZnO to be of the order of a pm/V.



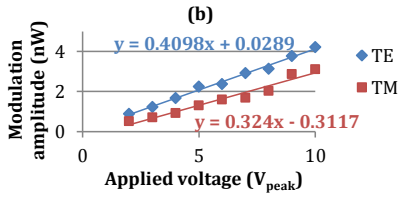


Fig. 2. (a) Transmission measurement. (b) EOM measurement (frequency 100 kHz).

In conclusion, by SHG measurements in PE-ALD ZnO thin films we find $\chi^{(2)}$ values up to 14 pm/V in line with bulk ZnO crystals (χ_{zzz} = -14.31 pm/V) [1] and larger than what has been reported before in ALD ZnO (χ_{zzz} = -4.0 pm/V) [2]. Furthermore, we have observed the linear EO effect in SiN waveguides with a PE-ALD ZnO overlay. Using an Al_2O_3 seed layer can improve $\chi^{(2)}$ in future EOMs. Considering the SHG results, we expect high-speed modulation to be possible with an appropriate electrode design.

[1] M. C. Larciprete, M. Centini, *Second harmonic generation from ZnO films and nanostructures*, Appl. Phys. Rev. 2, 031302, 2015

[2] A. Wickberg *et al.*, *Second-harmonic generation from ZnO/Al_2O_3 nanolaminate optical metamaterials grown by atomic-layer deposition*, Adv. Opt. Mater. 4 (8), 1203-1208, 2016

[3] S. Clemmen *et al.*, *Atomic layer deposited second-order nonlinear optical metamaterial for back-end integration with CMOS-compatible nanophotonic circuitry*, Opt. Lett. 40 (22), 5371-5374, 2015

High Optical Quality, Electrically-driven-compatible InP-on-Si Hybrid Interface elaborated at 300°C

Anne Talneau, I. Sagnes and G. Patriarche
CNRS-C2N Centre de Nanosciences et de Nanotechnologies, route de Nozay, F-91460 Marcoussis
Corresponding author: anne.talneau@lpn.cnrs.fr

Abstract:

In the domain of Silicon photonic integrated devices, the ability to electrically operate the hybrid III-V on Si or SOI interface constitutes the last integration milestone yet to be achieved. This final milestone will open the full 3D field for completely new design of hybrid devices, and will bring immense gains in terms of thermal-budget improvement, chip power consumption, footprint and the integration of driving electronics to boost data transfer rates.

We demonstrate here that Ozone-activated bonding of III-V on Si, operated at 300°C to be CMOS-processing compatible, provides the thinnest -1nm thick- oxide-intermediate layer already achieved, and provides a high optical quality of the interface. Such a hybrid interface is very promising for electrical injection through the interface.

Oxide-free III-V on Si hybrid interface, obtained by bonding at a temperature above 400°C, has already demonstrated a high structural [1] and a high optical quality [2-3], and also electrical operation through the interface [4], but the annealing temperature necessary for such a bonding, which has to be larger than the congruence temperature of InP, prevents the oxide-free bonding approach to be introduced in the CMOS technology chart flow.

Reducing the bonding temperature in order to be compatible with CMOS processing requires an intermediate layer, which should be as thin as possible for electrical operation. Electrical operation through a GaAs on Si hybrid interface including a 2nm thick oxide layer has been demonstrated [5], but due to the relatively thick oxide layer, semiconductors materials had to be heavily doped in order to allow tunnelling operation.

We present here structural and optical characterization of an III-V on Si hybrid interface obtained by Ozone activation of both surfaces and annealing at 300°C.

Activation consists of hydroxyl dangling bonds that polymerize under annealing to generate covalent oxygen bridges. Both InP and Si surfaces are prepared oxide-free, and then activated by ozone during 30s. XPS measurements performed on the Si surfaces have evidenced –OH dangling bonds in the case of O3 exposure during 30s. Immediately after O3-activation, surfaces are put in contact and introduced in the oven. After annealing at 300°C during 3 hours under vacuum, bonding is ensured by covalent oxygen bridges formed following the reaction

$$InP\text{-}OH + Si\text{-}OH \rightarrow InP\text{-}O\text{-}Si + H_2O \quad [6\text{-}7]$$

For structural characterization, a 400nm-thick InP membrane has been bonded on an Si substrate. TEM characterization (Fig.1) shows a 1nm-thick, very homogeneous oxide layer at the interface. Such a thin layer is the thinnest reported for oxide-mediated bonding of III-V on Si.

For optical characterization, a 400nm thick InP membrane is bonded on an SOI wafer including a 300nm-thick Si guiding layer on top, kindly provided by SOITEC. Shallow

ridges are patterned by e-beam lithography using an HSQ resist and etched by an ICP Cl2-H2 process, through all the InP membrane and 30 nm down in the Si guiding layer. Waveguides with two cleaved facets have been measured on an end-fire set-up including polarization-maintaining tuneable sources and injection fibre for TE polarization. Propagation losses are calculated based on the fringe contrast. A 0.30 µm-wide, 470µm-long O3-activated hybrid waveguide transmission shows a 4 dB contrast (Fig.2). This 4 dB fringe contrast, assuming a facet reflectivity r=0.56, corresponds to propagation losses α=5.0 cm-1, a value that can be favourably compared to monolithic waveguides.

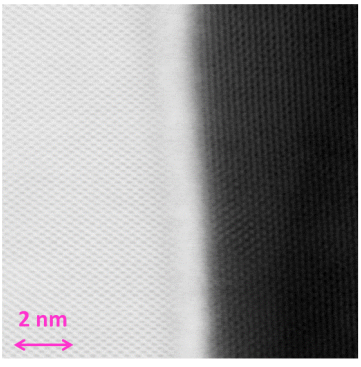


Fig. 1. Bright field STEM micrograph of the hybrid interface evidencing a 1nm oxide layer at the interface

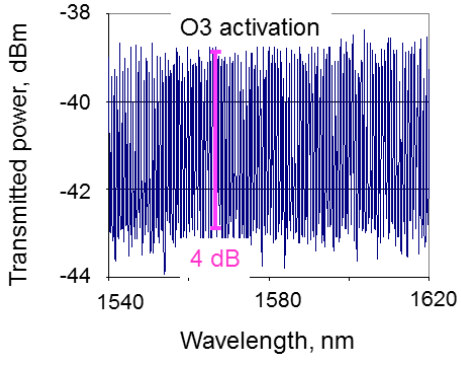


Fig. 2. Transmission measurements showing a 4 dB fringe contrast for O3 activation bonded hybrid waveguide

Conclusion: The high structural and optical quality of III-V on Si Ozone-activated bonding interface evidenced by the low propagation losses for the hybrid mode shows that the ozone-activation procedure proposed here is an efficient approach for bonding on silicon at T=300°C, a temperature which is CMOS-processing compatible.
Its relevance for electrical injection is under investigation.

References

[1] A. Talneau et al., Appl. Phys. Lett., 102, 212101 (2013)
[2] A. Talneau et al., Optics Letters, **40** (22), 5148 (2015)
[3] A. Talneau et al., ECIO 2016
[4] K. Pantzas et al., IPRM 2014, Montpellier, May 2014
[5] K. Tanabe, K. Watanabe and Y. Arakawa, Sci. Rep., **2**:349 (2012)
[6] Q.Y.Tong and U.Gosele, J.Electrochem.Soc. **143**, 1773 (1996)
[7] A.Itawi,K.Pantzas,I.Sagnes,GPatriarche and A.Talneau., J.Vac.Sci.Technol.,B **32**,021201(2014)

Chirp Managed Optical Link based on a Directly Modulated InP/Si DFB Laser

Amin ABBASI[1*] , Hongtao CHEN[1] , Jochem VERBIST[1,2] , Xin YIN[2] , Johan BAUWELINCK[2], Gunther ROELKENS[1] and Geert MORTHIER[1]

[1]Photonics Research Group, INTEC, Ghent University -imec, Gent, 9000, Belgium

[2]IDLab, INTEC, Ghent University - imec, Gent, 9000, Belgium

[*] amin.abbasi@ugent.be

In order to meet the requirement for applications such as inter-datacenter interconnection and PON systems, a high speed data transmission over at least 20 km of standard single mode fiber is desired [1]. Transmission over such long distances has been done traditionally using externally modulated light sources in the C band, because fiber losses are minimal in this wavelength band and the inherent chirp of directly modulated laser diodes decreases the dispersion tolerance of the link. This limits the transmission link distance for the directly modulated optical signal to about 5 km at 10 Gb/s.

Recently it has been shown that by an interesting technique called chirp management an optical signal from a directly modulated laser can be transmitted in standard single mode fiber over distances much longer than the dispersion limit [2]. This, together with the other advantages of direct modulation such as a better power budget, a smaller footprint and a lower cost makes this technology a promising solution for the medium distance optical link. In this approach, the transient chirp of the directly modulated laser diode is kept small by modulating the laser diode at high bias current with a small extinction ratio. Biasing the laser at high current supplies extra benefits such as high-output power, wide modulation bandwidth (BW), stable single-mode operation, and low timing jitter. The adiabatic chirp in this case (resulting in a '1' bit having a different optical frequency then a '0' bit) is then used to our advantage: using an optical filter at the output of the laser to suppress the logical '0' frequency then gives a higher extinction ratio.

In the past years, there has been interest in using silicon photonics for interconnects and PON applications and work on InP-on-Si lasers has caught quite some attention. Heterogeneously integrated laser diodes have been shown capable of high-speed direct modulation [3]. Here we present 10 Gb/s on-off-keying data transmission using a directly modulated InP-on-Si laser over 20 km of SSMF, together with an external tunable optical filter for chirp management. Our previous lasers were suffering from low frequency roll-off and because of this roll-off the performance of the link was PRBS pattern dependent [4]. As one can see in Figure 1-a, the heterogeneously integrated DFB laser consists of a central DFB section with two adiabatic tapers on both sides. These tapers act as semiconductor optical amplifiers which have a very low modulation bandwidth (a few GHz). In order to eliminate the cut-off effect of these taper sections, they were electrically isolated from the laser body by an ICP dry etching of the top InGaAs-P type contact layer. A small signal measurement was done with a KEYSIGHT PNA-X 67 GHz network analyzer after isolation. A 3dB modulation bandwidth of 15 GHz is obtained at a bias current of 100 mA (Figure 1-b). The active layer consists of 8 InAlGaAs quantum wells. Threshold currents at room temperature of 20 mA, output powers in the silicon waveguide above 3 mW at 100 mA, and a series resistance of 7 Ω were measured for these lasers.

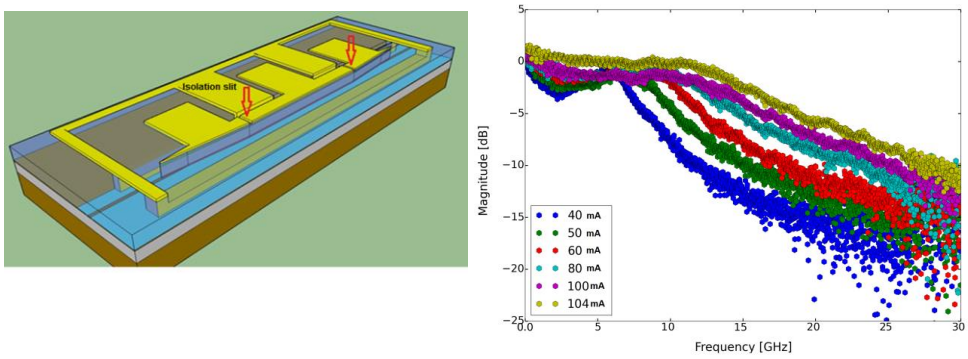


Fig. 1. Schematic of the DFB laser with isolated tapers (left), small signal response of the laser (right).

For the large signal measurement, a Santec-350 optical filter that is tunable in wavelength and bandwidth is inserted after the laser diode for the chirp management. The laser was biased at 50 mA. The large signal measurement has been done in two configurations: for back-to-back and after transmission over a 20 km SSMF. An RF signal of 0.6V from an SHF-PPG was applied for the modulation, but because of strong impedance mismatch between the laser and the 50 Ω transmission line, around 0.2 V was actually applied to the laser. Figure 2-b shows the effect of eye opening at 10 Gb/s when the optical filter is used. The extinction ratio of the signal was increased from 5.9 to 16.3 dB by the application of the optical filter. Two different PRBS pattern lengths of 2^7-1 and 2^{31}-1 were used in order to check the link pattern dependency. We did not observe any noticeable power penalty for two different patterns. However we measured 1.5 dB power penalty for transmission over 20 km SSMF.

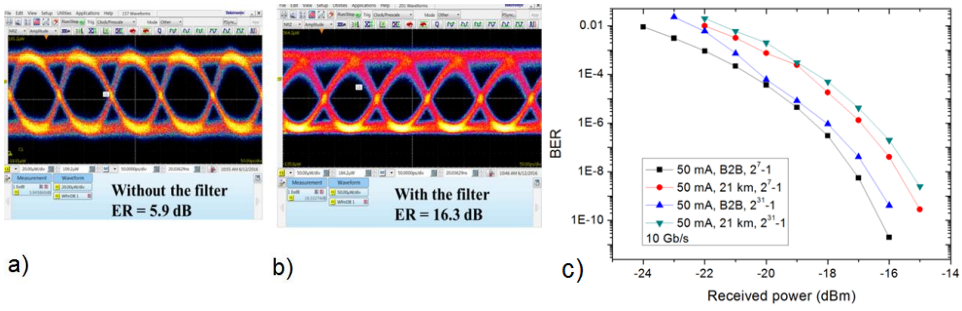


Fig. 2. Extinction ratio of the eye diagram at 50 mA bias without the filter (a), with the filter (b), BER vs received power at 10 Gb/s for two different PRBS patterns lengths (c).

References

[1] http://www.ieee802.org/3/ad_hoc/ngepon/public/may14/tao_ngepon_01_0514.pdf

[2] D. Mahgerefteh, et all, "*Chirp Managed Laser and Applications*," IEEE Journal of Selected Topics in Quantum Electronics, vol. 16, no. 5, p. 1126-1139, 2010

[3] A. Abbasi, et all, "*28 Gb/s Direct Modulation Heterogeneously Integrated C-band InP/SOI DFB Laser*", Optics Express, vol. 23, no. 20, p. 26479-26485, 2015

[4] A. Abbasi et al., "*Enhanced modulation bandwidth of heterogeneously integrated III–V-on-silicon DFB laser for 40 Gb/s NRZ-OOK direct modulation*", 2016 International Semiconductor Laser Conference (ISLC), Kobe, Japan, pp. 1-2, 2016

Fabrication of Add-Drop Multiplexers in Fused Silica by Femtosecond Laser Direct Writing

Vítor A. AMORIM[1,2*], João M. MAIA[1,2], D. ALEXANDRE[1,3], P. V. S. MARQUES[1,2]
[1]Center for Applied Photonics, INESC TEC, Rua Dr. Roberto Frias, Porto, 4200-465, Portugal
[2]Department of Physics and Astronomy, University of Porto, Rua do Campo Alegre, Porto, 4169-007, Portugal
[3]Department of Physics, University of Trás-os-Montes e Alto Douro, Quinta de Prados, Vila Real, 5000-801, Portugal
[*] vitor.a.o.a@hotmail.com

Optical add-drop multiplexers (OADMs) [1] can be used in telecommunication networks for wavelength-division multiplexing (WDM). Fig. 1 (a) shows a schematic of a possible OADM configuration, which is based on a Mach-Zehnder interferometer and that has been investigated in this work.

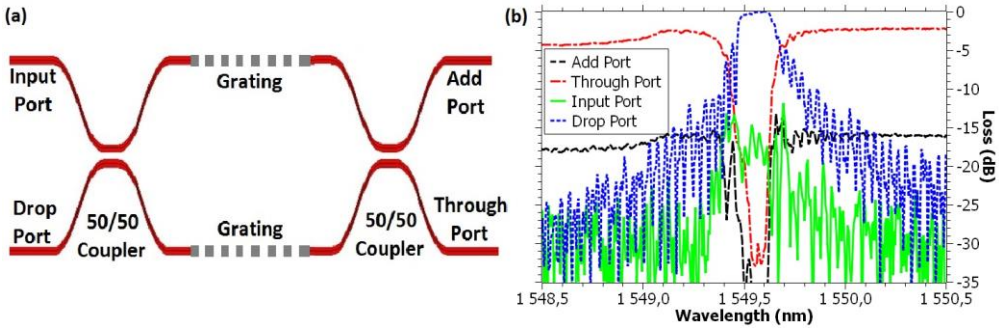


Fig. 1. (a) Schematic of the optical add-drop multiplexer configuration. (b) Measured reflection and transmission spectra of the input, drop, add, and through-port.

The input signal that is composed of several wavelength channels is split equally by the first directional coupler and then guided to two identical Bragg gratings where the resonant wavelength is reflected to the drop port to be read, while the remaining transmitted signals emerges at the through port. Similarly, new information at the resonant wavelength can be sent via the add port. In this configuration the Mach-Zehnder interferometer is responsible for the routing of the signals. In order to perform this routing correctly both arms must have an almost identical optical path length, within nanometer range differences.

Integrated OADMs based on this configuration can be fabricated using photolithographic techniques together with UV photoinscription of Bragg gratings and phase trimming because these allow the fabrication of devices with low insertion losses as well as low intra and inter-channel crosstalk. However, in this work, the more recent femtosecond (fs) laser direct writing technique [2] was used to fabricate, for the first time to our knowledge, this kind of device. For that a Satsuma HP fiber amplified fs-laser system, emitting a second harmonic beam at 515 nm with a pulse duration of 250 fs at 500 kHz, was used to induce the refractive index modification in homogeneous pure silica substrates. The laser beam was focused at a depth of 50 μm below the substrate surface using a 0.55 numerical aperture aspherical lens. The substrate was mounted on X-Y Aerotech stages (ABL10100-LN) and translated orthogonally to the incident laser beam. This technique enables 3D modification of the refractive index of the substrate with very high spatial resolution, allowing, for example, the fabrication of first order gratings.

To fabricate a complete monolithic OADM waveguides, first order Bragg grating waveguides (BGWs), and directional couplers were optimized and integrated in the Mach-Zehnder configuration represented in Fig. 1 (a). Optimal writing conditions were achieved for a 250 nJ pulse energy and 400 μm/s translation velocity at a depth of 50 μm, with a propagation loss of approximately 0.14 dB/cm and a coupling loss of 0.37 dB per facet being obtained for the implemented waveguides at 1550 nm. For the BGWs a propagation loss of 0.8 dB/cm was measured at 40 % modulation duty cycle in order to achieve a grating strength around 30 dB in a 20 mm long grating. The directional couplers showed a splitting ratio of 51/49 %, at wavelengths around 1550 nm, for a separation distance of 15 μm and an interaction length of 1.77 mm.

The results presented here show a device that had a good phase balance as written; real time phase trimming was not tested yet. The input, drop, add, and through-port spectra around the Bragg wavelength are shown in Fig. 1 (b) for horizontally polarized testing light. As can be seen, the reflected signal is emerging from the input and drop-port correctly, with an isolation of approximately 14 dB between ports, showing that the optical path difference between both arms is either very close to zero or a multiple of λ / $(2n_{eff})$ to allow constructive interference at the drop-port. It is also observable that the signal transmitted by the add and through-ports correspond roughly to the ideal behavior, with a deviation of approximately 14 dB. The transmission spectra exhibit, at the Bragg wavelength, an isolation better than -30 dB, enabling low intra-channel crosstalk. Regarding the reflection spectrum on the drop-port, it corresponds to the usual uniform Bragg grating spectrum with the undesired side lobes. The 3 dB bandwidth is 0.19 nm and a side lobe suppression of 20 dB is achieved for Δλ=±0.75 nm. A total insertion loss of 4.9 dB and 3.7 dB was measured for the through port and the drop port respectively.

Future improvement of this device is related to the fine tuning of the ports output by compensating phase errors with resourse to real time laser trimming. The same laser used to write the waveguides should be used to adjust the optical paths, first optimizing the drop port and after the through port. Also, the grating profile should be optimized in order to enhance, for example, channel crosstalk. This can be done through apodization [3].

Acknowledgements

Vítor A. Amorim acknowledges the support of Calouste Gulbenkian Foundation through the Stimulus to Scientific Research Program (Grant no. 141773). This work was also supported by Project "NORTE-01-0145-FEDER-000036" which is financed by the North Portugal Regional Operational Programme (NORTE 2020), under the PORTUGAL 2020 Partnership Agreement, and through the European Regional Development Fund (ERDF).

References

[1] T. Erdogan, T. A. Strasser, M. A. Milbrodt, E. J. Laskowski, C. H. Henry, G. E. Kohnke, *Integrated-optical Mach-Zehnder add-drop filter fabricated by a single UV-induced grating exposure*, Applied Optics, vol. 36, no. 30, pp. 7838-7845, 1997.

[2] G. Della Valle, R. Osellame, P. Laporta, *Micromachining of photonic devices by femtosecond laser pulses*, Journal of Optics A: Pure and Applied Optics, vol. 11, no. 1, art. no. 013001, 2008.

[3] P. Zeil, C. Voigtländer, J. Thomas, D. Richter, S. Nolte, *Femtosecond laser-induced apodized Bragg grating waveguides*, Optics Letters, vol. 38, no. 13, pp. 2354-2356, 2013.

InP based generic platform: the complete and versatile solution for photonic integrated circuits

Luc AUGUSTIN[1*]
[1]SMART Photonics B.V, Horsten 1, Eindhoven, 5612AX, The Netherlands
[*]luc.augustin@smartphotonics.nl

Introduction

InP based photonic components have been around for some time and have proven to be a reliable source for communication systems. InP is the material of choice for monolithic integration of active and passive components, and with the introduction of generic integration platforms the technology has received a large boost. Researchers at TU Eindhoven have been pioneering generic photonic integration technology since the beginning of the century. In cooperation with a number of partners the generic integration technology has reached maturity [1]. The model has proven successful and InP based integration technology is currently commercially offered by two foundries [2].

Figure 1 displays a schematic representation of the technology. The integration platform makes use of butt-joint technology, this allows the integration of different material properties without compromising the performance. In this way Multi Quantum Well (MQW) gain material, optimized e.g. for high gain, can be integrated with bulk InGaAsP passive waveguides for low low losses.

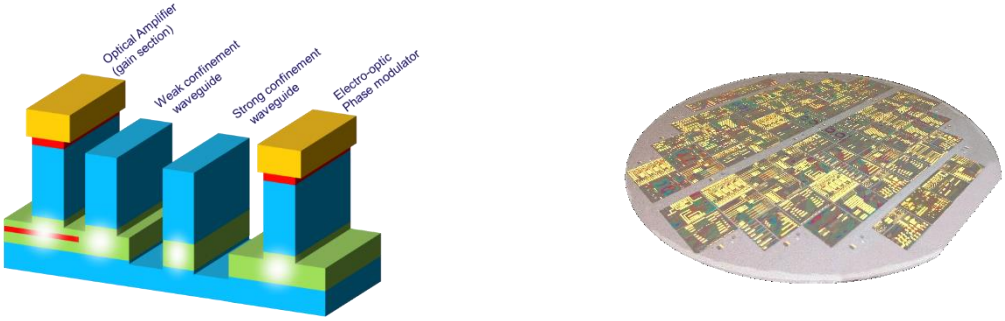


Figure 1 Schematic overview of the generic integration platform (left) and a Multi Project Wafer (right).

With this set of materials a number of Basic Building Blocks are designed and offered. These Building Blocks are offered through a Process Design Kit, implemented in software. This allows users to design on a functional level and speed up the development cycle. Most building blocks are parameterized and have their own characteristic parameters. The designer only needs to build the circuit by connecting the building blocks (with the desired parameters). This circuit can be used to run simulations to achieve the design objectives.

The standardization of the process has another big advantage. Because the process is the same for every design, for prototyping and small series, their process can be combined in a Multi Project Wafer (MPW). These MPWs offer a large cost advantage for the users, as they all share the cost of a single run.

The scale-up to larger volumes is facilitated much easier than in the case of a dedicated process. The standard process is at an industrial level already with process specifications and yield data available to allow a smooth transition from prototyping to production.

Applications

The generic model brings the technology within reach not only for large companies but also for SMEs and universities. And more importantly it opens up the technology for a number of different markets. This has been proven in the commercial MPW runs. At SMART Photonics only, approximately 200 different designs have been fabricated over the last 3 years.

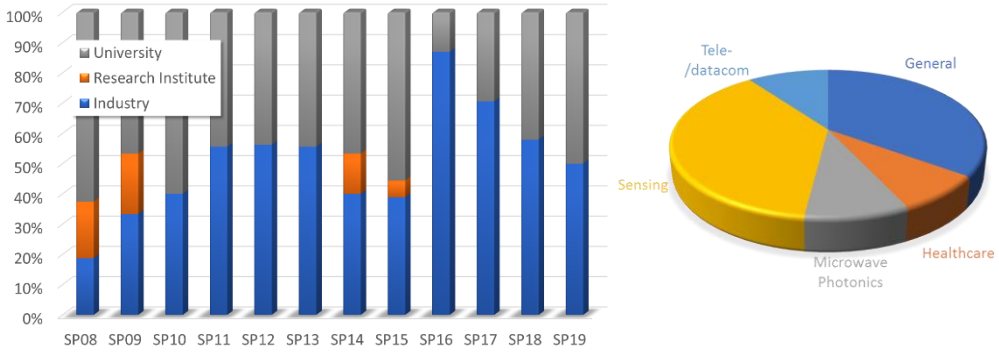


Figure 2 The percentage of users from academia and industry in the various MPW runs (left) and the application field of the designs (right)

As shown in Figure 2, the MPW were populated mainly by universities at the start, but now the share of industry is becoming larger. Overall the MPW are a good mix of product development and forward looking research with a fair share for both industry and academia. The rightmost graph shows the application fields of the users of the MPW runs for as far as this data is available. This also demonstrates the variety of markets and applications that can profit from this technology.

Conclusion

InP offers the possibility to monolithically integrate high performance active and passive components. These aspects, and the introduction of generic platforms: highly standardized industrial photonic integration processes that enable realization of a broad range of applications, will lead to a dramatic reduction of the development costs of PICs which will bring them within reach for many.

References

[1] Smit, M.K., et al. (2014). An introduction to InP-based generic integration technology. Semiconductor Science and Technology, 29(8)

[2] Joint European Platform for Photonic Integration of Components and Circuits (JePPIX) www.JePPIX.eu

EUROPEAN CONFERENCE ON INTEGRATED OPTICS

1x2 Multimode interference coupler with ultra-low reflections in membrane photonic integrated circuits

A.J. MILLAN-MEJIA*, J.J.G.M. VAN DER TOL, M.K. SMIT
Photonic Integration Group (PhI), Dept. of Electrical Engineering, Technische Universiteit, Eindhoven, De Rondom 70, 5612AP, Eindhoven, The Netherlands
* a.millan.mejia@tue.nl

Multimode interference (MMI) couplers are basic building blocks in most photonic integration circuit platforms. Such devices are used as splitters and combiners. However, they are heavily affected by parasitic reflections, mainly because of the resonances due to the self-imaging properties of the structures and the abrupt transitions they comprise [1]. These reflections can compromise the expected performance of the integrated circuits.

In a splitter mode, the main source of the reflection is the limited imaging resolution of the device. This constrain allows some light to be imaged on the back edge of the structure, which will be reflected to the input. On the other hand, when the MMI is in combiner mode the reflections will be low when the two inputs are in phase. Nevertheless, when the inputs are out of phase, the optical field will be imaged on the black plane next to the output waveguide and then the reflection will be strong due to the imaging properties of the structure.

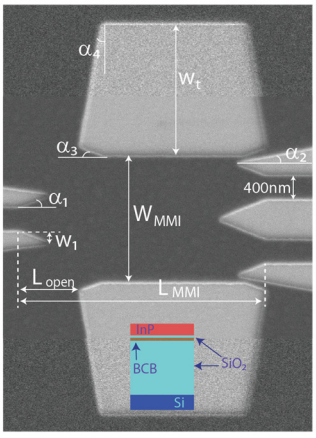


Fig. 1. SEM picture of the device on SiNx and the cross section of the chip.

In membrane platforms this problem is magnified due to the high contrast index regime. In order to alleviate this problem, we propose a butterfly geometry based on the design of E. Kleijn [2]. In this design, the areas next to the waveguides, where the parasitic reflections are originating but which do not play an important role in the MMI function, are removed. In the remaining structure angles are added so that light being reflected there is directed out of the main propagation path. In our case, we optimize the device for an InP membrane on Silicon (IMOS) platform of 300nm thick [4]. Figure 1 shows a SEM picture of the SiNx mask for the realization of the optimized device with all the parameters highlighted and a cross section of the IMOS chip included.

We design a 2 μm wide MMI. The length for a 1x2 MMI was calculated to be $L_{MMI} =$

$3L_\pi/8 = 4\mu m$, with $L_\pi = 4nw_{eff}{}^2/3\lambda$ [1]. We optimize the geometry in a combiner mode, since this gives the worst case situation. An evaluation function is chosen to maximize the output power and reduce the reflections. We define this function as $F_{eval} = 0.2[-10log_{10}(P_{reflection\ to\ 1} + P_{reflection\ to\ 2})] - 3P_{\ out}/(P_{\ out} - 0.8)$. The first term increases the value when the back reflected power reduces. The second term increases F_{eval} when more light is coupled to the output waveguide, but it penalizes drastically if the power is lower than 90%. We run a particle swarm optimization method for 16 generations with 20 elements each. We use as initial values similar parameters as in [2]. The optimized parameters are $\alpha_1 = 22.2°$, $\alpha_2 = 10°$, $\alpha_3 = 20°$, $\alpha_4 = 10°$, $w_1 = 183nm$, $w_t = 2\mu m$ and $L_{open} = 940nm$. With these parameters, a transmission of $-0.2255dB$ (94.94%) and reflections of $-49.9dB$ are obtained. In figure 2 (right) we compare this structure with standard square (left) and angled (centre) MMIs [3]. In the upper part, there is the electric field on the structure for the out of phase situation. It is clear that the reflections are minimized in the new structure as compared to the other geometries by allowing the field to escape from the structure. In the lower part, the transmitted power and the reflections to the input waveguides are plotted against the phase difference. It shows at the out of phase condition an improvement of 28 dB and 8 dB, respectively, with respect to the square and angled geometries.

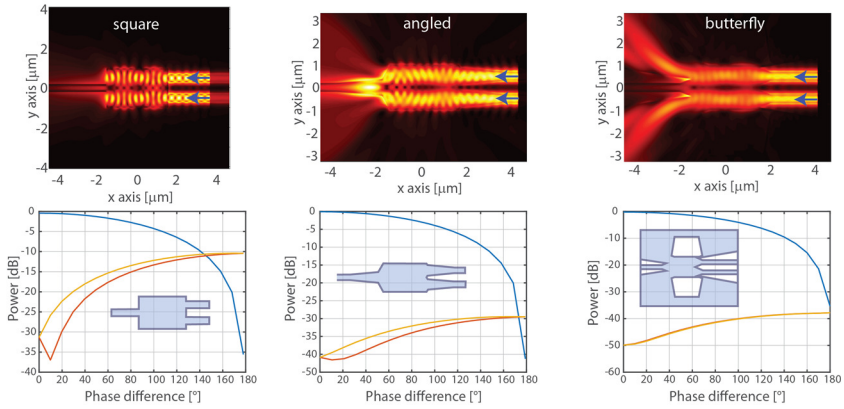


Fig. 2. Top: the electric field distribution of the different MMI geometries. Down: The transmission (blue line) and reflection to the upper (yellow) and low (red) waveguides

We have presented a new geometry for a MMI in membrane photonics. The predicted reflections are -38dB in a combiner mode with out of phase inputs (-50dB for in phase), 8 dB lower than the optimized angled corners MMI. The geometry is optimized for the IMOS platform, but can easily be implemented for SOI chips.

References

[1] E. C. M. Pennings *et al.*, *Reflection Properties of Multimode Interference Devices*, IEEE PTL, Vol. 6, No. 6, 1994.

[2] E. Kleijn *et al.*, *Multimode interference couplers with reduced parasitic reflections*, IEEE PTL, Vol. 26, No. 4.

[3] R. Hanfoug *et al.*, *Reduced reflections from multimode interference couplers,* Electronics letters, Vol. 42, Issue 8, 2006.

[4] J. Pello, Building up a membrane photonics platform in Indium phosphide, PhD thesis, TU Eindhoven, 2013.

Fully Integrated Serial Dual-Polarization Electro-absorption Modulator PIC in InP

Moritz Baier*, Francisco M. Soares, Marko Gruner, Tom Gaertner, Martin Moehrle, Norbert Grote, Martin Schell
Fraunhofer HHI, Einsteinufer 37, 10587 Berlin, Germany
*moritz.baier@hhi.fraunhofer.de

With the advent of stokes space modulation [1], polarization multiplexing no longer is only relevant for coherent long haul communications. In this work, we propose and demonstrate a novel serial configuration to generate true dual-polarization (DP) electro-absorption modulated data from a single chip.

The fundamental idea of the proposed PIC relies on the fact that ordinary multi quantum-well (MQW) based electro absorption modulators (EAM) only operate on TE-polarized light, which is a consequence of the heavy- and light hole splitting in the normally compressively strained MQWs.

A schematic of our DP-EAM PIC is shown in fig. 1(a). For incident light, only the TE component will be modulated by the signal applied to the first EAM. The entire polarization state is then turned by 90°, effectively swapping the TE and TM components. The second EAM will only modulate the previously unmodulated component and leave the already modulated component unaffected. The serial nature of this design brings two advantages: no splitters or combiners are needed, and there is no routing which requires bends. All this makes the design more compact and reliable. Most critical in this concept is a polarization converter (PC) with a high polarization-conversion efficiency. We reported on PCs in [2] recently. With respect to [2], here we introduced tapers to the design to lower the PC insertion loss. The PC is oriented perpendicular to the large flat of the wafer (as opposed to parallel to the large flat in [2]), resulting in a circular sidewall instead of a slanted one, see fig. 1(c). This enables an identical orientation of the PCs and the EAMs.

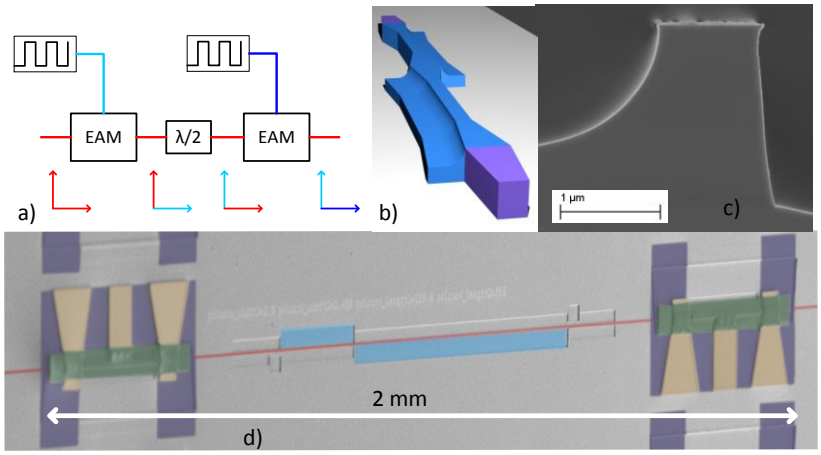


Fig. 1. a): Schemtic of the proposed configuration. b): 3D view of the polarization converter (PC). c): SEM picture of the PC's cross section. d): colorized SEM photo of the fabricated device as in a), comprising two EAMs and the PC of b).

We fabricated the proposed PIC using our generic InP foundry technology. After introducing the PC into the integration platform as described in [2], we now added an EAM structure into the platform. No modifications were done to our standard

fabrication process. The PC is around 900 µm in length, and the EAMs feature an active length of 200 µm each. A SEM picture of the fabricated device is shown in fig. 1.

At first, we carried out measurements of the individual EAM and PC structures. The results are shown in fig. 2. The PC shows ~1 dB of loss for TM polarized light, but 1 dB more in TE mode. We attribute this to a yet non-optimal design of the tapers in the different sections of the component. Due to a higher series resistance on this particular wafer run, the bandwidth is limited to around 11 GHz. We also measured the voltage-dependant birefringence of the EAM to gain a deeper understanding of the overall device.

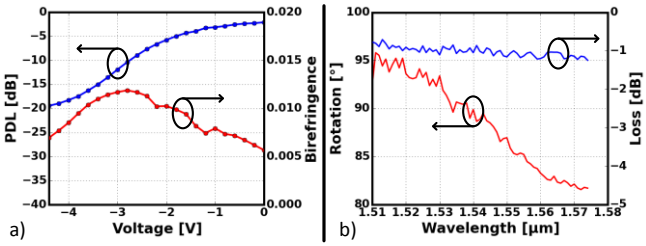


Fig. 2. Experimental characteristics of the EAM at 1575 nm (a) and the polarization converter (b). The insertion loss of the EAM at 1575 nm and 0 V is 7 dB for TE and 3 dB for TM. The TM insertion loss is independant of the bias voltage.

Experimental results are shown in fig. **3**. We measured the Müller matrices of the integrated device at different bias voltages of the two EAMs. To visualize this, we plot the trajectory of the total device's exiting Stokes vector when sweeping the biases of the two EAMs (for a given incident Stokes vector). The resulting trajectory spans a half-circle on the Poincaré sphere, so a full transition from TE-polarized light to TM-polarized light. To further verify the PIC performance, we performed a data transmission experiment with 12.5Gbit/s per polarization. Clean eye diagrams were achieved.

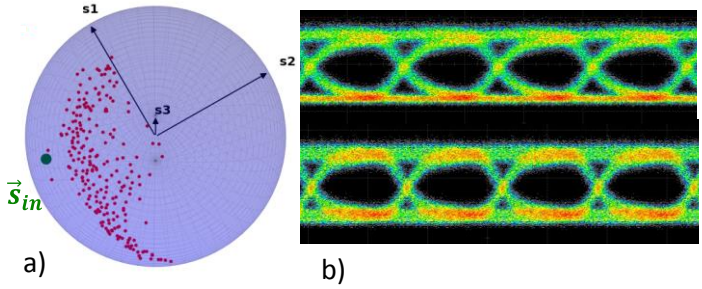


Fig. 3. **a): Trajectory on the Poincaré sphere of the DP-EAM when sweeping the two bias voltages. The Stokes vector of the incident light is the big green dot around (0,-1,0), corresponding to a 50/50 mix of TE and TM. The output Stokes vectors are the smaller dots. b): Eye diagrams at 12.5Gbit/s for the TE (top) and TM (bottom) polarization.**

In conclusion, we proposed a novel DP-EAM structure featuring a serial design. We have successfully implemented the device on our generic photonic integration platform and demonstrated data transmission in both polarization states.

References

[1] M. Morsy-Osman, M. Chagnon, and D. V. Plant, "Polarization division multiplexed intensity, inter polarization phase and inter polarization differential phase modulation with stokes space direct detection for 1λ×320 Gb/s 10 km transmission at 8 bits/symbol," ECOC 2015

[2] Moritz Baier, Francisco M. Soares, Martin Moehrle, Norbert Grote, and Martin Schell, "A New Approach to Designing Polarization Rotating Waveguides," ECIO, Warsaw, 2016.

EUROPEAN CONFERENCE ON INTEGRATED OPTICS

First comparison of InGaAsP and InGaAlAs electro-absorption modulator in COBRA generic platform

Marija TRAJKOVIC[1,2*], Florian LEMAITRE[1,2], Helene DEBREGEAS[2], Kevin A. WILLIAMS[1], Xaveer J. M. Leijtens[1]

[1]COBRA Research Institute, Eindhoven University of Technology, P. O. Box 513, 5600 MB Eindhoven, Netherlands

[2]III-V Lab, Campus de Polytechnique, 1 avenue Augustin Fresnel, F-91767 Palaiseau Cedex, France

[*] m.trajkovic@tue.nl

Introduction Electro-absorption modulators (EAMs) are an attractive solution in applications where high speed modulation is required with high extinction ratio, low drive voltage and integration with lasers. They are particularly promising for high-bandwidth optical communication systems. The possibility of using InGaAlAs compounds, instead of InGaAsP, has shown improved performance at high operating temperatures due to the favourably high band offset for electrons [1].

We have previously fabricated InGaAsP/InP (P quaternary or P-Q) multi-quantum well (MQW) EAMs with a bandwidth of 12.5 GHz [2]. This device is used in here as a reference for comparison with a recently fabricated InGaAlAs/InP (Al-Q) MQW wafer containing EAM structure. The devices on the second wafer are processed to match the COBRA generic integration platform requirements [3].

Device structure The operation principle of an EAM is based on changing the absorption coefficient with the applied electric field. In a MQW structure the effect responsible for this change is the quantum confined Stark effect (QCSE). In response to a DC voltage applied to the device, there is an induced electric field in the undoped MQWs. As the applied electric field increases, the bandgap of the modulator experiences red shift. This also decreases the detuning between the modulator's bandgap and lasing wavelength. For a given detuning we measure the extinction ratio, and its slope determines the optimum operating voltage. Our device is 200 μm long with a 2μm wide shallow ridge structure grown epitaxially on n-InP substrate. The optical confinement factor in MQW is $\Gamma = 0.04$. While a higher optical confinement would be used for lower voltage operation, we have used the same structure as previously fabricated P-Q to enable a direct comparison.

Experimental results The optical transmission of the modulator is measured as a function of the wavelength and of the applied reverse bias. For measurements we have used an amplified spontaneous emission (ASE) source, polarization controller and an optical spectrum analyser (OSA). The operating temperature is 25°C and the results presented here are performed for an input TE polarization. The measured transmission characteristics are shown in Figure 1 (left) as a function of wavelength at zero bias. The

coupling with fibre introduces 3dB loss on each side, and we keep the reflectance low by antireflection coating. In our case the optical loss is higher, as the lensed fibres used are not optimal for these structures. Therefore we obtain a zero-bias −14dB insertion loss for all of the measured structures. This loss takes into account coupling loss, passive waveguide loss and the device internal loss. The latter two are negligible compared to the first one and the loss within the EAM is estimated to be 3-4dB.

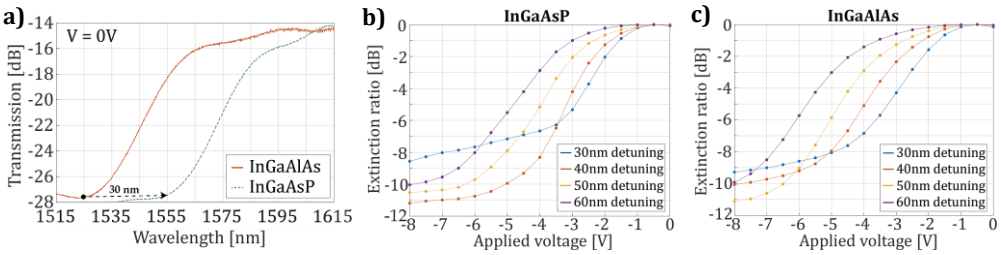


Fig. 1. (a) Transmission spectrum of P-Q and Al-Q at zero bias. Normalized extinction ratio of the InGaAsP (b) and InGaAlAs (c) structure for different detuning wavelengths.

The bandgap of the EAM in the case of P-Q is at 1555 nm, whereas in the case of Al-Q is at 1525 nm. According to this, we have recorded the extinction ratio at corresponding detuning wavelength for each wafer (Figure 1 – middle and right). Both Al and P-Q EAMs show similar extinction ratio for the same detuning. For highest extinction ratio the optimum operating point is at 40nm detuning, where we obtain 11dB extinction for a voltage change of 5V. The Al-containing structures show slightly better extinction ratio for higher detuning wavelengths. At high temperature operation of the EAM integrated with a laser, the detuning would be lower due to lasing wavelength drift and the required voltage for the same extinction ratio becomes lower.

Conclusion We have fabricated and measured the InGaAsP and InGaAlAs electro-absorption modulators in the COBRA generic integration platform. EAMs are integrated with passive waveguides enabling the first like-for-like comparison of P-Q and Al-Q EAM performance in an integration platform. Comparable performance is observed at room temperature for the same number of quantum wells and device length. The successful inclusion of Al-Q devices is expected to enable high performance at high temperature, ultimately enabling semi-cooled and cooler-free operation.

Acknowledgement The reported P-Q devices were fabricated by Smart Photonics through the JePPIX.eu MPW service. The authors would like to thank Nadine Lagay, Jean Decobert and René van Veldhoven for the Al-Q growth, and the European Commission for funding this research through the Marie Curie GeTPICs project.

References

[1] W. Kobayashi et al, "Design and Fabrication of 10-/40-Gb/s, Uncooled Electroabsorption Modulator Integrated DFB Laser With Butt-Joint Structure," *Journal of Lightwave Technology,* vol. 28, no. 1, 2010.

[2] M. Trajkovic, H. Debregeas, K. A. Williams and X. J. M. Leijtens, "20 Gbps operation of the electro-absorption modulator in the COBRA generic integration platform," in *European Conference on Integrated Optics*, Warsaw, 2016.

[3] M. Smit et al, "An introduction to InP-based generic integration technology," *Journal Semiconductor Science and Technology,* no. 8, pp. 1-41, 2014.

Pockels Effect in Strained Silicon Waveguides

Mathias BERCIANO[1*], Pedro DAMAS[1], Xavier LE ROUX[1], Guillaume MARCAUD[1], Paul CROZAT[1], Carlos ALONSO RAMOS[1], Daniel BENEDIKOVIC[1], Delphine MARRIS-MORINI[1], Eric CASSAN[1], Laurent VIVIEN[1]

[1]Center for Nanoscience and Nanotechnology (C2N), Bat 220 rue André Ampère – CNRS, Université Paris-Sud, Université Paris-Saclay, Orsay, 91405, France

[*]mathias.berciano@u-psud.fr

With the increasing demand of data current chip-scale communication systems based on metallic interconnects suffer from rate limitations and power consumptions. In this context, Silicon Photonics has emerged as an alternative solution replacing the classical copper interconnects by silicon waveguides while taking advantage of the well-established CMOS foundries techniques to reduce fabrication costs. Silicon is now considered as an excellent candidate for the development of integrated optical functionalities.

Among all photonic devices required for an optical link, optical modulator is one of the main building blocks. One of the main challenges of Silicon Photonics is the reduction of both power consumption and swing voltage of optical silicon modulators while increasing the data transfer rate speed. However silicon is a centrosymmetric crystal, vanishing the second order nonlinear effect i.e. Pockels effect which is intrinsically high speed.

Nevertheless it has been showed [1] that mechanical stresses, provided by depositing a strained overlayer, can break the crystal symmetry and eventually unlock Pockels effect in silicon. Since then several studies have been performed [2-4] in order to improve the later. But a recent investigation [5] demonstrated that carrier effects have a drastic influence on the measured electro-optic effect. Indeed both plasma dispersion effect and Pockels effect act together under an electric field in strained silicon which have led to an overestimation of the second order nonlinear susceptibility. One way to separate these effects consists in the increasing of the modulation speed [6] in order to minimize the impact of free carriers.

In this work, we have studied the effect of the stress layer in the modulation characteristics based on Mach-Zehnder interferometers (Fig. 1) in the microwave range. DC and high speed characteristics (Fig. 2) will be presented and discussed.

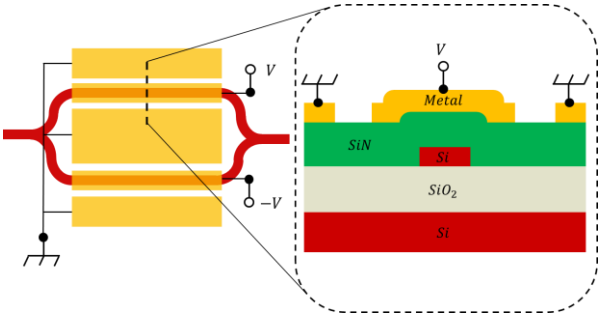


Fig. 1. Top view (on the left) of one Mach-Zehnder modulator. Cross-section view (on the right) of one arm of our Mach-Zehnder interferometer.

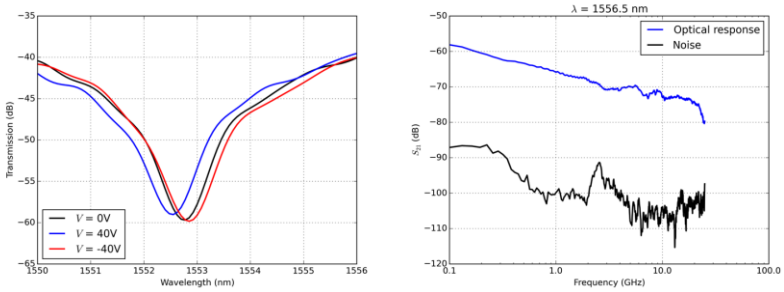


Fig. 2. DC characteristics (on the left) and high speed characteristic (on the right) of our Mach-Zehnder interferometer.

Acknowledgements: Authors acknowledge STMicroelectronics for the financial support of the P. Damas's scholarship. This project has received funding from the European Research Council (ERC) under the European Union's Horizon 2020 research and innovation program (ERC POPSTAR – grant agreement No 647342).

References

[1] R. S. Jacobsen *et al.*, *Strained silicon as a new electro-optic material*, Nature, vol. 441, pp. 199-202, 2006

[2] B. Chmielak *et al.*, *Pockels effect based fully integrated, strained silicon electro-optic modulator*, Optics Express, vol. 19, no. 18, pp. 17212-17219, 2011

[3] B. Chmielak *et al.*, *Investigation of local strain distribution and linear electro-optic effect in strained silicon waveguides*, Optics Express, vol. 21, no. 21, pp. 25324-25332, 2013

[4] P. Damas *et al.*, *Wavelength dependence of Pockels effect in strained silicon waveguides*, Optics Express, vol. 22, no. 18, pp. 22095-22100, 2014

[5] S. S. Azadeh *et al.*, *On the measurement of the Pockels effect in strained silicon*, Optics Letters, vol. 40, no. 8, pp. 1877-1880, 2015

[6] M. Borghi *et al.*, *High-frequency electro-optic measurement of strained silicon racetrack resonators*, Optics Letters, vol. 40, no. 22, pp. 5287-5290, 2015

Integrated III-V Photonic Crystal – Si waveguide platform with tailored Optomechanical coupling

Victor TSVIRKUN[1], Alessandro SURRENTE[1], Fabrice RAINERI[1,2], Grégoire BEAUDOIN[1], Isabelle ROBERT-PHILIP[1], Rémy BRAIVE[1,2*]

[1] Centre de Nanosciences et de Nanotechnologies, CNRS, Univ. Paris-Sud, Université Paris-Saclay, C2N Marcoussis, 91460 Marcoussis, France

[2] Université Paris Diderot, Sorbonne Paris Cité, 75207 Paris Cedex 13, France

[*] remy.braive@lpn.cnrs.fr

Optomechanical systems, in which the vibrations of a mechanical resonator are coupled to an electromagnetic radiation, have permitted the investigation of a wealth of novel physical effects. Typically for the most of these systems, optomechanical coupling originates from a dispersive dependence of the nanocavity resonance frequency on its geometry, which is modulated by mechanical motion. Dissipative optomechanical coupling consists in the modulation of the lifetime of the cavity photons through the motion of a mechanical oscillator. Very recently, it has been demonstrated that this effect is observed in a wide variety of devices [1-2]. Dissipative couplings may significantly enhance the detection sensitivity in optomechanically-based sensing schemes [3] and open new possibilities in optomechanical control with systems featuring both types of coupling mechanisms [4], where a tailored coupling strength is highly desired.

To fully exploit these phenomena in realistic devices or circuits, the integration of optomechanical resonators on a standard semiconductor platform is required. Here, we propose a novel approach to heterogeneously integrate arrays of two-dimensional photonic crystal defect cavities on top of silicon-on-insulator waveguides (Fig 1a). Added to that, quantum dots (QD) are incorporated in the middle of the III-V photonic crystal membrane with an emission spectrum around 1.55 µm (Fig 1b-d).

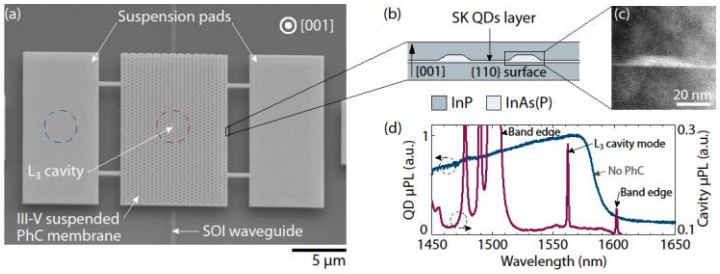


Fig. 1. (a) S.E.M. picture of the photonic crystal membrane with an L3 cavity in the center above a Silicon waveguide. Inside the membrane, InAs(P) Stranski-Krastanov Quantum Dots (SK-QD) have been incorporated (b) in the InP membrane. A T.E.M. image is shown in (c). The emission spectrum of these QD is represented in blue (Fig. 1d) and the spectrum of the L3 cavity is in purple.

We are abled to extract the dissipative and dispersive contributions of the optomechanical coupling of these devices. Tailoring of different contributions was demonstrated using external mean or integrated controls on the geometry of the optical access channel to the nanocavity

Control with the geometry

By performing systematic measurements of the optomechanical response of the fabricated optomechanical resonators as a function of the probe laser wavelength, we showed consistently that the most significant contribution to the optomechanical transduction was of dissipative nature. We observed a different relative sign of the dispersive and external dissipative coupling coefficients by varying the waveguide

width (Fig. 2 a-b), which can be regarded as a way to finely tailor the optomechanical coupling strength [5]. Simulations also demonstrate that our system has an additional 'knob' to coarsely tune the optomechanical coupling, represented by suspension height of the membrane.

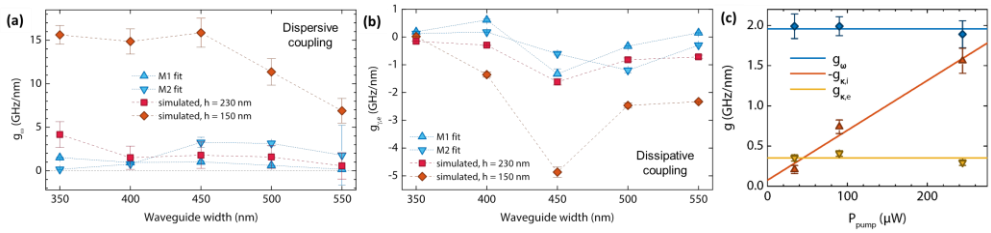


Fig. 2. (a) Dispersive coupling coefficient g_ω and (b) external dissipative coupling coefficient $g_{\kappa,e}$ plotted against waveguide width w_{wg}. Blue, up-pointing triangles: fit of experimental points for the first mechanical mode (M1). Blue, down-pointing triangles: fit of experimental points for the second mechanical mode (M2). Red squares: simulated values, air gap of 230 nm. Orange diamonds: computed values, air gap of 150 nm. (c). Experimental evolution of the different optomechanical coupling strengths with the power of the external non-resonant pump.

External control with QD

We propose the possibility of exerting an external optical control exclusively on the intrinsic dissipative component of the optomechanical coupling within a hybrid optomechanical system by making use of a layer of semiconductor quantum dots. By introducing a non-resonant pump source, we achieve a deterministic modulation of the optical losses of the cavity induced by the quantum dot absorption at the frequency close to the cavity resonance. We show that such an optical modulation is sensitive to the mechanical motion of the device, coupled to the optical cavity resonance via an optomechanical interaction. Non-resonant external pumping of the quantum dots layer can saturate their absorption at wavelengths close to the cavity resonance, thus lowering or eliminating one of the intrinsic loss mechanisms of the cavity. The intrinsic dissipative coupling can be therefore controlled externally (Fig. 2(c)), deterministically and independently of the other coupling mechanisms [6], which in turn can lead to a straightforward implementation of optomechanical resonator capable of reaching the optimal mixed coupling ratio in view of achieving an optimal optical cooling of the mechanical mode [4].

References

[1] M.Li et al, *Reactive Cavity Optical Force on Microdisk-Coupled Nanomechanical Beam Waveguides,* Physical Review Letters, 103, 223901 (2009)

[2] M. Wu et al, *Dissipative and Dispersive Optomechanics in a Nanocavity Torque Sensor*, Physical Review X, vol. 4, pp. 021052, 2014

[3] S. Forster et al, *Cavity Optomechanical magnetometer*, Physical Review Letter, 108 120801 (2012)

[4] T. Weiss et al, *Quantum limits of laser cooling in dispersively and dissipatively coupled optomechanical systems*, Physical Review A, 88, 023850 (2013)

[5] V. Tsvirkun et al, *Integrated III-V Photonic Crystal – Si waveguide platform with tailored optomechanical coupling*, Scientific Report, 5, 16526 (2015)

[6] V. Tsvirkun et al, *External control of dissipative coupling in heterogeneously integrated photonic crystal – SOI waveguide optomechanical system*, Photonics, 3, 52 (2016)

Evanescent Field based Optofluidic Platform in TriPleX for Sensitive Absorbance Detection of Chromophores

Geert A.J. BESSELINK*, Denys MARCHENKO, Lennart S. WEVERS, René G. HEIDEMAN
LioniX BV, Hengelosestraat 500, Enschede, 7521 AN, The Netherlands
* g.a.j.besselink@lionixbv.nl

Integrated-optical chemical sensors are attractive candidates for low sample volume applications as they can be miniaturized rather easily and offer a high intrinsic sensitivity [1]. Part of the transduction mechanism is the very local probing of the relevant optical parameters of the sample by the evanescent field component of the propagating light at the boundary between waveguide core and sample in the region of the so-called sensing window. In this very region, the waveguide core directly contacts the applied sample. The modified Lambert-Beer formula states the relation between the evanescent wave absorbance A (=logP_0/P, with P_0 and P the optical power output measured for the reference and the sample, respectively) and the concentration of the light absorbing species c by considering the evanescent wave modal fraction σ (present within the sample domain), the molar absorption coefficient ε and the path length l (Eq. 1, left part). From this it can be derived easily that the sensitivity of the measurement A/c is determined by l as well as σ (Eq. 1, right part).

$$A = \sigma \varepsilon l c \quad \rightarrow \quad \frac{A}{c} \sim \sigma l \tag{1}$$

The current work shortly describes the design of SiO_2/Si_3N_4 waveguide based sensors, fabricated by means of the TriPleX™ technology, and their absorption sensing performance. These optical waveguides show good transparency for light of the near-infrared and the visible spectrum and, in addition, are known to have low propagation losses (<0.1 dB/cm)[2]. A new design was developed that allows for an optimal coupling to input- and output fibers (single stripe layout) and an effective sensing window definition (ridge layout) while keeping the propagation losses minimal. Furthermore, a design was used that allows for the incorporation of long waveguide lengths (50 cm and longer) inside a rather small sensing window (dimensions: 2.2x0.11 cm (*lxw*)) as the waveguide may loop multiple times in a form of a spiral before leaving the sensing window. This way, the path length is configurable by design over a wide range (Fig. 1).

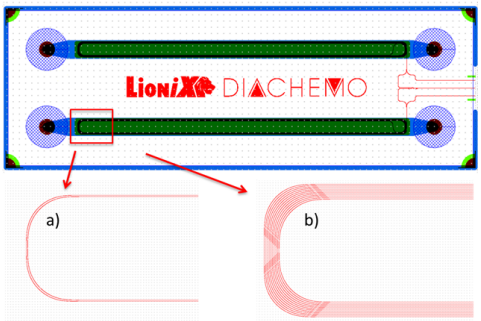


Fig. 1. Layout of the newly developed absorption sensor employing increased path length within the sensing window. Two design examples are shown corresponding to a path length of 9 cm (a) and 53 cm(b).

This generic approach helps to improve the sensitivity, as may be needed for the more demanding applications, while maintaining the chip compact. Several path lengths were

realized, ranging from 2 up to 53 cm. In Fig. 2A, a chip with the path length of 9 cm is shown during in-coupling of light at different wavelengths in order to illustrate the propagation performance in the visible light spectrum. It can be observed that the propagation losses of light in the current chips increases with decreasing wavelength, which is caused by Rayleigh scattering. Currently, the maximum path lengths for light of 638, 532 and 488 nm are ~15, ~10 and ~5 cm, respectively.

In order to verify the model and to assess the value of the evanescent wave modal fraction σ, experimental testing of the sensitivity was done using the chromophore bromothymol blue (BTB). BTB is useful as a model analyte as it absorbs red light (strong absorption peak at 617 nm) as well as green light (moderate absorption peak at 532 nm). Absorbance of red light and green light was measured as a function of BTB concentration in order to determine the sensitivity. Testing was done as a function of path length in the range from 0.5-13 cm. In Fig. 2B the results are shown as were obtained on a chip with a path length of 9 cm.

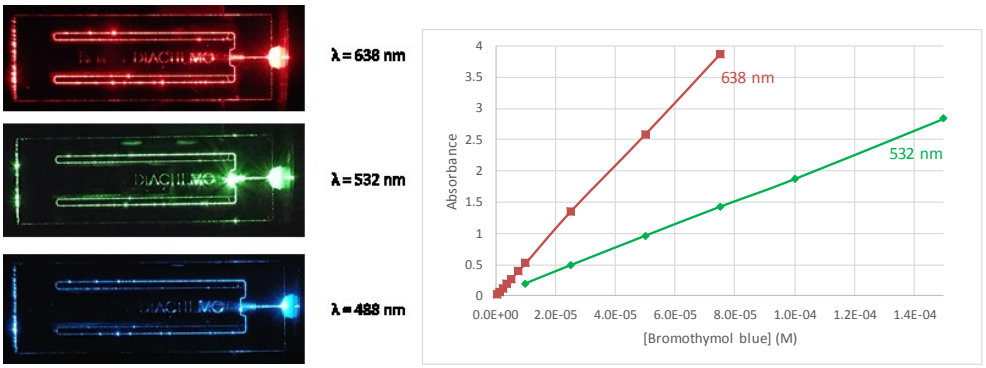


Fig. 2. <u>Left</u>: Photographs of one of the absorption sensor chips (path length 9 cm) with in-coupling of light at the indicated wavelength <u>Right</u>: Absorbance of red light and green light by bromothymol blue solutions in water (20 mM NaOH) as a function of dye concentration at a path length of 9 cm. For calculation of absorbance, background correction was applied.

Testing of a series of chips revealed a good linear correlation between the sensitivity and the path length as predicted by the modified Lambert-Beer formula (Eq. 1, right part). Furthermore, values of ~0.2 were derived for the evanescent wave modal fraction σ, which compared well with simulation results. Detection limit for BTB is well below 0.5 µM when using sensor chips with 9 cm path length.

References

[1] G. Testa, G. Persichetti, *Optofluidics: a new tool for sensing,* in Proceedings of SPIE, Vol. 8794, 879402-1, 2013

[2] K. Wörhoff, R. Heideman, *TriPleX: a versatile dielectric photonic platform*, in Advanced Optical Technologies 4, pp. 189-207, 2015

This project has received funding from the European Union's Horizon 2020 research and innovation programme DIACHEMO under grant agreement No 633635

EUROPEAN CONFERENCE ON INTEGRATED OPTICS

Silicon Photonics and its Applications in Life Science

Roel Baets[1,2*]
[1]Ghent University – imec, Photonics Research Group, Technologiepark-Zwijnaarde 15, 9052 Gent, Belgium
[2]Ghent University, Center for Nano- and Biophotonics, Belgium
[*] roel.baets@ugent.be

With the technology of silicon photonics gaining maturity there is a tendency to consider it as a generic technology that can serve a diverse range of markets, not only in datacom and telecom, but also in sensors, biosensors and biomedical instruments. The driver is always the same: create compact and low-cost integrated circuits with a functionality and performance at par with otherwise bulky and costly implementations. Examples of this trend include PIC's for sensing bioparticles such as proteins and DNA, PIC's for spectroscopic detection of various molecules (glucose, ammonia, markers for food spoilage etc), PIC's for optical coherence tomography or for laser Doppler vibrometry.

In those new applications the "traditional" wavelengths of silicon photonics (1.3 and 1.55 μm) are not necessarily optimal from the application's point of view. This has led to the recent trend to "translate" silicon photonics to other wavelength domains, as much as possible without shying away from its major asset which is to fabricate the chip in a CMOS fab. Many groups are pushing the frontiers of silicon photonics towards longer wavelengths (mid-infrared), mainly driven by the promise of using the technology for vibrational spectroscopy. In parallel other groups are pushing towards shorter wavelengths, so as to be more compatible with biological media, fluorescent markers and Raman spectroscopy. In this case the silicon core needs to be replaced by a material that is transparent in the visible, silicon nitride being a good candidate. In those applications silicon itself changes hat and becomes the near-perfect material for detection.

Below a bibliography is given of work the author has been involved in on the use of silicon and silicon nitride PICs in a life science context.

References

[1] A. Dhakal, P.C. Wuytens, F. Peyskens, K. Jans, N. Le Thomas, R. Baets, Nanophotonic waveguide enhanced Raman spectroscopy of biological submonolayers, ACS Photonics, 3(12), p.2141-2149 (2016).

[2] A. Dhakal, F. Peyskens, S. Clemmen, A. Raza, P.C. Wuytens, H. Zhao, N. Le Thomas, R. Baets, Single mode waveguide platform for spontaneous and surface-enhanced on-chip Raman spectroscopy, Interface Focus, 6(4), United Kingdom, p.article 20160015 (2016).

[3] F. Peyskens, A. Dhakal, P. Van Dorpe, N. Le Thomas, R. Baets, Surface Enhanced Raman Spectroscopy Using a Single Mode Nanophotonic-Plasmonic Platform, ACS Photonics, 3(1), p.102-108 (2016).
[4] P.C. Wuytens, A. Subramanian, W. H. De Vos, A. G Skirtach, R. Baets, Gold nanodome-patterned microchips for intracellular surface-enhanced Raman spectroscopy, Analyst, 140(24), p.8080-8087 (2015) .
[5] A. Subramanian, E.M.P. Ryckeboer, A. Dhakal, F. Peyskens, A. Malik, B. Kuyken, H. Zhao, S. Pathak, A. Ruocco, A. De Groote, P.C. Wuytens, D. Martens, F. Leo, W. Xie, U.D. Dave, M. Muneeb, Pol Van Dorpe, Joris Van Campenhout, W. Bogaerts, P. Bienstman, N. Le Thomas, D. Van Thourhout, Zeger Hens, G. Roelkens, R. Baets, Silicon and silicon nitride photonic circuits for spectroscopic sensing on-a-chip , Photonics Research, 5(3), p.B47 (2015) .
[6] G. Yurtsever, Nicolas Weiss, Jeroen Kalkman, Ton G. van Leeuwen, R. Baets, Ultra-compact silicon photonic integrated interferometer for swept-source optical coherence tomography, Optics Letters, 39(17), p.5228-5231 (2014) .
[7] A. Dhakal, A. Subramanian, P.C. Wuytens, F. Peyskens, N. Le Thomas, R. Baets, Evanescent excitation and collection of spontaneous Raman spectra using silicon nitride nanophotonic waveguides, Optics Letters, 39(13), p.4025-4028 (2014).
[8] E.M.P. Ryckeboer, R. Bockstaele, M. Vanslembrouck, R. Baets, Glucose sensing by waveguide-based absorption spectroscopy on a silicon chip, Biomedical optics express, 5(5), p.1636-1648 (2014) .
[9] G. Yurtsever, Boris Povazay, Aneesh Alex, Behrooz Zabihian, Wolfgang Drexler, R. Baets, Photonic integrated Mach-Zehnder interferometer with an on-chip reference arm for optical coherence tomography, Biomedical Optics Express, 5(4), p.1050-1061 (2014) .
[10] E.M.P. Ryckeboer, J. Vierendeels, A. Lee, S. Werquin, P. Bienstman, R. Baets, Measurement of small molecule diffusion with an optofluidic silicon chip, Lab on a Chip, 13(22), p.4392 - 4399 (2013) .
[11] Y. Li, P. Segers, J. Dirckx, R. Baets, On-chip laser Doppler vibrometer for arterial pulse wave velocity measurement, Biomedical Optics Express, 4(7), p.1229-1235 (2013) .
[12] N.A Yebo, S. P. Sree, E. Levrau, C. Detavernier, Z. Hens, J. A. martens, R. Baets, Selective and reversible ammonia gas detection with nanoporous film functionalized silicon photonic micro-ring resonator , Optics Express, 20(11), p.11855-11862 (2012) .
[13] N.A Yebo, P. Lommens, Z. Hens, R. Baets, An integrated optic ethanol vapor sensor based on a silicon-on-insulator microring resonator coated with a porous ZnO film, Optics Express, 18(11), p.11859-11866 (2010) .
[14] K. De Vos, Jordi Girones Molera, T. Claes, Y. De Koninck, Stepan Popelka, Etienne Schacht, R. Baets, P. Bienstman, Multiplexed antibody detection with an array of silicon-on-insulator microring resonators, IEEE Photonics Journal, 1(4), p.225-235 (2009) .
[15] T. Claes, J. Girones Molera, K. De Vos, E. Schacht, R. Baets, P. Bienstman, Label-Free Biosensing With a Slot-Waveguide-Based Ring Resonator in Silicon on Insulator, IEEE Photonics Journal, 1(3), p.197-204 (2009)
[16] K. De Vos, J. Girones, S. Popelka, E. Schacht, R. Baets, P. Bienstman, SOI optical microring resonator with poly(ethylene glycol) polymer brush for label-free biosensor applications, Biosensors and Bioelectronics, 24(8), p.2528-2533 (2009) .
[17] K. De Vos, I, Bartolozzi, E, Schacht, P. Bienstman, R. Baets, Silicon-on-Insulator microring resonator for sensitive and label-free biosensing, Optics Express, 15(12), p.7610-7615 (2007)



On-chip Enhanced Raman spectroscopy using metal slot waveguide

Ali Raza[1, 2*], Pieter Wuytens[1, 2, 4], Frederic Peyskens[1, 2, 3], Pol Van Dorpe[5], Stephane Clemmen[1, 2] and Roel Baets[1, 2]

[1]Photonics Research Group, Ghent University - imec, 9052 Ghent, Belgium
[2]Center for Nano- and Biophotonics (NB-Photonics), Ghent University, 9052 Ghent, Belgium
[3]Department of Electrical Engineering & Computer Science, MIT, Massachusetts 02139, USA
[4]Department of Molecular Biotechnology, Ghent University, B-9000 Ghent, Belgium
[5]IMEC, Kapeldreef 75, 3001 Heverlee, Belgium
[*] Corresponding author ali.raza@ugent.be

Surface enhanced Raman scattering (SERs) is a technique that facilitates Raman spectroscopy of challenging samples such as thin layers, dilute solutions, or nanoparticles in a low concentration. SERS relies on localized plasmonic resonances that arise at ultra-small metallic gaps, tips or edges from a rough metallic surface, or an engineered nanostructure (antenna). Those plasmons lead to orders of magnitude of field enhancement but in a volume limited to a radius of 10-50 nm. However, plasmonic enhancement doesn't require a resonance. Propagating surface plasmon polaritons are electronic excitations that propagate in the metal over relatively long distances (several microns) while still enabling a large field enhancement. Here, we use it to increase the Raman scattering in a hybrid photonic-plasmonic structure whose centrepiece is a metallic slot waveguide.

The structure is depicted in figure 1a. It behaves as a perfect slot waveguide (fig. 1b) as the field is strictly confined to the void of the structure. Dielectric slot waveguides have been recently used for Raman spectroscopy as they increase the interaction length [1,2] with an analyte (liquid or monolayer). However, these dielectric waveguides have a moderate refractive index so that the confinement in the void of the structure is imperfect (see figure 1b) which results in lesser Raman scattering from the analyte and stronger photoluminescence from the dielectric core, hence limiting the signal to noise ratio. Having a perfect slot waveguide is therefore very appealing. A metallic slot waveguide relies on the actual excitation of a plasmon-polariton, thus limiting the interaction length due the exponential decay over a propagation distance of only a few microns. Furthermore, the mode profile in the metallic slot is significantly smaller than that of a regular dielectric (SiN) waveguide used to manipulate/analyze light on a photonic chip so that a dedicated tapering section is required to couple efficiently light between such a waveguide and the metallic slot-waveguide (fig. 1a). The taper efficiency and the field enhancement in the metallic slot-waveguide are strongly dependant on the void width. For optimization, a figure of merit (FOM) for this photonic-plasmonic device is formulated [3] that depicts the back-scattered Raman power P_s normalized with total pump power P_0 at input facet can be estimated:

$$FOM = \frac{Ps}{Po} = \frac{(\eta_{NTP}\sigma_{NTP}\rho_{NTP}) \times (\gamma)^2 \times (\Gamma)^2 \times \exp(-2\alpha_{SiN}L_{SiN}) \times (1 - \exp(-2\alpha_g L_g))}{2\alpha_g}$$

where η_{NTP} is the Raman conversion efficiency, the Raman crossection of NTP σ_{NTP}=0.358× 10^{-30} cm^2/Sr, its surface density ρ_{NTP} = 5.56× 10^{18} molecules/m^2, the coupling efficiency at the SiN waveguide facet $\gamma = 5dB$ and Γ is the photonics-plasmonic mode transition efficiency. We have optimized Γ and the FOM using FTDT LUMERICAL software as a function of the gap in the void. The results of this simulation (fig. 1b) show that the FOM varies over 2 orders of magnitude for width between 10 and 80 nm.

The silicon nitride waveguide and the gold slot are made using 2 subsequent e-beam lithography steps. The actual width of the void in the metallic slot is 31 nm, its length is 6 µm and the taper length is 1µm. To perform a proper characterization of the metallic slot-waveguide, we have coated it with a single layer of 4-nitrothiophenol (NTP) that selectively binds to gold but not to silicon nitride. A confocal Raman microscope is used to excite the TE mode of the silicon nitride rib waveguide from its facet. The guided light then excites the NTP-coated metallic slot-waveguide thus generating a Stokes field both in forward and backward directions. The microscope collects the backward scattered light resulting in a Raman spectrum displayed in fig. 2b showing clearly the expected NTP Raman resonances highlighted by dotted lines. An additional spectrum is measured from a SiN waveguide that is not coupled to any metallic slot-waveguide. The comparison shows that NTP spectrum is linked to the presence of the metallic slot-waveguide while the broad background and sharp peak at 2330 cm^{-1} are due to the photoluminescence of the 2.5 mm long SiN waveguide.

This first demonstration of Raman spectroscopy using a metallic slot-waveguide is a promising approach for enhancing Raman signal from analyte present in limited quantity or concentration such as a monolayer. A first measurement indicates negligible background associated to the plasmonic structure and further measurements are expected to quantify more accurately the enhancement in term of signal to noise ratio as compared to previously reported on-chip Raman sensors.

The authors acknowledge FWO and ERC-InSpectra for their financial support.

References

[1] C. C. Evans, et al., *ACS Photonics*,*3*(9), pp1662,(2016)
[2] A. Dhakal, et al. Optics letters, 39(13), pp.4025-4028 (2014)
[3] F. Peyskens, et al. ACS Photonics 3(1), 102–108 (2016)

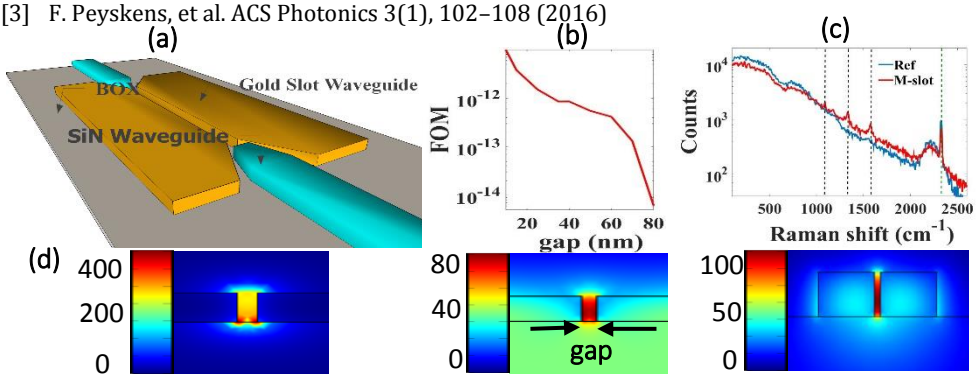


Fig. 1(a) Schematic of photonic-plasmonic structure (b) Optimized figure of merit (FOM) vs gap of metal slot waveguide. (c) Raman spectra measured from NTP-coated metallic-slot waveguide (red) and from bare SiN waveguide (blue) on same chip (laser power of 10mW and acquisition time of 1s) (d) Mode profile (Normalized E-field) of a metallic slot waveguide (left), a SiN slot waveguide of identical structure (center) and optimal dimension (right).

Rare-earth doped selenides active waveguides for integrated mid-infrared sensing applications

Loïc BODIOU[1*], Jonathan LEMAITRE[1], Aldo GUTIERREZ-ARROYO[1], Walid EL AYED[1], Yannick DUMEIGE[1], Isabelle HARDY[1], Joel CHARRIER[1], Florent STARECKI[2], Emeline BAUDET[2], Radwan CHAHAL[2], Virginie NAZABAL[2], Jean-Louis DOUALAN[3], Alain BRAUD[3], Patrice CAMY[3], Petr NEMEC[4]

[1]FOTON, UMR-CNRS 6082, ENSSAT BP80518, F-22305 Lannion Cedex, France
[2]ISCR, UMR-CNRS 6226, Glass and Ceramics Team, 35042 Rennes, France
[3]CIMAP, UMR CEA-CNRS-ENSICaen, Université de Caen, 14050 Caen, France
[4]Department of Graphic Arts and Photophysics, Faculty of Chemical Technology, University of Pardubice, 53210 Pardubice, Czech Republic
[*] loic.bodiou@univ-rennes1.fr

Mid-infrared (mid-IR) absorption spectroscopic techniques can provide inherent molecular selectivity and reach very low detection limits. They have therefore found applications in environmental, health or security domains. In parallel to the growing demand for the detection of traces molecules, the development of compact sensors is also urged to extend the operational range of these sensors to on-site measurements. Sophisticated on-chip mid-IR transducers [1] have been implemented using different integrated optical platforms (Si, Ge, SiNx, arsenides, chalcogenides…). However, despite the versatility of light sources spanning the whole mid-IR (synchrotron, globar, optical parametric oscillator, quantum/interband cascade laser (QCL/ICL) or supercontinuum sources), on-chip integration of mid-IR broadband light sources still remains a challenge. In particular, integrated broadband light sources and amplifiers operating in the 3-5 µm window would be of great interest as this spectral range overlaps an Earth's atmosphere transmission window and strong characteristic vibrational transitions displayed by chemical molecules such as hydrocarbons, carbon dioxide and carbon monoxide (Fig.1a).

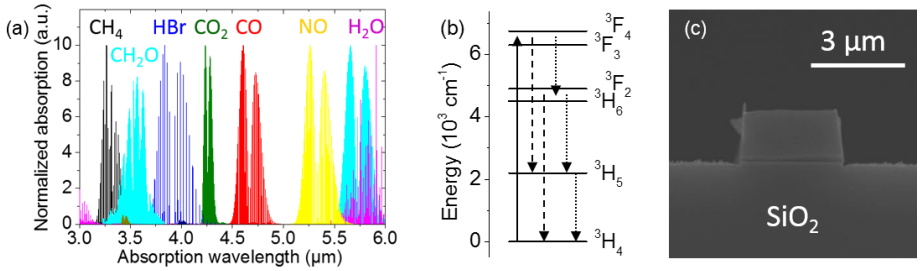


Fig. 1. a) Absorption bands of selected molecular species in the mid-IR range, b) Simplified low energy part of the energy level diagram of Pr^{3+} ions and c) Scanning electron microscope image of the processed waveguide after ICP-RIE.

Mid-IR lasers based on rare earth (RE) ions have already been demonstrated in fibers [2]. The transfer of these results in integrated technology is expected to have a tremendous impact on the development of mid-IR-lab-on-a-chip sensing applications. The transmission range of chalcogenides spans a large part of the mid-IR thanks to their low phonon energies. Efficient mid-IR waveguiding properties have also been demonstrated [3]. Praseodymium (Pr^{3+}) ions feature characteristic radiative transitions in the mid-IR under convenient pumping around 1.5 and 2 µm (Fig.1b).

In this paper, we report the optical design, fabrication and mid-IR optical characterizations of integrated active ridge waveguides based on praseodymium (Pr^{3+})-doped selenides.

RF magnetron sputtering was used to deposit a 1.7-µm thick Pr^{3+}-doped chalcogenides guiding layer based on the quaternary system composed of Ga, Ge, Sb and Se atoms on different cladding layers (thermally oxidized silicon and selenide-based materials). Refractive indices of doped films were measured by ellipsometry and values of 2.607 and 2.565 were, respectively, obtained at 1.55 µm and 4.70 µm. Ridge waveguides patterning was subsequently performed using i-line photolithography and fluorine-based RIE/ICP dry etching techniques.

Optical field distribution of the propagating modes and the corresponding effective indices were simulated, as a function of waveguide width and wavelength, using a commercial mode solver. At 1.55 µm, the waveguides were found multimode for widths larger than 0.3 µm. Single-mode operation at the propagating wavelength of 4.70 µm can be obtained for waveguide widths smaller than w=1.9 µm (h=1.7 µm). Fig. 2a shows the simulated intensity profile of the fundamental transverse electric (TE) mode propagating at the wavelength of 4.70 µm in a 1.7 × 1.5 μm^2 (height × width) ridge waveguide.

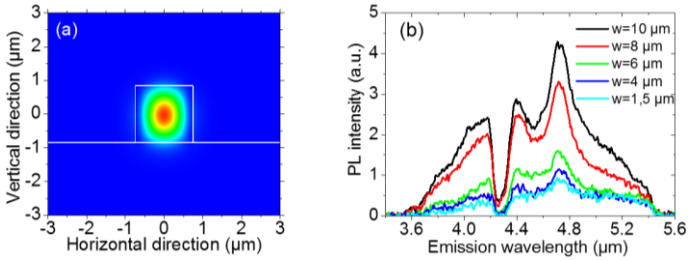


Fig. 2. a) Simulated TE fundamental mode at λ=4.70 µm for a 1.7 × 1.5 μm^2 ridge waveguide, b) Mid-IR PL spectra for different waveguide widths (h=1.7 µm).

Guided photoluminescence (PL) experiments were performed between 3.5 and 5.5 µm using a continuous wave excitation at 1.55 µm in co-propagative configuration. PL was investigated as a function of waveguide width (from 10 µm down to 1.5-µm wide) and pumping power (4-30 mW). Fig. 2b displays typical mid-IR PL spectrum recorded at room temperature in the 3.6-5.4 µm wavelength range. The dip in PL intensity located around 4.3 µm originates from the vibrational absorption of CO_2 from atmosphere and emphasizes the potential of these active waveguides for mid-IR spectroscopic sensing (Fig. 1a).

In conclusion, ridge waveguides were fabricated by RF magnetron sputtering and subsequent patterning using standard photolithographic steps. Geometrical dimensions (width and height) of the waveguides were adjusted to obtain single-mode propagation at mid-IR wavelengths. Under 1.55 µm optical excitation, guided broadband mid-IR emission above 4 µm is demonstrated from Pr^{3+}-doped selenides ridge waveguides. These results correspond to the longest wavelength emission ever recorded from RE-doped integrated waveguides and underscore the potential of RE-doped chalcogenides for the development of low-cost on-chip mid-IR amplifiers or lasers that could be used, in particular, for sensing applications.

References

[1] M. Sieger, B. Mizaikoff, *Toward on-chip mid-infrared sensors*, Anal. Chem., 88, 5562 (2016).
[2] S.D. Jackson, *Towards high-power mid-infrared emission from a fibre laser*, Nat. Photonics, 6, 423 (2012).
[3] A. Gutierrez-Arroyo, E. Baudet, L. Bodiou, J. Lemaitre, I. Hardy, F. Faijan, B. Bureau, V. Nazabal, J. Charrier, *Optical characterization at 7.7 µm of an integrated platform based on chalcogenide waveguides for sensing applications in the mid-InfraRed*, Opt. Express, 24, 23109 (2016).

Photonic lab-on-a-chip nanobiosensors for early diagnostics at the point-of-care

Laura M. LECHUGA*
Nanobiosensors and Bioanalytical Applications Group
Catalan Institute of Nanoscience and Nanotechnology (ICN2)
CSIC, The Barcelona Institute of Science and Technology and CIBER-BBN. Barcelona (Spain)
* Laura.lechuga@icn2.cat

Portable point-of care (POC) devices for *in-vitro* diagnostics will be a milestone for the achievement of universal healthcare and environmental protection. Motivated by potential benefits such as sensor miniaturisation, multiplexing capabilities and relevant sensitivities in a label-free scheme, Silicon photonics based-biosensors are the most suitable candidates to achieve such ambitious POC devices [1]. These photonic biosensors consist of compact waveguides contained on chips which can be easily miniaturized and fabricated in arrays of identical sensors for multiplexed analysis.

Several years ago we introduced in this area an innovative photonic sensor design based on a bimodal waveguide (BiMW) interferometer [1], a single channel Si_3N_4 waveguide which mechanism is based on the interference of two waveguide modes of the same polarization, operating at visible wavelengths with monochromatic and polarized (TE or TM) light. Light is first coupled into a rib waveguide supporting a single transversal mode. After some distance, this mode is coupled into a thicker waveguide which contains the sensing window and supports two transversal modes. As the fundamental and the first order modes have different evanescent field profiles at the core-cladding interface, the interference pattern is a function of the refractive index in the sensing area. The final layout design included dozens of chip-integrated waveguides into a single wafer substrate using silicon technology ($Si/SiO_2/Si_3N_4/SiO_2$). The single mode waveguide has a thickness of 150 nm of Si_3N_4 (n=2.00) and the bimodal part is 350 nm thick, while the width of the waveguide is of 3 µm. The rib height is below 3 nm. The simplicity of our BiMW design is quite attractive while its sensitivity of around $1x10^{-7}$ RIU in bulk [1] is comparable to more complex interferometric schemes.

We have been working in the full integration of the BiMW technology in a photonic POC platform. For the achievement of the complete platform, several units need to be incorporated, including the BiMW sensors, the microfluidics and the flow delivery system, the multiplexed in and out-coupling of the light and the light read-out. Moreover, a specific and custom-designed biofunctionalization protocol must be developed for each sensor depending of the targeted application. Even if all these individual components are

well known, the subsystem interfaces between them are difficult to optimize and these are still the major barriers to be overcome.

One of the main drawbacks of BiMW sensors is the complex interferometric nature of the output signal which require a modulation system to translate the standard interferometric signal into an unambiguous linear phase response. In order to improve the integration and cost of the final device, we have introduced a new all-optical wavelength modulation system where the emission wavelength of a low-cost commercial laser diode was modulated ±2 nm by controlling its output power. After a Fast Fourier Transform deconvolution, the linear response of the BiMW sensor is obtained [2].

For microfluidics integration, one major constrain is the minimum separation between waveguides (only few hundred of microns). For the fabrication of the microfluidics channels we employ several routes, including polydimethylsiloxane (PDMS) channels fabricated by soft lithography or SU-8 microfluidics delivery channels fabricated at wafer level by standard lithography. We recently have proposed the integration of a fully automated and active PDMS optofluidic system with the BiMW technology [3].

One main challenge for the BiMW POC sensing technology is the demonstration of its utility in the clinical practise being able to handle and directly analyse minimum amounts of body fluids without previous labeling, detecting biomarkers in their natural form. After the development of the appropriate biofunctionalization protocols [4], we have demonstrated the suitability of our BiMW nanophotonic platform for the real clinical diagnostics, as for example: (i) quantitative detection of *Escherichia coli* in undiluted human ascitic fluid from cirrhotic patients at very low concentration (40 cfu·mL^{-1}) [5] (ii) detection of specific tumor-related autoantibodies in serum, which indicates the onset of a colorectal cancer in its preliminary stage (iii) detection and quantification of miR-181a at attomolar concentrations (LOD = 23 aM) directly, and for the first time, in human urine samples of bladder cancer patients with no need for prior sample purification or amplification steps [6]. In all cases, the BiMW nanosensor has shown excellent robustness with high reproducibility and sensitivity, rendering in a valuable tool for fast diagnostics of bodily fluids samples.

References

[1] A.B. González-Guerrero, J. Maldonado, S. Herranz, and L.M Lechuga. *Trends in photonic lab-on-chip interferometric biosensors for point-of-care diagnostics*. Analytical Methods, vol. 8, pp. 8380 – 8394, 2016

[2] S. Dante, D. Duval, D. Fariña, A.B. González-Guerrero and L.M. Lechuga. *Linear read-out of integrated interferometric biosensors using a periodic wavelength modulation*. Laser & Photonics Reviews vol. 9, no. 2, pp. 248-255, 2015

[3] C. Szydzik, et al. *Towards an Integrated Optofluidic System for Highly Sensitive Detection of Antibiotics in Seawater Incorporating Bimodal Waveguide Photonic Biosensors and Complex, Active Microfluidics*. SPIE Proceedings, SPIE Biophotonics Australasia (2016).

[4] A.B. González-Guerrero et al.. *Direct and label-free detection of the human Growth Hormone in urine by an ultrasensitive Bimodal Waveguide biosensor*. J. of Biophotonics, vol. 1–7, 2017

[5] J. Maldonado, A.B. González-Guerrero, C. Domínguez and L.M. Lechuga. *Label-free bacteria detection by a bimodal waveguide immunosensor: an approach to early diagnosis of chronic liver failure*. Biosens & Bioelec., vol. 85, pp. 310-316, 2016

[6] C. S. Huertas, D. Fariña and L.M. Lechuga. *Direct and label-free quantification of micro-RNA-181a at attomolar level in complex media using a nanophotonic biosensor*. ACS Sensors, vol. 1, pp. 748–756, 2016



GaSb-based single-mode distributed feedback lasers for sensing

James A. GUPTA*, Andrew BEZINGER, Jean LAPOINTE, Daniel POITRAS, Geof C. AERS

National Research Council of Canada, M50 Montreal Road, Ottawa K1A 0R6, Canada

* corresponding author e-mail

GaSb-based tunable single-mode diode lasers can enable rapid, highly-selective and highly-sensitive absorption spectroscopy systems for gas sensing. In this work, single-mode distributed feedback (DFB) laser diodes were developed for the detection of various trace gases in the 2-3.3um range, including CO2, CO, HF, H2S, H2O and CH4. The lasers were fabricated using an index-coupled grating process without epitaxial regrowth, making the process significantly less expensive than conventional DFB fabrication.

The devices are based on InGaAsSb/AlGaAsSb separate confinement heterostructures grown on GaSb by molecular beam epitaxy. DFB lasers were produced using a two step etch process. Narrow ridge waveguides were first defined by optical lithography and etched into the semiconductor. Lateral gratings were then defined on both sides of the ridge using electron-beam lithography and etched to produce the index-grating.

Effective index modeling was used to optimize the ridge width, etch depths and the grating pitch to ensure single-lateral-mode operation and adequate coupling strength. The effective index method was further used to simulate the DFB laser emission spectrum, based on a transfer matrix model for light transmission through the periodic structure.

The fabricated lasers exhibit single-mode operation which is tunable through the absorption features of the various target gases by adjustment of the drive current. In addition to the established open-path sensing applications, these devices have great potential for optoelectronic integrated gas sensors, making use of integrated photodetectors and possibly on-chip Si photonics waveguide structures.



EUROPEAN CONFERENCE ON INTEGRATED OPTICS

Ultra-Low Loss Si3N4 Waveguide Passive and Active Next Generation Photonic Integration for Optical Gyroscopes and Communications Applications

Daniel J. Blumenthal
University of California at Santa Barbara, Room 2221F Engineering Sciences Building, Santa Barbara, CA, 93106, USA
danb@ece.ucsb.edu

The ultra low-loss Si3N4 waveguide platform has yielded a wide range of passive and active components that open up new PIC applications. Devices and applications including long delays, 3D stacking, gratings, filters, erbium amplifiers switches, vertical couplers and optical gyros, lasers and adaptive dispersion compensators.

I. Ultra-Low Loss (ULLW) Passive and Active Devices

The ULLW design employs a silica-based planar waveguide with high aspect ratio Si3N4 core to achieve a record low loss (0.045 ± 0.04) dB/m [1]. The waveguides support dilute modes using a high aspect-ratio stoichiometric Si3N4 core that minimizes scattering at the core-cladding sidewalls (Fig. 1a). Ultra low-loss optical delay-lines have been fabricated including single-layer small-area coils [1], single layer coils with 90 degrees low-loss crossings [2], and large area coils with low loss stitching [3] (Fig. 1b). Longer delay and multi-layer function is achieved by moving these designs into a 3D stacked delay lines with 0.5dB layer to layer coupling loss[4][5] (Fig. 1c). Other ULLW devices include grating filters and wavelength dependent mirrors using periodic Si3N4 sidewall gratings [6] (Fig. 1d) that can be designed as extremely long gratings on-chip with low kappa. By incorporating a reactive co-sputtered Al2O3-Er3+ layer with the ULLW, active waveguides can be realized [7] (Fig. 1e).

II. Integrated Optical Gyros

Chip-scale integration of interferometric optical gyros where the optical delays are integrated on-chip instead of using a fiber coil are designed to reach a detection limit of 19°/hr/√Hz (Fig. 1f). The operating principle is identical to the FOG where two counter-propagating light signals experience different phase shifts proportional to the rotation rate and the desired signal is measured by interfering these signals on a photodetector. Preliminary results for an integrated 3-meter long Si3N4 waveguide coil are reported in [2] with minimized scattering and reflection impairments can reach down to 19°/hr/√ Hz for a loss of 1dB/m and 4.2°/hr/√ Hz for a loss of 0.1dB/m.

III. Communications Applications

ULLW PICs enable a wide range of communications applications at the chip-level and offer solutions to handle functions normally done with electronics into the optical domain in order to save power and space. WDM DFB and DBR lasers have been demonstrated with record threshold powers and slope efficiency by combining active waveguides and sidewall gratings [7]. Due to the low thermal characteristics of glass

laser performance with small threshold and wavelength shifts have been reported t0 400C [8]. True time delay (TTD) circuits have been fabricated by combining ULLW delays with thermally controlled 2x2 MMI switches [9]. 10-stage programmable matched optical filters can be used to replace power hungry DSPs for optical dispersion compensation [10] (Fig. 1g).

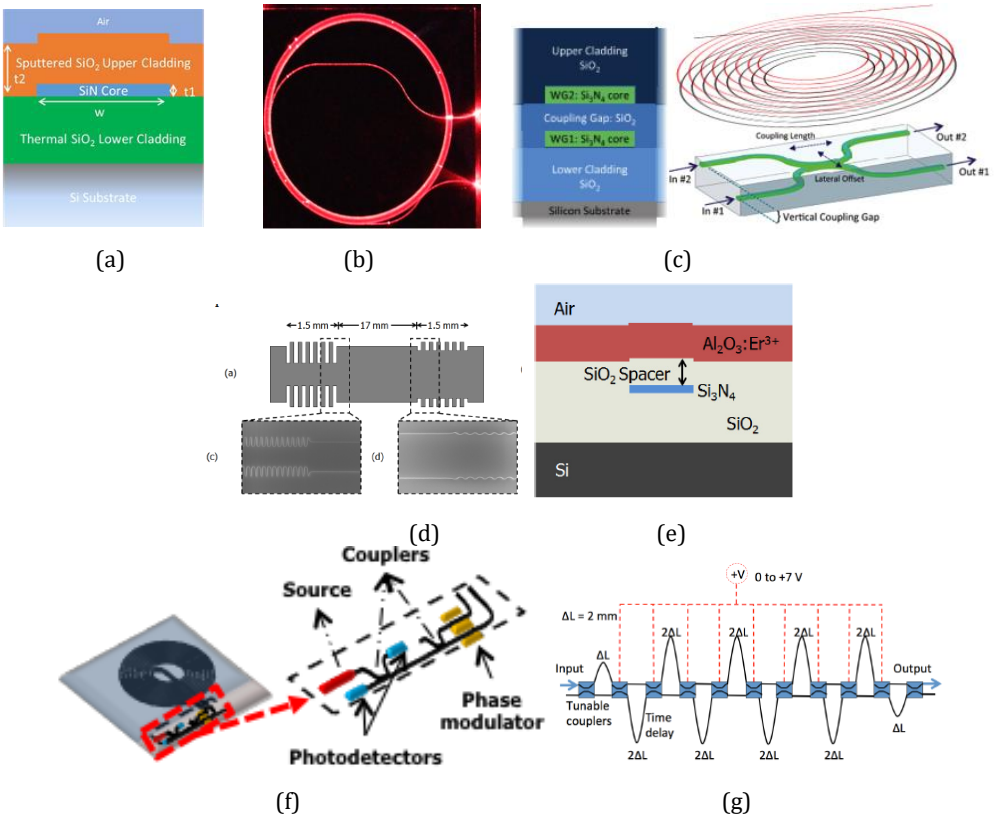


Fig. 1. (a-c) ULLW passive waveguide design, large area coils and 3D stacking. (d-e) Sidewall gratings, active erbium design and lasers. (f-g) Integrated optical gyro and dispersion compensator applications.

This work was supported by DARPA iPhoD HR0011-09-C- 0123 and iWOG HR0011-14-C-0111 contracts and the Terabit Optical Ethernet Center (TOEC). The views and conclusions contained in this document are those of the authors and should not be interpreted as representing official policies of the Defense Advanced Research Projects Agency or the U.S. Government.

References

[1] J. Bauters, et. al., IEEE Photonics Conference (PHO), 2011
[2] S. Gundavarapu, et. al., OFC/NFOEC, 20–22 March 2016, paper W4E.5 (2015)
[3] T. Huffman, et. al., IEEE PTL, Volume PP, Issue 99 (2016)
[4] D. John, et. al., IEEE PTL, Vol. 24, No. 11, June 1 (2012)
[5] R. Moreira et. al., Advanced Photonics 2013, OSA Technical Digest (online)
[6] M. Belt, et. al., Optics Express, V 21, No. 1, pp. 1181-1187, January 10 (2013)
[7] M. Belt, et. al., Optics Letters, Vol. 38, Issue 22, pp. 4825-4828 (2013)
[8] M. Belt and D. J. Blumenthal, OFC/NFOEC 2015, OSA Technical Digest, Paper Tu2C.7 (2015)
[9] R. L. Moreira, et. al., IEEE PTL, vol.25, no.12, pp.1165 - 1168, June15 (2013)
[10] R. L. Moreira, et. al., *Optics Express, vol. 24 No. 15 (2016)*

Integrated Quantum Photonics on a III-V platform

Andrea FIORE[1*], Maurangelo PETRUZZELLA[1], Giulia DIGERONIMO[1], Simone BIRINDELLI[1], Francesco PAGLIANO[1], Frank W.M. VAN OTTEN[1], Lianhe H. LI[2], Edmund H. LINFIELD[2]

[1]Dep. Applied Physics, Eindhoven University of Technology, Eindhoven, 5600 MB, The Netherlands

[2] School of Electronic and Electrical Engineering, University of Leeds, Leeds, LS2 9TJ, United Kingdom

[*] a.fiore@tue.nl

A new generation of photonic integrated circuits (PICs) is being developed for application in quantum communications and quantum simulations. While the passive functionalities needed in these quantum PICs are very similar to those of their classical counterparts, light generation and detection must be controlled at the single-photon level. III-V semiconductors are very well suited for quantum PICs in view of their direct bandgap and corresponding ability to produce single photons by radiative recombination of excitonic states in nanostructures [1]. In this talk I will review our recent progress in the development of multifunctional quantum PICs, including the demonstration of fully-tuneable waveguide-coupled single-photon sources and of efficient waveguide single-photon detectors on nanobeams.

References

[1] C.P. Dietrich, A. Fiore, M.G. Thompson, M. Kamp and S. Höfling, *GaAs integrated quantum photonics: Towards compact and multi-functional quantum photonic integrated circuits*, Laser Photonics Rev., vol. 10, no. 6, pp. 870-894, 2016

Stochastic Resonance with an Integrated Nano-Electro-Mechanical Photonic Crystal Membrane

Avishek CHOWDHURY[1], Sylvain BARBAY[1], Marcel CLERC[2], Isabelle ROBERT-PHILIP[1], Rémy BRAIVE[1,3*]

[1] Centre de Nanosciences et de Nanotechnologies, CNRS, Univ. Paris-Sud, Université Paris-Saclay, C2N Marcoussis, 91460 Marcoussis, France

[2] Departamento de Fısica, Facultad de Ciencias F´ısicas y Matem´aticas, Universidad de Chile, Casilla 487-3, Santiago, Chile

[3] Université Paris Diderot, Sorbonne Paris Cité, 75207 Paris Cedex 13, France

[*] remy.braive@lpn.cnrs.fr

In a large number of experiments or devices, noise is usually viewed as an undesirable disturbance, hindering the measurement sensitivity or device performances. In some circumstances however, noise-induced phenomena can help, as in the case of stochastic resonance whereby a weak coherent signal, compared to the barrier height of a double-well potential, gets amplified resonantly by application of external noise. Stochastic resonance occurs in a wide class of nonlinear systems, in neurobiology [1], mesoscopic physics [2], photonics [3], atomic physics [4], mechanics [5, 6]...

If a weak periodic forcing is applied to the oscillator, the initially symmetrical double-well potential gets tilted asymmetrically up and down, periodically raising and lowering the potential barrier. Although the periodic forcing is too weak to let the membrane switch periodically from one potential well into the other one, noise-induced hopping between the potential wells can become synchronized with the weak period forcing. This time coincidence takes place when the average waiting time between noise-induced interwell transitions is comparable with half the period of the periodic forcing. Thus stochastic resonance corresponds to the noise-assisted amplification of a weak coherent input that is too feeble to induce hopping between the two stable states.

It has been mainly reported in non-linear systems driven by a coherent signal together with an additive noise, more scarcely a multiplicative noise. We report here on stochastic resonance in a bistable device with the assistance of such a non-linear noise.

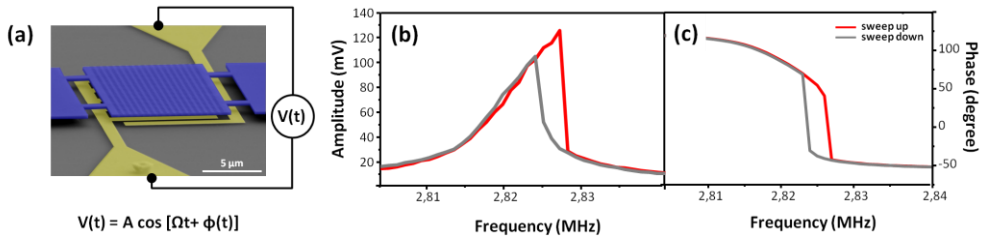


Fig. 1. (a) S.E.M. image of the suspended photonic crystal membrane (in blue) above the interdigitated electrodes (in yellow). By applying an AC voltage V(t), the amplitude (b) and the phase (c) are recorded across the fundamental mechanical resonance of the photonic crystal oscillator by sweeping the driving frequency Ω up and down. Thus a bistable region is observable.

Our mechanical resonator consists of an InP suspended membrane with a thickness of about 260 nm and a 10×20µm² surface (Fig. 1a). Holes are drilled on in the membrane to perform a perfect photonic crystal used as a reflector at normal incidence for the probe laser. A coherent weak signal is introduced by applying a modulated electrostatic force on the membrane and driving its out-of-plane motion. This force is generated by applying an AC-bias at the frequency inside the hysteresis region (Fig. 1b-c), on integrated interdigitated electrodes placed underneath the membrane at a distance of

about 400 nm (Fig. 1a). In the same manner, phase noise is added on the AC applied voltage, which is proportional to the actuation force. Last, the mechanical response of the membrane is probed optically in an interferometric testbed, in which the membrane is used as one of the end mirrors. With an actuation strong enough, the oscillator can enter in a non-linear regime and exhibits bistability (Fig. 1b-c).
In order to match the time coincidence conditions, an in-depth characterization of these time-scales is performed on the device.

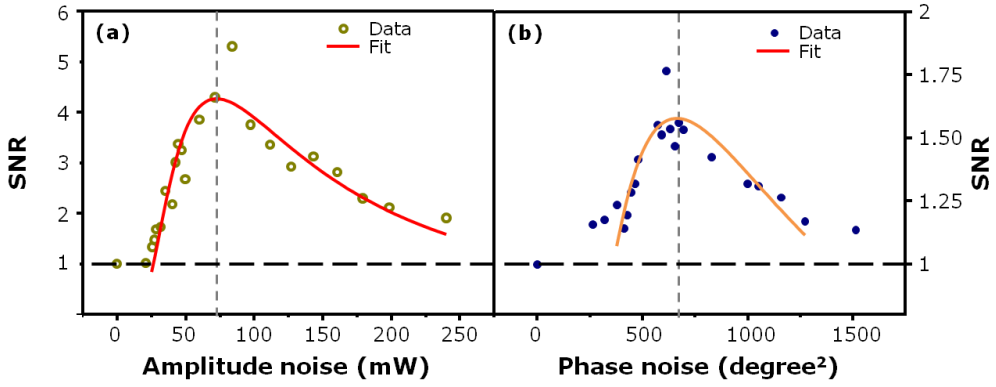


Fig. 2: Signal to Noise Ration (SNR) normalized with respect to no noise intentionally induced either in amplitude (a) or in phase (b)

Thus, we were able to demonstrate stochastic resonance with phase noise in a non-linear oscillator, consisting of a nano-electromechanical device with an amplification of a factor 1.75. In addition to that and thanks to numerical simulations, we show that phase noise has to be taken into account as a multiplicative noise to reproduce experimental results. At the same time, pure amplitude noise stochastic resonance has also been investigated and could simply be understood with additive noise. To enhance amplification with phase, alignment of the modulation along the preferential path between the two states in the potential could be a solution.
Such stochastic resonance obtained by assistance of phase noise may enable various noise-aided applications, including signal transmission telecommunication with intensively used Phase Key Shifting protocol, or metrology with improved detection in noise-floor limited systems.

References

[1] S. Bezrukov and I. Vodyanoy, *Noise-induced enhancement of signal transduction across voltage-dependent ion channels*, Nature vol. 378, pp. 362-364, 1995
[2] A. Hibbs *et al*, *Stochastic resonance in a superconducting loop with a Josephson junction*, J. Appl. Phys. vol. 77, pp. 2582, 1995
[3] S. Barbay, G. Giacomelli and F. Marin, *Stochastic resonance in vertical cavity surface emitting lasers*, Phys. Rev. E, vol. 61, pp. 157, 2000
[4] D. Wilkowski *et al*, *Instabilities in a magneto-optical trap: Noise-induced dynamics in an atomic system*, Phys. Rev. Lett. vol. 85, pp. 1839, 2000
[5] F. Mueller *et al*, *Optomechanical stochastic resonance in a macroscopic torsion oscillator*, Phys. Rev. A vol. 79, pp. 031804, 2009
[6] W. Venstra et al, *Stochastic switching of cantilever motion*, Nat. Comm. vol. 4, pp. 2624, 2013

MEMS-assisted fiber-chip coupling

X.J.M. Leijtens[1*], R. Santos[2], M. Tichem[3], K. Wörhoff[4] and K.A. Williams[1]
[1]Institute for Photonic Integration, TU Eindhoven, The Netherlands; [2]Smart Photonics, Eindhoven, The Netherlands; [3]Delft University of Technology, Delft, The Netherlands; [4]LioniX BV, Enschede, The Nethelands; *X.J.M.Leijtens@tue.nl

Abstract - A long standing problem in integrated photonics is the attachment of optical fibers to an integrated photonic IC. The EU-funded project PHASTFlex takes an innovative approach to this and uses micro-electro-mechanical systems that actuate the silicon oxide-nitride optical waveguides to provide the required sub-micron alignment accuracy. Here we report on the measured movement range and coupling efficiency.

Introduction

Optical mode dimensions in single-mode waveguides are typically in the order of a few micrometer. For a low-loss connection to an optical fiber an alignment of sub-micron is required, which is beyond the capability of state-of-the-art pick-and-place assembly equipment.

The PHASTFlex project[1] tries to solve this problem with an intermediate TriPleX[2] interposer that has waveguides which match the size of the waveguide mode of the PIC on one side and that of a standard single-mode fiber (SMF) at the other side. To achieve the sub-micron alignment accuracy between the PIC and the interposer, we exploit micro electro-mechanical systems (MEMS) that are integrated in the TriPleX interposer, and which can move flexible ends of the optical waveguides. The alignment between TriPleX and SMF is not so critical because the mode dimensions are in the order of 10 µm.

Alignment is now a two-step procedure: firstly, the assembly machine positions the PIC and the interposer with an alignment accuracy between one and two microns; secondly, the MEMS move the flexible waveguide ends to provide the sub-micron alignment; thirdly. The concept is shown in figure 1.

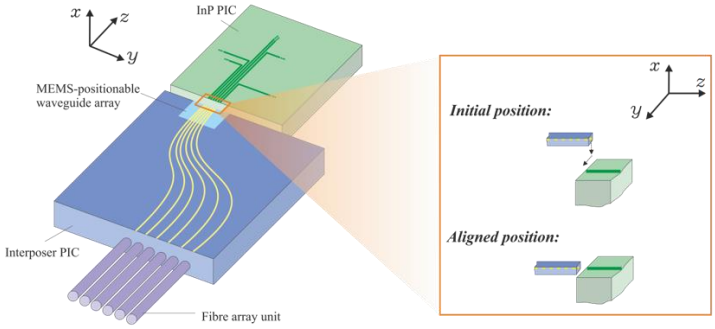


Fig. 1. Concept of alignment.

Experiments

We have conducted a number of experiments on the MEMS movement. For this we have used a TriPleX sample with out-of-plane thermal actuators. These are heaters on top of flexible SiO_2 beams. Figure 2 shows a microscope image of one set of short actuators with optical waveguides in between. We also characterized a set of long actuators, where the heaters extend over the full length of the flexible beams.

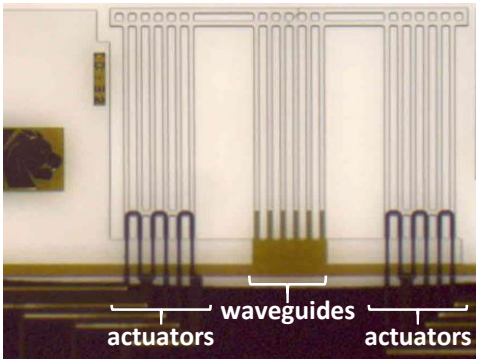


Fig. 2. MEMS inTriPleX with actuators for out-of-plane movement and optical waveguides in between.

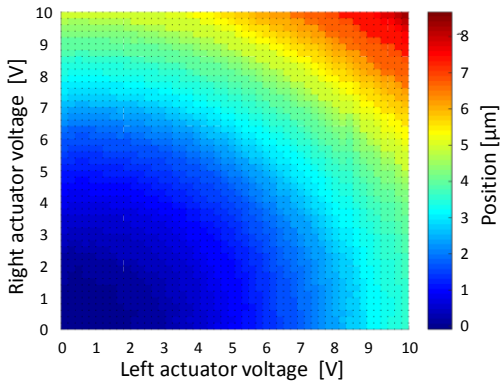


Fig. 3. Movement versus left and right actuator voltage.

The difference in thermal expansion between the poly-silicon, the metal and the SiO_2 causes the beams to deflect. By providing different powers to the left and right actuators, the end of the beams, and hence the waveguide ends, can be tilted, to compensate for an initial angular misalignment. Microheaters with an electrical resistance of approximately 1 kΩ are part of two actuators that are mechanically connected with a T-bar to displace the waveguides. Figure 3 depicts the achievable waveguide deflection in the out-of-plane direction as a function of applied voltage, showing a movement range up to 8 µm, which is more than sufficient to overcome the positional misalignment due to the accuracy of the assembly machine. The alignment requirements depend on the size of the optical mode in the waveguides. We have used an InP PIC for testing which has waveguides with a mode size which is expanded at the facet to approximately a $1/e^2$ diameter of 2.8 µm. The TriPleX mode size is similar. A requirement of a maximum excess coupling loss of 1 dB translates to a maximum out-of-plane misalignment of 1 µm. From the measurements shown in Figure 3, a voltage change of 0.1 V results in a displacement of less than 100 nm, which is already adequate for an optimized coupling.

The coupling concept was tested in a lab bench where the PICs were mounted in two alignment stages. The two chips were aligned coarsely and the final alignment was achieved using the MEMS structures. This allowed for precise alignment and an 80% coupling efficiency was achieved. The remaining loss is attributed to a residual mode-size mismatch and reflection loss in the non-coated TriPleX waveguides.

Conclusions

In this work a novel concept for attaching an optical fiber to a InP PIC has been exploited. The MEMS structure showed movement range of more than 8 µm. This movement range is much larger than the position accuracy of the automated assembly tools enabling optimization of the coupling between the two chips. We acknowledge the support from the EU through the FP7 Programme FP7-ICT-2013-11 Project 619267-PHASTFlex.

References

[1] “EU FP7 project PHASTFlex: Photonic Hybrid Assembly Through Flexible Waveguides.” http://phastflex.jeppix.eu.

[2] K. Wörhoff, R. G. Heideman, A. Leinse, and M. Hoekman, “TriPleX: a versatile dielectric photonic platform,” Advanced Optical Technologies, vol. 4, pp. 189–207, Apr. 2015.



Photonic Biosensors Enabled by MEMS and Microfluidics Integration

Kristinn B. GYLFASON[1*], Carlos ERRANDO-HERRANZ[1], Reza Z. SHAFAGH[1], Floria OTTONELLO-BRIANO[1], Hans SOHLSTRÖM[1], Wouter VAN DER WIJNGAART[1], Frank NIKLAUS[1], Göran STEMME[1], and Tommy HARALDSSON[1]

[1]Micro and Nanosystems, KTH Royal Institute of Technology,
Osquldas väg 10, SE-10044 Stockholm, Sweden
[*] gylfason@kth.se

Photonic biosensors have in recent years progressed rapidly towards the goal of mobile biochemical analysis, which will enable new applications such as field-deployable medical diagnostics, mobile environmental monitoring, and distributed health-care. This progress has been achieved by leveraging the capability of photonics for precise optical metrology, and by using wafer-scale micro- and nanofabrication for mass-producing sensors, in particular from silicon and related materials. However, to deliver on the full promise of photonic biosensors, remaining challenges include the handling of liquids on the microscale and the on-chip integration of light sources and detectors. Here, we discuss our recent work on these two fronts.

Biosensors, by definition, employ a biological recognition element to bind a target analyte of interest. In this way, the sensor can exploit the work already done by biological evolution to create highly specific molecular bindings. This approach elegantly solves one of the main challenges of sensing: specificity. However, biological reactions only work in water based solutions, and thus biosensors must handle liquid.

While the planar wafer-scale micro- and nanofabrication technology developed by the microelectronics and photonics industries has been deployed to mass-produce photonic sensors, the liquid handling structures have, so far, been produced by post processing at chip-level [1]. To address this limitation, we developed a new family of off-stoichiometric thiol-ene (OSTE) polymers that can be processed using the familiar wafer-scale lithography techniques [2], [3]. Using these polymers and processes, the photonic sensors can be biofunctionalized at wafer-scale, followed by integration of a complete microfluidic system through transfer-bonding [4].

The second challenge of light-source and detector integration is not unique to photonic biosensors, but shared with most other low-cost photonic systems. Silicon photonics has the mass-production capability required for economical deployment of photonic biosensors, but for robust mobile application, the light-source and detector must be integrated in the sensor chip. Without such integration, the requirement for precise optical alignment between the passive sensor chip and the light-source makes robust mobile sensing with user-replaceable sensor cartridges extremely challenging.

For sensors operating in the mid-IR region, nanoscale thermal sources and detectors are an interesting option, due the efficient coupling that can be achieved between these sub-wavelength structures and single-mode waveguides. We have recently demonstrated platinum-nanowire-based light- sources [5] and bolometric detectors [6] that are easily integrated onto a standard silicon photonics wafer using the manufacturing techniques of microelectromechanical systems (MEMS). Due to their small thermal mass, these devices have a very fast response (up to a few MHz). Furthermore, their sub-wavelength optical dimensions lead to partially coherent operation, enabling the shaping of radiation patterns and of spectral properties.

For the interrogation of high-Q resonant photonic biosensors, such as ring resonators and photonic crystal cavities, however, tunable narrow-linewidth coherent light-sources are preferred. Although significant progress has recently been made, both on monolithically integrated germanium lasers and on heterogeneously integrated III-V lasers on silicon, an economical solution for light in silicon remains elusive. On this front, we have developed MEMS tunable ring resonators that could serve as tunable laser cavities in either type of integrated laser [7]. Finally, if external sources must be employed, the coupling problem can be mitigated using our MEMS tunable grating couplers to relax alignment tolerances of fiber-to-chip coupling [8].

In conclusion, we have developed solutions towards mobile photonic biosensors with integrated liquid sample handling, light-sources, and detectors, with the aim to bring photonic biosensors out of the lab and into the field, e.g. into challenging situations such as infectious disease epidemics. Furthermore, the reduced cost of these sensors will enable many new industrial and consumer applications within such diverse fields as agriculture, environmental monitoring, and personal health care.

References

[1] C. F. Carlborg *et al.*, "A packaged optical slot-waveguide ring resonator sensor array for multiplex label-free assays in labs-on-chips," *Lab Chip*, vol. 10, no. 3, pp. 281–290, Feb. 2010.

[2] C. F. Carlborg, T. Haraldsson, K. Oberg, M. Malkoch, and W. van der Wijngaart, "Beyond PDMS: off-stoichiometry thiol-ene (OSTE) based soft lithography for rapid prototyping of microfluidic devices," *Lab Chip*, vol. 11, no. 18, pp. 3136–3147, 2011.

[3] C. F. Carlborg, A. Vastesson, Y. Liu, W. van der Wijngaart, M. Johansson, and T. Haraldsson, "Functional off-stoichiometry thiol-ene-epoxy thermosets featuring temporally controlled curing stages via an UV/UV dual cure process," *J. Polym. Sci. Part Polym. Chem.*, vol. 52, no. 18, pp. 2604–2615, Sep. 2014.

[4] C. Errando-Herranz *et al.*, "Integration of microfluidics with grating coupled silicon photonic sensors by one-step combined photopatterning and molding of OSTE," *Opt Express*, vol. 21, no. 18, pp. 21293–21298, Sep. 2013.

[5] F. O. Briano *et al.*, "A sub-µs thermal time constant electrically driven Pt nanoheater: thermo-dynamic design and frequency characterization," *Appl. Phys. Lett.*, vol. 108, no. 19, p. 193106, May 2016.

[6] F. Ottonello Briano, M. Colangelo, C. Errando-Herranz, H. Sohlström, and K. B. Gylfason, "A fast uncooled infrared nanobolometer featuring a hybrid-plasmonic cavity for enhanced optical responsivity," presented at the 30th IEEE MEMS conference, Las Vegas, 2017.

[7] C. Errando-Herranz, F. Niklaus, G. Stemme, and K. B. Gylfason, "Low-power microelectromechanically tunable silicon photonic ring resonator add–drop filter," *Opt. Lett.*, vol. 40, no. 15, p. 3556, Aug. 2015.

[8] C. Errando-Herranz, M. Colangelo, S. Ahmed, J. Björk, and K. B. Gylfason, "MEMS tunable silicon photonic grating coupler for post-assembly optimization of fiber-to-chip coupling," presented at the 30th IEEE MEMS conference, Las Vegas, 2017.

Silicon photonics: from present status to future developments

Piero ORLANDI[1*], Marco PIAZZA[1], Luca MAGGI[1], Antonio CANCIAMILLA[1]
Giuseppe CUSMAI[1], Matteo TRALDI[1], Charles BAUDOT[2], Antonio FINCATO[3]
[1]STMicroelectronics Agrate, Via Camillo Olivetti 2, Agrate Brianza, 20864, Italy
[2]STMicroelectronics Crolles, Rue Jean Monnet 850, Crolles, 38920, France
[3]STMicroelectronics Castelletto, Via Tolomeo 1, Cornaredo, 20010, Italy
[*] piero.orlandi@st.com

Silicon photonics gathered a great amount of investments during the last decade. Both research centres and major industries directed their resources towards this promising technology. As a result, different technological platforms have been proposed [1- 7] and some of them are now accessible through multi-project wafer services. This interest was fuelled by the idea of exploiting CMOS fabs capability to implement a large scale industrialization of low cost and highly integrated electro-optic chips. The amount of digital data exchanged is in fact constantly increasing: by the end of 2020 global IP traffic will reach 2.3 ZB per year, growing at a compound annual growth rate (CAGR) of 22% [8]. This trend is pushing the need for high data-rate optical communication systems toward shorter and shorter distances, from intra-data centers to on-board and on-chip communications [9]. Silicon photonics is seen as the most promising technology to reach the required cost per bit and level of integration and nowadays its evolution is mainly driven by the data centers market.

In this scenario, STMicroelectronics has developed an industrial silicon photonics platform in a 300 mm manufacturing facility [1]. The photonic technology, named PIC25G, employs 193 nm lithography and has been optimized to maximize the performance of passive and active photonic components of the Photonic Integrated Circuit (PIC). Particular attention has been posed to 1310nm and 1490nm wavelength ranges but also the transmission around 1550 nm is supported. The Electronic Integrated Circuit (EIC) is fabricated with a separate process and then flip-chip assembled to the wafer through copper pillars (see Fig. 1a). This choice allows to optimize both technologies separately, giving maximum design flexibility and minimal degradation with respect to fully integrated solutions.

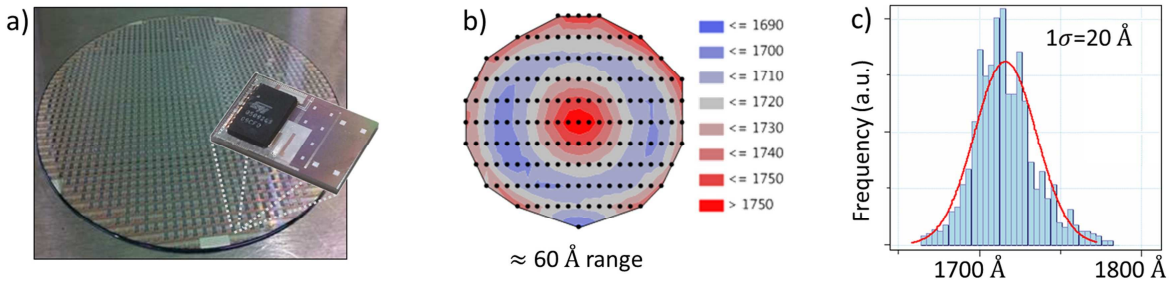


Fig. 1. (a) EIC die to 300 mm silicon photonics wafer assembly; (b) within-wafer remaining silicon thickness; (c) wafer-to-wafer remaining silicon thickness statistic.

Both PIC and EIC are tested separately at wafer level before assembly, using for both a fully automatic 300 mm compatible electro-optical probing station. This feature, fundamental for large scale industrial production, is enabled for the PIC by grating couplers. After the assembly of EICs on the PICs wafer, an Electro-Optical Wafer Sorting (EOWS) is finally performed with the same tool.

To ensure performance repeatability and uniformity of the devices at wafer level, a fine control of all the process steps is fundamental. For instance, focusing on grating couplers definition, silicon etching is the most critical step. PIC25G process control gives a within-wafer remaining Si thickness variability range of 6 nm (see Fig. 1b) while the wafer-to-wafer standard deviation is about 2 nm (see Fig. 1c). This process control allows a peak wavelength dispersion of grating coupler with a $\sigma \sim 2.4$ nm, able to guarantee strict specifications required by field applications. The SEM and TEM images of some of the active and passive devices developed in PIC25G are reported in Fig. 2. This set of devices, together with fundamental passive building blocks such as bends, multi-mode waveguides, tapers, directional couplers, and Y-junctions, forms a complete photonic technological platform, allowing to realize complex photonic integrated circuits. STMicroelectronics silicon photonics platform enables the fabrication of multi-channel transceivers with aggregate data-rate of 100 Gbps and beyond [1]. Transmission of non-return to zero (NRZ) modulated signals at 25 Gbps and 56 Gbps per-lane has been recently demonstrated with lower power consumption with respect to the state-of-the art [10].

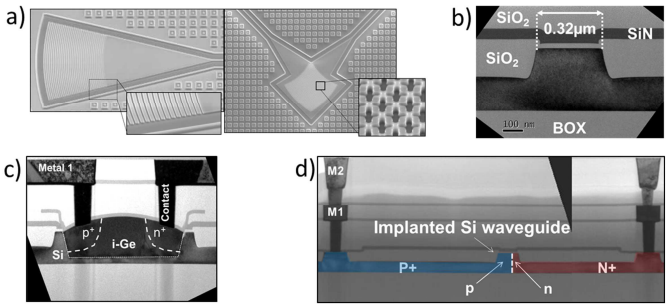


Fig. 2. (a) SEM top view of single polarization and polarization splitting grating couplers. TEM cross section of (b) single mode waveguide (c) photodiode and (d) PN junction based phase modulator.

In order to enable a fast, safe and product-oriented design, all the devices developed are included as building blocks in process-dedicated libraries within a Product Design Kit (PDK). The PDK provides an integrated environment for schematic-level photonic circuit design, circuit mask layout generation and performances simulations based on devices accurate modelling. The PDK also provides automatic check decks as Layout Versus Schematic (LVS) and Design Rules Checker (DRC), assuring compliancy with process design rules, a key point to guarantee manufacturability. Finally, the possibility of a full co-simulation of electrical and optical devices and circuits in 3D configuration is also included.

The next step for Silicon Photonic transceivers is addressing Wavelength Division Multiplexing (WDM) transmission systems. In order to move towards this kind of applications, a key element is the introduction of devices enabling for multi-wavelength management (Mux/DeMux). When the number of channels to be handled is low (i.e. 2, 4), Mach-Zehnder-based lattice filters [11, 12] represent the best solution to obtain low-loss and flat-band filters. However, in order to allow performance control and repeatability to maintain a high-yield, the design needs to be optimized minimizing sensitivity to process tolerances. The device has been fully engineered to achieve this task. Waveguide cross section has been optimized by using multi-mode waveguides for filter delay lines [11] and geometry of the single stage is engineered in order to minimize optical path lengths. Fig. 3a shows the measured response of a ninth-order filter designed to separate two channels compliant with the Coarse WDM grid requirements.

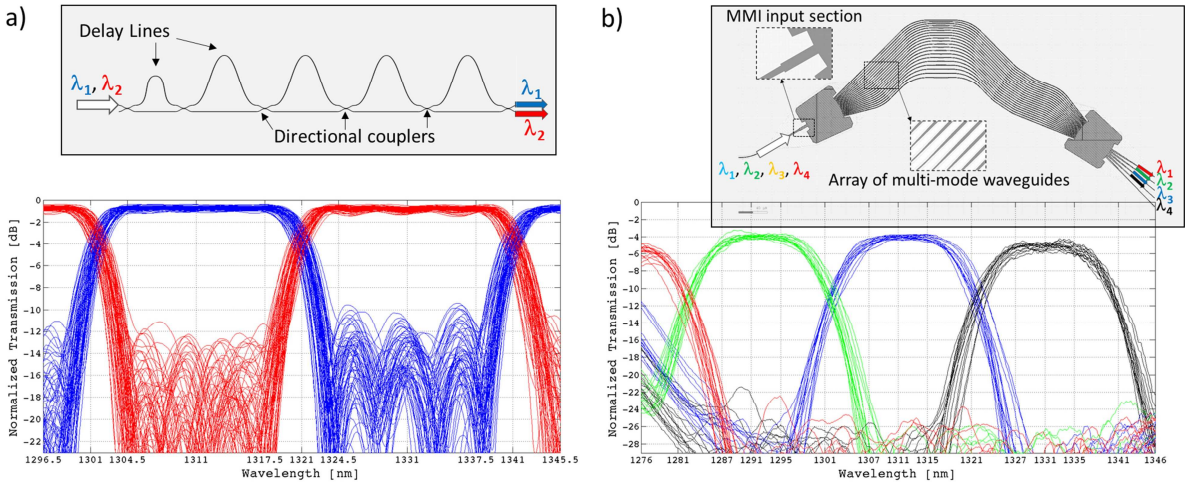


Fig. 3. (a) Measured transmission of 65 replicas (over different wafers) of a ninth order lattice filter. (b) Measured transmission of 20 replicas (over different wafers) of an AWG. Note that all spectra have been normalized by the means of reference grating couplers.

The measurements of 65 replicas of the same device (over different 300 mm wafers) are superimposed in the picture to highlight the good performance and the high repeatability obtained. Considering a channel bandwidth of 13 nm, the maximum Insertion Loss (IL) varies from 0.6 dB to 1.5 dB, with a median value of 1 dB, while the minimum Cross Talk (XT) varies from 8.4 dB to 16 dB, with a median value of 11.8 dB. A straightforward technique to achieve XT values usually required to fulfil system-level specifications, is to cascade the same filter as in [12]. This allows in fact to double the XT at the price of doubling the IL. When a larger number of channels has to be handled and a smaller footprint is required, Arrayed Waveguide Gratings (AWGs) are usually the preferred solution. Employing again multi-mode waveguides to reduce fabrication tolerance sensitivity, we designed and fabricated an AWG working on the CWDM grid with flattened band as in [13]. In Fig. 3b the measured spectra of the same AWG over 20 chips on different 300 mm wafers are reported. As for the lattice filter case, good performance repeatability is obtained. We demonstrated band flattening, 4.0

dB IL, 10nm -1dB bandwidth and 20 dB Crosstalk.

The reported results demonstrate that silicon photonics technology can play a role also for WDM applications in the near future. A future where, in order to keep up with the needs for larger aggregate bandwidths, also transmissions at higher bit-rates per lane (e.g. 56 Gbps) and with advanced modulation formats (e.g. PAM and QAM) will have to be provided. In order to implement novel functionalities, the development of new basic components and the improvement of the platform technology are required. The potential of silicon photonics can be enhanced by adding different active and passive optical materials through hybrid or monolithic integration [14]. Promising results have been recently shown in literature [15, 16]. Once the solutions most suitable for the chosen applications will be identified and selected, the main challenge will be reaching the requirements of the large volume production: high yield, efficient testing and sustainable supply chain.

Acknowledgments

The contribution of Antonio Fincato and Charles Baudot to this work was partially supported by the European Community's Seventh Framework Programme (FP7/2007-2013) under grant agreement n° 318178-PLAT4M

References

[1] F. Boeuf *et al.*, *Silicon Photonics R&D and Manufacturing on 300-mm Wafer Platform*, Journal of Lightwave Technology vol. 34, pp. 286-295, 2016
[2] S. Assefa *et al.*, *A 90nm CMOS integrated Nano-Photonics technology for 25Gbps WDM optical communications applications*, In International Electron Devices Meeting, San Francisco, CA, pp. 33.8.1-33.8.3, 2012
[3] http://www2.imec.be/be_en/services-and-solutions/silicon-photonics.html
[4] L. Zimmermann, *Monolithic Electronic-Photonic Co-Integration in Photonic BiCMOS*, In Proceedings of 42nd European Conference on Optical Communication (ECOC), Dusseldorf, Germany, W3F5, pp. 1-3, 2016
[5] D. J. Shin *et al.*, *Integration of silicon photonics into DRAM process*, In Proceedings of Optical Fiber Communication Conference and Exposition and the National Fiber Optic Engineers Conference (OFC/NFOEC), Anaheim, CA, OTu2C.4, pp. 1-3, 2013
[6] D. Feng, B. J. Luff, S. Jatar and M. Asghari, *Micron-scale silicon photonic devices and circuits*, In Proceedings of Optical Fiber Communication Conference and Exposition (OFC), San Francisco, CA , Th4C.1 pp. 1-3, 2014
[7] B. Szelag *et al.*, *Multiple wavelength silicon photonic 200 mm R&D platform for 25Gb/s and above applications*, In Proceedings of the SPIE, vol. 9891, pp. 98911C (15 pp.), 2016
[8] CISCO White Paper, *The Zettabyte Era: Trends and Analysis*, July 2016
[9] M. Zuffada, *The industrialization of the Silicon Photonics: Technology road map and applications*, In Proceedings of the European Solid-State Device Research Conference (ESSDERC), Bordeaux, pp. 7-13, 2012
[10] E. Temporiti *et al.*, *Insights Into Silicon Photonics Mach-Zehnder-Based Optical Transmitter Architectures*, IEEE Journal of Solid-State Circuits, vol. 51, no. 12, pp. 3178-3191, 2016
[11] F. Horst *et al.*, *Cascaded Mach-Zehnder wavelength filters in silicon photonics for low loss and flat pass-band WDM (de-) multiplexing*, Optics Express, vol. 21, pp. 11652-11658, 2013
[12] S. Dwivedi *et al.*, *Coarse wavelength division multiplexer on silicon-on-insulator for 100 GbE*, in Proceedings of the IEEE 12th International Conference on Group IV Photonics (GFP), pp. 9-10, 2015.
[13] S. Pathak *et al.*, *Optimized Silicon AWG With Flattened Spectral Response Using an MMI Aperture*, IEEE Journal of Lightwave Technology, vol. 31, no. 1, pp. 87-93, 2013
[14] http://www.h2020-cosmicc.com/
[15] W. D. Sacher *et al.*, *Multilayer Silicon Nitride-on-Silicon Integrated Photonic Platforms and Devices*, IEEE Journal of Lightwave Technology, vol. 33, no. 4, pp. 901-910, 2015
[16] T. Ferrotti *et al.*, *O-Band III–V-on-Amorphous-Silicon Lasers Integrated With a Surface Grating Coupler*, IEEE Photonics Technology Letters, vol. 28, no. 18, pp. 1944-1947, 2016

Ultralow-capacitance opto-electronic devices for femtojoule/bit photonics

Kengo NOZAKI[1,2*], Shinji MATSUO[1,3], Takuro FUJII[1,3], Koji TAKEDA[1,3], Eiichi KURAMOCHI[1,2], Akihiko SHINYA[1,2], and Masaya NOTOMI[1,2]

[1]Nanophotonics Center, [2]NTT Basic Research Laboratories, [3]NTT Device Technology Laboratories, NTT Corporation, 3-1, Morinosato Wakamiya Atsugi, Kanagawa 243-0198, Japan

[*]nozaki.kengo@lab.ntt.co.jp

Future microprocessors will need an unprecedented many-core architecture providing chip-scale optical communication, and for on-chip-com networks in particular, this architecture should be fully integrated with transmitters, photoreceivers, and other functional nanophotonic devices with low energy consumption. One of the challenges with these opto-electronic devices is to realize a device capacitance (C) as small as the fF level or less. Such devices are able to operate in the femtojoule/bit energy regime, which is required for future chip-scale photonic technology [1].

For a photodetector (PD), a low C would allow connection to a high impedance load while retaining the RC bandwidth, and this would eliminate the need for power-consuming electrical amplifiers. Such a device is called a receiver-less PD and it provides ultralow-energy operation [2, 3]. Photonic crystals (PhCs) are promising as such small PDs because of their strong light confinement in an ultrasmall dimension. In this work, we use PhC-PDs with an embedded InGaAs absorption layer in an InP-based PhC waveguide, which we obtained using a compact buried-heterostructure (BH) (Fig. 1a and 1b). This structure can confine both photons and carriers in an ultrasmall space, and hence the length was reduced to just 1.7 μm and the capacitance was less than 1 fF (Fig. 1c). Even with such a small size, the optical responsivity remains high at 1 A/W and there is clear eye opening for a 40-Gbit/s signal (Fig. 1d). These features meet the demand for an amplifier-free PD terminated with a high impedance load. We investigate the integration of the PD with a several-kΩ load resistor to demonstrate on-chip light-to-voltage conversion. A conversion efficiency as high as 4 kV/W was observed, and the expected bandwidth exceeds 10 GHz. This suggests that the optical energy required for generating a CMOS voltage level (assumed to be 0.2 V) is less than 1 fJ/bit, which can be obtained without electrical amplifiers [3]. These results reveal a successful way of realizing an ultrasmall/ultralow-energy photoreceiver.

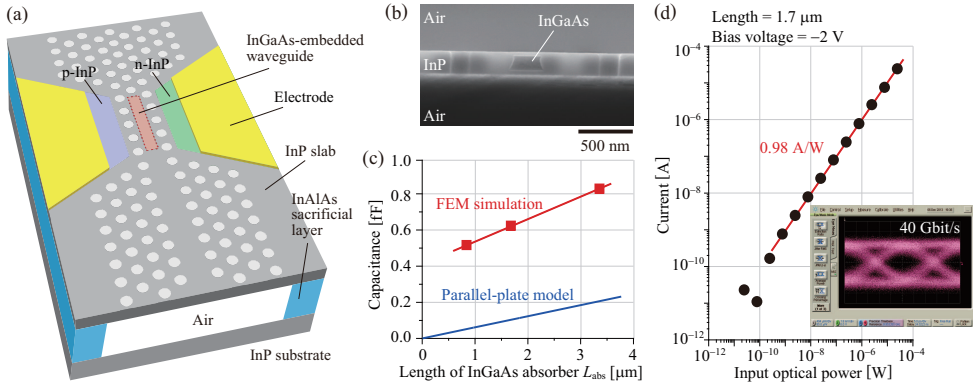


Fig. 1 PhC-PD. (a) Schematic of PD structure. (b) Cross-sectional view SEM images of fabricated device. (c) Calculated capacitance of PhC-PD. The blue curve is calculated from the parallel-plate model. The red plots are results simulated by the finite-element method with a 3-D model. (d) Photocurrent versus optical power characteristic and eye diagram for 40-Gbit/s NRZ optical signals.

We also studied an electro-absorption modulator (EAM) based on a PhC waveguide with the aim of realizing an ultralow-energy transmitter. An EAM has great potential for reducing the size, C, and driving voltage V_{pp}, compared with those of an electro-optic modulator involving the phase shift of light. However, the additional energy associated with the photocurrent flow under reverse voltage will increase the total electrical energy consumption. In this work, we demonstrated an EAM based on an InGaAsP-embedded PhC waveguide (Fig. 2a) [4]. This revealed a broadband optical modulation (Fig. 2b) and a dynamic modulation bit rate of up to 56 Gbit/s (Fig. 2c). The air-bridge structure and a device length of 100 μm or less result in a small C of ≤ 13 fF while operating with a V_{pp} of < 1 V, and this results in a charging energy of 1.6 fJ/bit. In particular, operation at a low reverse voltage of −0.2 V for a 3-dB extinction ratio effectively reduces the photocurrent energy. As a result, the total electrical energy needed for our EAM remains < 2 fJ/bit. This energy is lower than that of any waveguide EAM. These results show that our EAM overcomes the significant energy bottleneck exhibited by previous EAMs.

Our results suggest the potential for using our EAM and PD as a small-footprint low-energy transmitter and receiver, respectively. Monolithic integration with PhC nanolasers [5] that have a similar BH structure should be possible on the same InP-PhC platform, and even integration on silicon would be possible with a heterogeneous fabrication technique. This is an attractive way of constructing a dense nanophotonic functional architecture on a CMOS chip.

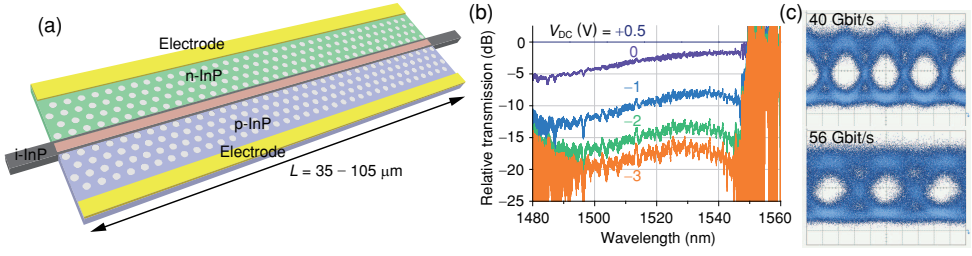


Fig. 2 PhC-EAM. (a) Schematic of EAM structure. (b) Relative transmission spectra for different V_{DC} in L_{EAM} = 105 μm device. All the spectra are normalized with the spectrum of V_{DC} = +0.5 V. (c) Eye diagrams at bit rates of 40 and 56 Gbit/s. The V_{pp} was 2.0 V (swing from –1.5V to +0.5 V).

Acknowledgement

This work was supported by CREST, Japan Science and Technology Agency.

References

[1] D. A. B. Miller, *Device requirements for optical interconnects to silicon chips*, Proceedings of the IEEE, vol. 97, pp. 1166-1185, 2009

[2] C. Debaes, A. Bhatnagar, D. Agarwal, R. Chen, G. A. Keeler, N. C. Helman, H. Thienpont, and D. A. B. Miller, *Receiver-less optical clock injection for clock distribution networks*, IEEE Journal of Selected Topics in Quantum Electronics, vol. 9, pp. 400-409, 2003

[3] K. Nozaki, S. Matsuo, T. Fujii, K. Takeda, M. Ono, A. Shakoor, E. Kuramochi, and M. Notomi, *Photonic-crystal nano-photodetector with ultrasmall capacitance for on-chip light-to-voltage conversion without an amplifier*, Optica, vol. 3, pp. 483-492, 2016

[4] K. Nozaki, S. Matsuo, T. Fujii, K. Takeda, M. Ono, A. Shakoor, E. Kuramochi, and M. Notomi, *Ultralow-energy InGaAsP modulators based on a photonic crystal waveguide/nanocavity involving the Franz-Keldysh effect*" in CLEO Pacific Rim, Busan, 27P2-69, 2015

[5] K. Takeda, T. Sato, A. Shinya, K. Nozaki, W. Kobayashi, H. Taniyama, M. Notomi, K. Hasebe, T. Kakitsuka, and S. Matsuo, *Few-fJ/bit data transmissions using directly modulated lambda-scale embedded active region photonic-crystal lasers*, Nature Photonics, vol. 7, pp. 569-575, 2013

Germanium-on-Silicon Photonic Devices

Yasuhiko ISHIKAWA*, Kazuki ITO, Michiharu NISHIMURA, Yuji MIYASAKA, Naoki HIGASHITARUMIZU, Motoki YAKO

Department of Materials Engineering, The University of Tokyo,
7-3-1 Hongo, Bunkyo, Tokyo, 113-8656, Japan
* y-ishikawa@material.t.u-tokyo.ac.jp

Ge epitaxial layers on Si have been studied for near-infrared (NIR) photodiodes (PDs) in Si photonics as well as for optical modulators and lasers. In this presentation, our recent progresses [1-5] are presented on waveguide-integrated vertical pin PDs using Ge epitaxial layers grown on Si-on-insulator (SOI) layers as well as Ge/SiGe heterostructure technologies for higher-performance photonic devices.

For practical telecommunication applications, there exist severe requirements in the device performance for Ge PDs, (1) high photodetection efficiency at 1.3 - 1.6 μm, (2) high operation frequency more than 10 GHz, (3) low dark leakage current as small as 1 μA or below, etc. These requirements should be satisfied even at temperatures as high as 80°C. High-quality Ge layers on Si are necessary, and the device structures and processes should be optimized. A typical optical microscope image for a fabricated Ge pin PD and the schematic cross-section are shown in Fig. 1. Waveguide-integrated Ge PDs were successfully fabricated using Ge epitaxial layers selectively grown on SOI layers by chemical vapor deposition (CVD).

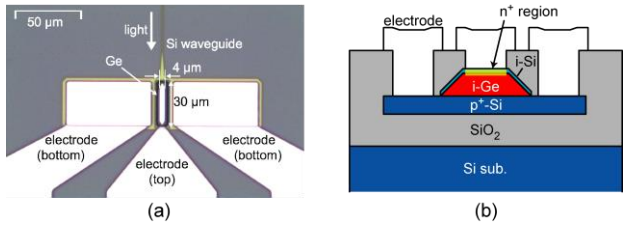


Fig. 1. (a) Typical optical microscope image and (b) schematic cross-section for Ge PD integrated with Si optical waveguide.

Figure 2(a) shows typical current-voltage (I-V) characteristics under dark and under the illumination of 1.55-μm light through the Si waveguide. The dark leakage current showed a small value of 0.02 μA at the 1-V reverse bias. The current was increased with the illumination, revealing a successful PD operation. A high responsivity was obtained to be 1.0 A/W.

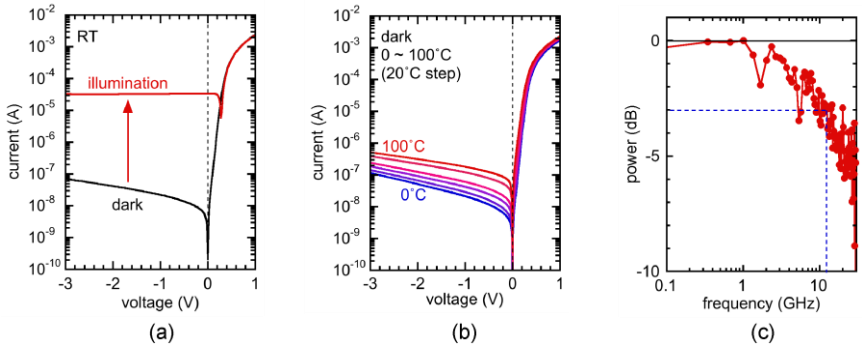


Fig. 2. (a) I-V characteristics with and without illumination of 1.55-μm light, (b) I-V characteristics under dark at different temperatures, and (c) frequency response.

Temperature dependence of I-V characteristics was measured under dark, as in Fig. 2(b). The dark current was less than 1 μA even at the increased temperature of 100°C, which is typically required for the practical applications. Figure 2(c) shows a typical frequency response. The 3-dB cutoff frequency was as large as 12 GHz, which was limited by the RC delay due to the high series resistance. The reduction of series resistance should lead to the 3-dB cutoff frequency more than 30 GHz.

SiGe/Ge heterostructures have potential applications to higher-performance devices. An example is low-noise and low-voltage avalanche photodiode (APD), where a SiGe layer is inserted at the interface between the optical absorption layer of Ge and the carrier-multiplication layer of Si or Ge, as in Figs. 3(a) and 3(b). The band discontinuity at the interface can realize low-noise and low-voltage APDs, resulting from an enhanced impact ionization for photo-generated carriers injected from the Ge optical absorption layer via SiGe. As in Fig. 3(c), the measured multiplication gain for hole-injection Ge/SiGe/Ge APDs was reduced in comparison with APDs without SiGe. This indicates that the SiGe/Ge heterojunction is effective for the low-voltage APD operation, although the excess noise characteristics are under investigations. Band engineering is also discussed using strained SiGe, which serves as a stressor to externally apply a stress to Ge mesa stripes selectively grown on Si.

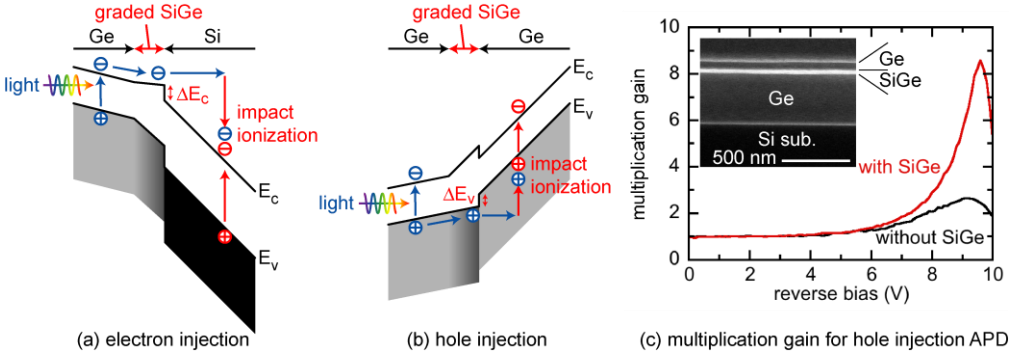


Fig. 3. Schematic band diagrams for Ge/SiGe heterostructure APDs.

Acknowledgements

This work was partly supported by "R&D on optical PLL device for receiving and monitoring optical signals", the Commissioned Research of National Institute of Information and Communication Technology (NICT), Japan.

References

[1] Y. Ishikawa, S. Saito, *Ge-on-Si photonic devices for photonic-electronic integration on a Si platform*, IEICE Electronics Express, vol. 11, 20142008, 2014.

[2] K. Yamada, T. Tsuchizawa, H. Nishi, R. Kou, T. Hiraki, K. Takeda, H. Fukuda, Y. Ishikawa, K. Wada, T. Yamamoto, *High-performance silicon photonics technology for telecommunications applications*, Science and Technology of Advanced Materials, vol. 15, 024603, 2014.

[3] Y. Miyasaka, T. Hiraki, K. Okazaki, K. Takeda, T. Tsuchizawa, K. Yamada, K. Wada, Y. Ishikawa, *Ge/graded-SiGe multiplication layers for low-voltage and low-noise Ge avalanche photodiodes on Si*, Japanese Journal of Applied Physics, vol. 55, 04EH10, 2016.

[4] M. Nishimura, Y. Ishikawa, *Band engineering of Ge layers on Si using SiGe stressors*, in Proceedings of the 7th International Symposium on Advanced Science and Technology of Silicon Materials, pp. 255-258, 2016.

[5] K. Ito, T. Hiraki, T. Tsuchizawa, Y. Ishikawa, *Waveguide-Integrated Vertical pin Photodiodes of Ge Fabricated on p^+ and n^+ Si-on-Insulator Layers*, accepted for publication in Japanese Journal of Applied Physics, vol. 56, 2017.